Quantitative Microstructural Evaluation of 12Cr Creep Aged Steels after Welding

Genevéve Marx

2016

Quantitative Microstructural Evaluation of 12Cr Creep Aged Steels after Welding

by

Genevéve Marx

(née Deyzel)

Submitted in fulfilment of the requirements for the degree of

Magister Scientiae

in the Faculty of Science at the Nelson Mandela Metropolitan University

Supervisor: Dr. J.E. Westraadt

Co-Supervisor: Prof. J.H. Neethling

January 2016

This dissertation is dedicated to my husband and parents.

For their endless love, support and encouragement

DECLARATION

In accordance with Rule G.5.6.3 of the General Prospectus,

5.6.3 A treatise/dissertation/thesis must be accompanied by a written declaration on the part of the candidate on the part of the candidate to the effect that it is his/her own original work and that it has not previously been submitted for assessment to another University or for another qualification. However, material from publications by the candidate may be embodied in a treatise/dissertation/thesis.

I, **Genevéve Marx (née Deyzel)** with student number **210059257**, hereby declare that this **dissertation** for the **degree Magister Scientiae** is my own work and that it has not previously been submitted for assessment or completion of any postgraduate qualification to another University or for another qualification.

Signature: _____

Date: _____

ACKNOWLEDGEMENTS

First and foremost, I would like to praise and give thanks to my Lord and Saviour, Jesus Christ, for the grace and strength He has provided me throughout this study.

I express my sincere thanks to the following people and organisations:

My supervisor, Dr. J.E. Westraadt, and co-supervisor, Prof. J.H. Neethling, for their guidance, support and advice throughout the duration of this project.

The National Research Foundation (NRF) and Nelson Mandela Metropolitan University (NMMU) for their financial assistance towards this research.

Eskom and Miss T. Rasiawan for supplying the samples.

My family for their guidance and encouragement.

My husband for his love, understanding and continuing support.

The assistance from the following people is also gratefully acknowledged:

Dr. J.E. Westraadt from the Centre for HRTEM for his assistance with the TEM.

Mr. W.E. Goosen from the Centre for HRTEM for his assistance with the SEM.

Mr. E.G. Minnaar from the Centre for HRTEM for his assistance with the FIB-SEM.

Mr. N. Mfuma from the Centre for HRTEM for his assistance with sample preparation.

Mr. M. Koopman from eNtsa for his assistance with the hardness measurements.

Dr. N. Fischer from UCT for his assistance with the XRD measurements.

LIST OF ABBREVIATIONS

Abbreviation	Meaning
ADF	Annular Dark Field
BC	Band Contrast
bcc	body-centered cubic
BF	Bright Field
BM	Base Material
BRT	Bulk Replication Technique
BSE	Backscattered Electron
CBED	Convergent Beam Electron Diffraction
CCT	Continuous Cooling Transformation
CCD	Charged Coupled Device
CGHAZ	Coarse-Grained HAZ
CL	Camera Length
CM	Critical Misorientation
CSEF	Creep Strength Enhanced Ferritic
DF	Dark Field
DH	Dislocation Hardening
EBSD	Electron-Backscatter Diffraction
EBSP	Electron Backscatter Diffraction Pattern
EDS	Energy Dispersive Spectrometry
EEL	Electron Energy-Loss
EELS	Electron Energy-Loss Spectroscopy
EFTEM	Energy-Filtered TEM
EM	Electron Microscopy
fcc	face-centered cubic
FEG	Field Emission Gun
FGHAZ	Fine-Grained HAZ
FIB	Focused Ion Beam
FWHM	Full-Width at Half-Maximum

GB	Grain Boundary
GIF	Gatan Imaging Filter
GR	Grain Reconstruction
HAADF	High-Angle Annular Dark Field
HAZ	Heat Affected Zone
HTPP	High Temperature Pressure Pipework
ICHAZ	Inter-Critical HAZ
IPF	Inverse Pole Figure
LB	Lath Boundary
LI	Linear Intercept
MHT	Microindentation Hardness Testing
MMA	Manual Metal Arc
ND	Normal Direction
PH	Precipitate Hardening
PWHT	Post-Weld Heat Treatment
RD	Rolling Direction
RGB	Red, Green and Blue
SAED	Selected Area Electron Diffraction
SBH	Sub-Boundary Hardening
SE	Secondary Electrons
SEM	Scanning Electron Microscope
SDD	Silicon Drift Detector
SGB	Subgrain Boundary
SSH	Solid-Solution Hardening
STEM	Scanning TEM
TD	Transverse Direction
TEM	Transmission Electron Microscope
TKD	Transmission Kikuchi Diffraction
WM	Weld Metal
X20	X20CrMoV12-1
XRD	X-Ray Diffraction

LIST OF FIGURES

LIST OF TABLES

SUMMARY

This dissertation focuses on the quantitative microstructural evaluation of new and creep aged X20 (12 Cr) stainless steel after welding. X20 stainless steel has been widely used in the high temperature and pressure pipework of coal-fired power plants. Consequently, this material has to withstand extreme conditions of high temperature and stress during service exposure. Under these conditions, creep deteriorates the strength of the material. The material's resistance to creep damage due to its microstructure can be quantitatively described by the back-stress. There are four microstructural contributions to the back-stress: Precipitate Hardening, Sub-Boundary Hardening, Solid-Solution Hardening and Dislocation Hardening. Fusion welding is performed on creep aged materials when a component needs to be replaced. This high temperature process results in the formation of different microstructural regions within the weldment. These creep damaged components have a weldability limit as set by the life management strategy of the power plant company.

Measuring techniques capable of quantifying the microstructural contributions (precipitates, subgrains and dislocations) were developed and evaluated in this study. These techniques were then used to characterise the different microstructural regions within a new and creep aged X20 steel weldment. Differences in the microstructure of the new and creep aged X20 steel was illustrated by the results of this study. The measured size and number densities of the precipitates in the creep aged X20 material showed that there is a decrease in PH during creep exposure. There was a decrease in SBH and DH stress for the creep aged X20 material due to coarsening of the subgrains and annealing of dislocations during creep exposure.

The quantitative techniques demonstrated in this study opens up the possibility to perform life assessment on weldments with inhomogeneous microstructures by following a microstructural based approach.

Keywords: power plant steels; microstructure; electron microscopy; life-assessment; welding.

TABLE OF CONTENTS

CHAPTER 1

INTRODUCTION

1.1 BACKGROUND

Coal-fired power plants burn coal to generate heat. The materials used in power plants are exposed to severe conditions of high temperature and stress during operation. The two critical components of a power plant are the high pressure steam pipes and the turbine blades in the turbine generator. The materials used to withstand these extreme conditions are normally Creep Strength Enhanced Ferritic (CSEF) steels with varying additions of chromium to impart corrosion resistance (Abe, Kern *et al.* 2008).

When a component needs to be replaced, fusion welding is most commonly used to join a new component into the existing system. Welding is also used in the construction of new power plants. Bhadeshia (2001) is of the view that welding is one of the most complex fabrication processes since it represents practically every metallurgical phenomenon: solidification, solid-state phase transformations, heat treatment, residual stress development and subtle chemical composition effects. The microstructure and hence the mechanical properties of the joined materials is significantly altered by the welding process.

Initial studies of weldments have revealed that a Heat-Affected Zone (HAZ) forms in the weld, which is a narrow zone of Bulk Material (BM) adjacent to the weld fusion line that has been altered by the weld thermal cycle. It was concluded with regards to the creep strength, that the HAZ was the weakest link in the weldment. Creep is a material aging process whereby the material loses its strength and ductility under a load over an extended period (Abe, Kern *et al.* 2008). Several failures, including catastrophic failures, of welded steam piping systems in the 1990's have increased the need to understand the creep behaviour of weldments. Initially these failures were ascribed to improper fabrication, installation, or unsuitable service conditions. Then it was observed by the industry that with increasing service hours, various other cracks, leaks and ruptures occurred which indicated the problems caused by the use of welded ferritic steel components. One such instance is when a main steam pipe of a newly

commissioned boiler ruptured within a few hours of service and Nebhnani, Bhakta *et al.* (2002) found root cracking in the weld joints. These failures of weld joints prompted an increase in research on failure characterisation, remaining life prediction methods, non-destructive testing methods, repair technology and ultimately the development of new improved steel grades and welding procedures. It was found that the weldability of a material decreases with creep ageing and a limit is reached where welding cannot be permitted on aged material. Consequently, the understanding of creep behaviour in weldments has become important over the last few decades (Middleton, Timmins *et al.* 1996). Today, similar efforts are put into the characterisation of weld metals and weldments to determine the creep properties as with base metals (Cerjak and Mayr 2008).

Aside from welding, another main problem for power plant companies is the life assessment of their power plant components. Throughout the years many methods have been used to perform life assessment. Interval services is the widely used approach. Power plant companies replace the component after it has operated for its design life time without any further life assessment, which is not a cost-effective practice. Subsequently, these companies has life management strategies in place that provide healthy operation of their power plant and these life management strategies have been modified over the years to provide the best performance out of their systems. Weldability limits for each material are also set in the life management strategies, which is usually done with respect to the creep damage accumulated during service. The current weldability limits are normally too conservative and do not allow full exhaustion of the useful life of a component (Van-Zyl 2000).

The life-assessment is usually done using a technique known as surface replication (Marder 1989). This technique entails quantifying the amount of creep damage of the component by counting the number of creep voids within a replica prepared from the surface of the component. A component is then replaced if the number of voids per area exceeds a pre-defined cut off value.

Research done by Holzer (2010), Sonderegger (2012), Molokwane (2014), Aghajani Bazazi (2009) and Eggler (1987) has shown that it is possible to use a microstructural based approach for determining the extent of creep damage. These studies are based on the fact that there are four microstructural contributions to creep strength:

precipitates, dislocations, grains and subgrains, and solid solution. This approach involves the calculation and/or modelling of the creep strength of the material by considering these contributions. Micro-mechanical modelling is the scientific basis for advanced power plant life assessment methods. For these models, it is important to establish the density of the free dislocations throughout the creep process (Pesicka, Aghajani *et al.* 2010). However, these micro-mechanical models consider the material to be single crystalline. The material of the components are in fact polycrystalline and hence macro-mechanical models are required. Macro-mechanical models can be obtained from the micro-mechanical models using a constant known as the Taylor factor (Holzer 2010; Sonderegger 2012). Even though these models provided more realistic results, they are still an approximation.

The area of research of this study is the creep resistance and welding limits of power plant steels such as X20 steel. Most of the previous research on the microstructural contributions has been performed on only the base material and not on the different regions of a weld. The situation becomes more complex for weldments and hence there is still a research gap on the creep strength of weldments. This study aims to narrow the research gap of the creep strength of weldments by evaluating to some extent the microstructural contributions in the various weld regions. Also, it forms part of a larger study for quantification of microstructure for creep weldability limits.

1.2 PROBLEM STATEMENT

Power plants have an ageing fleet of components. It is of high importance to replace the component before creep damage deteriorates it to the point where failure is inevitable. X20 steel is extensively used in the High Temperature Pressure Pipework (HTPP) of power plants. Failure of these HTPP could be catastrophic and must be avoided as it could result in life threatening accidents and unscheduled down-time. Complete system replacements are not economical and should be avoided if possible. Consequently, in order to perform replacements, selective welding has to be conducted on creep aged (damaged) components. These creep aged components have a weldability limit as set by the life management strategies. However, these weldability limits are not well defined for the different materials. Life assessment methods that will allow setting of realistic weldability limits are required for full exploitation of the components' useful life and safe operation of the component.

The approach of using surface replication for life assessment methods is too conservative for determining the remaining life of a component since it only considers the surface and not the volume within the specimen. In addition, surface replication is a macro technique and therefore does not take into account the microstructure of the component material.

The creep resistance of power plant steels such as X20 depends on the microstructure, which is complex and has various contributions to the creep strength of the steel. Subsequently, the evolution of the microstructure of the component material with service life can act as an indicator of the remaining life of a component. The creep resistance can be describe by the back-stress concept (Holzer 2010). Another important aspect to consider is that the microstructure of these steels are not stable, but it evolves during creep. Since creep limits the service life, there is an important need to understand the microstructural stability of CSEF steels during creep exposure, especially during long-term creep exposure (Kotska, Tak *et al.* 2007). Thus, there is constant research into developing better microstructure characterisation techniques and improved microstructure models (Hald 2008).

To further complicate matters, welding is one of the most complex fabrication processes and imparts microstructural and chemical changes to the steel, lowering the creep strength (Bhadeshia 2001). These changes results in void formation in the material. With creep, these voids grow together to form cracks in the material which could lead to catastrophic failure of the component. The main failure mechanism for CSEF steel weldments is Type IV cracking (Abe, Kern *et al.* 2008). This type of cracking occurs in the HAZ of the weldment and is a common problem. It is often the bottleneck of new building and maintenance projects of power plant companies. Surface bearing cracks appear only late in life. Consequently, it is not representative to only do surface examination of creep-exposed weldments to determine the amount of damage (Cerjak and Mayr 2008).

The main problems associated with the microstructural-based approach for weldments are:

- Quantification of the microstructural contributions.
- The representivity of the sampling of the true microstructure.

- Inhomogeneity of the weldment microstructure.

The main focus of this study is to develop quantitative microstructural measurement techniques that overcome these problems in order to characterise the microstructure of weldments by evaluating the precipitates, subgrains and dislocations. Since the solid solution strengthening is superimposed onto the other strengthening mechanisms, its contribution is not considered in this study. The results acquired in this study can then be used to refine existing or develop more accurate structure-property models for the determination of the back-stress. This will in turn make a contribution to more reliable and accurate life assessment strategies.

1.3 RESEARCH QUESTIONS

Three main questions relating to the quantitative measurement of the microstructural contributions, were generated for this study:

- How to measure precipitates?
- How to measure sub-grain size?
- How to measure dislocation density?

1.4 RESEARCH OBJECTIVES

- To develop and critically evaluate the best possible quantitative microstructural measuring techniques to assess for CSEF steel weldments the:
    - precipitates
    - subgrains
    - dislocations.
- To apply these techniques to new and creep damaged X20 weldments in order to show differences in microstructure.
- To contribute to a better understanding of the processing-structure-property relationships in creep exposed weldments.

1.5 SCOPE OF THE STUDY

Service exposed X20 steel pipework from Eskom power plants have been made available to study the evolution of microstructure and mechanical properties during welding. Weldments consisting of both new and service exposed X20 steel were prepared during welding procedure qualification and is analysed in this research project.

This study uses advanced electron microscopy techniques to evaluate the microstructure of the new and creep damaged X20 steel weldments. The quantitative evaluation is mainly performed on the BM of the weldments. These measurements are then used to calculate the back-stress using existing structure-property models. The other welding zones are qualitatively, and to some extent quantitatively, evaluated with a view of Type IV cracking, using the appropriate techniques.

In this project no attempt is made to fit creep prediction curves, to perform modelling of creep strength and no mechanical properties (other than hardness) will be measured on the creep damaged steel weldments.

1.6 SIGNIFICANCE OF THE STUDY

The techniques developed in this study will allow results to be obtained that will help refine life-assessment models for welded critical power plant components by using a microstructural based approach. Accurate life assessment models are needed to decide when a component must be safely replaced in a cost-effective manner. By determining the actual creep damage of a component by using microstructural analysis, the component can be managed with greater confidence and the life of it can be significantly extended. In addition, the best practice for repeatable and accurate microstructural assessment of creep-resistant materials is identified in this study.

1.7 OUTLINE OF DISSERTATION

The outline of the dissertation is as follows. In Chapter 2 a full literature review on the microstructure of power plant steels and the different strengthening mechanisms is provided. Included is the evolution of the microstructure of creep-resistant steels during creep exposure. A summary on creep resistant weldments and the

microstructural changes that occur during welding is also provided. Finally, a brief overview of X20 stainless steel is given.

Chapter 3 provides a discussion on the relevant experimental methods followed in this study. The sampling, methodology and sample preparation methods used to prepare the various specimens from the X20 steel weldments for analysis is given. These methods include sectioning, polishing, etching, bulk replication, twin-jet electro polishing, and Focused Ion Beam Scanning Electron Microscopy (FIB-SEM). Also provided, is a concise summary of the equipment and theory used in this study to perform analyses with Vickers Microindentation Hardness Testing (MHT), Transmission Electron Microscopy (TEM) and Scanning Electron Microscopy (SEM).

The results from the evaluation of the precipitates, subgrains and dislocations are presented and discussed in Chapters 4, 5 and 6, respectively. In addition, background is given with reference to previous studies that have performed quantification of the precipitates, subgrains and dislocations in order to extract the required microstructural parameters. The experimental procedures followed in this study to determine the precipitate parameters, subgrain size and dislocation density, are respectively discussed in each of these chapters. Lastly, the conclusions derived from the findings of the study are discussed in Chapter 7.

CHAPTER 2

LITERATURE REVIEW

2.1 CREEP AND DIFFUSION

Creep can be defined in numerous ways. Plastic deformation is known as an irreversible process that consists of both time-independent and time-dependent components, one of which is creep. Therefore creep can be seen as the slow and continuous plastic deformation of a material under a load over an extended period of time. Since diffusion can assist creep at elevated temperature, creep is normally associated with plastic deformation at elevated temperatures even though it can take place at any temperature above absolute zero Kelvin (Abe 2008).

Similarly, creep deformation is also defined as time-dependent straining under a constant applied stress or under a given load. In essence, creep results from complex dislocation behaviour. Diffusion acts as one of the most fundamental processes governing creep deformation. Oikawa and Iijima (2008) can be consulted for further discussion on the role of diffusion in creep deformation

There are three main stages of creep: primary or transient creep; secondary or steady state creep; and tertiary or acceleration creep (Abe 2008). Figure 2.1 illustrates these stages on creep curves and corresponding creep rate curves.

During the primary creep stage (until t_1) the creep rate decreases with time, which has been ascribed either to strain hardening or a decrease in free or mobile dislocations. The creep rate (between t_1 and t_2) remains constant during secondary creep, therefore it is described as steady-state creep. The common notion is to attribute this steady-state as a state of balance between the rate of recovery of dislocations which contributes to softening and the rate of generation of dislocations which contribute to hardening. During the tertiary creep stage (between t_2 and t_r) there is an increase in the creep rate with time until rupture at time t_r (refer to Figure 2.1). It is important to note that under the constant tensile load, the stress continuously increases as creep progresses. The most distinct effect of the increase in stress on the creep rate is

observed during the tertiary creep stage. Consequently, the increase in creep rate during the tertiary creep stage can be attributed either to increasing stress or microstructural evolution, which includes the evolution of damage due to creep. Microstructural evolution consists of various phenomena such as dynamic recrystallisation, dynamic recovery and coarsening of precipitates, which leads to softening and results in a decrease in creep resistance of the material. On the other hand, damage evolution includes the formation of creep voids and cracks mainly along the grain boundaries (Abe 2008).

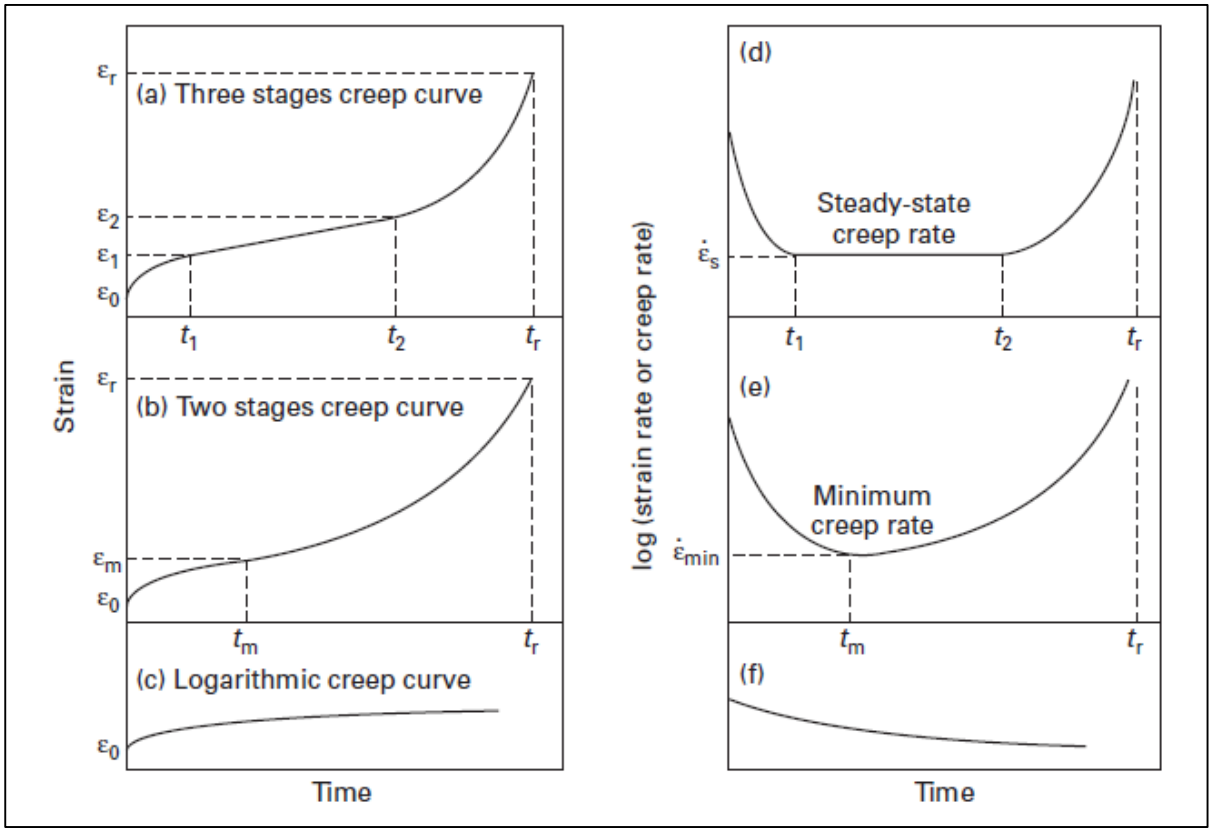

Figure 2.1: *(a), (b) and (c) Examples of creep curves of steels under constant tensile load and temperature. (d), (e) and (f) Corresponding creep rate curves as a function of time. (Abe 2008)*

2.2 9-12% Cr STEELS FOR POWER PLANT APPLICATION

There have been major changes in the power generation industry in the past decades. The issue of green energy is the main motivation behind these changes. For the fossil fuel power plants the major change was the implementation of the ultra-super critical (USC) unit generator technology. This technology improves the generating efficiency

and reduces CO_2 emission (Yan, Wang *et al.* 2013). The problem however with this technology is that it requires the power plant to operate under higher steam temperature and/or steam pressure. Consequently, tempered martensite 9-12%Cr ferritic steels such as T/P91 have been developed to meet these extreme operating condition demands (Maruyama, Sawada *et al.* 2001).

The different components of a boiler in a coal fired power plant, such as the superheater, water wall, reheater, header and main steam pipe, and their typical materials are illustrated in Figure 2.2.

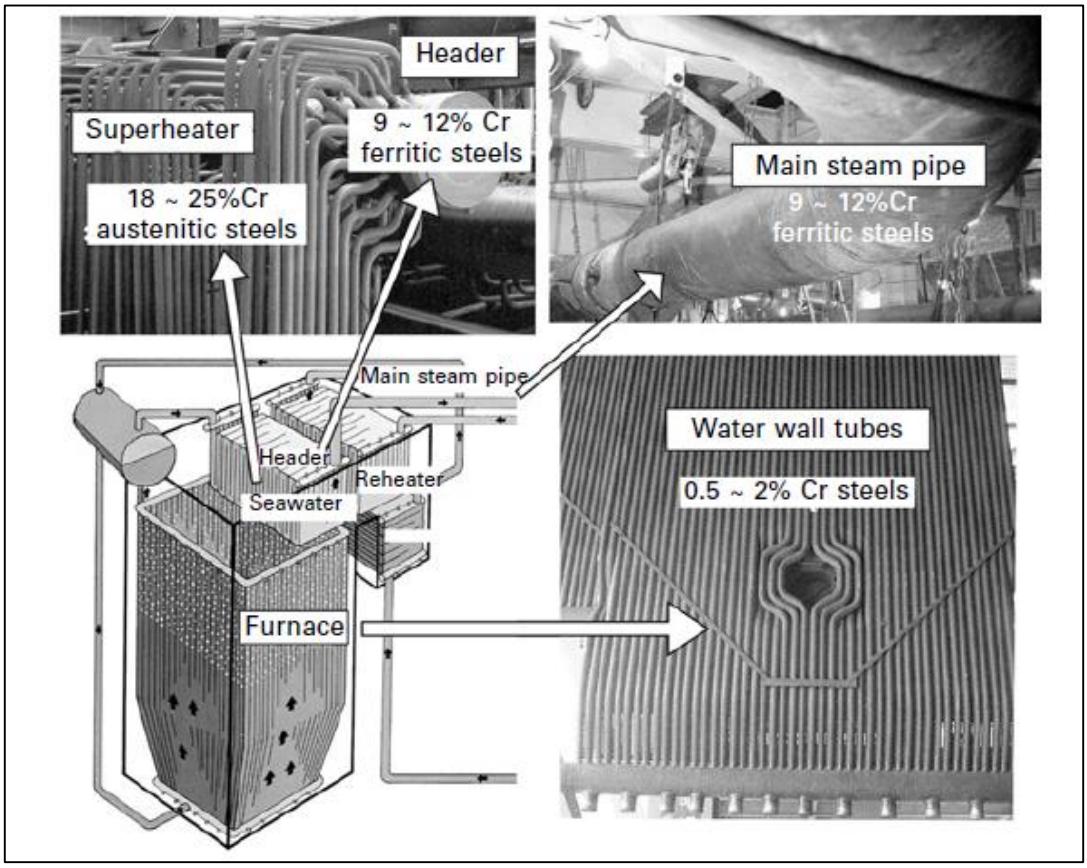

Figure 2.2: *Schematic illustration and images of components of a boiler in coal fired power plant and the typical component materials. (Igarashi 2008)*

As can be seen, tempered martensite ferritic or creep-resistant steels with 9-12% Cr content are mainly used for the header and main steam pipes that operate at temperatures between 500 °C and 650 °C in the creep range. In the header pipe the superheated steam is collected and the main steam pipe then transfers the high pressured steam to a turbine system (Aghajani Bazazi 2009).

The term “tempered martensite ferritic steel” indicates that the tempered martensite heat treatment regime was performed on the material and that the material has a ferrite matrix after heat treatment (Kotska, Tak *et al.* 2007). *For simplicity, anywhere in the text the term “9-12% Cr ferritic steel” will refer to “tempered martensite 9-12% Cr ferritic steel”.*

2.3 CREEP STRENGTH AND MICROSTRUCTURE OF TEMPERED MARTENSITE 9 – 12% Cr FERRITIC STEELS

The following section discusses the tempered martensite microstructure and its contribution to the creep strength of the material. A brief overview on the martensitic transformation is also provided. Lastly, the evolution of the tempered martensite microstructure and degradation of creep strength during service is discussed.

2.3.1 INITIAL MICROSTRUCTURE

The 9-12% Cr ferritic steels share the common feature of tempered martensite microstructure which is a consequence of their (slightly differing) complex chemical composition in combination with their large-scale processing (Holzer 2010; Yan, Wang *et al.* 2013).

The chemical composition of these steels are mainly characterised by a relatively low quantity of C and a Cr content in the range of 9 to 12 wt. %. Table 2.1 provides the rest of the alloying elements used in these steels, where Mo and W are the important solid solution strengtheners. Hofer (1999), Schaffernak (2000) and Yan, Wang *et al*. (2013) provide more detailed discussions on the alloying elements and their effect on the properties of 9- 12%Cr ferritic steels.

Tempered martensite is a single phase microstructure with a balance between high strength and high toughness which leads to achieving desired high creep strength (Yoshizawa and Igarashi 2007). The Fe-Cr-C phase diagram, provided in Figure 2.3, forms the basis for martensitic stainless steels.

Table 2.1: *Chemical compositions of typical 9-12% Cr ferritic steels (Yan, Wang et al. 2013).*

Element	Mass fraction /%								
	Steam pipes steel					Cladding structural steel			
	12CrMoV	P91	E911	P92	9Cr3W3CoB	Euro97	CLAM	9Cr2WVTa	F82H
C	0.2	0.1	0.1	0.1	0.1	0.1	0.1	0.1	0.1
Si	–	–	–	–	–	0.05	0.01	0.2	0.1
Cr	12.0	9.0	9.0	9.0	9.0	9.0	9.0	9.0	8.0
Mo	1.0	1.0	1.0	0.5	–	–	–	–	–
W	–	–	1.0	1.8	3.0	1.0	1.5	2.0	2.0
Co	–	–	–	–	3.0	–	–	–	–
Ni	0.5	0.1	0.3	0.05	–	–	–	–	–
V	0.3	0.2	0.2	0.2	0.2	0.2	0.2	0.2	0.2
Nb	–	0.05	0.05	0.06	0.05	–	–	–	–
Ta	–	–	–	–	–	0.08	0.10	0.07	0.04
N	–	0.06	0.07	0.06	–	0.02	0.02	0.02	–
B	–	–	–	0.001	0.014	–	–	–	–

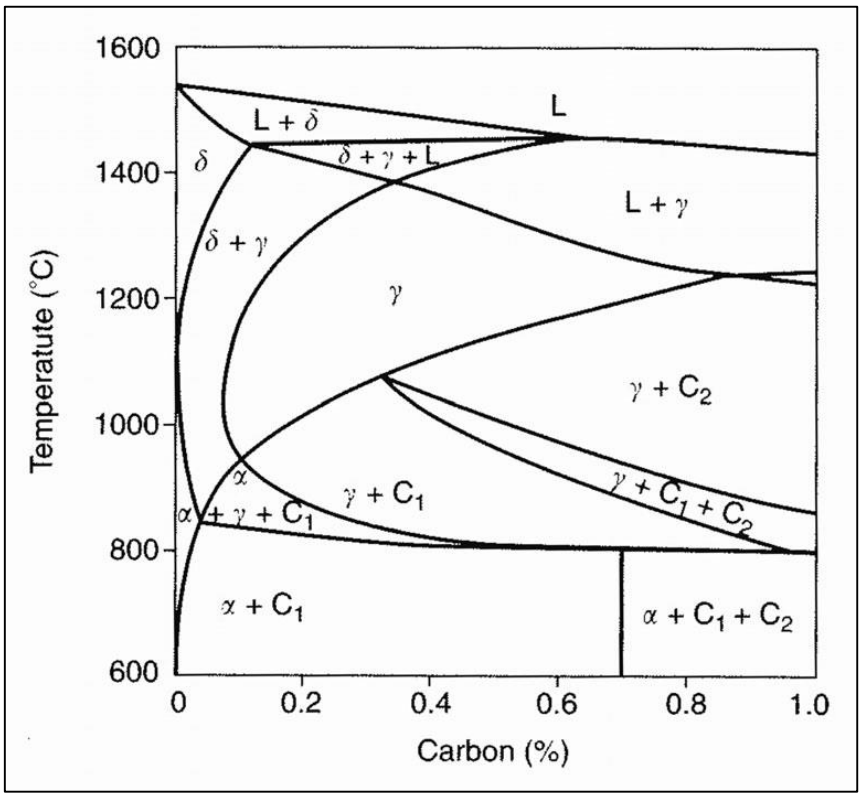

Figure 2.3: *Pseudo-binary phase diagram of Fe-Cr-C. C_1 and C_2 denote carbide phases. (Hedström 2007)*

The first step in the heat treatment of these steels is a normalising treatment known as austenitising where ferrite or α-Fe (body centered cubic (bcc)) transforms into austenite or γ-Fe (face centered cubic (fcc)) by heating above the Ac_1 temperature (between 1040°C and 1100°C) (Maruyama, Sawada *et al.* 2001; Aghajani Bazazi

2009). This is then followed by several tempering cycles in the range of 650°C to 780°C (below the A_{e1} temperature), depending on the type of component, for example, for pressurised components such as steam pipes, the high end of the range is used to achieve high toughness (Holzer 2010; Yan, Wang *et al.* 2013). As a result of the high Cr concentration, the material completely transforms into martensite during air cooling that follows after austenitising. Martensite is a highly strained body-centered tetragonal form of ferrite that is supersaturated with carbon (Bhadeshia 2002). The martensitic transformation is discussed in more detail in the next section. Consequently, a cellular dislocation structure with high dislocation density is introduced which provides strong structural hardening (Abe 2008). At this point the microstructure consists of prior austenite grains that are divided into packets and further into blocks of martensite laths of similar orientation (Abe 2008; Holzer 2010). Several phenomena occur during tempering: the martensitic lath structure changes into an elongated ferritic subgrain structure (Maruyama, Sawada *et al.* 2001; Aghajani Bazazi 2009); the dislocation density decreases (Holzer and Kozeschnik 2010); a dislocation substructure is introduced within the elongated subgrains due to the recovery of the dislocation cell structures (Maruyama, Sawada *et al.* 2001; Abe 2008); precipitation of secondary phase particles on prior austenite grain boundaries (GBs), subgrain boundaries (SGBs) and dislocations inside subgrains (Aghajani Bazazi 2009). From these observations, a simplified schematic illustration, as in Figure 2.4, can be drawn of the initial microstructure of a 9-12% Cr ferritic steel.

The dislocation substructure is composed of a subgrain structure, which is boundary dislocations that form small angle grain boundaries as a result of the rearrangement of the dislocations during the tempering treatment, and the free dislocations within the subgrains (Maruyama, Sawada *et al.* 2001; Holzer 2010). As can be seen from Figure 2.4, these subgrains are bounded by several boundaries: prior austenite GBs, blocks of martensite laths, martensite laths and subgrains within the laths. The first two boundaries are known as high-angle GBs that are characterised to have misorientations above 10 to 15° across the boundaries (Abe 2008). Both the small angle GB and martensite Lath Boundaries (LBs) have lower misorientations. It has been shown by Sonderegger (2008) that the small angle grain boundaries have

random small misorientations, whereas martensite LB show preferential axes-angle combinations.

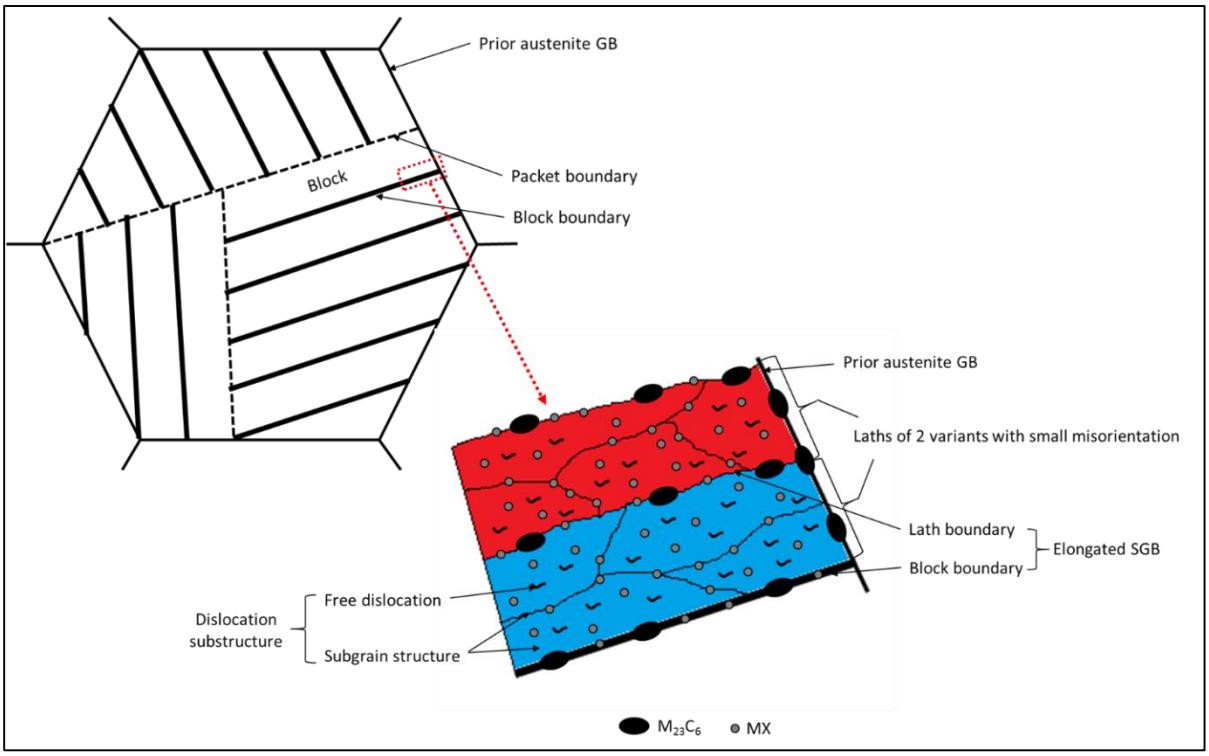

Figure 2.4: *Schematic illustration of the initial microstructure of tempered martensite microstructure in 9-12%Cr ferritic steels.*

The chemical composition determines which secondary phase particles form during tempering. The main strength determining precipitates that form are the $M_{23}C_6$ (M = Cr, Fe, Mo) carbides and MX (M = V, Nb and X = C, N) carbonitrides (Holzer 2010; Yan, Wang *et al.* 2013). A part of the Cr atoms in the Cr-enriched $M_{23}C_6$ carbide is replaced with Fe and other alloying elements. The MX carbonitrides are normally grouped into VN and NbC. C and N can substitute some of the N atoms in VN and C atoms in NbC, respectively (Maruyama, Sawada *et al.* 2001). $M_{23}C_6$ carbides, which are 50 to 100 nm in size, are larger than the MX carbo-nitrides that range from 20 to 50nm in size in the “as-received” condition (Holzer 2010). It can be seen from Figure 2.4, that the $M_{23}C_6$ carbides are located at the GBs and SGBs, and the MX carbo-nitrides are uniformly distributed within subgrains and along SGBs. The precipitation of these secondary phase particles may continue during creep (Maruyama, Sawada *et al.* 2001).

2.3.2 THE MARTENSITIC TRANSFORMATION

The martensitic transformation is also referred to as a shear or displacive transformation. This transformation is diffusionless due to very rapid cooling and Bhadeshia (2002) provides the evidence for this statement. Consequently, there are two significant aspects of this type of transformation (Stone 2014):

i. There is no change in the composition of the parent and product phases.
ii. There exists a crystallographic relationship between the parent and product phases, i.e. shear.

Accordingly, all martensitic transformations lead to a reproducible orientation relationship between the parent and product lattices. The interface plane between austenite and martensite is known as the habit plane. This interface plane is flat for unconstrained transformations, but when the transformation is constrained by its surroundings, for example other grain boundaries, then strain energy minimization introduces some curvature (Bhadeshia 2002). This is illustrated in Figure 2.5 and it explains the formation of the lath structure.

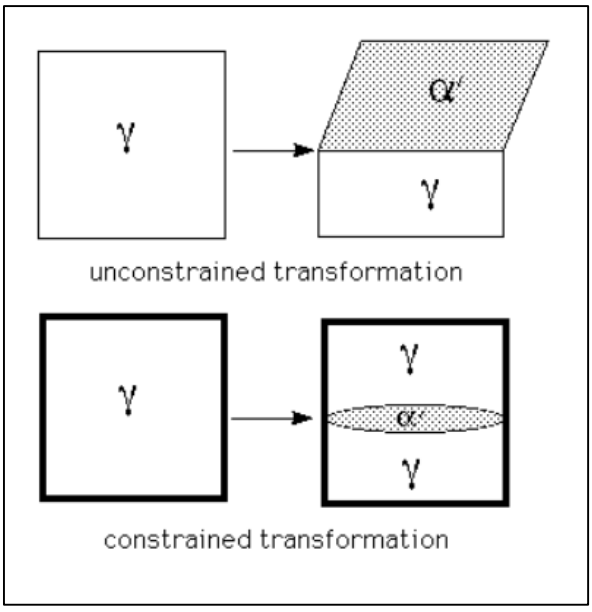

Figure 2.5: *Schematic illustration of the habit plane between austenite (γ) and martensite (α'). (Bhadeshia 2002)*

For low-alloy steels with less than 0.4 wt% C, the habit plane is the $\{111\}_\gamma$ plane (Porter, Easterling *et al.* 2009). For 9-12% ferritic steels the habit plane is approximately the $\{111\}_\gamma$ plane. The habit plane in steels changes with increase in

carbon concentration. Typical dislocated martensite laths have a Kurjumov-Sachs (KS) crystallographic relation to the parent austenite. There are other relations such as the Nishiyama–Wasserman (NW), but the KS relation is the most commonly used (Bhadeshia 2002; Morris, Kinney *et al.* 2013; Stone 2014). The KS relation aligns the phases so that they share a close-packed plane and a close-packed direction, resulting in a minimisation of energy. Thus, the following KS orientation relationship is implied for the planar match in the martensitic transformation in low-alloy steels:

$$\begin{matrix} \{111\}_\gamma \parallel \{011\}_\alpha \\ < 10\bar{1} >_\gamma \parallel < 11\bar{1} >_\alpha \end{matrix} \quad (2.1)$$

For example, there is a total of six KS relations or orientations for the planar match $(111)_\gamma \| (011)_\alpha$. The reasoning for this is fully explained by Morris, Kinney *et al*. (2013). Since there are four independent {111} reference planes, there is a total of 24 independent KS orientations possible for the martensite laths produced by the transformation of a single austenite grain. Subsequently, these orientations define the possible variants of the martensite laths.

The strain required to transform the fcc lattice of austenite into the bcc martensite lattice is known as the "Bain Strain" (Bhadeshia 2002; Bhadeshia and Honeycombe 2006; Porter, Easterling et al. 2009; Morris, Kinney et al. 2013; Stone 2014). To obtain the martensite variant from the parent austenite, there is a compression along one of the $<100>_\gamma$ cube axes and a uniform expansion in the perpendicular planes until it becomes bcc. All of this is illustrated in Figure 2.6. This is followed by a rotation and a slight shear of the transformed crystal in order to match the close-packed planes and the crystal directions. Consequently, the crystal is both strained and rotated. The cube axis of compression is the most important feature of martensite and is known as the Bain axis. This axis determines the transformation strain and the relative orientation of its {100} planes. Therefore, the previous example of six KS variants for the planar match $(111)_\gamma \| (011)_\alpha$ corresponds to two representatives of each of the three Bain variants, i.e. compression along the x, y or z directions.

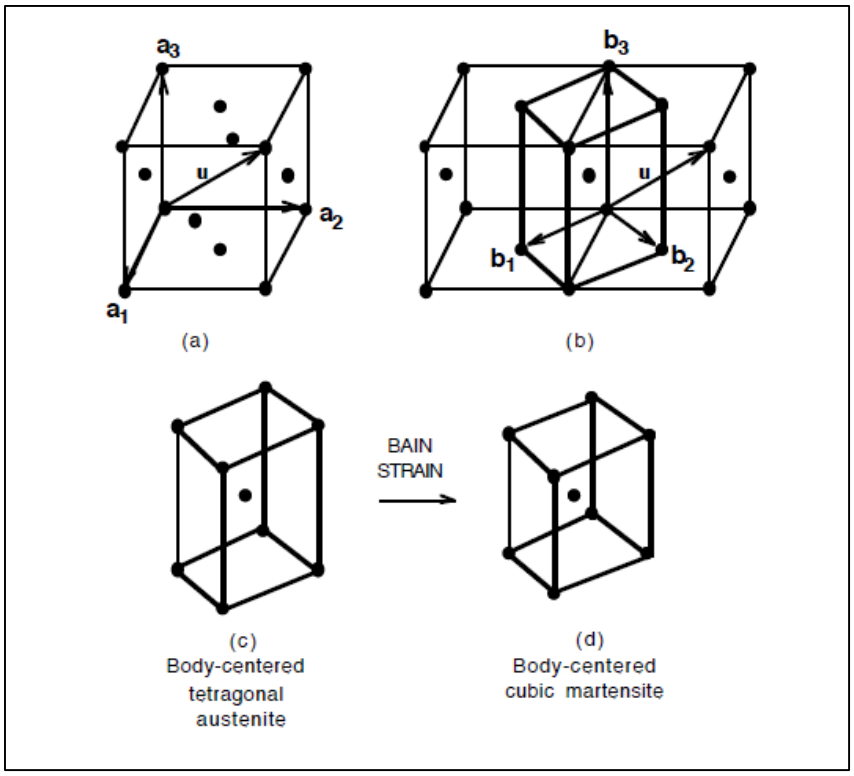

Figure 2.6: *Schematic illustration of (a) a conventional fcc unit cell, (b) relation between fcc and body-centered tetragonal austenite, (c) a body-centered tetragonal cell of austenite, and (d) the Bain Strain that deforms the body-centered tetragonal lattice into a bcc martensite lattice. (Bhadeshia 2001)*

In addition, a packet can also be defined as a set of blocks that share the same one of the four independent $\{111\}_\gamma$ planes of the parent austenite. Therefore, if orientation is considered, there are only four distinguishable packets possible. However, if the prior austenite grains are small, not all four of these packets will be visible in a single grain. It is also possible to define a block as a group of laths composed of two KS variants with small misorientation or, similarly, of the same Bain variant.

2.3.3 BASIC STRENGTHENING MECHANISMS AT ELEVATED TEMPERATURE

The 9-12%Cr ferritic steels are also known as Creep Strength Enhanced Ferritic (CSEF) steels due to various types of obstacles in the microstructure to creep deformation (Maruyama, Sawada *et al.* 2001). These obstacles are mentioned in Section 2.3.1 and they are SGBs, free dislocations within subgrains, and $M_{23}C_6$ and MX precipitates. The main microstructural sources of creep deformation are the

movement of dislocations (dislocation creep) and SGB (Hald 2008). Therefore the material has high creep strength due to the hindering of dislocation motion by the microstructural features. It should be noted that solute atoms in solution, such as Mo and W, are another microstructural contribution to the creep strength (Maruyama, Sawada *et al.* 2001). Consequently, the different microstructural contributions provide the following strengthening mechanisms in 9-12% Cr ferritic steels (Holzer 2010):

- Boundary and sub-boundary hardening
- Precipitate hardening
- Dislocation hardening
- Solid solution hardening

These strengthening mechanisms and their contribution to creep strength in 9-12% Cr ferritic steels are discussed in the following sections. The potential of combining these strengthening mechanisms is also briefly discussed.

(i) Solid Solution Hardening

The increase in creep strength due to Solid Solution Hardening (SSH) is usually explained by considering the differences in atomic size and shear moduli of solute and solvent atoms. Local strain fields arise due to differing sizes of solute atoms, resulting in an increase in lattice resistance to deformation. The increase in creep strength due to SSH can be calculated using the following equation (Holzer 2010):

$$\Delta\tau_{ssh} = k \cdot c^n \qquad (2.2)$$

where k is a constant strengthening coefficient, c is the concentration of the solute atom in the matrix and n is a concentration exponent, usually between ½ and 1 depending on solute concentration and temperature. For a detailed derivation, the reader is referred to the discussion by Holzer (2010). Table 2.2 provides a summary of the k values that have been reported in literature for both substitutional and interstitial solute atoms in bcc Fe.

Substitutional solute atoms such as Mo and W have been preferred as effective solid solution strengtheners for CSEF steels, since they have much larger atomic sizes than solvent Fe atoms. The problem, however, is that the SSH contribution from Mo and W

to the overall creep strength is superimposed on other strengthening mechanisms such as Precipitate Hardening (PH) (Abe 2008). Sometimes the addition of Mo and W leads to the precipitation of a secondary phase particle known as the $Fe_2(Mo,W)$ Laves-phase and increases fine distributions of $M_{23}C_6$ carbides during exposure at elevated temperature. Consequently, the solute content of Mo and W in the matrix decreases and the contribution of Mo and W to SSH is reduced. Therefore when considering SSH in 9-12% Cr ferritic steels these effects due to precipitation of secondary phase particles need to be taken into account (Holzer 2010).

In the case of interstitial solute atoms, N is the well-known beneficial strengthener for long-term creep strength of CSEF steels through SSH as well as PH by fine carbo-nitrides (Abe 2008). Maruyama, Sawada *et al.* (2001) has shown that SSH is only effective in the absence of precipitate and dislocation hardening.

(ii) Precipitate Hardening

PH is one of the most important and effective strengthening mechanisms in 9-12% Cr ferritic steels. In order to optimally use this mechanism to strengthen the steel, these steels contain several types of secondary phase particles such as the carbides and carbo-nitrides discussed in Section 2.3.1, and intermetallic compounds (Abe 2008). These precipitates usually either form during heat treatment or during subsequent creep. They have different nucleation sites: GBs, SGBs and within subgrains (Holzer 2010). The precise explanation of how the precipitates provide strengthening to creep depends on the type of precipitate and its nucleation site (Maruyama, Sawada *et al.* 2001). In general, the precipitates act as obstacles to dislocation motion by acting directly with the mobile dislocations, and they retard the migration of GB and SGB by pinning the boundaries (Holzer 2010; Yan, Wang *et al.* 2013).

If there is a direct interaction between a precipitate and dislocation, there are several proposed mechanisms to determine the threshold stress that is required for the dislocation to bypass the precipitate (Abe 2008). Due to the character of these secondary phase particles in 9-12% Cr ferritic steels, it is assumed that the precipitates are not cut by the mobile dislocations (Holzer 2010). Consequently, the dislocation can overcome the precipitate only by general or local climb, or by the Orowan mechanism, depending on the temperature. These mechanisms have the greatest

contribution to creep deformation. Diagrams illustrating these mechanisms are given in Figure 2.7. The difference between these mechanisms is that the Orowan mechanism has little temperature dependence and becomes operative only under higher loads, while the climb mechanisms determine the strain rate at higher temperatures and lower stresses. For the purpose of this study, only the Orowan mechanism will be discussed. Holzer (2010) provides a clear description of the general and local climb mechanisms.

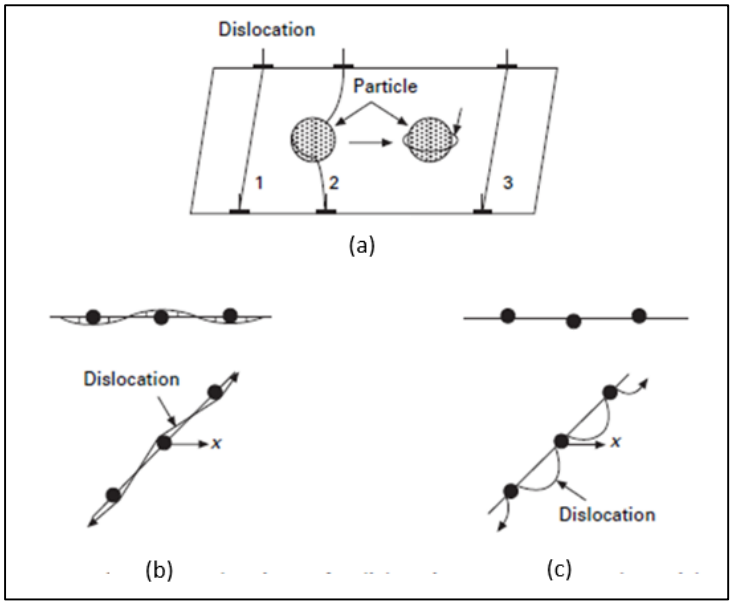

Figure 2.7: *Schematic illustration of how a dislocation will pass precipitates by (a) the Orowan mechanism, (b) the general climb mechanism and (c) the local climb mechanism (Abe 2008).*

A threshold stress for dislocation glide is introduced when a dispersion of particles intercept the glide plane of a dislocation. If it is assumed that these particles, with mean interparticle (planar) spacing λ, are strong enough so that they are not cut by the dislocation, then the threshold stress required to cause plastic flow is defined as the Orowan stress σ_{Or} (Holzer 2010). This Orowan stress σ_{Or} is described by the following equation (Abe 2008; Aghajani, Somsen et al. 2009):

$$\sigma_{Or} = \frac{0.8MGb}{\lambda} \tag{2.3}$$

where M is the Taylor factor, G is the shear modulus and b is the Burgers vector. Therefore it is evident from equation 2.3, that the Orowan stress can be calculated if

the interparticle spacing λ is known. A formula to determine the mean 2D surface-to-surface interparticle spacing λ is given by (Holzer 2010):

$$\lambda = \sqrt{\frac{\ln 3}{2\pi N_V \bar{r}} + 4\bar{r}^2} - 1.63\bar{r} \qquad (2.4)$$

where $\bar{r}$ is the mean particle radius and N_V is the number density. Thus, as can be seen from equations 2.3 and 2.4, the parameters of the precipitates play an important role in the creep strengthening of the material. Figure 2.8 shows the different stages of when a dislocation bypasses a precipitate (Holzer 2010): (a) when a mobile dislocation encounters precipitates, the dislocation segments in between the precipitates bend due to the acting shear stress in the glide plane; (b) if this acting shear stress, which is the driving force for dislocation motion, is large enough so that the dislocation segments are bent in such a way that they make contact behind the precipitate, there is annihilation of the segments at the contact point; (c) the segments can now move on, leaving behind a dislocation loop around each of the precipitates. Consequently, free dislocations in the matrix and subgrain structure is stabilised by a dispersion of fine precipitates, which in turn enhances Dislocation Hardening (DH) and Sub-Boundary Hardening (SBH) (Abe 2008).

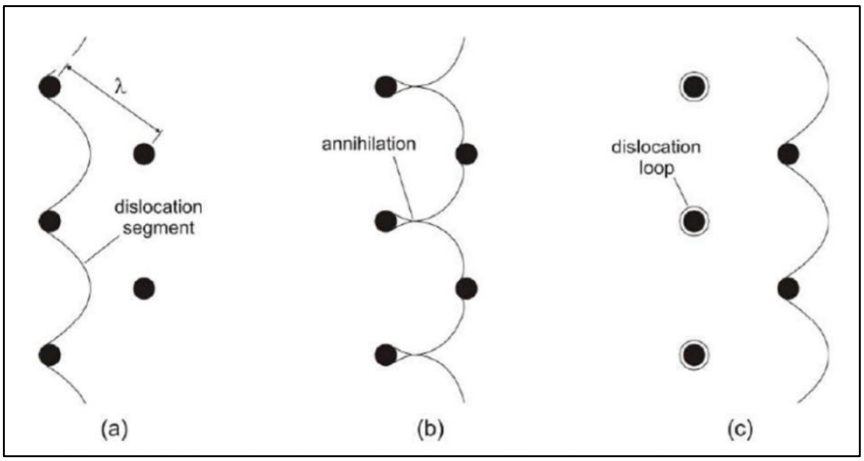

Figure 2.8: *Detailed illustration of the bypass of strong precipitates by a dislocation according to the Orowan mechanism, where the mean interparticle spacing is given by* ***λ.*** *(Holzer 2010)*

As mentioned in Section 2.3.1, the main strength determining precipitates in 9-12% Cr ferritic steels are the $M_{23}C_6$ (M = Cr, Fe) carbides and fine MX (M = V, Nb and X = C,

N) carbonitrides. Two explanations have been given for how MX precipitates within the subgrains contribute to PH (Maruyama, Sawada *et al.* 2001):

1) They themselves act as obstacles to movement of dislocations within the subgrains.
2) They retain DH for longer by slowing down the recovery of the dislocation substructure (subgrain structure with free dislocations).

Besides precipitate-dislocation interaction, the precipitates along sub-boundaries further increase the creep strength by effectively pinning the movement of SGB. Consequently, $M_{23}C_6$ (M = Cr, Fe) carbides contribute by carbide stabilised substructure hardening (Holzer 2010), which will be discussed in a later section.

In conclusion, PH by pinning of dislocations and SGBs should be considered the most important strengthening mechanism in 9-12% Cr ferritic steels. Consequently, the microstructure stability of these steels under creep load is dependent on the precipitate stability under creep load (Hald 2008).

(iii) Boundary and Sub-Boundary Hardening

As mentioned before, the 9-12% Cr ferritic steels usually have a tempered martensite microstructure that consists of prior austenite grains that are divided into packets and further into martensite block and lath SGBs that are normally elongated in shape (Abe 2008) (referred to as elongated SGBs). In addition, a dislocation substructure of small-angle grain boundaries with free dislocations is introduced during heat treatment (Holzer 2010). The GBs and elongated SGBs are high-angle boundaries. The advantages of high-angle boundaries are (Abe 2008):

- They interrupt the coherency of neighbouring crystallite lattices.
- They are in general impenetrable by mobile dislocations.
- They allow grains to slide relative to each other.
- They provide an effective short circuit path for diffusion of atoms.

Consequently, GBs and elongated SGBs have a strengthening effect known as Boundary and Sub-Boundary hardening (BH and SBH) that follows from the second point that they are impenetrable by dislocations and therefore act as major obstacles

against dislocation motion during creep. The small-angle subgrains do not contribute to SBH, since their low-angle boundaries results in planar dislocation networks and hence successful obstruction of dislocation movement is not possible.

The smaller the grains and subgrains, the higher the obstacle density and thus the higher the strength contribution. The classic Hall-Petch equation can be used to determine the strength contribution by grain refinement and is given by (Holzer 2010):

$$\tau_{gr} = k_{gr} \cdot {d_{gr}}^{-\frac{1}{2}} \tag{2.5}$$

where k_{gr} is the strengthening coefficient and d_{gr} is the grain diameter. However, in the case of 9-12% Cr ferritic steels the strength contribution from prior austenite grains is insignificant since their large size results in the fraction of GBs being very small compared to the fraction of SGB.

Maruyama, Sawada *et al.* (2001) states that it is in fact the elongated SGB (lath and block boundaries) that provide the SBH. A similar equation to equation (2.5) can be written for their strength contribution, which then leads to the SBH stress given by the following equation (Abe 2008):

$$\sigma_{sg} = \frac{10Gb}{\lambda_{sg}} \tag{2.6}$$

where λ_{sg} is the subgrain width or, in this case, the elongated subgrain short width. The constant 10 is derived from the Hall-Petch slope, which in turn is determined by considering the whole specimen and not a single grain within the specimen (Morito, Yoshida *et al.* 2006). Thus, the short width of the elongated subgrains λ_{sg} plays an important role in the creep strengthening of the material. In the 9-12% Cr ferritic steels, these short width values are in the range of 0.3 to 0.7 µm after tempering (Holzer 2010). Subsequently, high SBH stress σ_{sg} values are obtained and this led Maruyama, Sawada *et al.* (2001) to conclude that SBH is the predominant strengthening mechanism in 9-12% Cr ferritic steels and is therefore crucial to support creep strength in these materials. In other words, the SBH mechanism can provide more effective strengthening for higher creep strength than the Orowan mechanism of precipitates. To make full use of this SBH, subgrain stability is of great importance. The elongated

SGBs are stabilised by the fine distributions of $M_{23}C_6$ carbides and MX carbonitrides along these boundaries. Not only do these precipitates pin the migration of these elongated SGB, but they also exert a pinning force against the coarsening of these boundaries during creep (Abe 2008). To confirm this, it has been shown that carbide-stabilised elongated SGBs reduces the creep rate by orders of magnitude (Kotska, Tak *et al.* 2007). This suggests that strengthening by SBH is further enhanced by the dispersion of fine precipitates along the SGBs. Consequently, steels can have high creep resistance if there are fine and stable subgrains in the microstructure. The tempered martensite microstructure evolves into fine subgrains during long-term creep, which makes it the ideal microstructure for CSEF steels.

To clarify, during creep the elongated subgrains related to the martensitic transformation become equiaxed subgrains that is typical of creep deformation, which will be discussed in Section 2.3.4 (Maruyama, Sawada *et al.* 2001). Therefore the discussed SBH is in fact the martensitic lath structure hardening and the subgrain hardening only comes into action if this hardening is exhausted (Yan, Wang *et al.* 2013).

(iv) Dislocation Hardening

Dislocations are introduced into the microstructure through the martensitic transformation during air cooling and after austenitising (Section 2.3.1). The dislocation density after heat treatment is controlled by the tempering temperature since during tempering the dislocation density decreases and the temperature will determine the extent of this decrease. The dislocation substructure consists of small-angle subgrains with free dislocations. The free dislocation density ρ_f in the matrix contributes to the creep strength by Dislocation Hardening (DH) that is given by (Abe 2008):

$$\sigma_\rho = 0.5\, MGb\sqrt{\rho_f} \tag{2.7}$$

where M, G and b are the same as in equations 2.3 and 2.6.

Even after tempering, the 9-12% Cr ferritic steels usually contain a high density ($1 - 10 \times 10^{14}\, m^{-2}$ (Abe 2008)) of free dislocations ρ_f in the matrix. Therefore DH is an important strengthening mechanism at ambient temperature. Dislocations pass, with

the aid of an applied stress, through the dislocation substructure athermally at intermediate temperatures (Maruyama, Sawada *et al.* 2001). At elevated temperature, a high dislocation density increases softening by promoting the recovery of excess dislocations and recrystallisation of the deformed microstructure. In this case, diffusion assists dislocations in moving through the obstacles. Therefore, DH is only useful for short-term creep strength, but not for long-term creep strength at elevated temperature (Abe 2008).

(v) The Back-Stress Concept

When an external force is applied to a material, it can be assumed that the external forces acts simultaneously on each representative volume of the microstructure. If this external force is high enough, plastic deformation of the material occurs via the movement of dislocations, GBs and SGBs. The situation is different under typical creep deformation conditions of elevated temperature and small applied external load. In this case, a part of the external stress σ_{ex} is opposed by the heterogeneous constituents such as precipitates and interfaces (GBs and SGBs) of the internal microstructure. Subsequently, not the entire external load can be assumed to be responsible for the creep process, but only the part of the external stress σ_{ex} that exceeds the inner stress σ_i from the counteracting microstructural constituents, contributes effectively to the creep process. This is known as the *back-stress concept* since the inner stress $\sigma_i$reduces the effect of the external stress. Therefore it follows that the effective creep stress σ_{eff} can be given by (Kozeschnik and Holzer 2008):

$$\sigma_{eff} = \sigma_{ex} - \sigma_i \ . \tag{2.8}$$

Dimmler (2003) expresses the inner stress σ_i as a superposition of individual microstructural contributions from the dislocations and the precipitates. If the contribution from the SGBs are also taken into account then the following equation can be derived for the inner stress σ_i :

$$\sigma_i = M \cdot \sum \tau_i \ = M \cdot \left(\tau_\rho + \tau_{Or} + \tau_{sg}\right) = \sigma_\rho + \sigma_{Or} + \sigma_{sg} \tag{2.9}$$

where M is the Taylor factor, usually between 2 and 3 (Holzer 2010), σ are the individual back-stress contributions as determined by equations 2.3, 2.6 and 2.7, and

τ is the shear stress. It should be noted that SSH would not contribute to the inner stress σ_i since the solid solution is not a physical constituent that can oppose the external stress.

By including the Taylor factor M to determine the inner stress σ_i, it follows that the derived structure-property models (equations 2.3, 2.6 and 2.7) consider the material to be polycrystalline, i.e. consider microstructure of material as whole. The reason for this is that the inner stress σ_i represents the opposing stress from heterogeneous constituents from the entire material and hence the fact that it is determined by using equations 2.3, 2.6 and 2.7 means that these equations must also consider the polycrystalline nature of the material. Hence, these models can be classified as macro-mechanical models.

2.3.4 EFFECT OF CREEP: MICROSTRUCTURAL EVOLUTION DURING SERVICE EXPOSURE

It is evident that the higher the microstructural stability of a steel i.e. the lower the rate of evolution of its microstructure, the higher its creep strength will be under long-term service exposure. Consequently, by improving the microstructure stability of 9-12%Cr ferritic steels, their creep strength is enhanced at elevated temperature. To achieve this, the microstructural evolution of these steels during creep must first be well understood. The initial as-tempered martensite microstructure will always be inclined to evolve during service exposure (under conditions of high stress and high temperature) due to the fact that the tempered martensite phase is not a thermodynamic equilibrium phase. The evolution of the microstructure is normally characterised by lath widening, disappearance of prior austenite GB, emergence of subgrains, coarsening of precipitates and the precipitation of new phases (Yan, Wang *et al.* 2013). These microstructural changes is discussed further in the following sections.

(i) Evolution of Grains and Subgrains

Martensitic lath widening

Hu, Yan *et al.* (2011) has observed lath widening in a 10% Cr ferritic steel after creep at 600°C. The widened laths further expanded and finally evolved into equiaxed

subgrains after long-term creep (8 354h at 210MPa and 600°C). Sawada, Taneike *et al.* (2003) found that the mechanism of lath migration was that local parts of the lath boundary would bulge out and migrate. The reoccurrence of this bulging and migration of local parts then lead to the migration of the whole lath boundary. They made another observation that the relatively small laths would shrink until they finally disappear, while the larger laths would further widen. It has been reported that no lath widening occurs during aging due to the thermal stability of the lath structure in the as-tempered ferritic steels. This concludes that the driving force for the widening of the laths is the accumulation of strain during creep deformation. Consequently, the following conclusions can be made:

i. Strain, which can be seen as a stored energy, is the driving force for lath widening.
ii. Wide laths will grow larger and smaller laths will shrink and disappear.

As discussed before, in 9-12% Cr steels the migration of the lath boundaries are prohibited by having fine precipitates along the lath boundary to pin it. This is, however, not completely effective since the $M_{23}C_6$ carbides along the lath boundary are large and when the lath boundary bulges, it will move into the interior of the adjacent lath where there are only small MX carbonitride precipitates. The lath boundary can overcome these small obstacles much easier. Therefore, the bulging (or widening) of the lath boundary will not stop until it reaches other obstacles such as another lath boundary or GB (Yan, Wang *et al.* 2013).

Disappearance of Prior Austenite Grain Boundaries

The prior austenite GBs gradually disappear after long-term creep and what can be seen are the traces of these boundaries left by the precipitates that prefer to form along them. These boundaries can be seen as walls of dislocations that are able to trap and release dislocations. Even though the $M_{23}C_6$ carbides effectively pin the movement of prior austenite GB, their action is opposed by the formation of Laves-phase precipitates on these boundaries. The process is unavoidable since Mo and W are prone to segregate on the prior austenite GBs. The formation of Laves-phase has a two-fold effect:

i. These precipitates swallow the $M_{23}C_6$ carbides by nucleating and growing on them.
ii. Large Laves-phase precipitates cluster along the prior austenite GB, which leads to the swallowing of other useful precipitates.

These effects have the final result then of freeing the prior austenite GB from the pinning effect of the $M_{23}C_6$ and other precipitates along the boundaries. Consequently, the prior austenite GBs will eventually disappear by means of dislocation movement (Yan, Wang *et al.* 2013).

Development of Subgrains

Yan, Wang *et al.* (2013) observed for a CLAM steel that after short-term creep (98h at 600°C), the martensitic lath microstructure had developed into equiaxed subgrains. This transformation is shown in Figure 2.9.

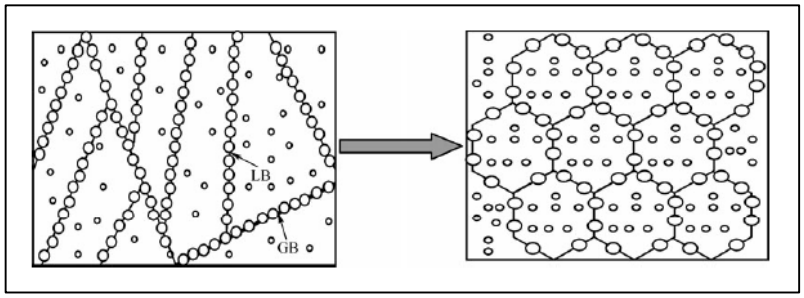

Figure 2.9: *Schematic illustration of the evolution of martensite laths into fine equiaxed subgrains (Yan, Wang et al. 2013).*

In the case where this is no creep deformation, i.e. during aging, it was found that no subgrains formed. Hence, it can be said that creep deformation causes the formation of subgrains during short-term creep. However, when the temperature was increased to 650°C, even the aged sample had newly formed subgrains and no laths. This suggests that it is both creep deformation and increase in temperature that promotes the formation of subgrains, which is in agreement with previous work (Cerjak, Hofer et al. 1999; Panait, Bendick et al. 2010). The effect of creep deformation and temperature on subgrain formation can be explained by considering the mobile dislocations in the microstructure. Creep deformation increases the number of mobile dislocations and a higher temperature increases the mobility of the dislocations. Thus, both of these instances will promote the interaction between the dislocations and hence accelerate

subgrain formation. As before, the driving force with creep deformation is the flowing of strain. The dislocations are driven forward by the strain. The subgrains are formed by the interaction of the dislocations with one another that leads to the formation of walls of dislocations. It is these dislocation walls that then make up the SGBs (Yan, Wang *et al.* 2013).

Subgrain Growth

It is well known that creep deformation, which involves the accumulation of strain, promotes growth of particles, whether it be precipitates or subgrains. At a given temperature, strain is required for the subgrains to grow and this was proved by Aghajani, Somsen *et al.* (2009) and Panait, Zielinska-Lipiec *et al.* (2010). They observed that the subgrain size increased during long-term creep exposure while during long-term aging the size was slightly affected. On the other hand Ghassemi Armaki, Chen *et al.* (2011) suggested that subgrain coarsening was controlled by strain only during short-term creep exposure and during long-term creep exposure it was controlled by the stability of the precipitates and not by the creep deformation. Both these viewpoints are correct and the same microstructural evolution after long-term creep was observed. The one group only paid attention to the strain or creep deformation aspect, while the other group only focused on the growth of the precipitates. There is an interaction between these two factors: strain or creep deformation will accelerate the coarsening of the precipitates and hence their pinning effect is lost, which in turn leads to subgrain coarsening. Therefore, strain has a noticeable effect on subgrain growth during short-term creep exposure, while during long-term creep exposure the stability of the precipitate plays an important role. It can be concluded that precipitate coarsening is the important feature during long-term creep exposure (Yan, Wang *et al.* 2013).

In summary, the tempered martensite laths evolve into a subgrain structure during long-term creep exposure. There are two important points that can be extracted from this evolution (Yan, Wang *et al*. 2013):

i. During short-term creep the main strengthening mechanism is the carbide-stabilised tempered martensitic structure strengthening.

ii. Subgrain strengthening is the main strengthening mechanism during long-term creep since it is critical to prevent the degradation of the creep strength.

Precipitate and Subgrain Interaction

In order to guarantee subgrain strengthening, that is crucial for long-term creep strength, it is important to stabilise the newly formed subgrains. The movement of the SGBs is controlled by the pinning force exerted by precipitates distributed along the boundary (refer to PH hardening section). This effect ensures a fine subgrain structure. Since the $M_{23}C_6$ carbides and MX carbonitrides are the main strengthening precipitates, the thermal stability of the subgrains depends on the stability of these precipitates (Yan, Wang *et al.* 2013). Previous studies have shown that the stabilisation of the SGBs was mainly due to the presence of fine $M_{23}C_6$ precipitates close to the boundaries (Cerjak, Hofer et al. 1999; Aghajani, Somsen et al. 2009; Armaki, Chen et al. 2011). The MX precipitates are rarely observed along the SGB and they are so small that they can easily be overcome by the movement of the SGBs. In contrast, the $M_{23}C_6$ precipitates have a similar size to the thickness of the SGB and therefore it is difficult for the SGB to cross them. As in the lath widening case, very large $M_{23}C_6$ precipitates are unfavorable. Therefore, in order to make full use of the stabilising effect of the $M_{23}C_6$ precipitates on the SGBs, it is important to inhibit coarsening of these precipitates.

(ii) Evolution of Precipitates

Coarsening of $M_{23}C_6$ precipitates

The $M_{23}C_6$ carbides are formed during tempering of the 9-12% Cr ferritic steels, as previously discussed. They nucleate along the GBs with high dislocation density. In the previous section it was seen that these precipitates are important for pinning the SGB. The disadvantage of the $M_{23}C_6$ precipitates are that they have a large coarsening rate during long-term creep exposure. It has been observed by Panait, Bendick *et al.* (2010) that the average equivalent circle diameter of the $M_{23}C_6$ precipitates in a P91 steel increased by approximately 120 nm after more than 100 000 h of creep exposure at 600°C. $M_{23}C_6$ precipitates that have a size of 100 to 200 nm are effective in pinning SGBs. In the long-term creep region, the coarsening is induced by strain from creep deformation. The chemical composition of the $M_{23}C_6$ precipitates also change during

long-term creep. It was found that the Cr content of the $M_{23}C_6$ precipitates increases with an increase in creep exposure time, i.e. the $M_{23}C_6$ precipitates become Cr rich after long-term creep exposure. The growth of the $M_{23}C_6$ precipitates can be inhibited by the addition of Co and B (Yan, Wang *et al.* 2013).

Dissolution of MX precipitates

The small MX carbonitrides are much more stable precipitates than the $M_{23}C_6$ carbides. They do not show any significant change in size, volume fraction or chemical composition during long-term creep exposure. However, the growth of the MX precipitates can be accelerated by creep deformation. There is a dissolution of the fine VN carbonitrides due to the precipitation of the modified Z-phase and this will be discussed further in the next section (Yan, Wang *et al.* 2013).

Precipitation of New Phases

Two new types of precipitates, that are not present in the initial as-tempered martensite microstructure, form during long-term creep and high-temperature exposure, namely the Laves-phase and Z-phase (Yan, Wang *et al.* 2013). In this study the Laves-phase is briefly considered in the chemical analysis of precipitates and the Z-phase is not at all investigated, but for completeness a brief discussion of each precipitate is provided below.

Laves-Phase

In 9-12% Cr ferritic steels, the Laves-phase is normally enriched with W and Mo and is designated as Fe_2W, Fe_2Mo or $(Fe, Cr)_2(W, Mo)$ precipitates (Panait, Bendick et al. 2010). They precipitate from the matrix, along the lath boundaries and have an initial short bar-like shape that develops into a large square shape. It was discussed how W and Mo are inclined to segregate along the LBs and GBs and therefore the Laves-phase precipitates are preferentially distributed along boundaries, especially the prior austenite GBs. Other elements such as Si and P have also been detected in Laves-phase precipitates. Laves-phase precipitates have a high growth rate and this rate increases with an increase in Mo and W content (Yan, Wang *et al.* 2013).

In general, the presence of Laves-phase in 9-12% Cr ferritic steels is not desirable since it degrades the mechanical properties of the steel, which included the creep strength. The Laves-phase forms at the expense of the solute W and Mo in the steel matrix and hence the solid solution strengthening effect is reduced. Also, when the precipitate size of the Laves-phase reaches a critical size due to its high coarsening rate during creep exposure, it triggers cavity formation. The consequence then is brittle intergranular fracture. The Laves-phase makes a small contribution to creep strength during short-term creep exposure, since its precipitation on the SGB, retards the recovery of the subgrain structure, but the effect quickly vanishes due to the high coarsening rate of the Laves-phase precipitates (Yan, Wang *et al.* 2013). The presence of Si and Cu accelerates the precipitation of the Laves-phase in tempered martensite steels (Aghajani Bazazi 2009).

Z-Phase

The Z-phase has a beneficial strengthening effect. The Z-phase precipitates very rapidly as small finely distributed rod like precipitates. The original CrNbN Z-phase has a tetragonal crystal structure. There is a modified Z-phase, where half of the Nb atoms are replaced by V atoms and therefore it has a chemical composition of Cr(V, Nb)N. The behaviour of the modified Z-phase is also different than that of the original Z-phase. The modified Z phase only precipitates after long-term creep exposure and after further exposure there are only a few coarsened precipitates left. As was the case with the Laves-phase, the LBs and prior austenite GBs are the preferred nucleation sites for the Z-phase precipitates. The driving force for the Z-phase formation is the Cr content. In steels with Cr content above 10.5%, the Z-phase precipitation is strongly accelerated. Another important element is N since it is another main element in the Z-phase. C and Co are elements that are not contained in the Z-phase, but can affect the driving force for Z-phase formation. Carbon atoms form $M_{23}C_6$ carbides that contain Cr and hence the Cr content is lowered, which reduces the Z-phase growth. In contrast, Co increases the growth of the Z-phase precipitates since it reduces the affinity of Cr to the ferrite matrix.

The Z-phase precipitates at the expense of the beneficial MX, specifically VN nitrides, which results in partial or complete dissolution of these precipitates and a reduction in the strength contribution of MX precipitates to PH. Therefore, the presence of the Z-

phase reduces the creep strength of a 9-12%Cr ferritic steel and can be detrimental for the service life of these steels. However, the extent of the effects of Z-phase formation on the mechanical properties of a steel is not clear yet (Yan, Wang *et al.* 2013).

(iii) Evolution of Dislocations

As mentioned before, plastic or creep deformation promotes the recovery of the dislocation substructure (subgrain structure with the free dislocations). There are two phenomena that occur during recovery: the subgrains widen and the deformed subgrains can reduce their stored energy by removing dislocations from their crystal structure, called an annihilation process (Pesicka, Aghajani *et al.* 2010). All of this leads to a decrease in the dislocation density within the subgrains. The increase in subgrain width with creep has been previously discussed. Pesicka, Aghajani *et al.* (2010) have shown that a tempered martensite 12% Cr ferritic steel has a very high initial dislocation density of $1.02 \times 10^{14}\ m^{-2}$, which is expected, and that this dislocation density rapidly decreases by an order of magnitude to $1.16 \times 10^{13}\ m^{-2}$ after short-term creep exposure (±12 000 h). After long-term creep exposure (±140 000 h), the dislocation density then gradually decreases down to $0.68 \times 10^{13}\ m^{-2}$. They also noted that the dislocations are not homogeneously distributed throughout the microstructure and attributed it to the orientation dependence of the recovery process in differently oriented subgrains. As mentioned in Chapter 1, these results contribute to the micro-mechanical modelling of 9-12% Cr ferritic steels. This type of modelling is the scientific basis for advanced power plant life assessment methods. For these models, it is important to establish the density of the free dislocations throughout the creep process (Pesicka, Aghajani *et al.* 2010).

2.3.5 EFFECT OF MICROSTUCTURAL CHANGES ON CREEP STRENGTH

There have been many efforts to explain the effect the above mentioned microstructural changes on the strengthening mechanisms and hence the creep strength of the 9-12% Cr ferritic steels (Holzer 2010). The following discussion will summarise from Section 2.3.4 by relating the microstructural evolution to loss in creep strength. Hald (2008) came to the conclusion that the stability of the microstructure of 9-12% Cr ferritic steels under creep load is equivalent to the precipitate stability. Therefore, the main creep strength loss mechanism is due to the evolution of the precipitates, which leads to a loss of PH and to a rapid coarsening of the dislocation substructure. The latter results in a decrease of SBH since the coarsening of the precipitates on the SGBs leads to an increase in particle size and decrease in number density with service exposure. Consequently, the obstacle (pinning) effect of the precipitates on SGBs and dislocation movement is significantly weakened (Holzer 2010).

The loss of PH has two causes. The first cause is the coarsening of the main strength determining precipitates namely the $M_{23}C_6$ carbides and MX carbonitrides. Subsequently, the interparticle spacing λ in equation 2.3 increases and the Orowan stress σ_{Or} value decreases. Precipitation of additional second phase particles, such as the Laves-phase and Z-phase, during service is the second cause for the decrease in the contribution by PH. The precipitation of these phases causes loss in creep strength over long-term creep exposure (Abe 2008).

The Laves-phase has a negative impact on creep strength due to the effect Laves-phase formation has on SSH. By referring to the section on Evolution of Precipitates above, the solute content of Mo and W, the main solid solution strengtheners, is considerably reduced by the precipitation of the Laves-phase. As a result of the large size and high coarsening rate of the Laves-phase, the decrease in creep strength cannot be compensated for by the PH effect of the Laves-phase. In addition, the Laves-phase triggers cavity formation.

Precipitation of the modified Z-phase in 9-12% Cr ferritic steels occurs after several thousand hours of creep exposure. It has been shown before that when the modified

Z-phase nucleates, a drop in creep rupture strength is observed. This loss of creep strength is due to the dissolution of the finely distributed VN precipitates within the subgrains at the expense of the formation of the modified Z-phase precipitates. The modified Z-phase only forms a few large precipitates and therefore it cannot make the same contribution to PH as the many fine VN precipitates (Holzer 2010).

2.4 CREEP STRENGTH AND MICROSTRUCTURE OF 9 – 12% Cr FERRITIC STEEL WELDMENTS

The thermal power generation industry uses creep resistant tempered martensite 9-12% Cr ferritic steels, referred to as creep-resistant ferritic steels or CSEF steels, extensively in the manufacturing of components (Section 2.2). Welding has been and still is the key fabrication process used to join and repair power plant components (Cerjak 2008). Bhadeshia (2001) is of the view that welding is one of the most complex fabrication processes since it represents practically every metallurgical phenomenon: solidification, solid-state phase transformations, heat treatment, residual stress development and subtle chemical composition effects. The microstructure and hence the mechanical properties of the joined materials is significantly altered by the welding process. The major design criterion for all components exposed to high temperatures during service, is the 100 000 h creep rupture strength of the base or Bulk Material (BM), Weld Metal (WM) and cross-welds (Cerjak and Mayr 2008).

In this section, firstly a brief overview is given on fusion welding. Then, the microstructural evolution of creep resistant ferritic steels during welding is described and the effect of creep on the weldment microstructure is discussed.

2.4.1 FUSION WELDING

Due to its extensive use in power plant construction works, fusion welding is an important type of welding process. Even though fusion welding can be carried out in many different ways, the basic process remains the same, namely welding components together by the solidification of a small amount of molten steel deposited within the gap between them (Bhadeshia and Honeycombe 2006). A very intense heat source is involved during fusion welding, leading to dilution or melting back of the BM. The extreme heating and cooling of the weld thermal cycle during fusion welding

results in high stresses and strains. Fusion welding is a complex process with many variables and each variable may have a significant effect on the final microstructure and properties of the weldment. For further reading on fusion welding the literature by Easterling (1992).

Manual Metal Arc (MMA) welding is the most common type of fusion welding process. A schematic diagram of MMA welding is given in Figure 2.12 and in Figure 2.10 is an image of an actual MMA weldment is provided. An electric arc, which has a high current (10-500 nA) and low voltage discharge (10–50 V) (Easterling 1992), acts as the heat source. The electrodes are a core of filler wire, and a flux coating that are composed of various silicates and metal oxides.

The term *steel weldability* refers to how preferably a steel can be welded without any weld defects and how well a weld joint of the steel can perform during service exposure (Yurioka 2001). Good weldability is a function of interrelating factors (Easterling 1992). If one of these factors are not suitable, it may cause cracking problems, which will be discussed in Section 2.4.4. Therefore, weldability can be also defined as the susceptibility of the steel to the various types of cracking mechanisms that are associated with steel weldments.

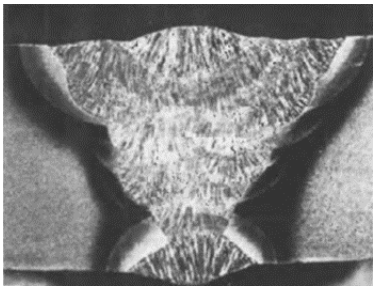

Figure 2.10: *Image of an actual MMA weldment. This is called a vee-butt weld due to its shape. (Easterling 1992)*

(i) Weld geometry

For the sake of completeness and later use in Chapter 3, a brief mention should be made of the weldment orientation axes. These directions are indicated in Figure 2.11 that provides a schematic illustration of a cross-section of a MMA (seam) weld performed on a steam pipe. The axes of a weldment are defined according to the processing geometry: the Rolling Direction (RD), the Normal Direction (ND) that is in

the direction of the through-thickness of the weld, and the Transverse Direction (TD) (Engler and Randle 2010).

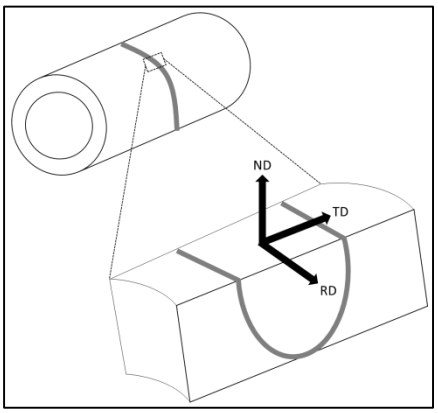

Figure 2.11: *Schematic diagram of a cross-section through a MMA weld performed on a steam pipe. The weld axes are given as the rolling direction (RD), normal direction (ND) and transverse direction (TD).*

2.4.2 EFFECT OF WELDING ON MICROSTRUCTURE

Fusion welding has a strong effect on the material properties since a new type of material, the WM, is deposited between the joined parts and the BM is transformed by the weld thermal cycle, which is a local and highly inhomogeneous heat treatment (Cerjak and Mayr 2008). The resulting metallurgy of the weld joint can be classified into two main regions known as the fusion zone and the Heat-Affected Zone (HAZ). The fusion zone has a solidification microstructure and represents both the deposited WM and the melted parts of the steel components. The HAZ is adjacent to the WM and includes the unmelted regions whose microstructures are only changed due to the heat flow during welding. An illustration of these fusion weld regions are given in Figure 2.12. A number of phase transformations can successively take place as the weld cools from the liquid state (Bhadeshia and Honeycombe 2006). It is the solidification in the fusion zone and the solid-state phase transformations in the HAZ during welding and subsequent cooling that cause the significant changes in the microstructure and properties of the weld joint (Walter 2001).

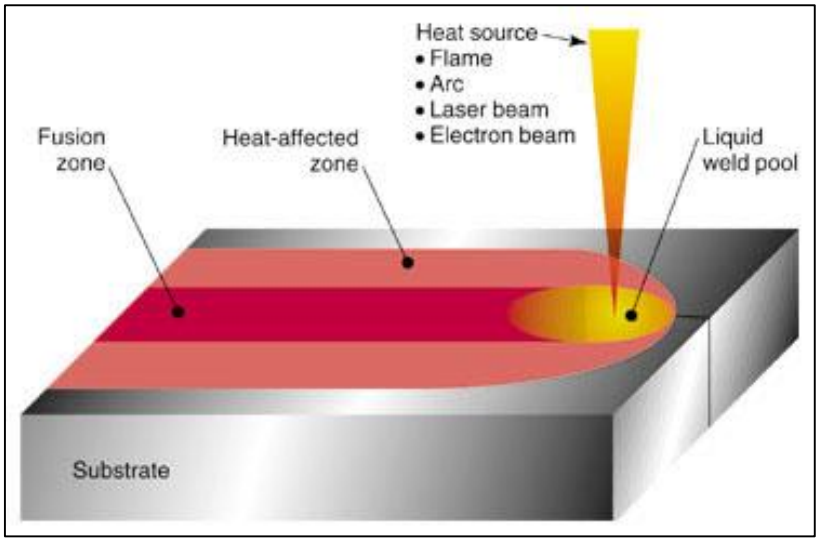

Figure 2.12: *Illustration of the fusion zone and HAZ of a fusion weld. (Walter 2001)*

MMA welding has a maximum heating rate of 200 – 300 $K \cdot s^{-1}$. As a result, there is a shift of the transformation temperatures to considerably higher temperatures than predicted by the equilibrium phase diagram of the steel. The recrystallisation temperature, coarsening rate and solution of carbides and nitrides, and the main proportion of grain growth are all parameters that are also affected by the heating rate (Cerjak and Mayr 2008).

The aim of this section is to only describe the microstructural evolution that occurs in the HAZ since it is the main region of interest. For overviews on the microstructural evolution of the fusion zone, including the microstructure of the WM, the literature by Easterling (1992) and Granjon (1991) can consulted.

(i) Heat-Affected Zone

As with the WM, the microstructure and properties of the BM is also significantly affected by the welding process. The original microstructure is altered and a HAZ is formed in the portion of the material which has not been melted, as a result of the heat flow during welding (Bhadeshia and Honeycombe 2006). The heat flow during fusion welding can be described by several heat-flow equations (Easterling 1992). The appearance of the HAZ is determined by the chosen welding procedure. The HAZ is completely austenitized during welding. The cooling rate then determines to which phase (ferrite, pearlite, bainite, martensite or a mixture) it transforms into upon cooling (Yurioka 2001). The phase transformations that occur in HAZ during fusion welding

are summarised in Figure 2.13 along with the calculated equilibrium phase diagram of P91 (X10CrMoVNb9-1) steel. The HAZ consists of different regions that form due to the temperature gradient, i.e. different peak temperatures T_p, experienced going from the WM to BM (Figure 2.13). These regions aren't separated by distinct borderlines, but it rather forms a continuous gradient from the fusion boundary between the deposited WM to the unaffected BM. Each of these regions have their own unique microstructure and properties (Cerjak and Mayr 2008). The range of peak temperatures T_p that are characteristic of each microstructural region is given in Table 2.2.

As mentioned in Section 2.3, PH is the most important strengthening mechanism in creep resistant ferritic steels and the microstructural stability is dependent on precipitate stability. Subsequently, precipitate stability is also a crucial factor in the HAZ of a weldment. There are three scenarios that must be considered when welding on a creep resistant ferritic steel (Cerjak and Mayr 2008):

1) The peak temperature is too low to have any visible effect on the precipitates;
2) The peak temperature is high enough to cause coarsening (grain growth) of favoured precipitates and partial dissolution of some precipitates;
3) The peak temperature is so high that it completely dissolves all precipitates, leading to loss of grain boundary pinning and hence enhanced grain growth.

Also discussed in Section 2.3, is SBH and its dependence on precipitate stability, which explains the third scenario. This type of strengthening is not only vital for good mechanical properties such as tensile strength, toughness and creep rupture strength, but also for determining the susceptibility of a steel to damage mechanisms like cold cracking, reheat cracking and Type IV cracking (Cerjak and Mayr 2008). The latter is discussed in Section 2.4.4. The sections that follow briefly describe the microstructures of the different weld regions shown in Figure 2.13 and have been compiled from the literature by Bhadeshia and Honeycombe (2006), and Cerjak and Mayr (2008).

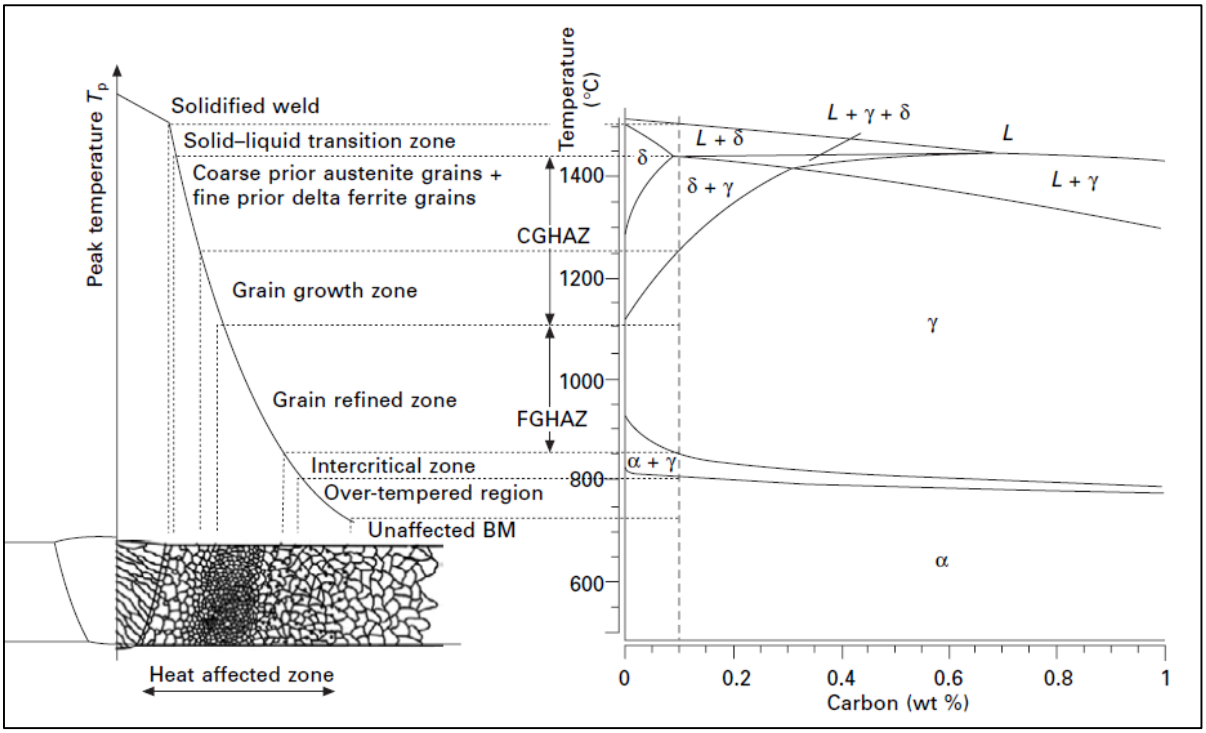

Figure 2.13: *Schematic illustration of the different microstructural regions in the HAZ correlated to the calculated equilibrium phase diagram of a P91 (X10CrMoVNb9-1) type steel. (Cerjak and Mayr 2008)*

Table 2.2: *Peak temperature T_p ranges for each microstructural region of the HAZ of a steel weldment. (Bhadeshia and Honeycombe 2006)*

HAZ microstructure (region)	Temperature range
Coarse-grained austenite (CGHAZ)	1500°C > T_p >1200°C
Fine-grained austenite (FGHAZ)	1200°C > T_p > A_{c3}
Partially austenitised zone (ICHAZ)	A_{c3} > T_p > A_{c1}
Tempered regions (Over-tempered)	A_{c1} > T_p

Grain Growth Zone (T_p >> A_{c3})

This region is adjacent to the weld fusion boundary and is also known as the Coarse-Grained HAZ (CGHAZ). Temperatures high above the Ac_3 transformation temperature

is experienced within this region as seen from Table 2.2. During continuous heating, austenite starts to form at A_{c1} = 800 °C and completely transforms at A_{c3} = 950 °C. These temperatures differ from the corresponding equilibrium temperatures since, as mentioned above, the temperature increases with heating rate. Therefore this region completely transforms to austenite. Any precipitates in this region dissolves, resulting in the formation of coarse or large austenite grains since the precipitates obstruct the growth of austenite grains at lower temperatures. In 9 -12% Cr steels delta ferrite grains may start to nucleate at a peak temperature of 1250 °C and higher, resulting in an overall decrease in grain size. Upon cooling, precipitates start to nucleate again and 9 – 12% Cr steels form a martensitic microstructure. This CGHAZ usually has the highest hardness value within the HAZ, but with corresponding low toughness values. During service and therefore under creep load, the CGHAZ is susceptible to reheat or Type III cracking.

Grain Refined Zone ($T_p > A_{c3}$)

This zone is referred to as the Fine-Grained HAZ (FGHAZ) and this region experiences lower peak temperatures of just above A_{c3} (± 1100°C). These temperatures lead to an improper development of the austenite grains, following the $\alpha \rightarrow \gamma$ transformation during heating, that produce small or fine austenite grains. Also the peak temperature may not be sufficiently high enough to completely dissolve all precipitates and therefore the undissolved precipitates can pin the austenite GBs, resulting in limited grain growth. New precipitates nucleate and the existing precipitates grow upon cooling. A fine grained martensitic microstructure is formed for 9 – 12% Cr steels. Due to the improper development of the austenite grains, the grains are too small for laths to form within them upon cooling. Subsequently, the prior austenite grains are in fact ferrite subgrains. The FGHAZ is considered the weakest link in weldments during creep loaded service. It has been observed that over longer periods of service and under lower stress levels most of creep-resistant ferritic steel weldments fail within the FGHAZ by Type IV cracking.

Partially Transformed Zone – Inter-Critical HAZ ($A_{c1} < T_p < A_{c3}$)

In this zone, a partial transformation of ferrite into austenite takes place upon heating since the peak temperature experienced in this region is between A_{c1} and A_{c3}. Within

this region, known as the Inter-Critical HAZ (ICHAZ), new austenite grains nucleate at preferred sites, such as prior austenite grain boundaries or martensite lath boundaries, while the tempered martensitic microstructure is only tempered for the second time by the weld thermal cycle. Due to the higher solubility of carbon in γ-Fe, the austenite that forms has a higher carbon concentration. Partial dissolution of the precipitates and coarsening of these undissolved precipitates occur in the ICHAZ. This effect is more pronounced if subsequent PWHT follows. Two microstructures co-exist after cooling: newly formed bainite for low chromium steels and pure martensite for higher chromium steels; and the tempered initial microstructure. A small grain size is observed in the ICHAZ and the lowest hardness values are measured in this region of the weldment. Consequently, the hardness values of the FGHAZ will be between the maximum value from the CGHAZ and minimum value from the ICHAZ. The ICHAZ and FGHAZ both show similar proneness to Type IV cracking.

Over-Tempered region

The peak temperatures experienced within this region is below the A_{c1} transformation temperature. Consequently, no phase transformation of the microstructure occurs and the initial microstructure is only locally tempered at temperatures higher than that of the annealed BM. The extent of tempering decreases with distance from the fusion boundary. As a result, a higher coefficient of diffusion at this temperature may escalate the coarsening of any precipitates within this region. Certain alloys have the lowest hardness value within this region.

Zone of unchanged base material

Temperatures of up to approximately 700 °C are experienced within the zone of unchanged BM and hence it seems that no changes in morphology of the components take place. Weakening of the creep strength in this region have been observed for welded low alloyed quenched and tempered steels such as 1% CrMoV steels, where over-tempering effects are evident within the region.

(ii) HAZ Simulation

It is difficult to perform basic investigations on the HAZ of actual welds since the microstructural regions in the HAZ are extremely narrow. To overcome this problem, it is possible to simulate the weld thermal cycle under laboratory conditions in order to

study the microstructural and properties changes in the HAZ during welding (Easterling 1992). Each microstructural region can be simulated separately and hence a large sampling volume with a homogenous microstructure of each region is available for analysis. The input data for the simulation is the time-temperature profile for each microstructural region during the weld thermal cycle. This data is obtained either by physical measurement, derivation by analytical solutions of the heat conduction equation or by using refined numerical heat flow models (Easterling 1992). GLEEBLE™ and Smitweld™ are the well-known weld simulator techniques (Buchmayr 2005).

2.4.3 CREEP BEHAVIOUR OF WELDED JOINTS

High temperature creep exposed creep-resistant ferritic steel weldments all show similar creep tendency behaviours, regardless of their chemical composition and other parameters such as applied welding procedure. It has been observed from numerous creep tests of cross-weld samples that there is no big difference at lower temperatures in the creep strength of the BM and cross-weld (Bhadeshia and Honeycombe 2006; Cerjak and Mayr 2008). A noticeable difference is observed at higher temperatures and lower applied stress levels. Consequently, the time it takes for the cross-weld creep strength to deviate from that of the BM is dependent on the creep testing conditions, material grades and welding prerequisites. This includes parameters such as applied stress level, temperature, welding procedure and PWHT parameters. It has also been observed that at higher stresses and lower testing temperatures, the failure occurs randomly either in the BM, WM or HAZ. As mentioned previously, at lower stress levels and higher testing temperatures, it seems that the HAZ of creep-resistant steel weldments is the weakest link.

2.4.4 FAILURE MECHANISMS IN CREEP-EXPOSED WELDMENTS

Cracking in creep-exposed creep resistant ferritic steel weldments is the main mechanism that leads to failure of a component. The cracks are classified into different modes depending on their location and orientation within the weldments. Figure 2.14 provides a schematic illustration of the different modes of cracks that can occur within a weldment. Each crack mode corresponds to a different failure or deformation mechanism. Cracks within the deposited WM are classified as Type I and Type II

cracks. Type I cracks remain in the WM, while it is possible for Type II cracks to propagate into the HAZ and even into the BM. Any other cracks occur within the HAZ. Type III cracks form within the CGHAZ that is adjacent to the fusion boundary and can also spread into the BM. Cracks that form very close to the fusion boundary in a fully refined HAZ structure with higher fracture ductility, are classified further into Type IIIa cracks. The cracks that form within the FGHAZ or ICHAZ that is next to the BM, are of Type IV and they remain restricted to these regions.

Type IV cracking is the main mechanism in creep-resistant ferritic steel weldments that leads to failure of a component and therefore in this section only the Type IV mechanism will be discussed. Cerjak and Mayr (2008) was used to compile this section and can be consulted for further discussion on the other failure mechanisms mentioned above.

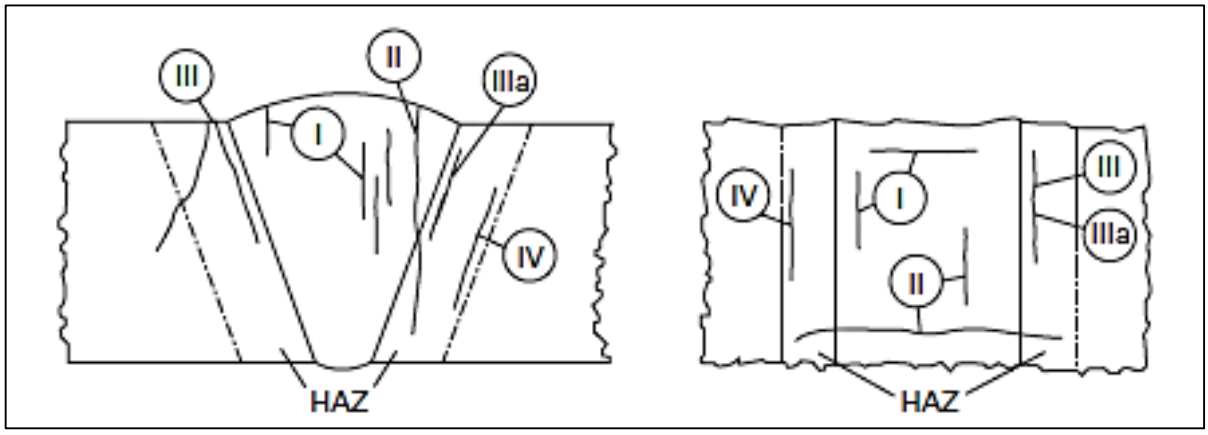

Figure 2.14: *Schematic illustration of the various cracking modes in a creep resistant ferritic steel weldment. (Cerjak and Mayr 2008)*

(i) Type IV Cracking

The formation and propagation of failures in the FGHAZ and ICHAZ defines Type IV cracking. It is in general difficult to distinguish between the FGHAZ and ICHAZ since they have similar microstructures. Presently, Type IV cracking is known as the main "end of life" failure mechanism for creep resistant ferritic steel weldments in power generation systems. Consequently, the Type IV mechanism is of great importance and numerous research has been done to understand this life limiting phenomenon in weldments. Type IV cracking has been observed in 9-12% Cr ferritic steels such as P91, X20CrMoV12-1 and P92 (Smith, Walker et al. 2003; Cerjak and Mayr 2008). The

time to rupture for Type IV failures depend on the stress state and applied loading direction.

At lower stress levels the fracture location shifts to the narrow FGHAZ and ICHAZ. Figure 2.15 provides an image of a macroscopic low deformation fracture (Type IV crack) located in the FGHAZ of a cross-weld sample prepared from an E911 pipe welded with matching filler and creep tested for 18 000 h at 600 °C. Type IV cracking is the result of a microstructural region of low creep strength that is surrounded by regions of stronger creep strength. Subsequently, this mismatch leads to a highly complex behaviour of the material.

Creep cavitation governs the Type IV failure mechanism. The creep voids nucleate in the sub-surface and grow by the diffusive mechanism. The formation of a very narrow band of voids in the outer region of the HAZ is shown in Figure 2.16 for a cross-weld sample prepared from an E911 pipe weldment and creep tested for 14 000 h at 600 °C. When the creep voids combine they from micro-cracks and these micro-cracks combine to form macro-cracks. It is these macro-cracks that then lead to failure. The particle/matrix interfaces that are associated with inclusions or secondary phase particles, are the preferred nucleation sites for the voids. From above, the precipitates are partially dissolved in the FGHAZ and ICHAZ due to the weld thermal cycle. Precipitation on the remaining large precipitates, such as $M_{23}C_6$, is favoured above re-precipitation of fine precipitates on grain boundaries. This occurs in order to decrease the interfacial energy of the microstructure. Thus, the remaining precipitates coarsen more rapidly during Post-Weld Heat Treatment (PWHT) than those in the BM or WM, which leads to them being preferred nucleation sites for creep voids (Cerjak and Mayr 2008).

Consequently, Type IV cracking is promoted by the microstructural changes, such as precipitate coarsening and Laves and Z-phase formation, that takes place in the HAZ during welding, subsequent PWHT and high temperature service (Albert, Matsui *et al.* 2002). Many researchers have shown that the kinetics of these microstructural changes are significantly faster for the ICHAZ than for any of the other regions in the weldment (Cerjak and Mayr 2008).

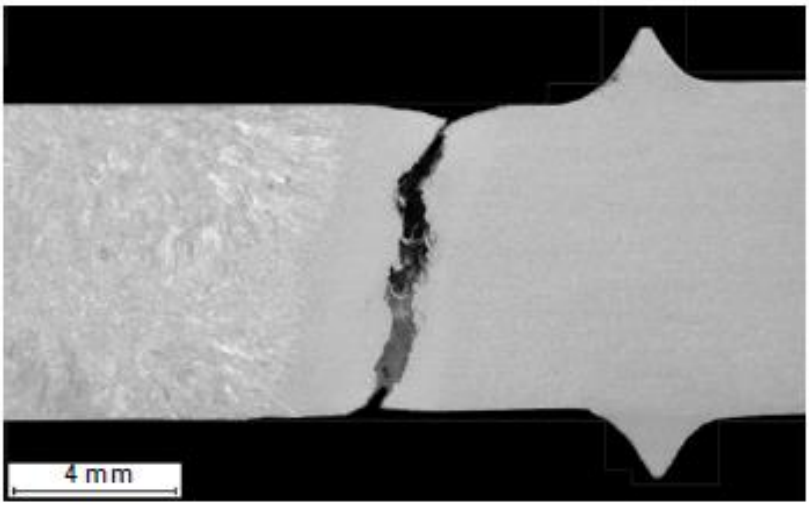

Figure 2.15: *Image of a macroscopic low deformation fracture in a cross-weld sample prepared from an E911 pipe welded with matching filler and creep tested for 18 000 h at 600 °C. The fracture is located in the FGHAZ and caused by the Type IV mechanism. (Cerjak and Mayr 2008)*

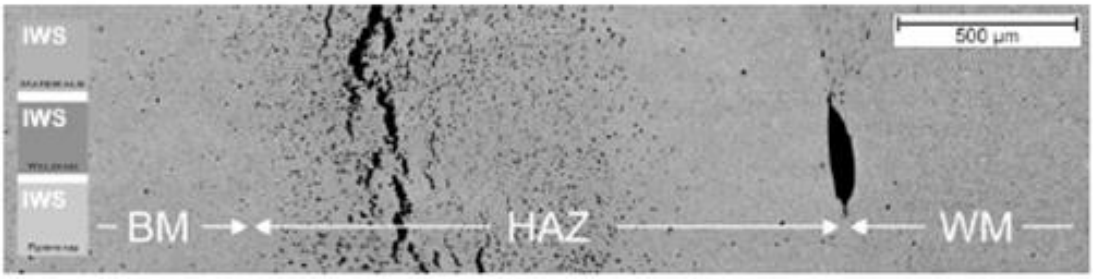

Figure 2.16: *Image of narrow band of voids at the outer region of the HAZ in a cross-weld sample prepared from an E911 pipe weldment and creep tested for 14 000 h at 600 °C. (Cerjak and Mayr 2008)*

Thus, in ferritic steel pipes, it has be seen that the predominant problem during long-term service is the creep damage accumulation in the ICHAZ by the Type IV mechanism. A common feature of Type IV failure is a low macroscopic failure strain that appears brittle. There is limited reported research on creep cavity accumulation in the narrow FGHAZ and ICHAZ (Smith, Walker *et al.* 2003). It is important to note that there is not always a direct relation between a “soft zone” with low hardness, and a low creep rupture stress (Cerjak and Mayr 2008).

2.5 X20 STAINLESS STEEL

For many years low alloy ferritic steels such as P22 grade (2.25Cr-1Mo steel) or equivalent grades has been extensively used in the main steam piping of coal-fired power plants. However, the problem is that this type of piping has a heavy wall thickness, which increases the overall weight. To overcome this problem, the martensitic stainless steel grade X20CrMoV12-1 was first developed in Germany as an alternative to P22. By using piping made of this steel, the wall thickness is reduced by up to 30% (Nebhnani, Bhakta *et al.* 2002).

This steel grade has been developed on the basis of the corrosion-resistant 13% Cr high temperature steels that contain up to 0.25% carbon in the tempered condition (EPRI 2006). X20CrMoV12-1 has been the first tempered martensite 9-12%Cr ferritic steel to be developed and has been widely used in European power plants for the steam pipes since the 1960s (Skobir, Godec *et al.* 2010). Initially, many problems have been encountered when welding was performed on X20CrMoV12-1 steel, which has not been experienced with the other steel grades and it was concluded that this steel requires stringent control during welding and PWHT of the steam pipes for successful application (Nebhnani, Bhakta *et al.* 2002). These weldability problems were overcome eventually in the late 1950s when crack-free X20CrMoV12-1 welds could be prepared for boilers and turbine piping operating at 560 °C steam temperature and 21.28 MPa service pressure (Molokwane 2014). Since then this alloy has been very successful for long-term service operation at 565°C. The DIN designation X20CrMoV12-1, known as X20, has been assigned as a standard (DIN 17175) for the 12CrMoV steels used in steam pipes (EPRI 2006). There are other standards of X20 steel due to slight chemical composition variations. Table 2.3 contains the chemical compositions for the different standards.

Table 2.3: *Chemical compositions of different standards of X20 steel grade. (Molokwane 2014)*

Standard (Designation)	Chemical composition (wt%)								
	C	**Si**	**Mn**	**P**	**S**	**Cr**	**Mo**	**Ni**	**V**
DIN 17175 (X20CrMoV12-1)	0.17-0.23	≤0.50	≤1.00	≤0.030	≤0.030	10-12.50	0.80-1.20	0.30-0.80	0.25-0.35
ISO 9327 (X20CrMoV11-1)	0.17-0.23	≤0.04	0.30-1.00	≤0.035	≤0.030	10-12.50	0.80-1.20	0.30-0.80	0.25-0.35
EN10222-2 (X20CrMoV11-1)	0.17-0.23	≤0.04	0.30-1.00	≤0.025	≤0.015	10-12.50	0.80-1.20	0.30-0.80	0.25-0.35

Since X20 is a 9-12% Cr ferritic steel, it has a high creep strength as discussed in Section 2.3. This enhanced creep strength is based on SSH and on the precipitation of $M_{23}C_6$ carbides (Aghajani Bazazi 2009). On the contrary, it is believed that the decisive factors for the high creep strength is the precipitation hardening by fine carbide intralaths and the stabilisation of the subgrain structure by the $M_{23}C_6$ carbides (Hu, Yang *et al.* 2008). This is supported by Section 2.3. It should be noted that since there is no Nb in X20 steel, only $M_{23}C_6$ (M = Cr, Fe, Mo) carbides and VX (X = C, N) carbonitrides are present in the microstructure of X20 steel. There have been numerous investigations on X20CrMoV12-1 steam pipes that have been exposed to long-term service (Storesund, Borggreen *et al.* 2006; Hu, Yang *et al.* 2008; Aghajani, Somsen *et al.* 2009; Auerkari, Salonen *et al.* 2013). The creep strength of X20CrMoV12-1 from each strengthening mechanism can be calculated using equations 2.2, 2.3, 2.6 and 2.7. Table 2.4 contains the values of the Taylor factor, shear modulus and Burgers vector for a tempered martensite 12% Cr ferritic steel (X20CrMoV12-1) operating at 550°C.

Table 2.4: *Summary of creep strength parameters for an X20CrMoV12-1 (DIN 17175) steel operating at 550 °C. (Aghajani, Somsen et al. 2009)*

Parameter	***Symbol***	***Value***
Taylor factor	M	3
Shear modulus	G	65 GPa
Burgers vector	b	2.5 x 10^{-10} m

X20 steel can be used for any components in both power generation and chemical plants that require high creep strength, corrosion and oxidation resistance under high temperature service. Superheater and reheater tubes, main steam pipes, and turbine cases and blades are some of these components (Figure 2.2) (EPRI 2006).

The mechanical, creep and fracture properties of X20 steels are highly dependent on the microstructure (Section 2.3). In turn, the microstructure is determined by the chemical composition and heat treatment history of the material. Standard testing methods are used to determine the material engineering properties in order to obtain information about the component design and service behaviour. Following Continuous Cooling Transformation (CCT) diagrams, the expected evolution of the microstructure can be determined. The CCT diagram for X20CrMoV12-1 steel is given in Figure 2.17. As can be seen, slower cooling rates, corresponding to near equilibrium conditions, results in ferrite formation. Under more rapid cooling conditions, bainite or martensite forms. The welding process typically includes rapid cooling rates for the WM and HAZ. Consequently, the CCT diagrams can be used for various manufacturing processes to develop and identify the thermal cycle that needs to be applied to obtain a desired microstructure (EPRI 2006).

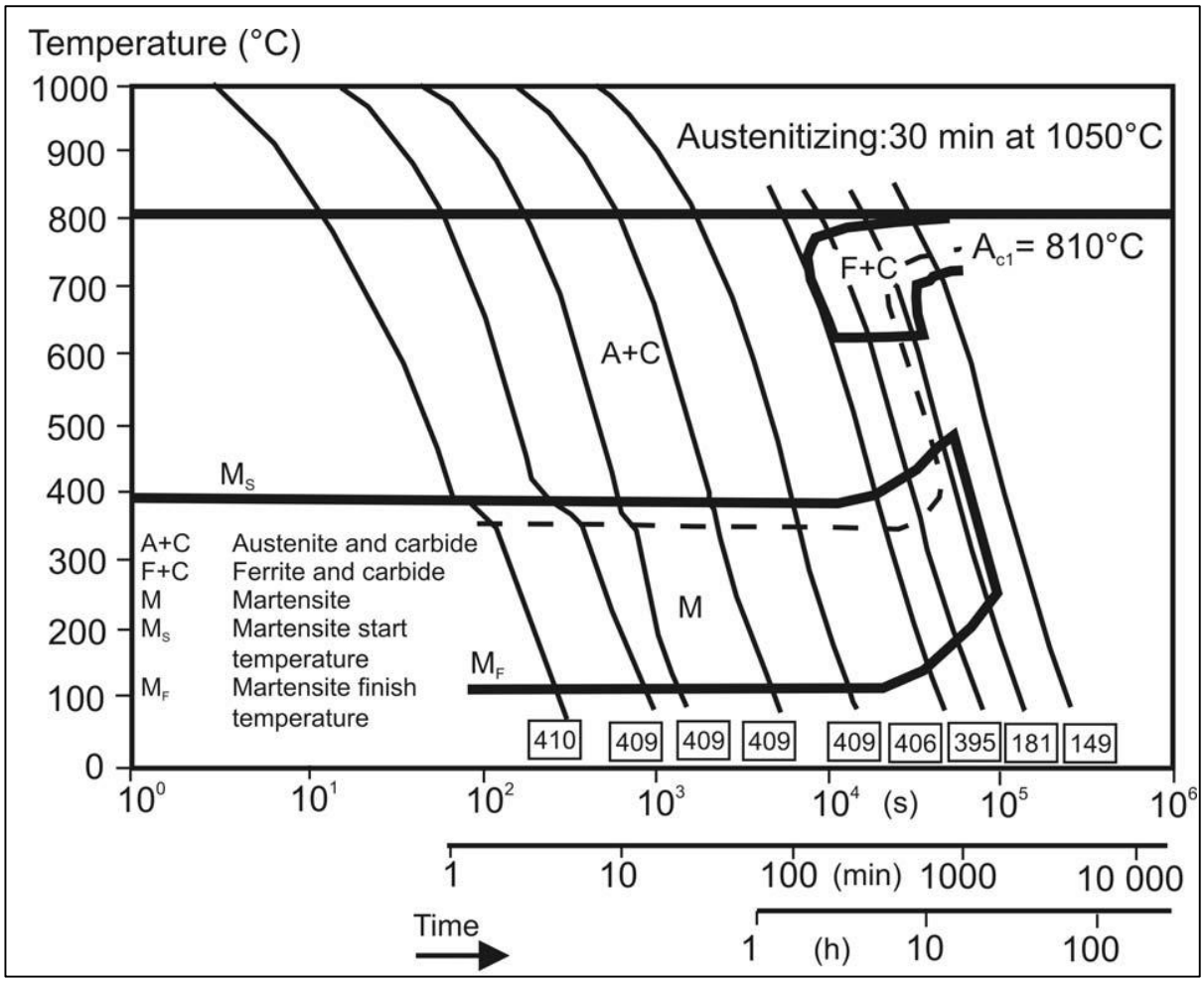

Figure 2.17: *CCT diagram for X20CrMoV12-1 steel. (Aghajani Bazazi 2009)*

CHAPTER 3

EXPERIMENTAL METHODS

3.1 INTRODUCTION

This chapter is of great importance, since one of the main objectives of this study was to develop and apply techniques that can be used to characterise the microstructure of a 12% Cr steel. Firstly, information is provided on the materials used in this study, which includes the welding procedures. The methodology followed to prepare the weldments and identify the different weld regions is discussed. Then, the methods used to prepare the various specimens for the different analyses is described. These methods include polishing, cutting, etching, Focused Ion Beam-Scanning Electron Microscopy (FIB-SEM) and twin-jet electropolishing. Also, a discussion will be given on a sample preparation technique known as the Bulk Replication Technique (BRT) that has been developed in this study for specific application to X20 steel.

This chapter also provides a summary of the theory related to the experimental techniques and equipment implemented in this investigation. The main techniques that will be discussed is the Electron Microscopy (EM) techniques used on both the Scanning Electron Microscope (SEM) and Transmission Electron Microscope (TEM). For more detailed literature on EM, some of the textbooks that can be referred to are Goodhew *et al.* (2001), Reimer and Kohl (2008), Williams and Carter (2009), Goldstein *et al.* (2003) and Zou *et al.* (2011). Metallurgy and mechanical techniques such as surface replication and Vickers microindentation hardness tests, is briefly discussed.

The exact procedures followed to investigate the microstructural contributions (precipitates, subgrains, dislocations) is described in detail under the Methodology section of Chapters 4, 5 and 6. This includes the methods used to process the results acquired using the techniques described in this chapter.

3.2 SAMPLING

3.2.1 Steel Sections

The X20 stainless steel analysed in this study is used in the High Temperature Pressure Pipework (HTPP) at Eskom's coal-fired power plants. This pipework delivers the high pressure steam from the final boiler superheater to the high pressure turbine (Eskom 2014). An image of this main steam pipework is shown in Figure 3.1(a). The pipework used for the specimens of this study had the following dimensions (Figure 3.1(b)): 255 mm ± 5 mm internal diameter and 35 mm ± 1 mm wall thickness.

Creep aged (damaged) /Ex-service X20 steel and virgin/new X20 steel pipework was provided by the Eskom Sustainability Division for research. Initially, the Bulk Material (BM), from which subsequent specimens are prepared for analysis, is classified as new X20 and X20_130_555. The latter being the service exposed X20 steel that has operated at Eskom's Tutuka plant. Table 3.1 summarises their operating conditions. As can be seen, X20_130_555 had operated at a higher temperature than the design temperature.

Figure 3.1: *Images of (a) typical main steam pipes used at coal-fired power plants (Bohler) and (b) the X20 steel pipework used in this research (Molokwane 2014).*

Table 3.1: *Operating condition data for service exposed X20 steel pipework.*

	Operating Temperature (°C)	Operating Pressure (MPa)	Design Temperature (°C)	Design Pressure (MPa)	Operating Hours
X20_130_555	555	17.5	545	19.4	129 801

From each pipework, a sample was sectioned and chemical analysis was performed on it by Scrooby's Laboratory Service Close Cooperation (Molokwane 2014). The chemical analysis results are provided in Table 3.2, as well as the chemical composition data for DIN 17175 Grade X20CrMoV12-1 from Table 2.4.

Table 3.2: *Chemical composition of X20 steel pipework used for this study.*

Element (wt%)	DIN 17175 (X20CrMoV12-1)	New X20	X20_130_555
C	0.17-0.23	0.19	0.20
Si	≤0.50	0.15	0.31
Mn	≤1.00	0.35	0.46
P	≤0.030	0.012	0.015
S	≤0.030	≤0.005	≤0.005
Cr	10-12.50	10	11.1
Mo	0.80-1.20	0.86	0.88
Ni	0.30-0.80	0.48	0.50
V	0.25-0.35	0.24	0.26
Cu		0.12	0.14
Al		0.025	0.038
Nb		≤0.005	≤0.005
Ti		≤0.005	≤0.005
B		≤0.001	≤0.001
W		≤0.005	≤0.005
Sn		≤0.002	≤0.002
As		0.0096	0.0157
Sb		≤0.005	≤0.005
N		676 ppm*	547 ppm*
Fe	Matrix	Matrix	Matrix

*parts per million (ppm)

Since the chemical composition of each sample falls within the specification range for DIN 17175, the X20 steel used for this study is X20CrMoV12-1. The other standards from Table 2.4 require the wt. % of Si to be lower than 0.04. The significant increase in Si content for the service exposed samples is due to the formation of Laves-phase (see Chapters 2 and 4).

3.2.2 Surface Replication

The X20 steel pipework was further classified according to the amount of creep damage on their surface using the technique known as surface replication. This technique is the conventional technique used by power plant companies to quantify the amount of creep damage and hence to determine the remaining life of a component. The surface replication technique is a well-developed microscopy technique that is used to conduct in-situ measurements of the microstructure of a specimen (Molokwane 2014). A schematic illustration of the technique is shown in Figure 3.2 and an extensive description of the technique is provided by Marder (1989).

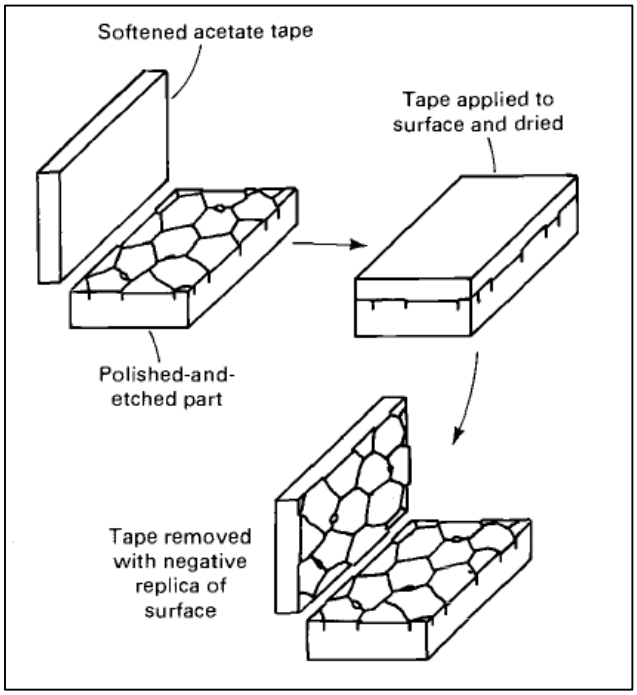

Figure 3.2: *Schematic illustration of the surface replication technique. (Marder 1989)*

Replica specimens were prepared of the surface of the X20 steel pipework and analysed at 500x magnification with a Leica optical microscope in order to determine

the amount of creep damage (Molokwane 2014). The measured creep void densities are given in Table 3.3.

Table 3.3: *Density of creep voids measured on the surface of the X20 steel pipework (Molokwane 2014).*

Bulk Material	***Creep Damage (voids/mm^2)***
New X20	No damage
Creep Damaged X20	340 ≤ x ≤ 485

As mentioned in the Chapter 1, this technique is too conservative and the acquired information about the creep damage is not representative of the complete microstructure of the entire specimen.

3.2.3 Welding

New X20 steel pipework was welded onto creep damaged X20 steel pipework (X20_130_555) using the Manual Metal Arc (MMA) welding process. Welding procedure qualification was performed in accordance with the American Society of Engineers IX (ASMEIX) Qualification Standard for Welding and Brazing Procedures, Welders, Brazers, and Welding and Brazing Operators (ASME 2008). The new X20 – X20_130_555 weld-joint was prepared with 12Cr-1Mo-0.25V-0.4W filler metal. A maximum heat input of 1.9 kJ/mm and preheat/interpass temperature of 200°C/250°C was used for the welding process.

Post-Weld Heat Treatment (PWHT) was performed on the weld-joint using parameters specified by Eskom. The annealing temperature is typically done at temperatures between 720°C and 780°C. Cooling below 150°C follows the welding process. However, it is not recommended that thick-walled tubes be cooled below 100°C prior to PWHT (EPRI 2006).

After welding, non-destructive and destructive testing was conducted in accordance with ASMEIX (ASME 2008). MATLAB laboratories performed the destructive testing, which includes tensile tests, guided-bend tests and notch-toughness tests.

3.2.4 Weldment Preparation

For easier handling, the welded X20 steel pipework needed to be sectioned. An 8 mm cross-weldment was sectioned from the top of the weld-joint. This is schematically illustrated in Figure 3.3(a). An image of the resulting X20 steel cross-weldment (new X20 – X20_130_555) analysed in this study is shown in Figure 3.3(b). The weldment of the new X20 steel material and the weldment of the creep damaged X20 steel material is also indicated.

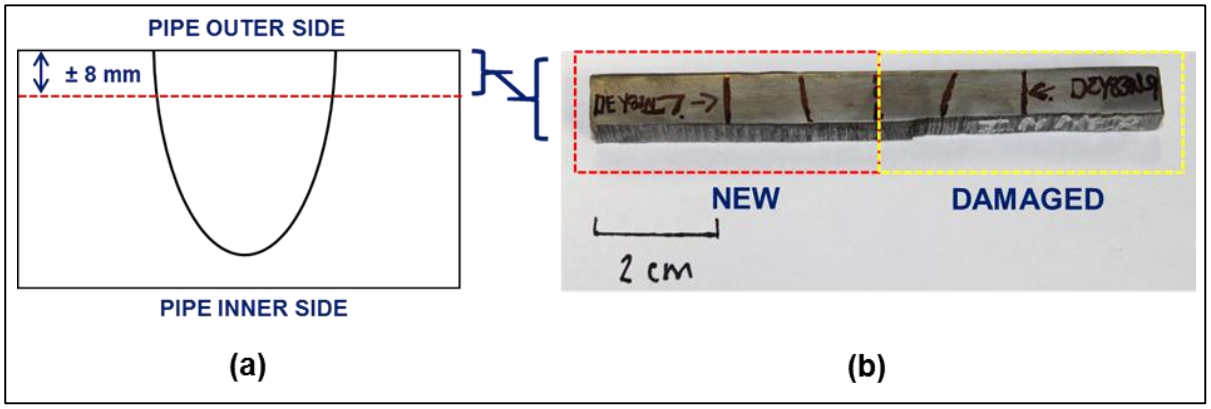

Figure 3.3: *(a) Schematic illustration of sectioning of welded X20 steel pipework. (b) Image of the X20 steel cross-weldment (new X20-X20_130_555) analysed in this study. Red outline corresponds to side of new X20 material and yellow outline corresponds to the side of the creep damaged X20 material.*

When the surface of a weldment specimen is slightly etched, the fusion Weld Metal (WM), fusion boundary, HAZ (Chapter 2) and BM can be distinguished by the naked eye. As an illustration of this, an image of the X20 steel (new X20 – X20_130_555) weldment shown in Figure 3.3(b), after its surface has been etched with Villella's reagent (1 g picric acid, 5 ml hydrochloric acid and 100 ml ethanol), is given in Figure 3.4. This identification then allowed for the lines to be drawn in onto the weldment as shown in Figure 3.3(b). These lines then acted as guides for further sectioning. The cross-weldment was then further sectioned as shown in Figure 3.5 into two separate weldments, namely a new X20 steel weldment and a damaged X20 steel weldment. These sectioned weldments were then used for further sample preparation and analysis. Optical micrographs of the etched surfaces of the weldments are also included in Figure 3.5. These optical micrographs were obtained using a Leica EZ4D optical microscope.

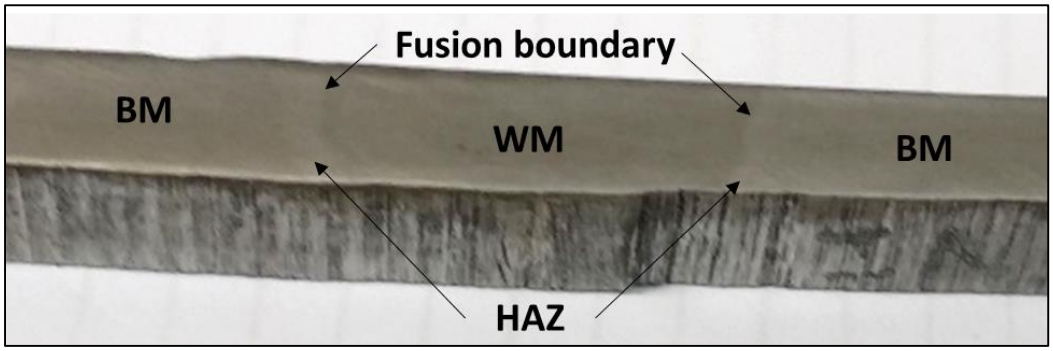

Figure 3.4: *Image of the X20 steel weldment analysed in this study after its surface has been etched with Villella's reagent.*

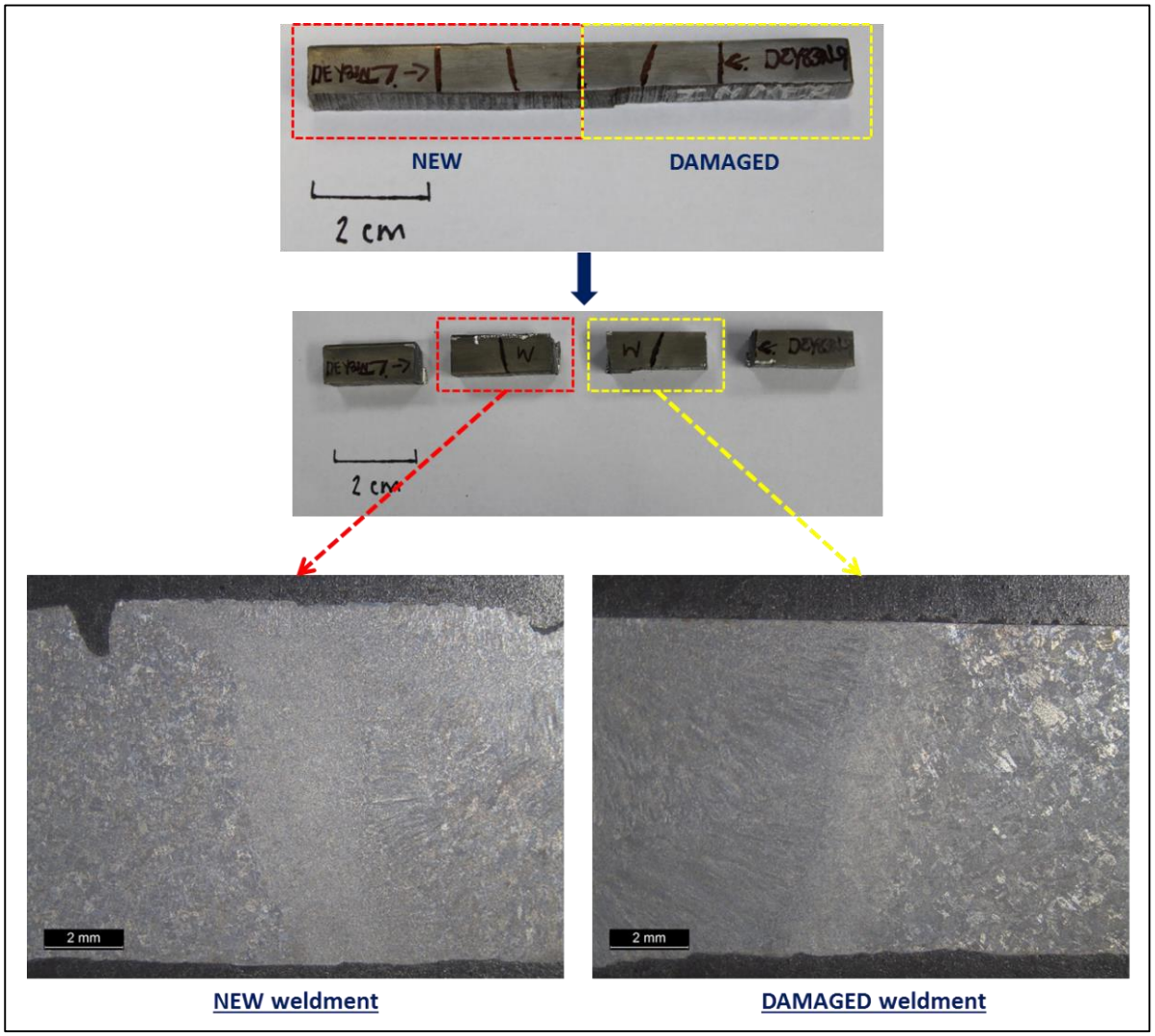

Figure 3.5: *Illustration of preparation of new and damaged weldments analysed in this study by sectioning of cross-weldment shown in Figure 3.3(b). Included is the optical micrographs of the new and damaged weldments, respectively.*

3.2.5 Stratification

Due to the inhomogeneity of the microstructure of a weldment (Chapter 2), stratification of the weldment is required to obtain specimens of homogenous microstructure. In this study this was achieved by first identifying each microstructural (weldment) region and then prepare specimens of each region using the FIB-SEM that allows site-specific specimen extraction. Consequently, specimens with homogenous microstructure is then obtained.

The problem, however, is that it is difficult to differentiate between the different microstructural regions within the HAZ. The HAZ forms a continuous gradient and there are no clear boundaries between the different HAZ regions (Chapter 2). Etching of the surface reveals the prior austenite GB. Consequently, the optical microscope can be used for closer examination of the regions and since the prior austenite GBs are clearly visible, it is even possible to distinguish the CGHAZ and FGHAZ. This method is not accurate and is limited by the magnification of the optical microscope. Higher magnification is required to observe slight differences in prior austenite grain size, especially for distinguishing between the FGHAZ and ICHAZ that have similar microstructures. On the other hand, it is known that the CGHAZ is expected to have the highest hardness and the ICHAZ the lowest, with the FGHAZ hardness values ranging between the two extremes (Chapter 2). Therefore, if one performs hardness measurements across a weldment, the HAZ regions can be identified by the hardness values.

In this study, Vickers Microindentation Hardness Testing (MHT) was performed on the weldments and used as an initial method of identifying the HAZ regions. To ensure correct identification, Electron-Backscatter Diffraction (EBSD) orientation maps are acquired at the different indents. Finally, each microstructural region corresponds to a set of indents. These indents are then used as markers in the FIB-SEM to prepare specimens of each microstructural region.

3.3 SAMPLE PREPARATION

3.3.1 Cutting and Polishing

Table 3.4 summarises the samples used in this study and from which subsequent specimens was prepared, such as extraction replicas, jet-electro polished and FIB-SEM specimens.

Any sectioning of the BM (pipework) and weldments was done by using a hacksaw or band saw, depending on the size of the sample being sectioned.

The sectioned weldments (Figure 3.5) and samples sectioned from BM were mounted in a bakelite resin and polished to a colloidal surface finish using successively finer diamond suspensions (6µm, 3µm, 1µm and 0.25µm) in order to remove any prior surface damage. Polishing with a 0.05µm colloidal silica suspension and an acid base is the final step. The specimens prepared from the new and damaged pipework were squares approximately 10 mm x 10 mm in size.

Table 3.4: *Samples used in the study*

New X20 material	***Damaged X20 material***
MMA weldment	MMA weldment
Bulk specimen	Bulk specimen

3.3.2 Focused Ion Beam-Scanning Electron Microscopy

In this study, the Focused Ion Beam-Scanning Electron Microscope (FIB-SEM) is used as a sample preparation technique to prepare thin site-specific specimens of uniform thickness for the TEM. A brief overview on the basic principles and operation of a FIB-SEM is given in this section and was compiled from the literature provided by Volkert and Minor (2007), Williams and Carter (2009), Suutula (2009), and Giannuzzi and Stevie (2005), which can be consulted for further reading.

A FIB-SEM is a “dual-beam” platform where the FIB column is supplemented with an additional SEM column. Figure 3.6 provides a schematic of the typical dual-beam

column configuration. As can be seen, the specimen is tilted 52° to allow milling normal to the specimen surface.

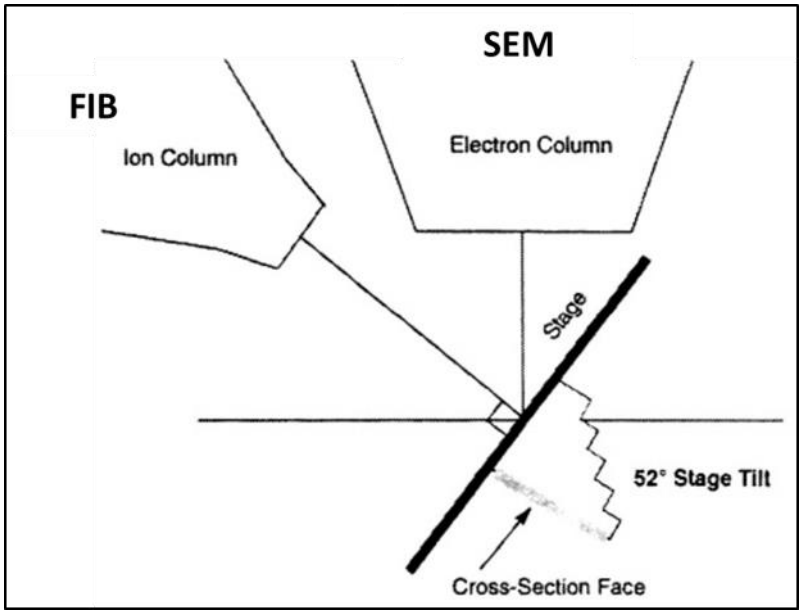

Figure 3.6: *Schematic illustration of dual-beam column configuration in a FIB-SEM. Adapted from Suutula (2009)*

The basic FIB column consists of: two lenses (a condenser and an objective lens); beam-defining apertures; deflection plates; cylindrical octopole lenses; and a beam blanker. The specimen is mounted onto a stage that is grounded and has three-axis (x, y and z) translation, rotation and tilt movement capabilities. A Liquid Metal Ion Source (LMIS) is used to obtain a tightly focused beam with a probe diameter of approximately 5 nm. The Ga-based blunt needle is the most commonly used LMIS where Ga-ions are used for the ion beam and their sputtering action allows exact machining of specimens. The electron beam is used to monitor the ion milling and to perform non-destructive imaging.

The main advantage of using FIB-SEM for specimen preparation is the ability of the ion beam to make a precise cut or cross section of 1 to 200 µm in size (Goldstein, Newbury *et al.* 2003).

After the identification of the various weld regions (bulk, over-tempered, ICHAZ, FGHAZ and CGHAZ) in the new and damaged X20 steel weldments as described in Section 3.2 above, TEM specimens of each region was prepared using a FEI Helios

NanoLab 650 FIB-SEM by extracting specimens in the vicinity of the hardness indents that correspond to that region (Table 3.5).

All FIB-SEM specimens were prepared using the standard procedure for steels:

i. Site of interest was identified and focused at a working distance of 4 mm.
ii. The specimen was then tilted to 52° relative to the electron beam.
iii. A 2 µm thick carbon layer was deposited in a 10 x 2 µm rectangle at 30 kV and 0.43 nA using the ion beam Chemical Vapour Deposition (CVD) process.
iv. Trenches were milled with Ga-ions at 30 kV and 47 nA in the form of a staircase on either side of the area of interest. Edges were then milled parallel with a ±3° tilt (relative to 52°) and 9.5 nA.
v. An Omniprobe Autoprobe 200 was attached to the specimen using the CVD process. The specimen was then cut free using 2.5 nA and lifted out using the Omniprobe and positioned onto a copper lift out grid.
vi. The specimen is then thinned to electron transparency (± 100 nm) using 30 kV at 790 pA and 230 pA, and 5 kV at 41 pA.
vii. Finally, ion-polishing at 2kV, 23 pA and 500 V, 36 pA was performed on the specimen.

3.3.3 Twin-Jet Electropolishing

Complimentary to FIB microscopy, twin-jet electropolishing, also known as twin-jet electrolytic thinning, is a technique used to prepare electron-transparent thin foils for analysis in the TEM. A brief overview of the technique and its operating principles is provided. The literature by Ayache *et al.* (2010) can be further consulted.

This method prepares a thin slice without strain hardening and by thinning until a perforation forms in the centre. The area around this centre is then electron-transparent thin. The usual dimensions of these thin foils are 3 mm in diameter and 50 to 100 µm thickness. A schematic diagram of the twin-jet electrolyte cell is provided in Figure 3.7. The twin electrolyte jets are two nozzles centered on both sides of the sample. The electrolyte is sent through the nozzles by an impeller with a variable flow rate and pressure. In effect, the twin electrolyte jets result in the formation of two dissolution basins that intersect in the middle of the specimen thickness. A flat shiny surface results from the differential dissolution rate that occurs on crevices and

projections of the rough sample surface, while dissolving the material. Consequently, the polishing layer is thinned by the force of the jets and finally a hole forms in the center of the thin-foil. As soon as the perforation forms in the centre of the specimen, the photoelectric cell or infrared detector system detects the light passing through it and etching is then stopped. There are several other types of electrolytic cells (Ayache, Beaunier *et al.* 2010).

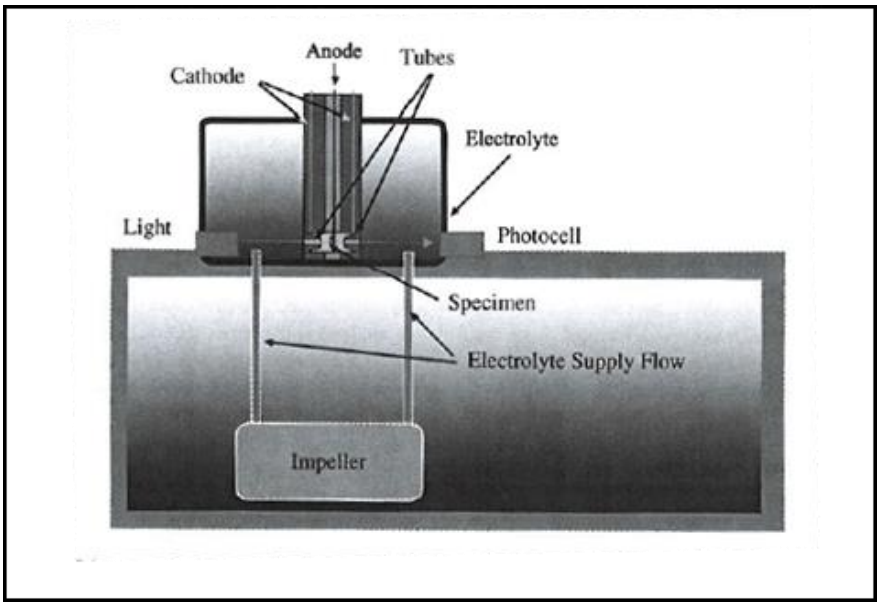

Figure 3.7: *Schematic diagram of twin-jet electrolytic cell used in this study.(Ayache, Beaunier et al. 2010)*

(i) Procedure

For TEM/STEM analysis, thin-foil specimens of the new and damaged bulk X20 material were prepared in this study using a Struers TenuPol-5 Automatic Twin-Jet Electropolisher. To prepare the specimens for the electropolisher, 3 mm disks were cut from the bulk materials with a disc punch system. A current-voltage graph is obtained from a test sample in order to determine the position of the electrolytic polishing plateau and hence the polishing potential as described by Ayache *et al.* (2010). The electrolyte bath was a solution of 5%$HClO_4$ at -20 °C and a voltage of 40 V was applied.

The main advantage of twin-jet electropolishing is that it prepares thin-foils without any mechanical damage and it generates no strain hardening or surface deformation. Subsequently, the prepared thin-foils are smooth and free of surface roughness. This

is, however, not the case with thin-foils prepared using the FIB-SEM since not all the damage caused by the ions used for sputtering can be removed. On the other hand, twin-jet electropolishing can only be applied to bulk samples, whereas site-specific specimens can be prepared with the FIB-SEM. The main limitation of twin-jet electropolishing is, especially with samples containing precipitates or segregations, is the difficulty in finding the correct electrolytic solution, temperature, potential and current conditions.

3.3.4 Bulk Replication

The thin-foil methods suffer from two drawbacks:

1) The magnetic sample interferes with the objective lens, which leads to a reduction in the spatial resolution.

2) The thin-foil (thickness ~ 20-200nm) will section the precipitates, reducing the measured precipitate sizes.

In order to overcome the sampling, stereological projection, magnetic interference and shape distortion problems of the thin-foil samples, extraction replicas of the surface can be made using a technique known as Bulk Replication Technique (BRT). The basic principle of the technique is based on the extraction of particles from the surface of a specimen in order to view them directly in the TEM (Ayache, Beaunier *et al.* 2010). For stainless steels, it entails trapping the precipitates in a carbon film in order to separate them from the metallic matrix, which is then chemically dissolved. The BRT is only applicable to bulk materials and can in some instances be applied site-specific, depending on the size of the extraction area. Since the microstructural regions within the HAZ of a weldment are very narrow, it is not possible to prepare extraction replicas of the various regions using this technique. However, a technique possibly capable of extracting site-specific replicas is the technique Region-Specific Replication (Mitchell and Sulaiman 2006). Future work will include developing such a technique for weldments.

No reference could be found where the BRT has been applied to X20 stainless steel. Mitchell and Sulaiman (2006) investigated the application of the BRT on P91 steel. Their work has been used as a guideline to develop the BRT for application to the new

and damaged bulk X20 steel material. Figure 3.8 provides a schematic illustration of the four main steps of the BRT.

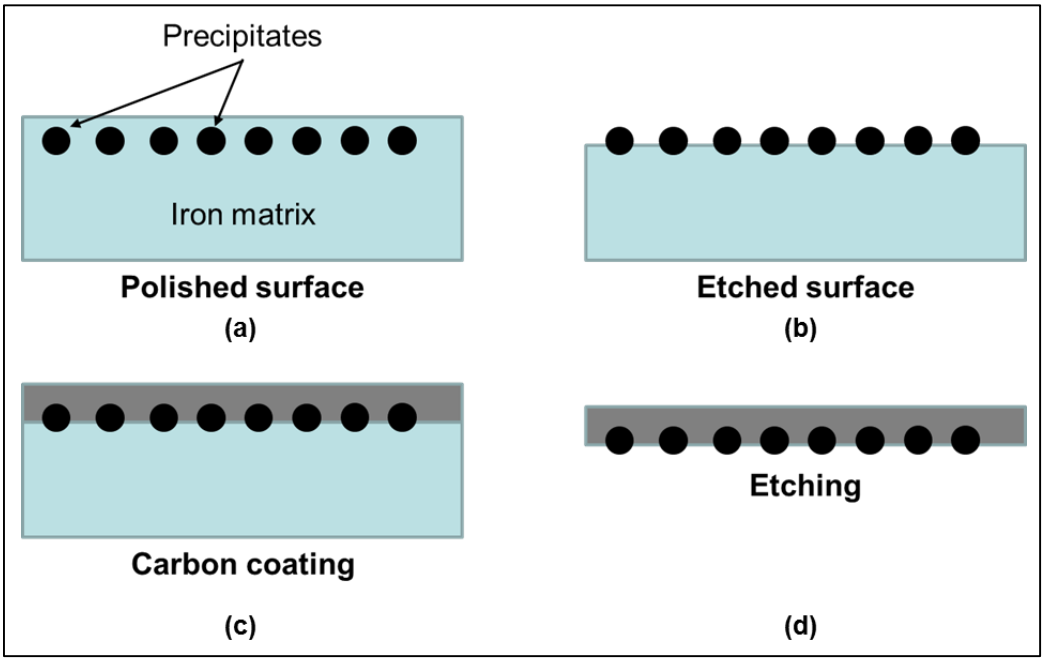

Figure 3.8: *Schematic illustration of the Bulk Replication Technique. (a) Polish the specimen surface. (b) Etch away top layer of iron matrix to expose the precipitates for extraction. (c) Deposit a carbon coat on top of specimen surface in order to cover the exposed precipitates. (d) Etch away rest of iron matrix, leaving a carbon coat specimen containing only precipitates.*

Firstly, the specimen was polished as described in Section 3.3.1 (Figure 3.8(a)). Extraction replicas were then prepared by etching away the top layer of the iron matrix using Vilella's reagent (1 g picric acid, 5 ml hydrochloric acid and 100 ml ethanol) for 2 minutes (Figure 3.8(b)). The precipitates were then exposed for extraction. This is followed by depositing a carbon coat of ±20 nm (evaporation of 4 pulses at 1 x 10^{-2} mbar) on the specimen surface in order to cover the exposed precipitates, using a carbon deposition system consisting of Quorum Emitech K950X Turbo Evaporator (Figure 3.8(c)). The specimen surface was then scored into 2.5 mm blocks and immersed in Villela's reagent until the foils floated off. The foils were washed in 10% methanol water and floated onto a copper TEM grid. The final result is a carbon coat specimen that only contain the precipitates (Figure 3.8(d)).

The main advantage of the BRT is that it produces TEM specimens with a much larger sampling area. Also, a large number of TEM specimens can be simultaneously prepared from a specimen. In Figure 3.9 the extraction replica size (±2.5 x 2.5 mm divided into ±50 x 50 µm squares on the copper grid) is shown relative to that of a FIB-SEM (±5 x 5 µm) and conventional (ion-mill or twin-jet electropolished) TEM specimen. Consequently, good statistical and representative results can be obtained about precipitate size, shape, structure and chemical composition (Mitchell and Sulaiman 2006; Ayache, Beaunier et al. 2010).

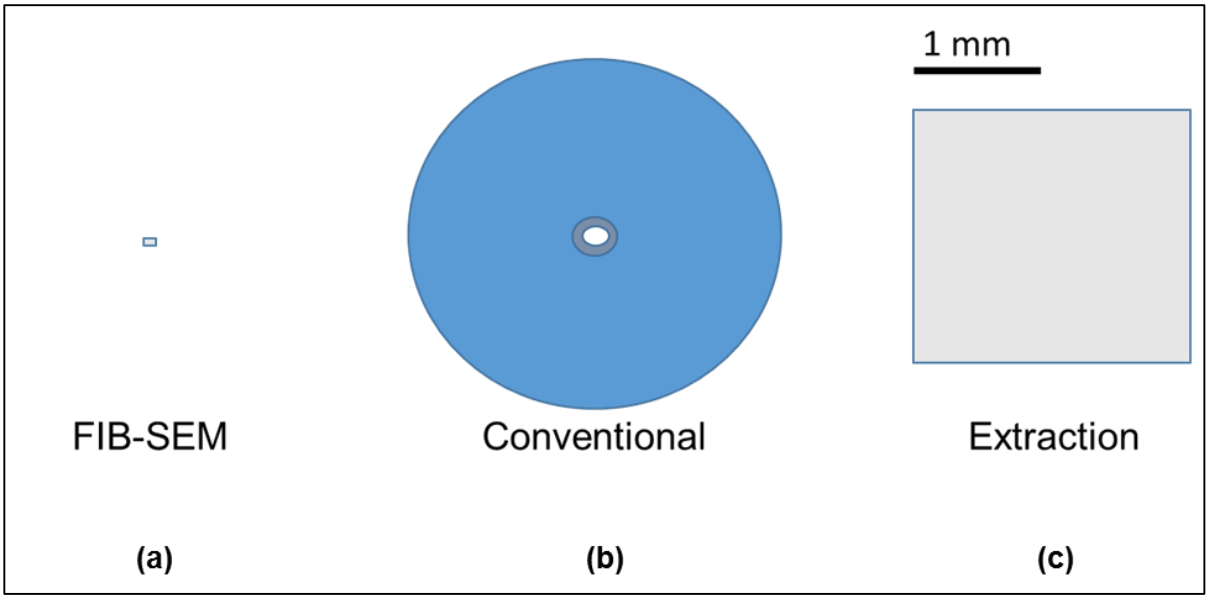

Figure 3.9: *Comparison of (a) FIB-SEM (±5 x 5 µm), (b) conventional (ion-mill, twin-jet electropolished) TEM and (b) extraction replica (±2.5 x 2.5 mm) specimen size relative to one another. The grey areas correspond to the area available for analysis.*

The BRT has the following limitations and issues that need to be considered:

i. The sampling volume or thickness of the etched layer from which the extraction replica was taken is an unknown quantity. Many efforts have been made to determine this extraction depth (Baker 2001). The approach took in this study to determine the sampling volume is discussed in Chapter 4.
ii. In the case of very small particles, the thickness of the etched layer is much larger than the particle diameter. Hence, these precipitates may not be extracted at all. This brings into question the extraction efficiency of the BRT, which is one of the least understood aspects of extraction replication. Baker

(2001) came to the conclusion that extraction replicas are suitable for obtaining particle size distributions in the range of 3 nm to 1 pm.

iii. Artifacts can be introduced during the replication process due the poor control of chemical dissolution. By choosing the correct etching chemical and chemical etching time, this problem can be overcome (Ayache, Beaunier *et al.* 2010). Mitchell and Sulaiman (2006) has shown that Villela's reagent does not create any contaminant films or attack the secondary phase precipitates ($M_{23}C_6$ and MX).

iv. To what extent the extraction replica reproduces the microstructure in the x, y and z directions is another major uncertainty with the BRT. In Chapter 4 it is shown that the microstructure seems to be reproduced in the x and y directions of the extraction replica. The reproducibility of the microstructure in the z direction, i.e. throughout the thickness of the extraction replica, still needs to be investigated. A possible solution, is to prepare double extraction replicas by depositing a carbon coat on each side of a thin-foil and etching the matrix away (Ennis, Zielinska-Lipiec et al. 2001; Ayache, Beaunier et al. 2010). The precipitates are then sandwiched between the carbon layers. Therefore, this will ensure that there was no movement of the precipitates in the z direction and the microstructure should be fully reproduced.

3.4 VICKERS MICROINDENTATION HARDNESS TESTING

An overview compiled from the literature by Bavarian (2014a; 2014b) on Vickers Microindetation Hardness Testing (MHT) is provided in this section. The reader is referred to ASTM E384 (2011) for a full description on standard Vickers MHT.

3.4.1 Instrumentation and Operating Principles

MHT is widely used to study fine scale changes in hardness. This type of hardness testing is often used by metallographers, metallurgists and failure analysts to characterise weldments, evaluate consistency, as an aid to identify phases or to determine the hardness of specimens too small for macroindentation (bulk) hardness tests. Although the term "micro" usually implies extremely low measured hardness values, this is not the case for MHT. In this case the "micro" refers to the fact that the applied load (test force) and resulting indent size that is small compared to bulk

hardness tests. Consequently, the same hardness value is obtained by both the micro- and macroindentation hardness testing methods.

ASTM E384 (2011) defines MHT as a hardness test that uses a calibrated machine to force a diamond indenter of a specific geometry smoothly into the surface of the material under investigation, with test forces in the range of 9.807 x 10^{-3} N to 9.807 N (1 to 1000 gf), and the diagonal(s) of the indentation are then measured with a light microscope after removal of the load. Vickers MHT uses a square-based pyramidal-shaped diamond indenter with 136° face angles. A schematic of a Vickers indenter and its impression is illustrated in Figure 3.10. Also illustrated are the two diagonals that need to be measured to obtain a Vickers hardness number (HV). This HV value is then calculated using the following formula (Bavarian 2014a):

$$HV = \frac{1\,854.4L}{d^2} \tag{3.1}$$

where L is the load in gf and d is the average diagonal in µm. This process can be automated using appropriate software. In metallurgy, hardness is defined as the ability of a material to resist plastic deformation and hence in the case of MHT, the resistance to indentation.

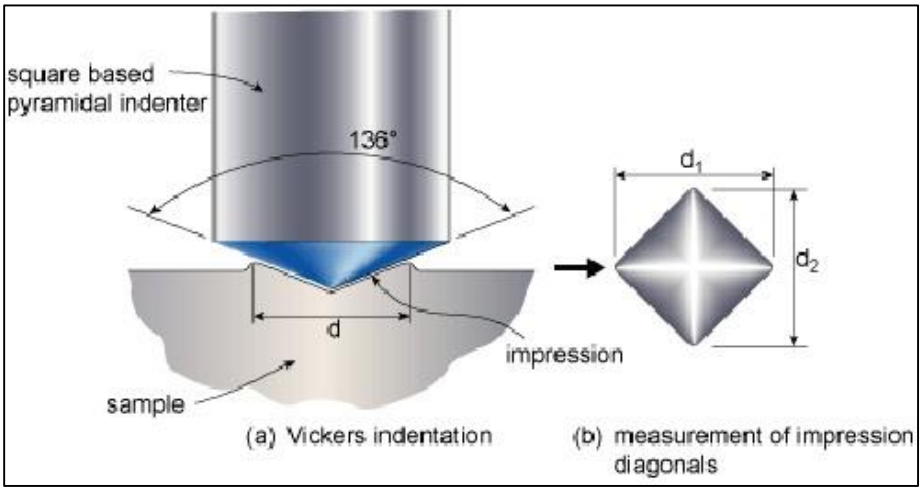

Figure 3.10: *Schematic illustration of Vickers square-based pyramidal-shaped diamond indenter and the impression it makes. (Academia 2013)*

3.4.2 Identification of Weld Regions

The approach discussed in Section 3.2.5 above was followed. The new and damaged X20 weldments were mounted and polished (Section 3.3.1). It is important that the surface is free from any damage to ensure accurate Vickers MHT results. The hardness tests were performed using an Automatic Micro Vickers Hardness Tester that is a combination of a Future-Tech FM-700 Microhardness Tester and a Future-Tech FM-ARS9000 Full-Automatic Hardness Testing System. A load of 300 gf was used for all Vickers hardness measurements, which is a standard for stainless steels. Before each set of measurements, the equipment was calibrated using a Cu block standard.

The same procedure was followed for each weldment. Firstly, starting in the bulk region, three lines (top, middle and bottom) of 0.5 mm spaced indents were made across the weldment. As an illustration of the position of the indents across the weldment, an optical micrograph of the new X20 weldment after indentation is provided is Figure 3.11. The Vickers hardness values were then measured from the diagonals of the indents using the software of the Vickers MHT. A plot of the hardness values were then made in order to make an estimation of where the HAZ should be, i.e. between lowest and highest hardness values.

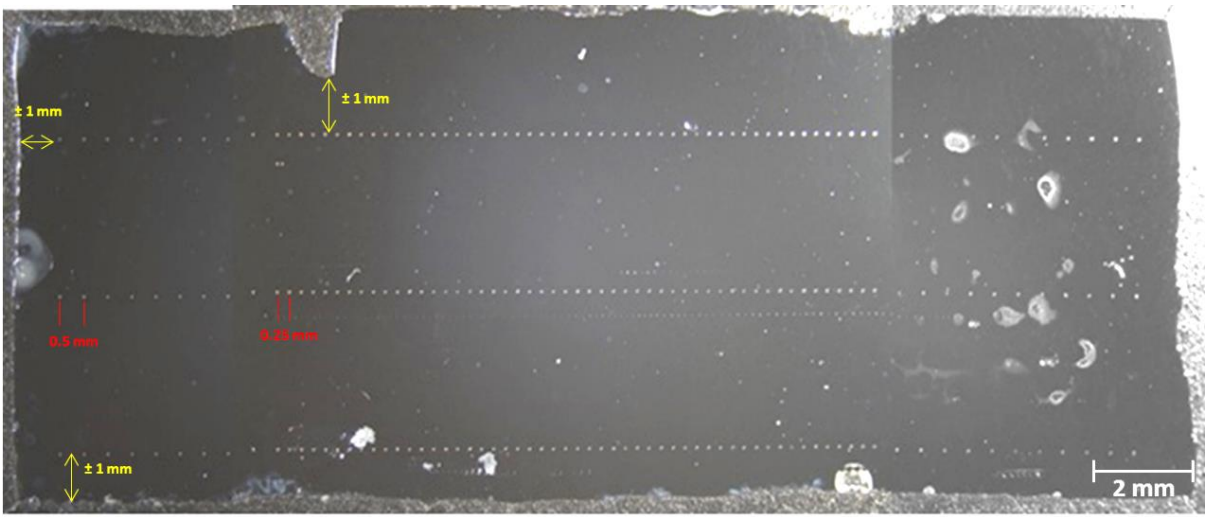

Figure 3.11: *Optical micrograph of new X20 weldment after Vickers hardness measurements.*

For better hardness resolution of the HAZ, a second set of 0.25 mm spaced indents were made along the previous indentation lines (Figure 3.11), but only for the region

approximately determined as the HAZ. It should be noted that only the hardness values of the 0.25 mm spaced indents in between the 0.5 mm spaced indents were measured, since every second 0.25 mm spaced indent coincides with a 0.5 mm spaced indent whose hardness is already known. The Vickers hardness profile of each indentation line is shown in Figure 3.12. All the profiles have similar shapes, but there is a shift in them due to the geometry of the HAZ (Figures 3.4 and 3.5).

To identify the different weld (microstructural) regions, the hardness measurements of the middle indentation line of each weldment was used. Since the indents were made in the middle of the sectioned weldment, it should provide the most representative results, i.e. free from any damage due to sectioning. The bulk region, ICHAZ and CGHAZ of the weldments were determined by considering the hardness profiles as shown in Figure 3.13. A maximum hardness value should correspond to the CGHAZ and a minimum to the ICHAZ, with the FGHAZ hardness values ranging between the two extremes (Chapter 2). Since each line of indents started in the bulk region, the first indent and subsequent indents with similar hardness values all fall within the bulk region. The over-tempered region is rather identified with just EBSD, which will be discussed in Chapter 5. Table 3.5 provides a summary of the indents preliminary assigned to the different weld regions. Also given in Table 3.5 is the Vickers hardness value of the CGHAZ and ICHAZ and the mean Vickers hardness value of the group of indents corresponding to the bulk and FGHAZ.

Table 3.5: *Preliminary assignment of indents and their Vickers hardness values to each weld region.*

Sample Name	Indent(s) #	Vickers Hardness (HV)
New weld FGHAZ	34 - 40	238.32 ± 10.07
Damaged weld FGHAZ	36 - 38	236.87 ± 55.57
New weld CGHAZ	41	260,66
Damaged weld CGHAZ	39	266,76
New weld ICHAZ	33	218,37
Damaged weld ICHAZ	35	207,04
New bulk	1 – 23	238.95 ± 1.98
Damaged bulk	1 - 25	208.56 ± 3.23

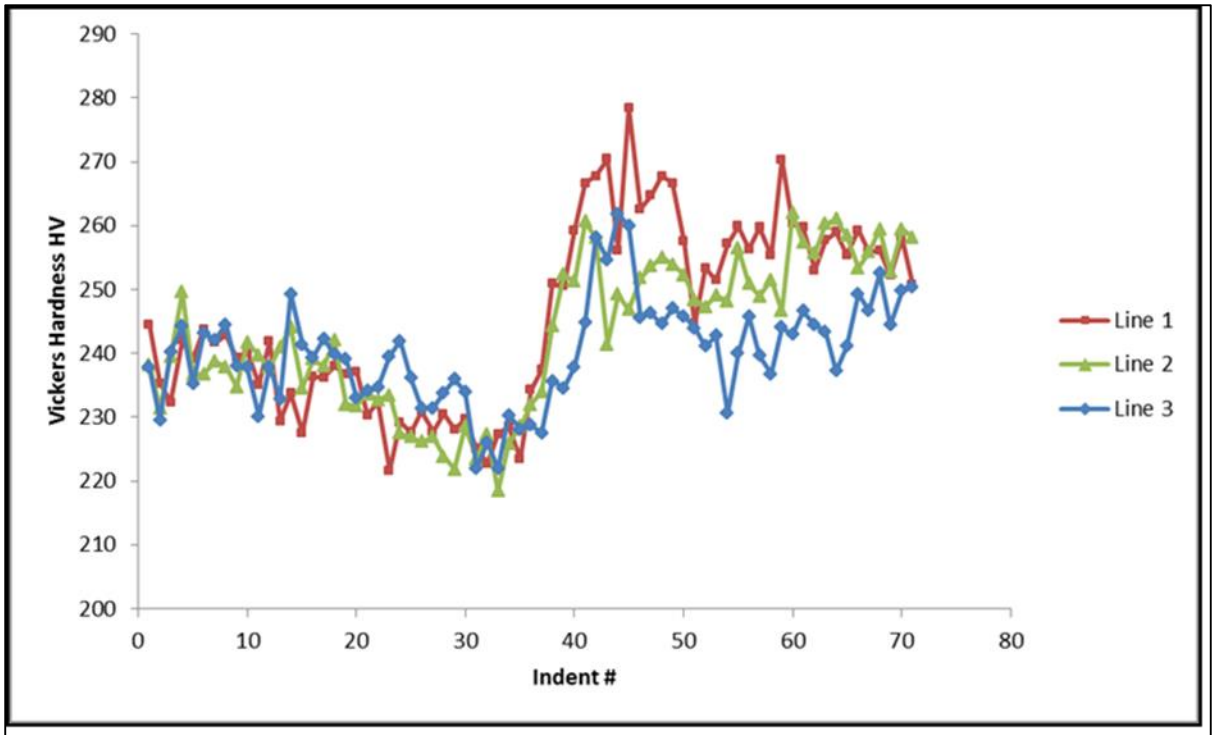

(a)

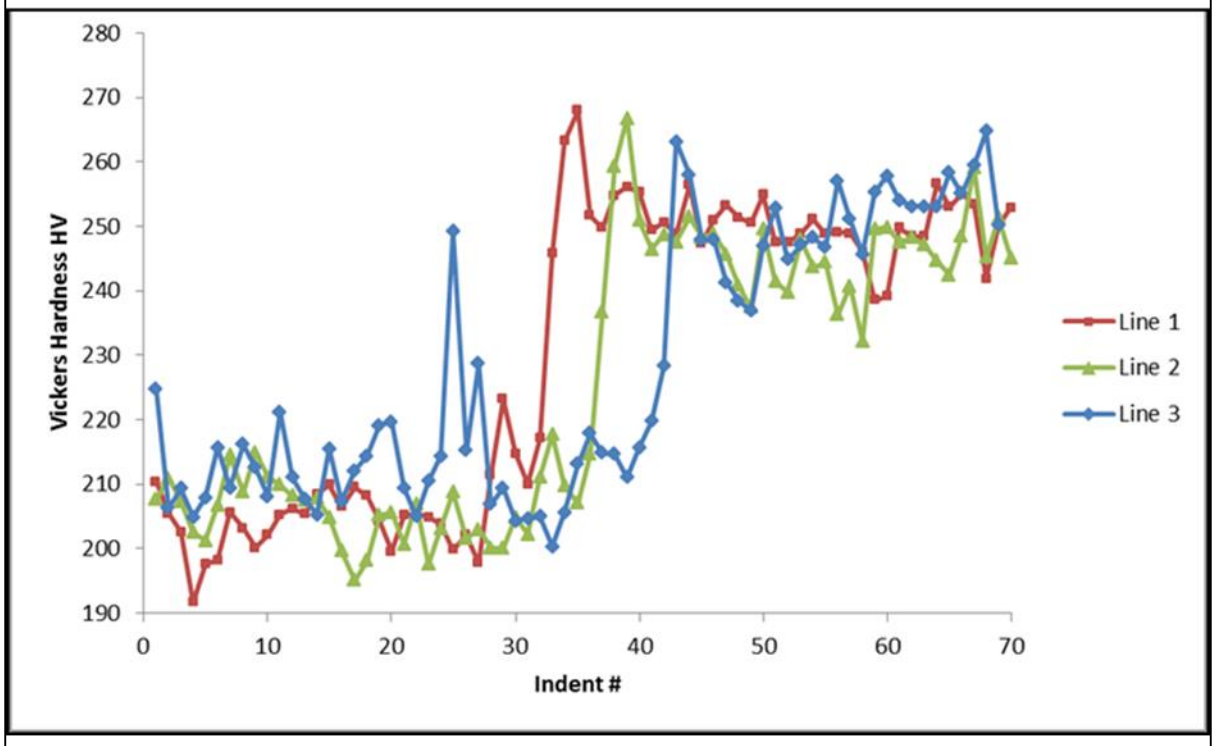

(b)

Figure 3.12: *Vickers hardness profiles of top (Line 1), middle (Line 2) and bottom (Line 3) indentation lines performed across the (a) new X20 and (b) damaged X20 weldments.*

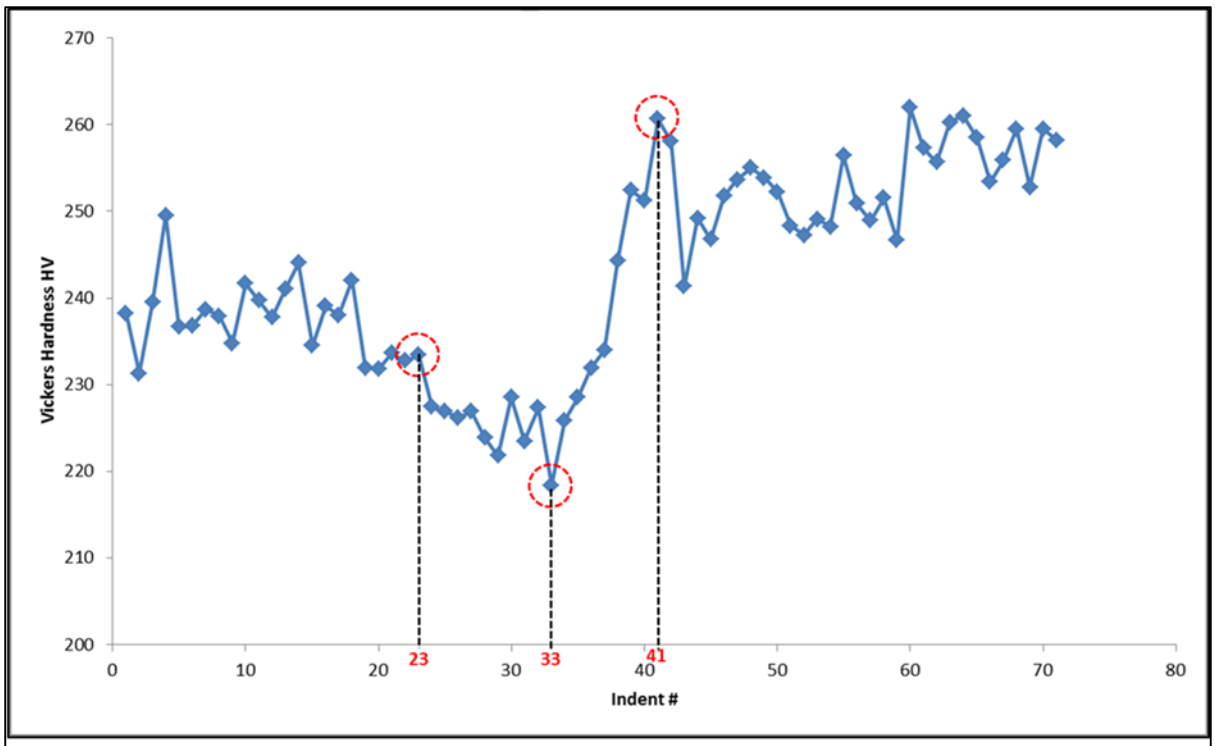

(a)

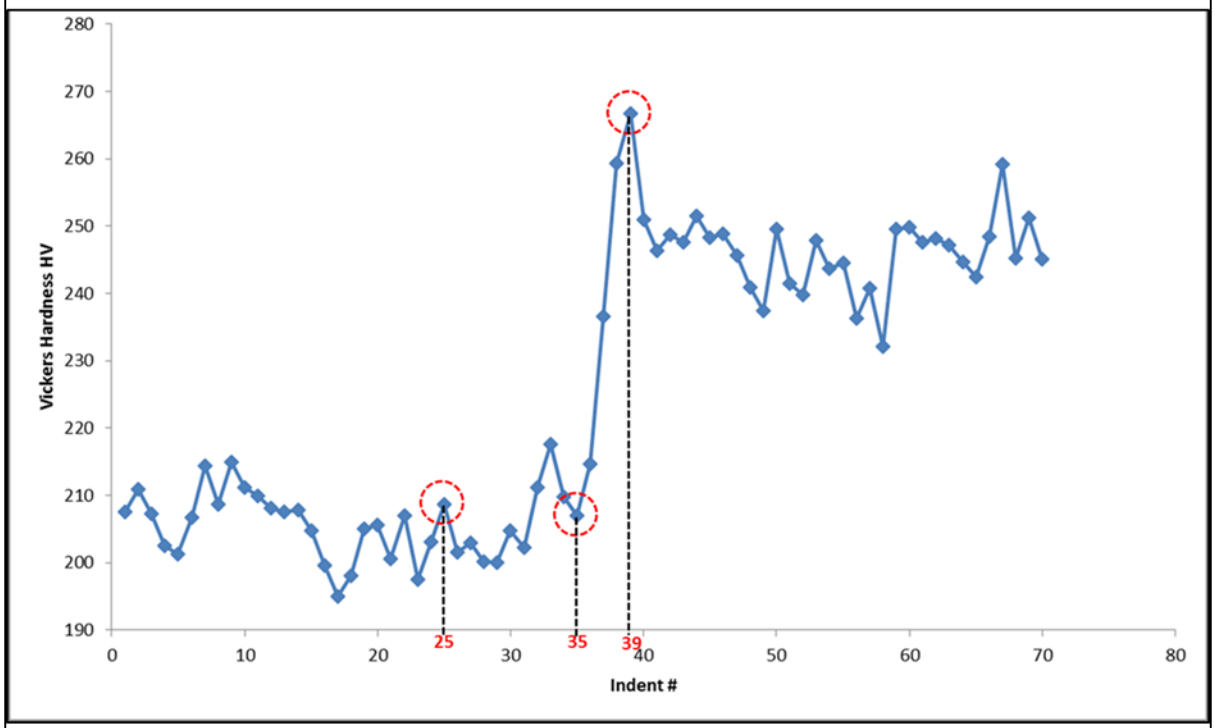

(b)

Figure 3.13: *Illustration of identification of bulk region, ICHAZ and CGHAZ from the hardness profile of middle line of indents in (a) new and (b) damaged X20 weldments.*

3.5 SCANNING ELECTRON MICROSCOPY

The Scanning Electron Microscope (SEM) allows observation, characterisation, and analysis of any material and surface from micrometer scale to nanometer scale. For that reason electron microscopes, in general, have much more to offer than the optical light microscope, which has a resolving power of only 0.2 µm (FEI 2006). This section provides a brief overview on the main aspects of the SEM and was compiled using the literature by Goldstein *et al.* (1992), Lawes (1987), Friel (2003) Trimby (2013), Aracil (2014) and Keller *et al.* (2013) and application notes by JEOL. EBSD and Transmission Kikuchi Diffraction (TKD) in the SEM are the main techniques used in this study and therefore more detail on these techniques is given.

3.5.1 Instrumentation and Image Formation

In the SEM, the area to be analysed is scanned with a finely focused electron beam in a raster pattern. As the electron beam penetrates the specimen it interacts with the atoms of the specimen. Consequently, the electron beam is scattered and many signals are generated from the beam and specimen interaction. Figure 3.14 provides a descriptive schematic diagram of the different types of signals generated by beam-specimen interaction in EM. The two most important imaging signals in the SEM are the Secondary Electrons (SE) and Backscattered Electrons (BSE). The reason for this being that these electrons, and hence their energies, vary primarily due to differences in surface topography. X-rays are also generated (Figure 3.14) and provide chemical information. For the SEM to form an image, an appropriate detector for each signal must be employed to convert the radiation into an electrical signal, for manipulation and display.

The SEM structure is composed of 3 major sections: (i) electron-optical column (electron gun and two or more electron lenses); (ii) vacuum system; (iii) visual and recording cathode ray tubes (CRTs), and electronics. Figure 3.15 provides a schematic diagram of a standard SEM. The main purpose of an electron gun is to act as an electron source and provide a large, stable current in a narrow electron beam. The most common electron guns are the Tungsten Thermionic Emission gun and the Field Emission Gun (FEG). Much higher resolution can be attained with a FEG, since it produces a much smaller probe. Electromagnetic (condenser and objective) lenses

are required to reduce the beam diameter of the source of electrons in order to produce a small electron probe, which is then focused onto and raster scanned across the specimen.

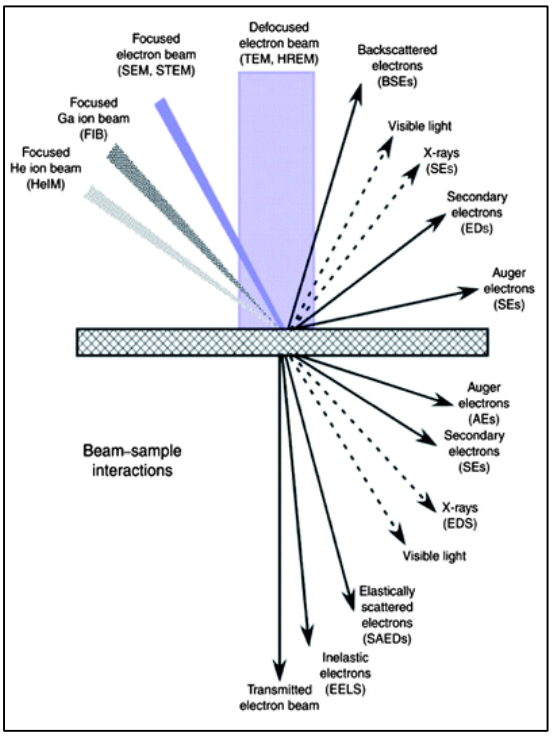

Figure 3.14: *Schematic diagram of the different types of beam-specimen signals generated in EM. (Linkov, Artemyev et al. 2013)*

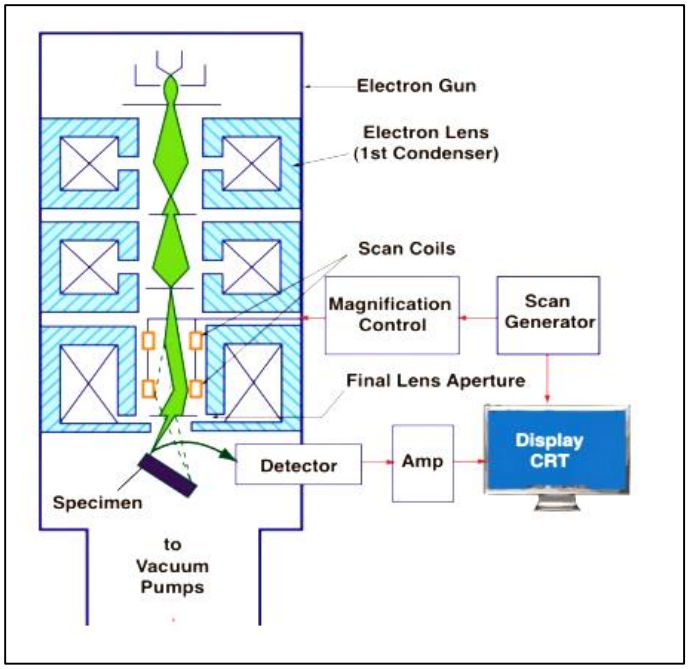

Figure 3.15: *Schematic diagram of the standard SEM. The optical-electron column and visual and recording CRT with electronics are shown. (Rosell Minerals 2016)*

3.5.2 Electron-Backscatter Diffraction

Electron-Backscatter Diffraction (EBSD) in the SEM has been developed into a commercial technique for routine quantitative characterisation of microstructures. However, the development of the hardware, software and applications of the technique continues. Its use for phase identification and orientation determination has led to new insights into the links between microstructure, crystallography, and physical properties of materials that could not be attained before. The technique is based on the acquisition of diffraction patterns from bulk speciemns in the SEM. A recent innovation has been the use of EBSD in conjunction with a FEG-SEM in order to increase spatial resolution. This section aims to provide some background on the EBSD technique. The texts by Goldstein *et al.* (2003), Humphreys (1998; 1999; 2001; 2004; 2004), Maitlind and Sitzman (2007), Engler and Randle (2010), and Josefsson (2012) were used as references and can be consulted for in-depth discussions.

Grains are defined as randomly oriented crystalline units. EBSD provides the quantitative information about the orientation of each grain in a SEM image. Modern EBSD equipment on a standard SEM allows the automatic acquisition, analysis and storage of diffraction patterns as the beam is scanned over the specimen. This results in a large amount of detailed crystallographic information about the specimen to be generated, including the distribution of orientations that provides a basis for detailed quantitative evaluation of the microstructure.

(i) EBSD Patterns

EBSD patterns are obtained in the SEM by focusing a stationary electron beam onto a highly tilted specimen. When the primary electron beam interacts with the crystal lattice, low energy loss BSE are produced. This diffraction of electrons causes the diffracted electrons to form flat cones of intensity above the specimen as shown in Figure 3.16.

These pairs of cones intercept the imaging plane, resulting in two nearly straight lines separated by an angle of $2\theta_B$ to be imaged. The diffracted electrons fluoresce the phosphor screen and a Kikuchi pattern or Electron Backscatter Diffraction Pattern

(EBSP) is formed. Subsequently, an EBSP consists of a large number of parallel lines, known as Kikuchi bands, as shown in Figure 3.17.

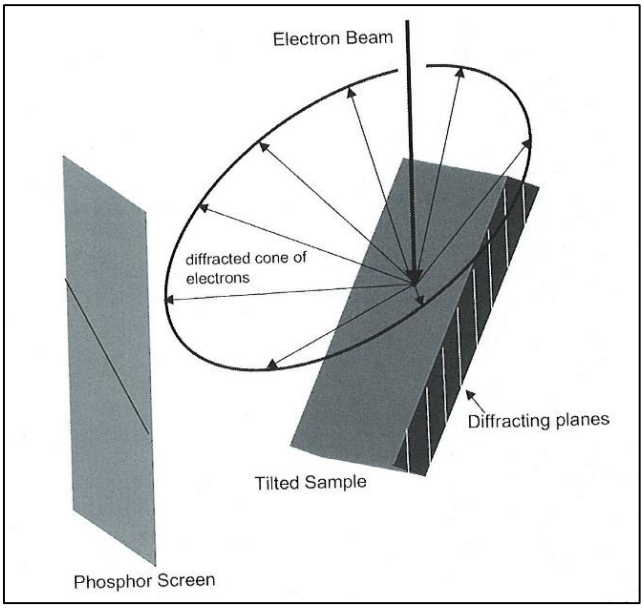

Figure 3.16: *Schematic diagram of the experimental arrangement of the specimen and the phosphor screen within the SEM in order to obtain an EBSP. Included is an illustration of the intersection of a single flat diffracted cone with the phosphor screen in order to form one Kikuchi band in the EBSP. (Goldstein, Newbury et al. 2003)*

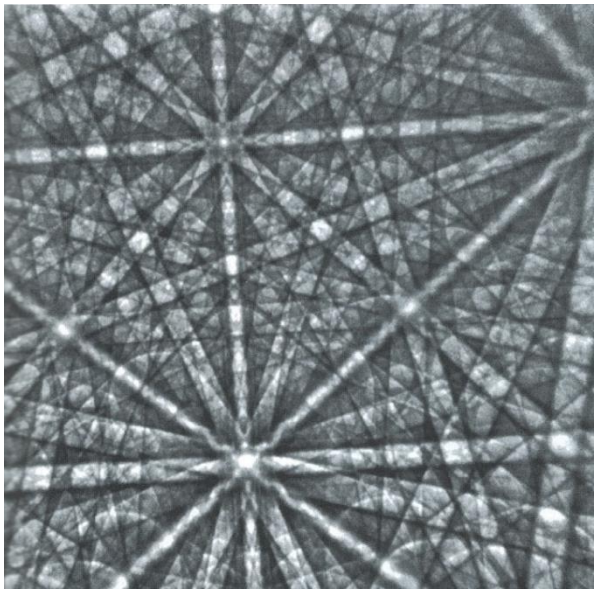

Figure 3.17: *Typical EBSP (EBSD pattern) acquired from mineral wulfenite with an accelerating voltage of 20kV and CCD-based camera. (Goldstein, Newbury et al. 2003)*

The intersections of the pairs of lines are zone axes and are related to unique crystallographic directions in the crystal. Consequently, the pairs of lines represent planes within the crystal structure and crystallographic directions within the crystal are represented by zone axes. The atomic spacing of the planes in the crystal are inversely proportional to the width of the pair of lines. The EBSP is an angular map of the crystal and the distance between any pair of Kikuchi lines can be related to an angle through Bragg's law given by (Zou, Hovmöller et al. 2011):

$$2d \sin\theta = n\lambda \tag{3.2}$$

where d is the interplanar spacing between the (hkl) crystal planes, θ is the scattering angle and n is an integer number.

(ii) Instrumentation and Operating Principles

An automated EBSD system is constructed by attaching an EBSD detector to a SEM. The detector then consists of a phosphor screen and Charge Coupled Device (CCD) camera that is connected to a computer that acts as an image processing system for pattern averaging and background subtraction. The phosphor screen essentially converts the diffracted electrons into a light signal suitable for the CCD camera to record as an EBSP. The basic EBSD setup is illustrated in Figure 3.18. EBSD operates by tilting a flat, highly polished specimen 60° to 70°, typically 70°, from the horizontal axis to generate patterns of sufficient intensity. The optimum position for examining the microstructure using BSE is when the specimen is mounted so that its surface is normal to the electron beam.

Electron diffraction occurs from the point of the incident electron beam on the specimen surface with accelerating voltage of 10 to 30 kV and 1 to 50 nA incident beam current. While the beam is stationary at this point, an EBSP arises spherically from the point. EBSD acquisition software controls the data acquisition, solves the diffraction patterns and stores the data. The software processes the image of the EBSP by transforming the image with a Hough transform in order to identify the Kikuchi bands automatically.

The candidate phases are selected within the software and the software can then determine all possible orientations for each phase. Subsequently, the detected

bands can be matched and indexed against the reference patterns in order to identify the phase and crystallographic orientation. An EBSP is considered indexed when both its orientation and phase are known. Additional software is required to analyse, manipulate and display the data.

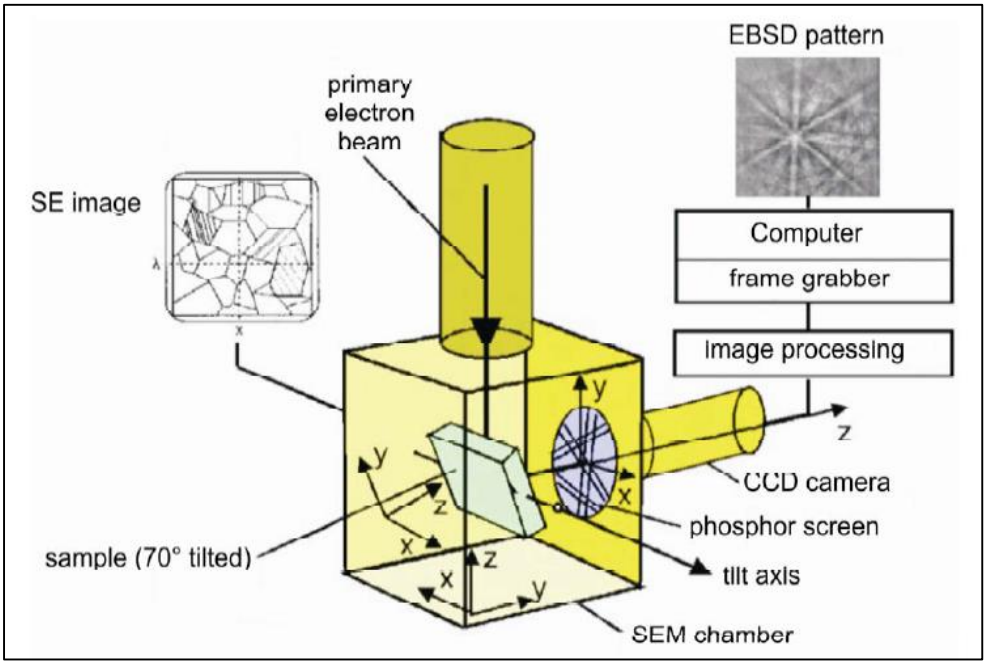

Figure 3.18: *Schematic diagram of the EBSD setup. (Aghajani Bazazi 2009)*

(iii) Data Measurement

To create an EBSD or Orientation Map (OM) of an area on the specimen, the electron beam is scanned across the area with a specified step size and at each pixel an EBSP is captured, analysed, the phase and orientation derived or a zero-solution recorded. Zero-solutions occurs at points where no EBSP is available, where overlapping EBSPs cannot be resolved, or when a new phase is encountered. EBSD gives rise to a 3D pattern that originates from a point that is recorded in 2D on the phosphor screen. Thus, for every point analysed on a specimen, a corresponding 2D image of the EBSP is analysed.

The position, phase, orientation and some data quality information such as goodness of fit and pattern quality, is stored at each pixel point in an EBSD map. Maitland and Sitzman (2007) provide full discussions on how these parameters are obtained.

From the Hough transformation an EBSP quality factor known as Band Contrast (BC) can be derived. BC expresses the average intensity of the Kikuchi bands with respect to the overall intensity within the EBSP. The pattern quality is often given by the BC. Therefore, pattern quality (BC) maps are generally grayscale maps and each point on the map is assigned a brightness based on the pattern quality of that point. Grain boundaries lead to zero-solutions due to overlapping EBSPs and hence they are visible as low pattern quality (dark) linear features.

The Inverse Pole Figure (IPF) is an orientation component that employs a basic RGB colouring scheme fitted to an inverse pole figure. A pole figure is used to represent the orientation of the crystal coordinate system in the specimen coordinate system. For cubic phases, grains whose <100>, <110> or <111> axes are parallel to the projection direction of the IPF, normally the ND (Chapter 2), are respectively assigned full red, green and blue. Subsequently, intermediate orientations have a mixed RGB colour.

The axes or orientation of another grain, usually a neighbouring grain, can be chosen as the reference coordinate system instead of the specimen coordinate system. The difference in orientation between the two crystal coordinate systems is known as the misorientation and it is described by an angle/axis of rotation (angle/axis of misorientation).

The Grain Boundary (GB) component draws a boundary in between map pixels whose orientations differ greater than a user-defined minimum. In other words, grain boundaries with misorientations in a certain range are given a specific colour.

(iv) EBSD Resolution

Spatial Resolution

Spatial and angular resolution of the EBSD system are the most important factors when small grains and subgrains are to be analysed. The area from which an EBSD map is acquired with an electron beam focused on a 70° tilted specimen is almost elliptical. Consequently, the resolution along the major axis, which is perpendicular to the tilt axis, is about three times larger than the spatial resolution along the minor axis, which is parallel to the tilt axis. EBSD is limited by the pattern source volume to spatial

resolutions in the order of 25 to 100 nm. Humphreys *et al.* (1999) found that 20 keV accelerating voltage and largest probe size available is the optimum FEG-SEM conditions for sufficient EBSD spatial resolution.

Angular Resolution

The angular resolution is defined as the accuracy with which the orientation between two adjacent data points can be determined. The number of pixels in the acquired EBSP and the accuracy of the indexing software determine the angular resolution. The angular precision of an EBSD system can be measured by measuring the misorientation angle between pixels within the same crystal, known as orientation noise. Presently, angular resolution is limited to approximately 0.5° to 1.5° (Humphreys 2001). Angular accuracy is especially important when characterising microstructures containing low angle grain boundaries with misorientations in the range of 1° to 5° since the orientation noise is typically about 1°.

(v) Pixel Binning

Pixel or camera binning is when the charge from neighbouring pixels on the camera sensor chip are combined. Binning increases the acquisition speed. The signal strength during the read out procedure is increased n fold by combining n neighbouring pixels and a lower exposure time is required. The disadvantage of binning is that fewer pixels results in less accuracy in band detection, which results in a decrease in spatial and angular resolution.

(vi) Grain and Subgrain Size Analysis

EBSD grain and subgrain size analyses uses changes in crystallographic orientation between neighbouring grid points of greater than a defined minimum to determine the position of grain boundaries. This minimum value is known as the Critical Misorientation (CM) and a grain boundary will be set between two pixels if the misorientation between the two adjacent pixels is larger than this value. In general, a subgrain is considered to be the region bounded by two adjacent low angle boundaries or between a low and high angle boundary. Similarly, two high angle boundaries bound a grain.

(vii) Linear Intercept Method

The Linear Intercept (LI) method entails analysing lines of data points, in the x or y direction, in an acquired EBSD map. The LI method is usually a built-in function in the EBSD data processing software. Essentially, the software draws a line across the EBSD map, counts the number of specified boundaries that intercept the line and then converts it to a grain/subgrain size value. The CM, direction of intercept line and number of intercept lines can be specified in the software. An advantage that EBSD has over normal metallography techniques, is the fact that you can specify the nature of a boundary to be measured. This method of analysis is similar to the LI methods used to measure grain sizes from optical or scanning electron micrographs.

(viii) Grain Reconstruction Method

The Grain Reconstruction (GR) method, also known as grain area determination, is a method for grain size and shape analysis from EBSD maps. This method is also a built-in function in normal EBSD data processing software. As before, a CM is specified so that the software can determine the position of the desired boundaries by checking the misorientation of each data point with its neighbouring points and assign points within the limit to the same grain/subgrain as the reference point. The software repeats this process until a complete grain is constructed that it bounded by the specified boundaries. Grain/subgrain size analysis is then performed by the software and several parameters are calculated for each grain/subgrain. This is a much slower measuring method than the LI method and it relies on obtaining a high resolution orientation map.

Subgrain size and misorientation of the subgrain boundaries, usually between 1 to 5° (Humphreys 2001), are the two most important parameters for CSEF steels (Chapter 2). Small subgrain sizes are normally measured using the TEM, but BSE imaging in the SEM allows subgrains as small as 0.5 µm (W-filament SEM) and 0.05 µm (FEG-SEM) to be measured (Humphreys 2001). Accuracy problems will arise if the subgrain size approaches the limit of the spatial resolution for EBSD and the subgrain misorientations approaches the limit of angular resolution of EBSD.

Diffraction patterns cannot be analysed when the grains or subgrains are smaller than the effective spatial resolution, in this case the effective spatial resolution in the direction perpendicular to the tilt axis L_P. It has been shown that for an error of less than 10% in determining the grain size, D must be 10 times larger than L_P and the pattern indexing must be at least 85% (Humphreys 2001). In the case of the GR method, only the smallest grains will be lost instead of smallest intercepts.

3.5.3 Transmission Kikuchi Diffraction

To overcome the spatial resolution limitation of EBSD, a relatively new SEM-based diffraction technique known as Transmission Kikuchi Diffraction (TKD) or transmission EBSD (t-EBSD) has been developed that uses an electron transparent specimen coupled with the conventional EBSD hardware and software. Spatial resolutions better than 10 nm can be achieved with TKD. This section aims to shortly describe the theory of TKD, including the experimental setup that implements an EBSD system in transmission mode. The literature used to compile this summary, and which can be further consulted, is that by Trimby (2013), Aracil (2014) and Keller *et al.* (2013).

(i) Instrumentation and Operating Principles

TKD specimens are prepared in the standard way as for the TEM, e.g. using twin-jet electropolising or the FIB-SEM. Thin specimens with a thickness of 50 to 150 nm provide the best TKD results. The specimen is mounted in a custom TEM specimen holder such that it is horizontal in the SEM chamber and at a level above the top of the EBSD detector's phosphor screen. Usually, the TEM specimen holder clamps the thin-foils at a tilted angle from the horizontal that is in the opposite direction of the normal tilt for conventional EBSD. The typical TKD geometry is schematically illustrated in Figure 3.19(a). This configuration ensures that the primary beam electrons go through the specimen and the forward scattered electrons can scintillate the phosphor screen. Figure 3.19(b) illustrates a TKD setup where the specimen is mounted using a pre-tilted holder and a small microclamp.

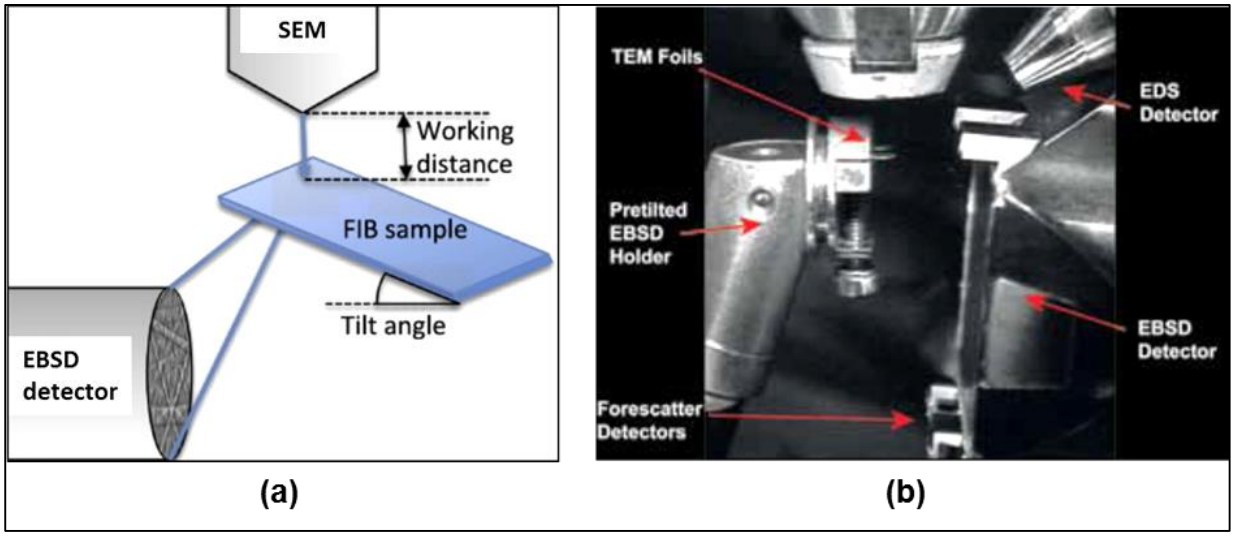

Figure 3.19: *(a) Schematic diagram of typical TKD specimen geometry. Adapted from Garber et al. (Garner, Gholinia et al. 2014) (b) Image of TKD setup within the SEM. (Trimby 2013)*

TKD is different from EBSD in the sense that when the electron beam illuminates the specimen, a fraction of the incident electrons are not backscattered, but scattered by the atoms through the specimen. Consequently, these electrons then form the Kikuchi pattern on the phosphor screen. Orientation mapping is performed identically as for conventional EBSD, with no tilt correction or dynamic focus required and step sizes can be chosen as small as 2 nm. Other components of the TKD setup are identical to that of the EBSD system. Also, the operating principles and post-processing tools of TKD are the same as in conventional EBSD. The geometries and interaction volumes of EBSD and TKD are compared in Figure 3.20. For TKD, the scattering is heavily skewed in the forward direction and hence many electrons can scatter near the exit surface. In addition, forward scattered electrons have small scattering angles, resulting in slight spreading within thin specimens. Consequently, much more high energy electrons reach the exit surface and the interaction volume is smaller. The size of the interaction volume determines the spatial resolution in the SEM. The angular resolution of TKD is similar to that of EBSD and it is in the order of 0.5° to 1°.

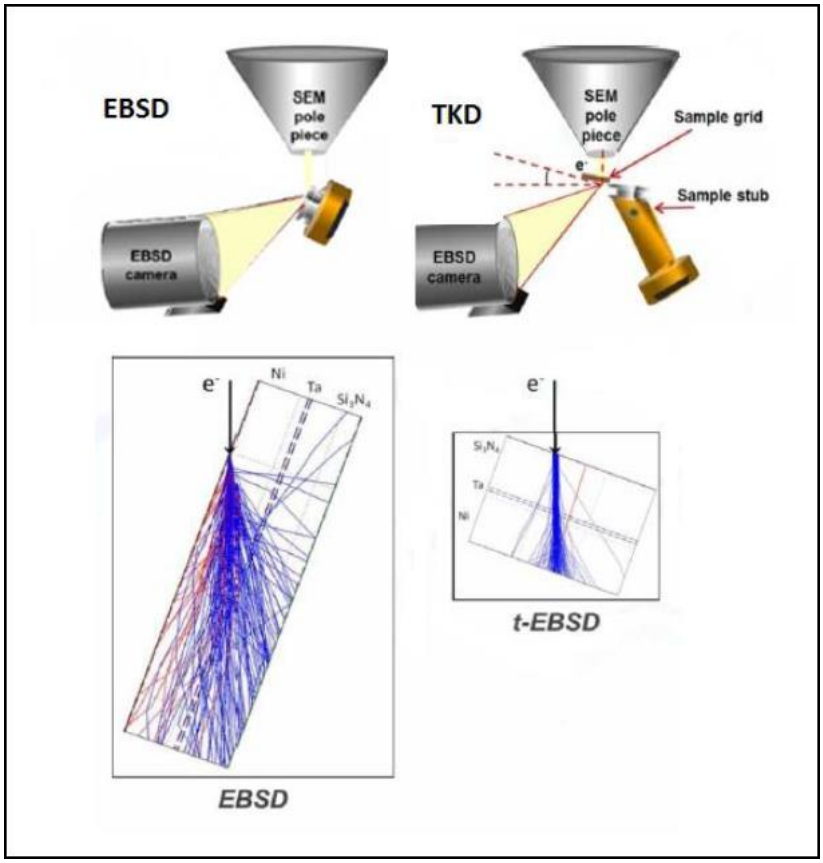

Figure 3.20: *Comparison of the geometry and corresponding Monte Carlo simulation of the interaction volume in an EBSD and TKD system. (Keller, Geiss et al. 2013)*

3.5.4 SEM Analysis

All SEM, TKD and EBSD analysis was performed on a JEOL 7001F FEG-SEM fitted with a Nordlys HKL system. The bulk X20 material and X20 steel weldments were analysed after being mounted and polished (Section 3.3.1).

3.6 TRANSMISSION ELECTRON MICROSCOPY

Transmission Electron Microscopy is a characterization technique where a beam of high energy electrons is transmitted through a thin specimen and they then interact with the specimen as they pass through. The Transmission Electron Microscope (TEM) is a flexible instrument that helps to image, measure and model the microstructures of nano-scale crystalline materials. Forward (electron) scattering through the thin specimen is the primary mechanism or signal that creates TEM images and diffraction patterns. It includes the direct beam, elastic scattering, diffraction (Bragg diffraction), refraction and inelastic scattering. Figure 3.14 illustrates

the signals that are generated in a TEM. The TEM not only provides crystalline information, but also topographical, morphological and compositional information. Therefore, the TEM also analyses the texture of the material. Any flaws, damages or fractures to the microstructure of a material can be identified using the TEM, which is not possible with X-ray diffraction analysis.

In this section only the main theory relating to the TEM and its analytical techniques such as Energy-Filtered TEM (EFTEM) and Energy Dispersive Spectrometry (EDS) used in this study is briefly discussed. An overview of Scanning TEM (STEM) is also provided. The literature from Williams and Carter (2009), Ducati (2013), Hull and Bacon (2001), Zou *et al.* (2011) and FEI (2006) which was used to compile this section, can be consulted for further reading.

3.6.1 Instrumentation and Image Formation

The TEM has four main components: (i) an electron optical column; (ii) a vacuum system; (iii) electronics such as lens supplies for focusing and deflecting the electron beam and a high voltage generator for the electron source (gun); (iv) software. Figure 3.21 below provides a schematic diagram of the general layout of a TEM, as well as a ray diagram illustrating the path of the electron beam which leads to diffraction in the TEM.

In the electron optical column there is an electron gun and a series of water-cooled electromagnetic lenses. The electron gun produces a stable beam of high energy electrons and usually consists of a filament (Tungsten or LaB_6), a Wehnelt cylinder and an anode. Another type of electron gun is a Field Emission Gun (FEG), similar to the one used in the SEM. There are usually 2 or 3 condenser lenses that control and collimate the electron beam onto the specimen. A condenser aperture controls the beam convergence angle onto the specimen. Consequently, a large area of the specimen may be uniformly illuminated at low magnification for EFTEM. The electron beam can also be strongly focused for higher magnifications or even an electron probe, of the order of a few nanometers, can be formed for STEM.

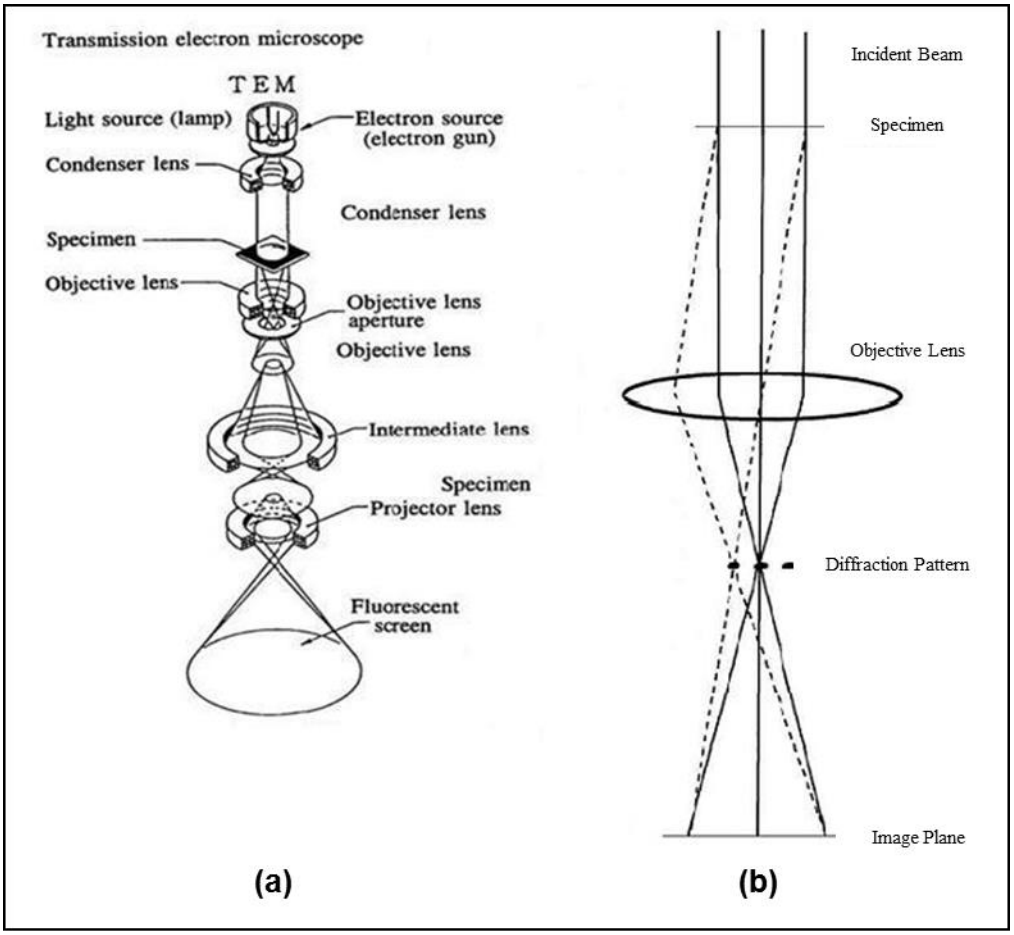

Figure 3.21: *(a) General layout of a TEM describing the path of the electron beam in a TEM. (b) A ray diagram illustrating the diffraction mechanism in the TEM. (Warwick 2010)*

An objective lens is used to form a TEM image of the specimen and surrounds the very thin specimen (thickness of less than 100 nm). It is the first and strongest image-forming lens. There are four other image-forming lenses that follow from the objective lens: a diffraction lens, an intermediate lens and two projector lenses. In the back focal plane of the objective lens there is an objective aperture that selects the beam used to form the TEM image. At the image plane of the objective lens the image of the specimen is formed. Ultimately, the image of the specimen is projected onto a fluorescent viewing screen from which the user directly observes. Digital images are recorded by a CCD which is stored in the camera chamber below the fluorescent screen. The orientation of the specimen with respect to the incident beam is controlled by the specimen stage. The specimen needs to be thin to allow for penetration or transmission of the electron beam.

Figure 3.22 provides ray diagrams that illustrate the difference in image mode and diffraction mode in the TEM. In diffraction mode, the objective lens focuses the forward scattered electrons into spots at the back focal plane. When in image mode, a magnified image is created in the image plane by inserting the objective aperture.

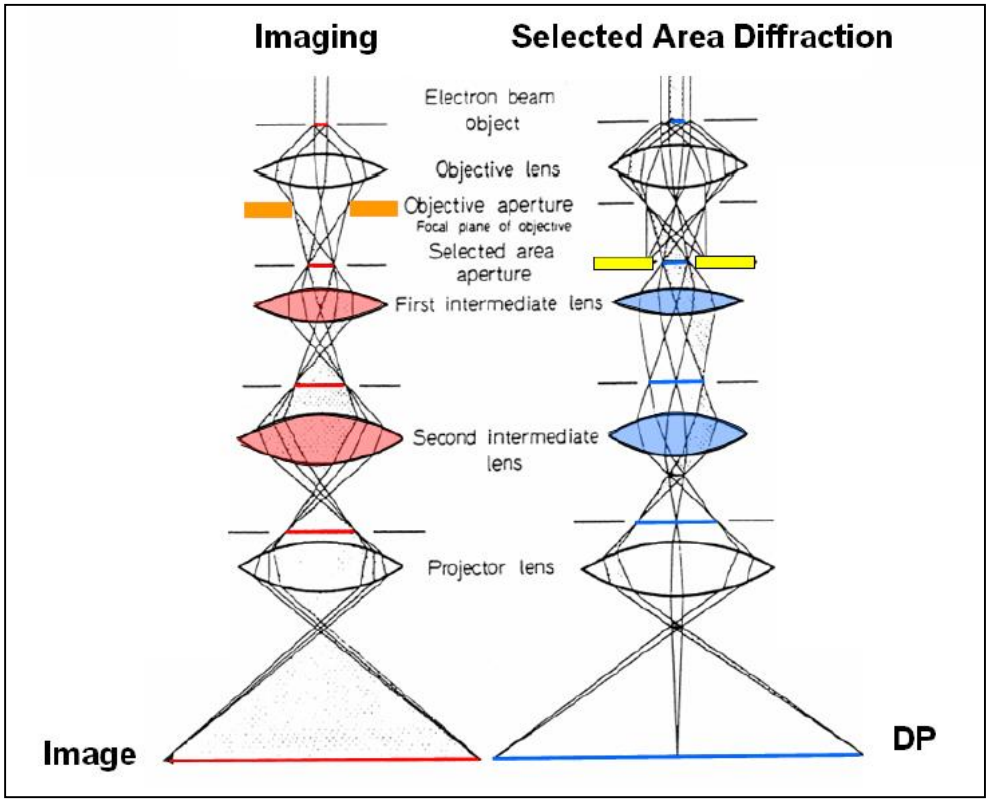

Figure 3.22: *Ray diagrams illustrating how the different apertures and post-specimen lenses form either an image or a diffraction pattern on the viewing screen. (Ducati 2013)*

3.6.2 Electron Diffraction Patterns

Diffraction is the interaction of high energy particles with the nuclei or valence electrons of atoms in the targeted specimen. The high energy particles can be electrons, protons or either X-ray photons (Neethling and Lee 2012). Crystal structure information, crystallite size and orientation of single crystals can all be determined by Electron Diffraction (ED). ED can be classified as a special case of elastic scattering. The TEM is used to study ED, since it can form a Diffraction Pattern (DP) of the distribution of scattered electrons. The Bragg condition gives that for two scattered waves to be in phase, their path difference should be an integer multiple of the

wavelength λ (equation 3.2). Therefore, diffraction peaks will occur in the diffraction pattern when the Bragg condition is satisfied. An ED pattern is a section through the reciprocal lattice of a crystal. Therefore, the knowledge from the Ewald sphere construction in reciprocal space can be used to construct these patterns. The different types of ED patterns that can be obtained from crystalline materials are shown in Figure 3.23.

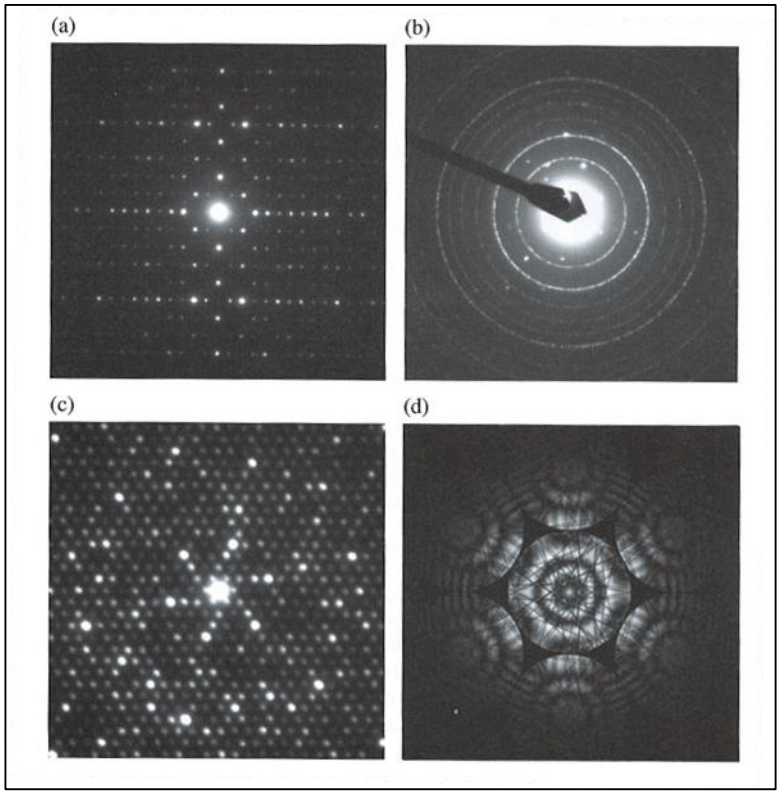

Figure 3.23: *The different types of ED patterns. (a) Spot SAED pattern from a single crystal. (b) Ring SAED pattern from a polycrystalline specimen. (c) Microdiffraction pattern (small convergent angle of the incident electron beam). (d) CBED pattern (large convergent angle of the incident electron beam). (Zou, Hovmöller et al. 2011)*

Figure 3.24 summarises the procedure for recording a Selected Area ED (SAED) pattern using the TEM. ED patterns are normally taken along a zone axis, since then all the reciprocal lattice points in the plane perpendicular to the zone axis will mostly satisfy the Bragg condition. Consequently, the specimen is tilted to the required zone axis, by following a specific Kikuchi line. The reason why the Kikuchi pattern is formed, is that the sample is thick enough to generate a large number of scattered electrons. These electrons are firstly inelastically and incoherently scattered and then elastically (Bragg) diffracted by the crystal planes, similar to the formation of an EBSP pattern.

The ED pattern simulation software known as Java Electron Microscope Simulator (JEMS) is usually used to index SAED patterns or identify possible zone-axes.

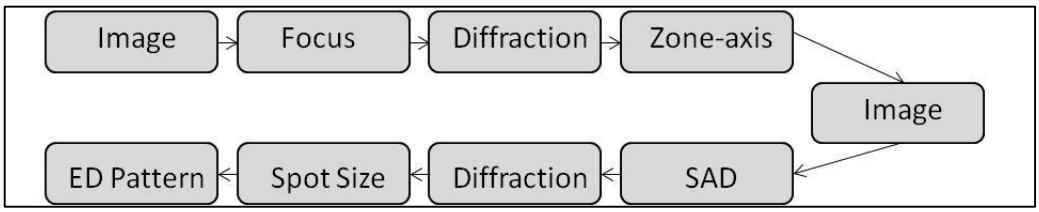

Figure 3.24: *Diagram illustrating the procedure for recording a SAED pattern using the TEM.*

To obtain a DP from a specific area of the specimen, such as a subgrain, a Selected Area Diffraction (SAD) aperture, while in image mode, must be inserted in the image plane of the objective lens (Figure 3.22). The SAD aperture size can be adjusted so that it encloses only the desired area.

3.6.3 Convergent Beam Electron Diffraction

Convergent Beam Electron Diffraction (CBED) is obtained when the incident electron beam is focused onto the specimen, whereas spot diffraction or SAED is obtained when the incident electron beams are parallel. The SAED and CBED diffraction modes are illustrated in Figure 3.25. CBED is a whole field on its own and in this section only a brief summary will be given on the important aspects of CBED pertaining to this study. For the full literature on CBED, the books written by Tanaka and Terauchi (1985), and Spence and Zou (1992) are recommended.

SAED is from a relatively large area of the specimen (>500 nm), while with CBED the illumination area is very small area (±1 nm) and determined by the size of the incident beam. The convergent beam at the specimen results in disks to form in the back focal plane of the objective lens and their diameter is depends on the convergence angle. The convergence angle of CBED is reasonably large (<0.1 - 1°) and therefore many details within the diffraction disks are obtained about the crystal that couldn't be obtained with SAED.

An example of a CBED pattern is shown in Figure 3.23(d). To have adequate intensity variation within the disks, the illuminated area of the crystal should have sufficient thickness. For every point in the 000 disk of a CBED pattern there is a corresponding

point in every other diffracted disc also satisfying Bragg's law (Vijayalakshmi, Saroja *et al.* 2003).

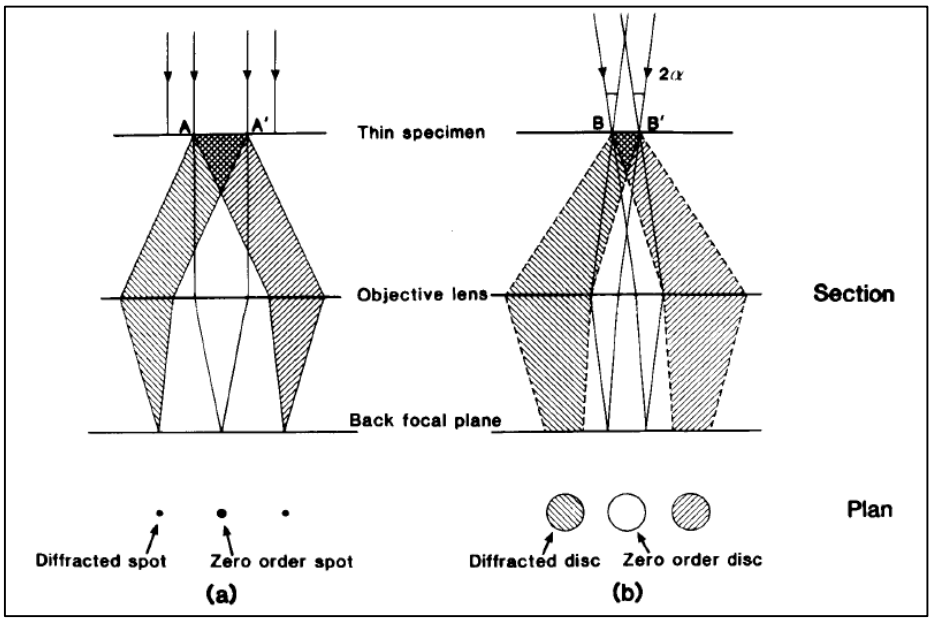

Figure 3.25: *Schematic ray diagram for the formation of (a) a SAED pattern and (b) a CBED pattern. The area AA' in (a) is selected by an aperture in the first image plane of the objective lens and the area BB' selected in (b) is determined by the probe size. (Champness 1987)*

(i) Thickness Measurement

To determine the thickness of a TEM thin-foil is crucial when calculating particle volume fraction or dislocation density. There are various methods available for determining thin-foil thickness using the TEM (Baker 2001). Using CBED patterns is one such method and it is clearly described by Williams and Carter (2009). A brief summary of the method is now given.

The CBED pattern is obtained under two-beam conditions of a low order reflection in order to simplify interpretation. By tilting the specimen to strong two-beam conditions, there is only one strongly excited hkl reflection and the Kikuchi line cuts the reflecting spot symmetrically. As a result, the CBED discs will contain parallel fringes instead of concentric intensity fringes as the case under zone axis conditions. The measurements required and graph plotted in order to calculate the specimen thickness is shown in Figure 3.26. From the intercept of the straight line ($\frac{1}{t^2}$) the thickness t was

then calculated. In addition the following equations are used (Williams and Carter 2009):

$$s_i = \lambda \frac{\Delta\theta_i}{2\theta_B d_{hkl}^2} \tag{3.3}$$

where λ is the electron wavelength of 2.508 pm (Williams and Carter 2009) for a 200 keV beam energy, θ_B is the Bragg angle for the diffracting hkl plane and d_{hkl} is the hkl interplanar spacing obtained using the lattice parameter a of ferrite as 2.87 Å (Kozeschnik and Holzer 2008).

$$\frac{s_i^2}{n_k^2} + \frac{1}{\xi_g^2 n_k^2} = \frac{1}{t^2} \tag{3.4}$$

where ξ_g is the extinction distance and n_k is an integer and k is an integer identical to i or differing by a constant integer not related to λ, from i.

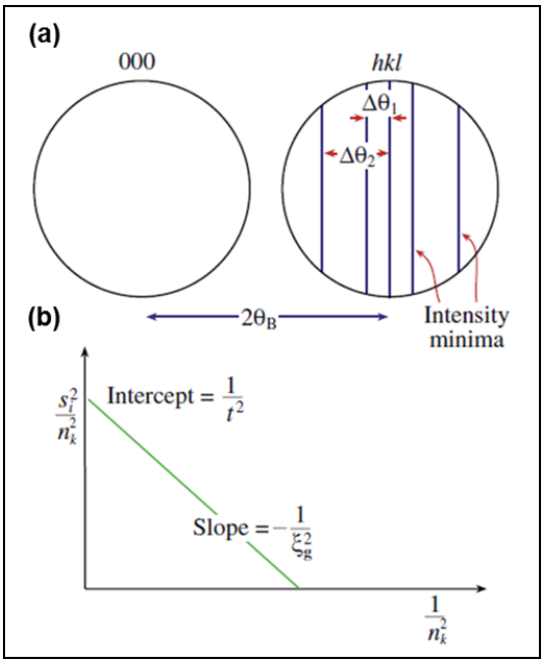

Figure 3.26: *(a) Schematic illustration of the required measurements to determine thickness from the K-M fringes. (b) Plot of* $\frac{s_i^2}{n_k^2}$ *vs* $\frac{1}{n_k^2}$*.(Williams and Carter 2009)*

3.6.4 Scanning Transmission Electron Microscopy

The Scanning Transmission Electron Microscope (STEM) is a special type of mode in the TEM. The STEM is similar to the SEM since the electron beam is focused into a small probe that scans the specimen in a raster pattern. This raster type scanning across the specimen makes the STEM suitable for analytical techniques such as EDS mapping, Electron Energy Loss Spectroscopy (EELS) and Annular Dark-Field (ADF) imaging. This information can be obtained simultaneously, which allows direct correlation of the STEM image with quantitative data extracted from these signals (Zou, Hovmöller *et al.* 2011). In this section STEM is briefly discussed. The literature by Williams and Carter (2009), Zou *et al.* (2011), and Pennycook and Nellist (2011), which was used to compile this section, can be consulted for detailed discussions on the topics covered.

(i) Instrumentation and Image Formation

The objective-lens optics in a STEM is more complex than in a TEM. Figure 3.27 provides a schematic diagram of the optical configuration in a STEM. The beam is focused by a series of lenses to form a probe onto a thin, electron-transparent specimen. The objective aperture imposes a diffraction limit on the smallest probe diameter that can be formed and it also restricts the amount of beam current available since the electrons that do not enter the aperture are lost. Unlike in a SEM where the scanning beam pivots about a point above the specimen, the scanning beam in the STEM must at all times scan parallel to the optic axis in order to imitate the parallel beam in the TEM even though it is scanning. To ensure that the probe remains parallel as it scans the specimen surface, a double-deflection process that incorporates two pairs of scan coils to pivot the point about the front focal plane of the upper-objective polepiece, is used.

Figure 3.28 illustrates the principle of image formation in the STEM. From each point scanned on the specimen surface, a STEM signal is generated, detected, amplified, and a corresponding signal displayed at an equivalent point on the computer display. The STEM is serial recording instead of parallel recording like in the TEM. Subsequently, the STEM imaging is a much slower process than TEM imaging.

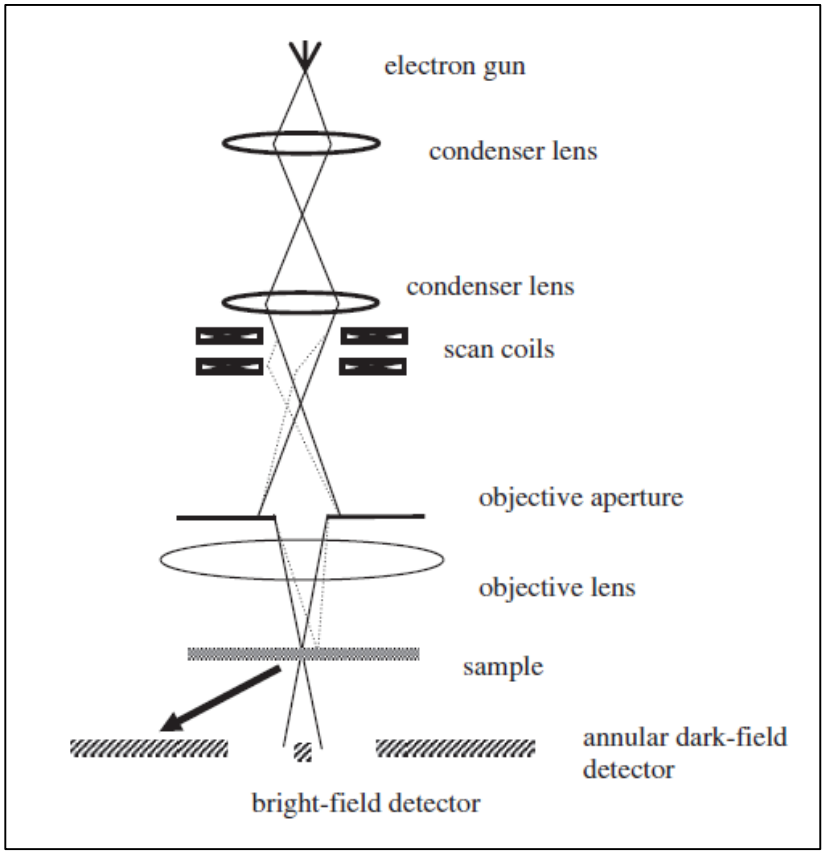

Figure 3.27: *Schematic diagram of the setup in a STEM. (Pennycook and Nellist 2011)*

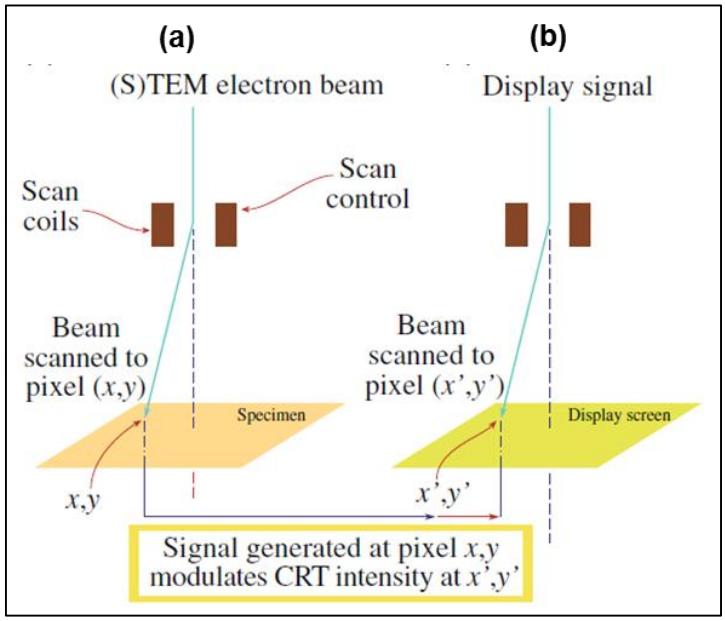

Figure 3.28: *Schematic illustration of the STEM operating principle to form a scanning image where the same scan coils control (a) the beam-scan on the specimen surface and (b) the beam-scan on the computer display of the STEM. (Williams and Carter 2009)*

There are various detectors that can be attached to the STEM to collect the different signals from beam-specimen interactions and plot the signal as a function of probe position to form a magnified image. This includes a SE detector, BSE detector, X-ray detector for EDS, EELS detector (PEELS) and BF/DF detectors. Figure 3.29 illustrates the position of these detectors in the TEM-STEM system.

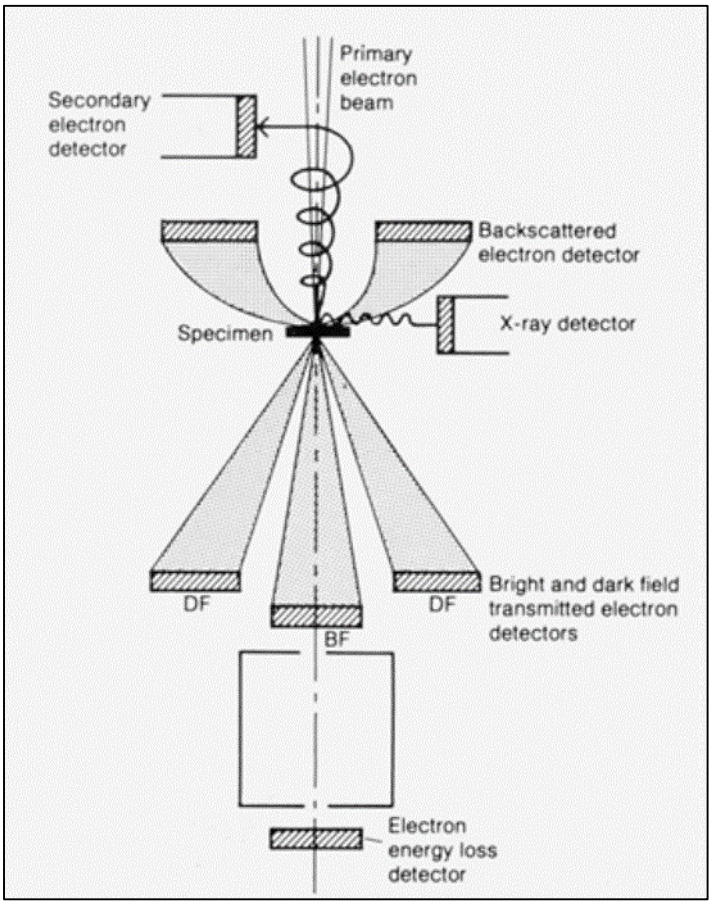

Figure 3.29: *Schematic illustration of different detectors that can be attached to a STEM system to collect various signals from beam-specimen interactions. (Cantoni 2013)*

The TEM is operated in diffraction mode to form a STEM image and a detector is inserted into the viewing chamber of the TEM, either above or below the screen. The stationary DP then falls onto the detector, which then sends the signal to the display.

The great advantage of STEM over TEM is that, just like in the SEM, no lenses are used to form the image. Consequently, any defects in the imaging lenses, such as chromatic aberrations, has no effect on the image resolution. This is advantageous for thick specimens. However, the image resolution is limited by the beam dimensions in

the same way as in the SEM. Hence, the STEM image quality depends on the probe and the probe has aberrations since it is formed by a lens, just not an imaging lens.

3.6.5 TEM and STEM Imaging

Williams and Carter (2009) provide the complete literature, including complex mathematical equations, that describe image contrast in the TEM and STEM. Only a short overview of specifically Bright Field (BF) and Dark Field (DF) imaging will now be given.

Bright Field Imaging

In the TEM BF mode, the objective aperture is positioned upon the direct beam, corresponding to a bright central spot in ED pattern (position A in Figure 3.09), to form a BF image. This is achieved by inserting the objective aperture into the back focal plane of the objective lens as illustrated in Figure 3.31(a). The image is then formed by only the transmitted beam and any low-angle inelastic scattering.

Figure 3.30: *The location of the objective aperture (circles) on the SAED pattern when forming (A) BF and (B) DF images. (Williams and Carter 2009)*

In the STEM, a detector is used instead of an aperture. To form a BF-STEM image, a BF detector is inserted onto the axis of the microscope and it intercepts the direct beam electrons regardless of where the beam is scanning on the specimen (Figure 3.31(c)). The position of the BF detector is shown in Figure 3.29.

Dark Field Imaging

A DF image is formed by any single diffracted beam, i.e. electrons scattered in a specific direction. In the TEM, the objective aperture is either positioned on a diffracted

beam (position B in Figure 3.30) or the beam is tilted as to allow the required diffracted beam to pass through the aperture. This is shown in Figure 3.31(b).

In STEM, a DF image is formed by shifting the stationary DP so that the desired scattered beam is on the optic axis and hits the BF detector. In this case the BF detector is used to form a DF image. Instead of using the BF detector for DF imaging, an annular detector that surrounds the BF detector can be used as shown in Figure 3.29. This Annular Dark-Field (ADF) detector collects all the scattered electrons to form an ADF image. Figure 3.31 summarises the BF and DF imaging mechanisms in the TEM and STEM.

In a STEM the collection angle of the detector can be changed by varying the camera length and in essence a variable objective aperture can be created. This makes the STEM more flexible than the TEM and there is better control over which electrons contribute to the image. The process of collecting high-angle electrons to form an image is known as High-Angle Annular Dark-Field (HAADF) imaging. The HAADF detector sits around the ADF detector. A semi-angle of 10 to 50 mrad (±0.6° to 3°) of the scattered electrons is gathered by the HAADF detector (Zou, Hovmöller *et al.* 2011).

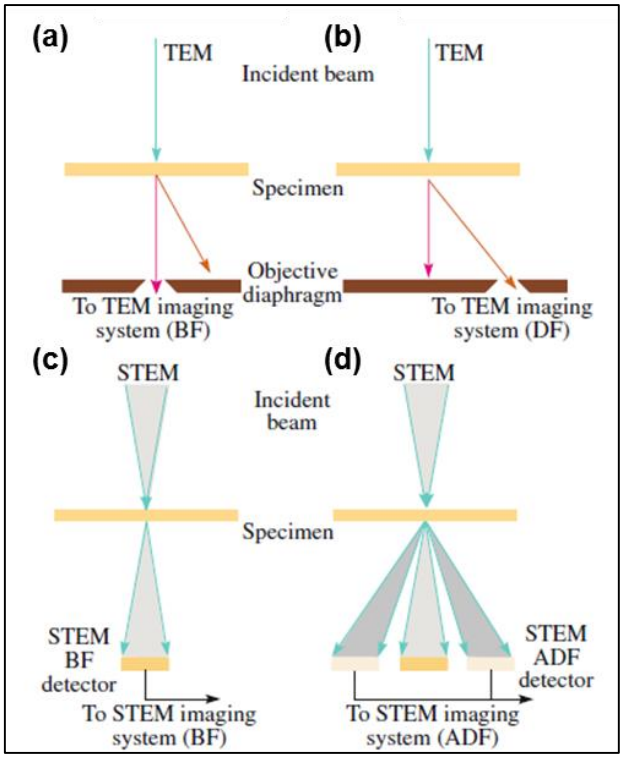

Figure 3.31: *Comparison of the formation of (a) BF and (b) DF images in the TEM by using an objective aperture to select the direct and scattered beam, respectively. In the STEM equivalent operations are performed by using (c) an on-axis detector for BF imaging and (d) an off-axis annular detector for DF imaging. (Williams and Carter 2009)*

3.6.6 Imaging of Dislocations

One of the main applications of TEM and STEM is to study defects in crystalline materials. Dislocations, which are linear defects, are the only type of defect of interest for this study. When imaging a dislocation, or a defect in general, to obtain the strongest contrast and most information about it, the following is required and Williams and Carter (2009) can be consulted for explanations:

i. The setting up of strong two-beam diffraction condition such that the diffraction vector $\boldsymbol{g}_{hkl}$, is known.
ii. The setting of the excitation error $\boldsymbol{s}$ to be slightly positive i.e. the specimen is slightly tilted away from the Bragg condition.

The reason for tilting the specimen to a two-beam diffracting condition, is that BF images formed under multi-beam diffracting conditions become perplexing when dislocation densities exceed 10^{14} m^{-2} (Baker 2001).

The Burgers vector $\boldsymbol{b}$ of a dislocation defines the magnitude and the direction of slip. In addition to the 2 requirements for imaging dislocations set out above, the diffracting vector $\boldsymbol{g}_{hkl}$ must be chosen such that the invisibility criterion $\boldsymbol{g} \cdot \boldsymbol{b} = 0$ is evoked (Baker 2001). The evoking of the invisibility criterion is a further measure to alleviate the difficulty of determining high dislocation densities, since the number of dislocations observed is reduced.

3.6.7 Energy-Filtered TEM

Energy-Filtered Transmission Electron Microscopy (EFTEM), also known as Energy-Filtered Imaging (EFI) or Electron-Spectroscopic Imaging (ESI), is an analytical electron microscopy technique that has the ability to produce reliable, quantitative two-dimensional maps of the chemical composition of a specimen with high spatial resolution and chemical accuracy (Thomas and Midgley 2002). By connecting an imaging filter known as the Gatan Imaging Filter (GIF) to a modern TEM, a spectrum of the energy-loss of inelastically scattered electrons (Figure 3.32) that pass through the specimen can be acquired. Subsequently, this spectrum is called an Electron Energy-Loss (EEL) spectrum. The EEL spectrum provides, in addition to quantitative compositional data, information on the physical properties such as the local thickness of the region under inspection that can be calculated from the scattering statistics of the complete spectrum. An energy-filter can be used to select any energy range of the spectrum in order to form an image of the electrons within this energy window.

EFTEM has the significant advantage to both record and quantify EEL spectra to obtain precise chemical information, and to create two-dimensional elemental maps by forming images using inelastically scattered electrons. In this section a brief outline of the theory of EELS and EFTEM has been compiled from good literature reviews provided by Thomas and Midgley (2002), Williams and Carter (2009), and Brydson (2001).

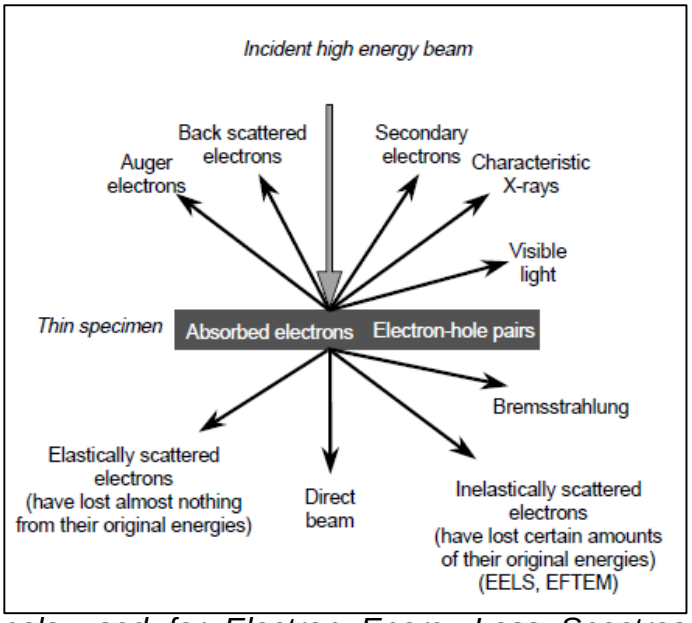

Figure 3.32: *Signals used for Electron Energy-Loss Spectroscopy (EELS) and Energy-Filtered Transmission Electron Microscopy (EFTEM). (Kothleitner 2000)*

(i) Electron Energy-Loss Spectroscopy

Electron Energy-Loss Spectroscopy (EELS) is the analysis of the energy distribution of electrons that have been transmitted through the specimen. As seen from Figure 3.32, the electrons may either be elastically or inelastically scattered. Subsequently, a spectrum of transmitted electron-energy loss (EEL spectrum) results and to examine these electron energies a magnetic-prism spectrometer is used. Presently, there is only one such spectrometer commercially available, which is manufactured by Gatan, Inc. It is termed a parallel-collection EELS (PEELS) and it is mounted on a TEM or STEM after the viewing screen or post-specimen detectors. The magnetic-prism disperses the electron energies similarly to the dispersion of white light by a glass prism. The prism essentially acts as a magnetic lens since it focuses electrons that suffer the same energy-loss, but travel in both on-axis and off-axis directions, back into the dispersion plane of the spectrometer.

A typical EEL spectrum is illustrated in Figure 3.33. As can be seen, each feature observed in an EEL spectrum can be categorised. A full discussion on these features and EELS as a whole is provided by textbooks such as that written by Egerton (1996). The zero-loss peak corresponds to the elastically scattered electrons. The high

energy-loss (>50 eV) portion of the spectrum contains the information from the inelastic interaction of the incident electron with inner or core shell electrons.

The high energy-loss spectrum is composed of ionization or core-loss edges on a rapidly decreasing plural (more than one) scattering background. It is very important for good EELS results that the specimen is as thin as possible to avoid plural scattering. The ionization loss signal is generated when an incident beam electron transfers sufficient energy to a core-shell electron in the specimen to displace it outside the attractive field of the nucleus and hence leave it ionized. This ionization process is characteristic of the involved atom and hence the signal is a direct source of the chemical and elemental information. The term “edge” is used instead of peak to refer to the ionization-loss signal in the EEL spectrum. These edges form the basis for elemental mapping.

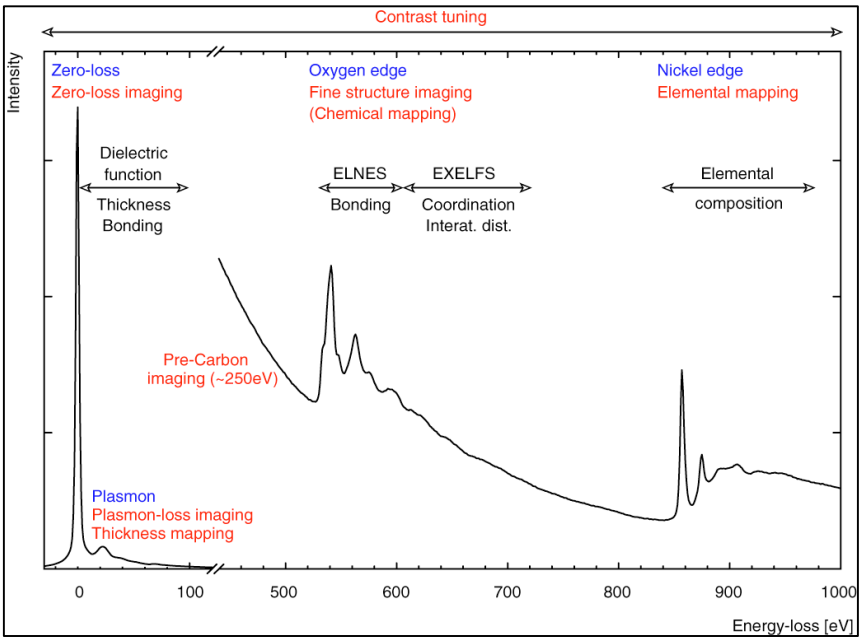

Figure 3.33: *Typical EEL spectrum. (Kothleitner 2000)*

(ii) EFTEM Elemental Mapping

EFTEM is an imaging-spectroscopy technique in which elemental mapping is performed using PEELS in the conventional fixed beam TEM by implementing an energy-filter that filters out electrons with a specific energy. This energy filter is based on the same concept as the magnetic-prism except it has the capability of forming images in addition to spectra. This energy-filter/ magnetic prism is a highly sensitive device since it provides an energy resolution of less than 1 eV.

The acquisition of the energy-loss data using EFTEM and STEM equipped with a PEELS is compared in Figure 3.34. During EFTEM data acquisition, the spectral and therefore chemical information is probed successively by acquiring a number of images separated in energy loss. The data cube acquired using STEM-PEELS is filled one spectrum at a time. All the data cubes are then combined to form an elemental image. Thus, the acquisition time of an elemental map using EFTEM is much shorter. EFTEM analysis provides similar spatial resolution to EEL spectrum imaging, which is about 1 nm (Thomas and Midgley 2002). EFTEM spatial resolution is determined by chromatic aberration that is limited by the objective aperture. In addition, EFTEM has a considerably better light element sensitivity than EDS.

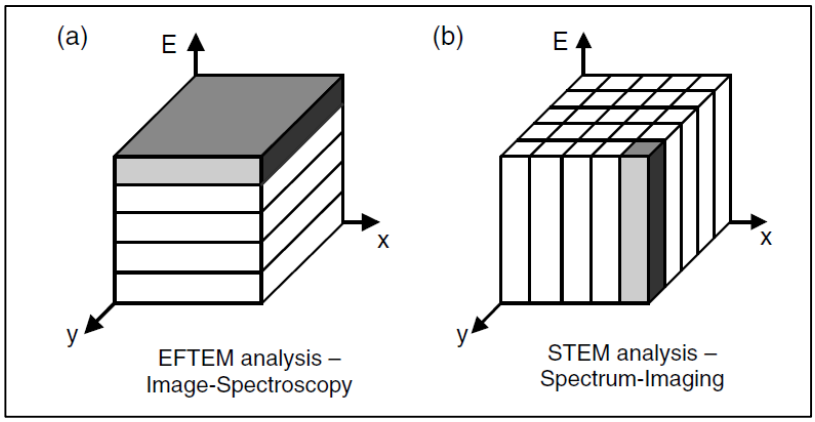

Figure 3.34: *Comparison of the acquisition of energy-loss data using (a) EFTEM and (b) a STEM equipped with a PEELS. (Thomas and Midgley 2002)*

(iii) Instrumentation and Operating Principles

EFTEM is performed by selecting or filtering out electrons of a specific energy coming through the spectrometer and then forming an image. An energy-selecting slit is inserted into the dispersion plane so that an energy-filtered image of the electrons contained in the selected energy window is observed. Consequently, the energy slit is positioned on an element-specific ionization edge. By applying an appropriate background subtraction, the EFTEM map will show the distribution of that particular element in the specimen.

There are two-types of energy-filters that produce EFTEM images: the in-column (Ω) filter and the post-column GIF. The energy-filter used in this study is the post-column GIF, which is attached to the bottom of the fluorescent viewing screen exactly like a PEELS. Consequently, the GIF is a Gatan PEELS with an energy-selecting slit after the magnetic prism and a 2D slow-scan CCD detector. Figure 3.35 shows a detailed illustration of the GIF. The dispersed spectrum is projected onto the energy-selecting slit.

Certain factors should be taken into account when choosing the CCD camera acquisition parameters, such as the exposure time and binning. A too long exposure time can lead to sample drift. Conversely, a too short exposure time leads to low count levels and hence noise-dominated images. Several ways of achieving higher spatial resolution in EFTEM is discussed by Thomas and Midgley (2002).

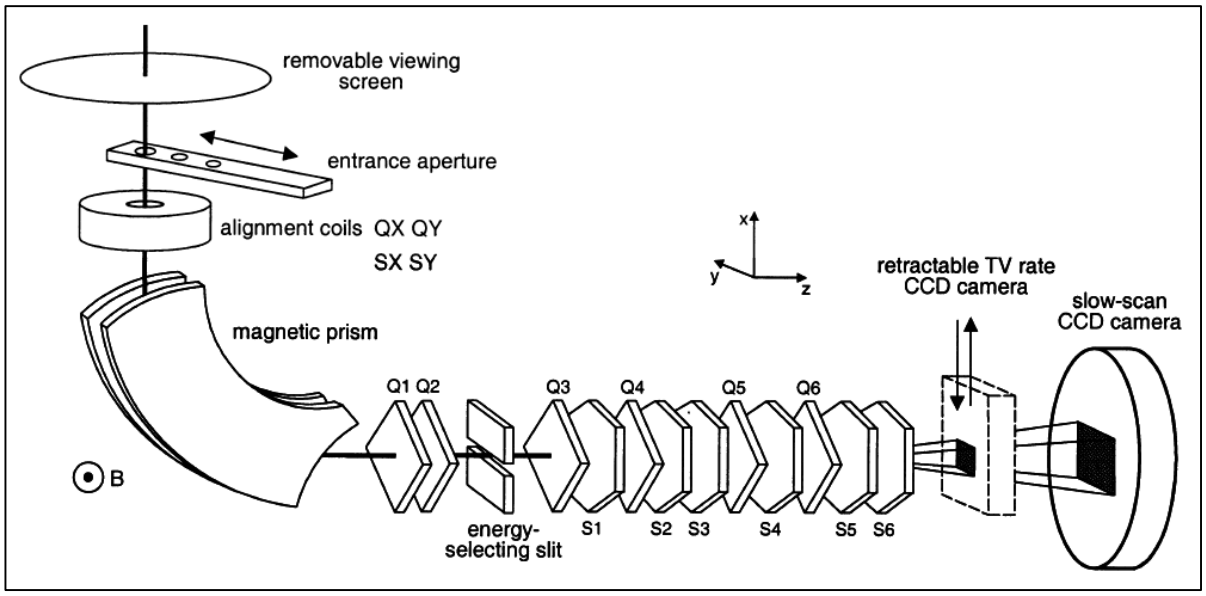

Figure 3.35: *Detailed schematic illustration of a GIF and its various components. The designations Q and S indicate a quadrupole and sextupole lens, respectively. (Thomas and Midgley 2002)*

The EFTEM process of acquiring elemental maps can be divided into five stages. An unfiltered image or DP is firstly formed and then transformed into a spectrum. A portion of the spectrum is selected using the energy-selecting slit and this extracted part of the spectrum is transformed back into an image or DP, now an energy-filtered image or DP. Lastly, this energy-filtered image or DP is recorded by the CCD detector.

(iv) Three-Window Method

When an energy-filtered image at an element-specific ionization edge is obtained, it does not imply that the image maps the distribution of the selected element. There is a background contribution from a variety of inelastic events occurring at lower energy losses, superimposed onto the edge signal. The actual intensity of the edge signal can be determined by subtracting the background intensity. A fitting can be made of the background intensity I using a power-law function of the following form (Brydson 2001):

$$I = A\,E^{-r} \tag{3.5}$$

where E is the energy-loss, and A and r are unknown constants that can be determined with two measurements. The most common method used to account for the background is the three-window method, which is quantitative in nature. This technique entails recording two pre-edge images and a post-edge image. The position of acquisition of these images are shown in Figure 3.36. The post-edge image contains both the spatial and chemical information of the chosen element, as well as the background contribution. The pre-edge images evaluate only the background contribution. For each individual pixel in the post-edge image, the background fitting parameters, A and r, are calculated based on the two pre-edge images. Subsequently, a background image is generated and subtracted from the post-edge image, leaving the core-loss signal remaining in the form of an elemental map. The other methods for background correction in EFTEM is discussed by Thomas and Midgley (2002).

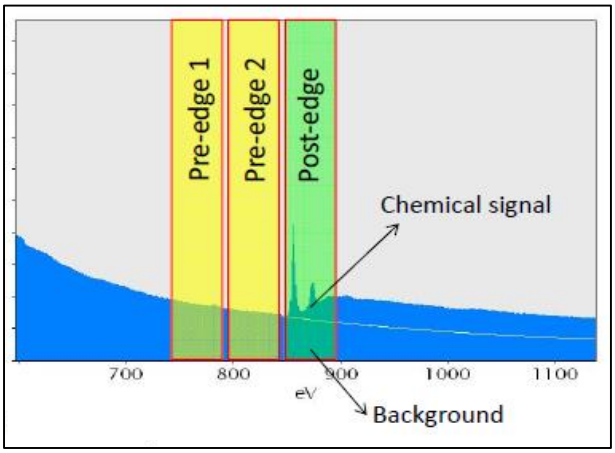

Figure 3.36: *Illustration of three-window method and position of pes- and post-images on EEL spectrum. (Erni 2013)*

(v) Thickness Determination

EFTEM thickness measurements has two advantages over the CBED method: it is a much faster technique and the specimen need not be crystalline. For example, the thickness measurement of each precipitate in an EFTEM elemental map can be performed with a simple algorithm, while with the CBED method one would have to take a DP for each precipitate.

By integration of the EELS signal, the EEL spectrum can provide a useful estimate of the thickness of both crystalline and amorphous specimens, in terms of the total inelastic mean free path λ', i.e. mean free path of the inelastic electrons. The mean free path λ' is the average distance an electron travels between scattering events. This value indicates how thin a TEM specimen must be so that plural scattering is not significant and single scattering theory can be applied. Poisson statistics can be used to describe the probability of plural scattering. Consequently, the ratio of the specimen thickness t to the total inelastic mean free path λ' can be written as (Thomas and Midgley 2002):

$$\frac{t}{\lambda'} = \ln\left(\frac{I_t}{I_0}\right) \tag{3.6}$$

where I_t is the total integrated spectra intensity and I_0 is the zero-loss integral. Subsequently, the specimen thickness t can be determined if the total inelastic mean free path λ' is known. A $\frac{t}{\lambda'}$ map is the spatially parallel EFTEM equivalent.

From equation 3.6 it follows that to acquire an EFTEM thickness ($\frac{t}{\lambda'}$) map, the logarithm of the ratio of unfiltered to zero-loss signal must be calculated. The pure elastic signal is recorded as a zero-loss image. The unfiltered image is obtained by acquiring an image with the energy-selecting slit removed, permitting both elastic and inelastic signals to be recorded by the detector. For both images the conditions must be identical. Both the three-window method and thickness measurement methods as discussed above, are incorporated into the EFTEM acquisition software.

3.6.8 Energy Dispersive Spectrometry

X-rays are also produced during the electron-specimen interaction when excited atom reverts back to its ground state (Figure 3.32). Hence, X-rays result from inelastic collision events. Microanalysis refers to the analysis of a specimen on a microscopic scale, resulting in the gain in structural, compositional and chemical information about the specimen. X-ray microanalysis is the best method for routine chemical analysis of small volume materials. Microanalysis in the SEM and TEM can be performed using Energy Dispersive X-ray Spectrometry (EDS or EDX). In this technique the energy of the individual photons are measured and then used to build up a digital histogram representing the distribution of energies of the X-rays (Tiedt 2002). The X-rays generated are characteristic of the atom involved and the produced signal is a direct source of the chemical information of the specimen. There are two X-rays signals that produce an X-ray spectrum, namely Bremmstrahlung (continuum) X-rays and characteristic X-rays.

The EDS system in the SEM and TEM/STEM are similar. This section provides a brief overview on EDS with the main focus on the TEM/STEM-EDS system. The literature was summarised from Williams and Carter (2009), Tiedt (2002), Watanabe (2011), Friel (2003) and Ducati (2013) and these texts can be consulted for further detailed discussions on EDS.

(i) Instrumentation and Operating Principles

An energy dispersive X-ray spectrometer is the device that determines X-ray intensity as a function of the energy of the produced X-ray radiation. A schematic diagram of an EDS system in a TEM/STEM is shown in Figure 3.37. EDS is basically a detector system where the detector converts the energy of each emitted X-ray into a voltage signal of proportional size. The most widely used EDS detectors are the Si(Li) detector and the Silicon Drift Detector (SDD).

The X-ray spectrum is given as count-rate against X-ray energy in keV. The count rate can be used to derive the concentration of the elements in the specimen. An EDS spectrum displays peaks at characteristic energies of the elements in the specimen.

The TEM is operated in STEM mode for X-ray microanalysis, where the probe size can be adjusted between 2 and 0.5 nm (Ducati 2013). As the beam is raster scanned across the specimen surface an X-ray spectrum is produced at each point.

The resolution of an energy dispersive spectrometer is a measure of the ability of the X-ray spectrometer to separate adjacent X-ray peaks. Resolution is inversely proportional to count rate.

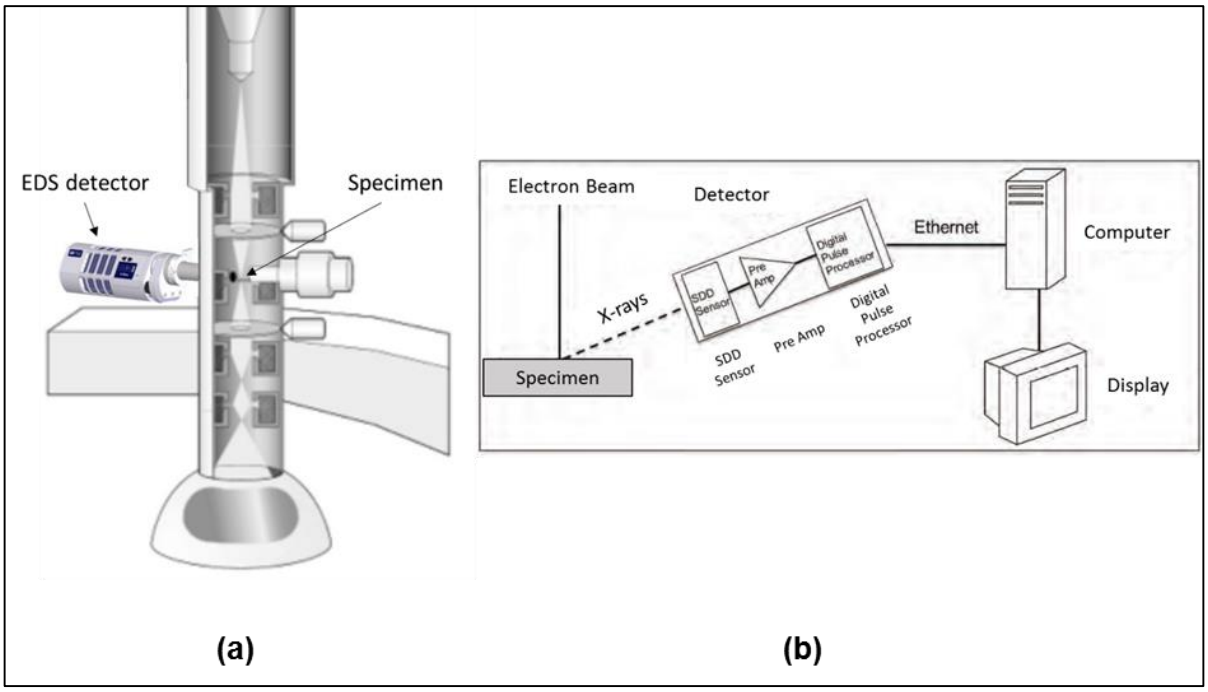

Figure 3.37: *Schematic of (a) a typical TEM/STEM-EDS system and (b) components of modern digital EDS system. Adapted from Oxford Instruments (2013), and Heath and Taylor (2015).*

(ii) Data Analysis

Qualitative Analysis

EDS qualitative analysis entails the identification of the elements in a specimen using the intensities of the characteristic X-ray peaks for each element. Modern computer based systems have a preloaded databases on their EDS software, from which they can identify and label peaks automatically.

Quantitative Analysis

Quantitative analysis can only be performed once qualitative analysis has been done. The X-ray counts cannot be taken as a direct measure of the concentration of each

element in the specimen as to perform EDS quantitative analysis. Therefore the intensities of a standard of an element is measured from its spectrum. Then the relative intensities for the element is compared between the standard and unknown specimen. However, some correction must be made. ZAF (Z-atomic number; A-absorption; and F-fluorescence) is the most important technique in correcting quantification results. Quantitative analysis accuracy becomes poor when the content of an element is less than 2% (Goldstein, Newbury *et al.* 2003). If the TEM specimen is thin enough, the ZAF corrections can be replaced by a single k- factor (Ducati 2013).

(iii) X-Ray Mapping

EDS can also perform an X-ray mapping technique which gives a 2D image of the distribution of the elements in the specimen for the area scanned by the acquisition of element specific maps. This technique is similar to EFTEM elemental mapping. Both qualitative and quantitative digital X-ray mapping can be performed. As with STEM-EELS, spectrum imaging is the preferred method for X-ray mapping, i.e. a full spectrum is collected at each pixel in the digital image. Subsequently, this can only be performed in STEM mode. X-ray maps for different elements are obtained simultaneously.

(iv) EDS vs EELS in TEM/STEM

In the TEM/STEM environment, EELS and EDS are complementary techniques for microanalysis and should be used in combination. EELS has a detection sensitivity in the range of 0.1 to 1 wt% for light elements ($Z < 11$), whereas more accurate analysis can be performed for heavier elements using EDS (Brydson 2001). At present, the spectral resolution in EELS is much higher (0.3 – 2 eV) than in EDS (>100 eV), which is determined by the probe size (Kothleitner 2000). Even in thin foils, EDS is impaired by the effects of beam broadening and hence it is not possible to perform high spatial resolution analysis like with EELS, where these effects are absent since the sampling area is limited by using a well-defined collection aperture. EELS is also a much more efficient mapping technique than X-ray mapping.

3.6.9 Summary of TEM Analysis

TEM/STEM analysis was performed using a JEM JEOL2100 (LaB_6) TEM at a primary energy of 200 kV. The TEM is fitted with a GATAN Quantum GIF and equipped with an Oxford Instruments X-Max 80 SSD. A summary of the specimens prepared for TEM analysis in this study, as well as what type of evaluation (precipitates, subgrains and dislocations) has been performed on each, is provided in Table 3.6.

Table 3.6: *TEM specimens prepared in this study and what type of analysis and technique has been performed on each.*

Sample Name	***FIB-SEM***	***Twin-jet electropolished***	***Extraction replica***
Bulk X20 material (new and damaged)	Dislocations (TEM/STEM) Precipitates (EFTEM)	Dislocations (TEM/STEM) Subgrains (TEM/STEM)	Precipitates (EFTEM, EDS)
FGHAZ (new and damaged weldments)	Precipitates (EFTEM)		
ICHAZ (new and damaged weldments)	Precipitates (EFTEM)		
CGHAZ (new and damaged weldments)	Precipitates (EFTEM)		
Over-tempered (new and damaged weldments)	Precipitates (EFTEM)		

3.7 X-RAY DIFFRACTION

X-ray diffraction is a complementary method to TEM and is referred to as the interaction of X-rays with a crystalline solid and then observing the diffracted X-ray beams. The angle between the incident X-rays beam and the plane of the crystallites,

i.e. diffracted beams, are given by Bragg's Law (equation 3.2) (Neethling and Lee 2012). A short overview of XRD and peak broadening analysis, compiled from the works by Suryanarayana and Norton (1998), Sardela (2008), Hammond (2009), Tang, Lynch *et al.* (2006), and Pesicka, Kuzel *et al.* (2003), is presented in this section.

3.7.1 Instrumentation and Operating Principles

Figure 3.38 provides an image describing the main components of an X-ray diffractometer and a ray diagram of a diffractometer fitted with a Position Sensitive Detector (PSD).

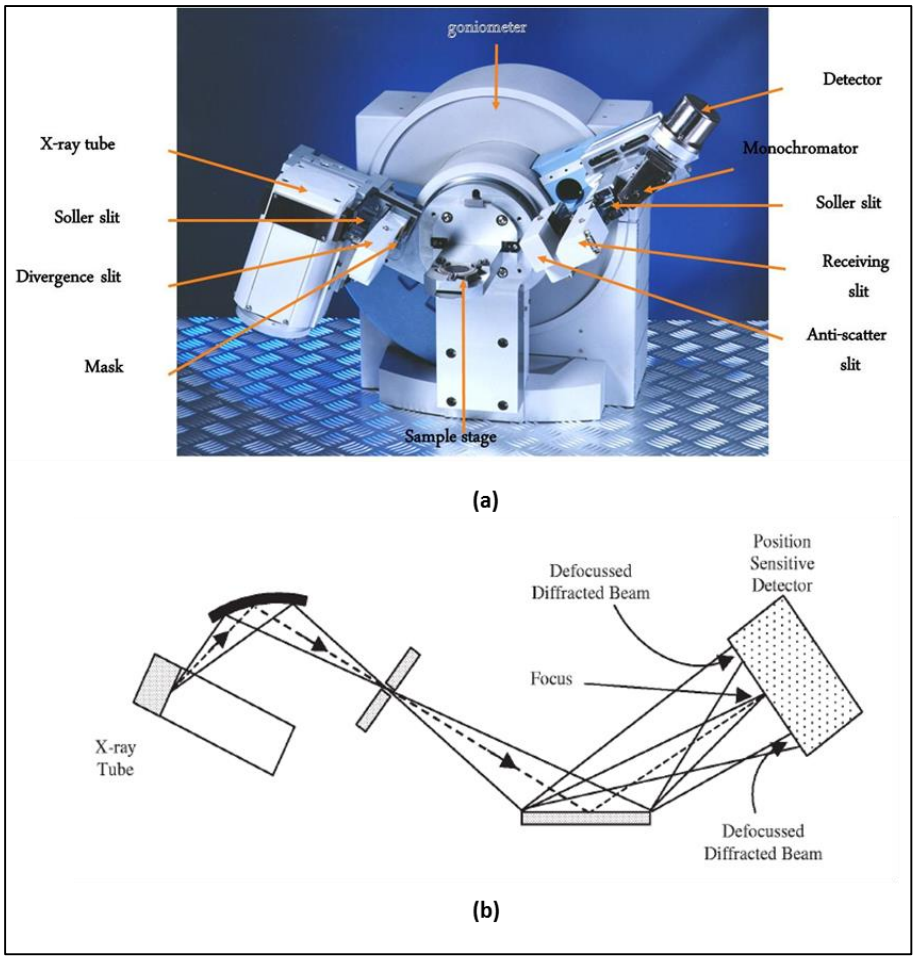

Figure 3.38: *(a) Descriptive image of a basic powder diffractometer. (Pan-Analytical 2013) (b) A simple ray diagram of a diffractometer with a PSD. (Cheary, Coelho et al. 2004)*

The θ-2θ (Bragg-Brentano) diffractometer is a widely used powder X-ray diffractometer and is the type used in this study. Its name originates from the fact that the angle between the plane of the specimen and the X-ray source is θ, which is the

Bragg angle. The angle between the detector and the X-ray source projection is 2θ. In this geometry, the detector moves through a range of angles while the X-ray source remains fixed. An X-ray tube generates the beam of X-rays. The monochromatic diffracted beam is detected by a detector. The detector counts the numbers of photons, which is given as intensity, at a certain 2θ position. Consequently, an XRD pattern of intensity versus 2θ is obtained. A linear PSD with a CCD is normally used in an XRD setup.

3.7.2 Crystallite Size and Strain Determination

Diffraction information regarding the crystallographic phase, orientation and lattice parameters are easily obtainable using XRD. In addition information regarding the crystallite size and micro-strain can be obtained by investigating the XRD pattern peak widths. The broadening of diffraction lines in an XRD spectrum can be attributed to either the instrumental effects or due to the specimen. The latter can be divided up into diffraction-order-independent (size) and diffraction-order-dependant (strain) broadening. Materials with small crystallite sizes (nano-particles) and high dislocation densities will have peaks with a larger FWHM.

If it is assumed that broadening is only due to dislocations and crystallite size, then strain broadening is caused by the extended displacement fields in the crystal caused by dislocations. The magnitude of the broadening depends on the type of dislocation and on the direction of the diffraction vector relative to the Burgers vector of the dislocation (Tang, Lynch *et al.* 2006). However, this information is convoluted with the instrumental line broadening contribution.

Furthermore, these line broadening effects needs to be deconvoluted in order to extract the crystallite size and micro-strain components. Deconvolution is normally performed by least-squares fitting of the experimental pattern with a particular instrumental model using a procedure called Rietveld refinement. Balzar *et al.* (2004) gives a good overview of the limitations of the different deconvolution methods.

The XRD software known as TOPAS^{TM} (Ungár 2001) can be used to determine crystallite size and micro strain from the acquired XRD powder diffraction patterns. TOPAS^{TM} implements the Fundamental Parameter Approach or Fundamental Parameters Line Profile Fitting (FPPF) in conjunction with the Rietveld Refinement

method. FPPF is a tool which analyses diffraction line broadening by simulating the experimental XRD pattern. It fits an XRD diffraction pattern by convolution. Corrections such as instrument line broadening and peak shift are inherent to the refinement and the refined parameters are determined by the diffractometer itself. There is no need for a reference sample if all the parameters of the instrument are well-defined. Cheary *et al.* (2004) provides further detailed discussion on FPPF.

3.7.3 Methodology

XRD samples were prepared from the new and damaged bulk specimens by cutting squares approximately 10 mm x 10 mm in size. These specimens were then mounted and polished as discussed in Section 3.3.1. XRD diffraction patterns were collected using a cobalt radiation ($K\alpha_1$ = 1.789 Å, $K\alpha_2$ = 1.793 Å and $K\beta$ = 1.392 Å) source. This was done to limit the low signal-to-noise ratio due to florescence when iron-based materials are analysed using copper radiation. The patterns were collected from 30º to 120º 2θ in 0.02º steps using the Brag-Brentano geometry. The instrumental line broadening was determined experimentally with a calibration standard made from a Corundum (Al_2O_3). The XRD pattern from the calibration standard was fitted using Rietveld refinement in order to model the angular dependence of the instrumental line broadening using the TOPAS^{TM} software. These instrumental line broadening coefficients were then fixed during subsequent refinements of the sample parameters. The experimental XRD patterns was then scanned for the new X20 materials as well as the creep aged materials.

The peaks (110, 200 and 211) were then inspected visually for evidence of line broadening for the different samples. The experimental scan results were imported into TOPAS^{TM} and each peak modelled using a split Pseudo-Voigt function in order to extract the Full-Width at Half Maximum (FWHM) of each peak (P1 = 52.1º, P2 = 76.9º and P3 = 99.3º). The results of the extracted FWHM of each specimen was compared to illustrate the line broadening.

The results were imported into TOPAS^{TM} in order to quantitatively extract the contributions of crystal size and micro-strain, and to deconvolute the effects of the instrument. A refinement was performed using the alpha-iron crystal structure (Ferrite: Im-3m, a_0 = 2.87 Å). Refinement of the (i) sample height, (ii) lattice parameter, (iii)

background, (iv) crystallite size L and (v) strain G were allowed while all the other parameters were kept constant. The peaks were fitted using the FPPF. The background was fitted using a Chebyshev polynomial of order 3. The assumptions made during the refinement was that the line broadening due to crystallite size is Lorentzian, while the line broadening due to micro-strain is Gaussian. LVol-IB was reported as the crystallite size measurement and the ε_0 was reported as the total micro-strain in the sample. The XRD results is provided and discussed in Chapters 5 and 6, respectively.

3.8 SUMMARY OF TECHNIQUES AND ANALYSIS

Table 3.7 provides a summary of the application of the techniques discussed throughout this chapter to perform the analyses of precipitates, subgrain, dislocations and solid solution. The exact methods that implement these techniques is discussed in Chapters 4, 5 and 6.

Table 3.7: *Techniques used to perform precipitates, subgrain and dislocation analysis.*

Technique	***Precipitate Analysis***	***Subgrain Analysis***	***Dislocation Analysis***
Light Microscopy		X	
SEM	X		
EBSD		X	
TKD		X	
TEM/STEM		X	X
EFTEM	X		
EDS	X		
XRD		X	X

CHAPTER 4

EVALUATION OF PRECIPITATES

4.1 INTRODUCTION

This chapter and the subsequent two chapters will show the application of various microscopy techniques to quantitatively determine the microstructural parameters (precipitates, grain size and dislocations) that play a role in the creep strength of 12Cr steel. Consequently, these chapters are of great importance since the main objective of this study was to develop and apply techniques that can be used to quantitatively characterise the microstructure of a 12% Cr steel.

This chapter focuses on the evaluation of the precipitates. Firstly, some background literature relating to previous studies of precipitates in ferritic steels will be discussed. This is then followed by the experimental procedure used to determine the various precipitate parameters. Lastly, the results from this part of the study is given and discussed.

4.2 BACKGROUND

CSEF steels, such as the X20 steel analysed in this study, are strengthened by $M_{23}C_6$ (M = Cr, Fe, Mo) carbide and MX (M = V, X = C, N) carbonitride precipitates in the martensite matrix (Chapter 2). The parameters of these precipitates (e.g. size, shape and composition) play an important role in the creep strengthening of the material. The material's resistance to creep damage due to PH can be quantitatively described by the Orowan stress.

In order to calculate the Orowan stress σ_{Or} of a material due to the precipitates, accurate measurements of the spatial distribution or mean interparticle distance λ, mean particle size d_m and number density N_V are required. The Orowan stress is calculated from these precipitate parameters using equations 2.3 and 2.4.

The most widely used method to determine the precipitate parameters is to obtain optical microscope and SEM micrographs of the polished or etched surface of the

specimen (Dimmler, Weinert *et al.* 2003). The precipitate size can then be measured from these micrographs and hence the distribution and surface density determined. However, even though this is a much simpler and faster technique, it is not possible to determine the chemical composition of the precipitates. It is normally assumed that the $M_{23}C_6$ precipitates are much larger than the MX precipitates in order to differentiate between them, which still does not lead to confident results. Furthermore, stereological corrections need to be applied to the measurements in order to account for the sectioning of the precipitates during polishing (Fruhstorfer, Mohles *et al.* 2002; Gegner 2006).

The precipitate parameters are often measured from images taken from thin-foils using the TEM (Holzer 2010; Sonderegger 2012). The images can be created using BF-TEM or STEM, or as elemental maps obtained by analytical techniques such EDS or EFTEM. Aghajani (2009) acquired HAADF-STEM images of thin foils of X20 steel and then performed EDS chemical analysis to identify the type of precipitates before measuring them. In order to obtain statistically reliable results, a large number of precipitates must be measured making it is a time consuming procedure. Similarly, Panait, Bendick *et al.* (2010) performed EDS-TEM on extraction replicas of a P91 steel in order to calculate the diameters of the different precipitates.

Since the precipitates are sectioned during thin-foil sample preparation, stereological corrections need to be applied to obtain the true precipitate size distribution. Correction factors for arbitrary precipitate distributions in TEM thin-foils was developed by Sonderegger (2006) in order to obtain the true precipitate size distribution. The thin-foil precipitate size correction method assumes that the precipitates are spherical and homogeneously distributed throughout the specimen.

One of the first EFTEM studies on the 9-12% Cr steels is that by Hättestrand and Andrén (2001). They measured the precipitate sizes in TEM thin-foils of a 9% Cr steel from EFTEM elemental maps. Stiller, Andrén *et al.* (2008) performed three-dimensional atom probe analyses and EFTEM as complimentary techniques on TEM thin foils of 9-12% Cr steels in order to determine the chemistry, size, volume fraction and number density of the precipitates. Other TEM and EFTEM studies on 9-12% Cr steels include that by Sonderegger, Kothleitner *et al.* (2006) and Hofer, Cerjak *et al.* (2001). EFTEM allows the accurate measurement of particle sizes down to a few nm

and has the ability to discriminate between individual precipitate types by elemental analysis (Hald 2008).

Skobir, Gobec *et al.* (2010) did studies on the orientation and volume fraction of carbides during coarsening in X20 steel, using EBSD. Numerous XRD studies have also been performed on the carbide phase precipitates in order to characterise their evolution during creep, e.g. Baltusnikas, Levinskas *et al.* (2008) studied the intensity of the diffraction peaks for the carbide phases, as well as the changes of the lattice parameters of the carbide phases during creep exposure. Mitchell and Sulaiman (2006) performed quantitative microanalysis on P91 steel using EDS in order to determine the metallic elements in the secondary-phase particles. Mitchell and Ball (2001) combined XRD and EDS to evaluate the carbide phases in a service-exposed 2.25Cr-1Mo power plant head by identifying the carbide type and frequency of occurrence. They made the conclusion that microscopy-based identification of carbides on the basis of composition alone is a valid approach.

Apart from identifying the different types of precipitates, EDS can be used to monitor the compositional changes of these precipitates in the steel during creep exposure. Vodarek and Strang (2001) performed EDS on a series of martensitic 12CrMoVNb steels in the as-received condition and after long term exposure at high temperatures, in order to evaluate the compositional changes of the minor phases. A similar approach on extraction replica specimens is followed in this study.

4.3 METHODOLOGY

The main aim of this part of the study was to use measurements from EFTEM elemental maps of TEM thin-foils and extraction replicas in order to quantitatively determine the precipitate parameters for CSEF steels. The intention was to use the two sampling techniques complementary to one another in order to minimise the limitations of each. The previous characterisation studies mainly focused on bulk material of 9-12% Cr ferritic steel to show the microstructural changes that occur during creep aging. In this study the use of EFTEM on thin-foils to characterise the precipitates in the different weld regions is illustrated. Also, the use of EDS to measure the composition changes in the precipitates is demonstrated in this study.

4.3.1 Sampling

The matrix of the specimens used for the evaluation of precipitates in the new and damaged bulk X20 material and steel weldments are summarised in Table 4.1.

Table 4.1: *Specimens used for evaluation of precipitates using EFTEM and EDS.*

Specimen		EFTEM	EDS
Extraction Replicas	Bulk	X	X
FIB-SEM specimens	Bulk	X	
	FGHAZ	X	
	CGHAZ	X	
	ICHAZ	X	
	Over-Tempered	X	

Quantitative analysis was performed on the EFTEM elemental maps in order to determine the precipitate parameters. EDS analysis of the precipitates was only performed on the extraction replica specimens prepared from the bulk X20 material since it only contains the precipitates and there is no iron matrix or sectioning of the precipitates that can influence the EDS results.

4.3.2 EFTEM Analysis

The EFTEM investigations was performed on the specimens as summarised in Table 4.1, using a GATAN quantum GIF fitted to the TEM. EFTEM elemental maps were acquired using a 200 µm condenser aperture to provide the highest signal. Also, an objective aperture was inserted in order to restrict the collection angle to 10 mRad. The $M_{23}C_6$ precipitates and MX precipitates in the Fe matrix were imaged by acquiring Cr, V and Fe elemental maps, respectively, using the three-window method. GATAN's Digital Micrograph (DM) software was used for the acquisition and display of the 2D EFTEM maps. A maximum of 2 areas could be imaged for the FIB-SEM specimens at 400x magnification, while the extraction replicas had a much larger sampling area

and the imaging of 4 different areas at 400x magnification was sufficient. For each area for the FIB-SEM specimen, the corresponding thickness (t/λ') map was generated by obtaining zero loss and unfiltered BF images. The mean free path λ' of 200 keV electrons in 12% Cr steels was taken to be 100 nm and was based on the calculation provided by Williams and Carter (2009). It should be noted that the error in this conversion is estimated to be of the order of 20%. Each map was acquired with a total 2048 x 2048 pixels and then a binning of 4 (for the elemental maps) and 1 (for the thickness maps) was applied. The energy windows and other experimental parameters used to acquire the EFTEM maps for the three-window method and thickness is summarised in Table 4.2.

***Table 4.2**: Window energies and acquisition parameters for various EFTEM maps*

Element	***V***	***Cr***	***Fe***	***Thickness***
Z	23	24	26	
Edge type	L	L	L	
Edge Energy (eV)	513	575	708	
Pre-edge 1 (eV)	465	527	644	
Pre-edge 2 (eV)	495	557	684	
Post-edge Energy (eV)	528	590	728	
Filter Slit Width (eV)	30	30	40	15
Exposure Time (s)	Auto (± 2-4)	Auto (± 3-5)	Auto (± 3-5)	Auto (± 0.1)
Pixel Binning	4	4	4	1

4.3.3 Determination of Precipitate Parameters

From the EFTEM Cr elemental maps obtained from the extraction replica specimens it was observed that there is overlap between of the Cr-enriched $M_{23}C_6$ precipitates. Subsequently, the $M_{23}C_6$ precipitate size was measured manually using the image processing software ImageJ (Abramoff, Magalhaes *et al.* 2004), assuming that the precipitates are elliptical particles. No overlap was observed for the V-enriched MX precipitates and hence thresholding in ImageJ was used to measure their size. Since the MX precipitates are very small, noise may be erroneously detected as a MX precipitate during thresholding. Therefore, for consistency all measured MX precipitate areas smaller than a cut-off value of 2.5 x 2.5 pixels (radius = 11,45 nm) was disregarded before performing further analyses. The measured mean diameter d_{m} of each precipitate was determined as the Equivalent Circle Diameter (ECD) obtained from the measured area. Table 4.3 contains the relevant formulas used to calculate the precipitate parameters.

For the precipitates in the TEM thin-foils, sectioning occurs. Thus the measured size is smaller than the original precipitate. To obtain the actual diameter d_i of every $M_{23}C_6$ precipitate for the TEM thin-foil specimens, the measured value was corrected with equation 4.1. No diameter correction was required for the MX precipitates in the thin-foil specimen since it is assumed they are too small to be sectioned. The extent of the sectioning will be determined by the thickness of the thin-foil. TEM thin-foils often have variations in thickness leading to different correction factors to be applied to the precipitate size. The foil thickness at each precipitate location was measured from the thickness map and used in the sectioning correction factor. This procedure was automated in ImageJ.

In this study it was assumed that the phase fraction f_v remains constant for a sample, irrespective of the sample preparation method. The TEM thin-foils was used to determine the phase fraction f_v of the precipitates using equation 4.2. This value was then used to determine the sample volume for the extraction replica. The 2D surface-to-surface interparticle spacing λ, which is the mean particle distance in the slip plane of the dislocation, is the important parameter for PH contribution and not the 3D particle distance (Holzer 2010). Equation 2.3 and Table 2.5 was used to calculate the Orowan stress σ_{Or}.

Table 4.3: *Formulas used to calculate precipitate parameters.*

Corrected diameter of i^{th} precipitate ***(Sonderegger 2006)***	$$d_i = \frac{2}{\pi}\left(d_{m,i} - t_i\right) + \sqrt{\frac{2}{\pi}\left(d_{m,i} - t_i\right)^2 + \frac{4 d_{m,i} t_i}{\pi}}$$	(4.1)	Where: $\boldsymbol{d_{m,i}}$ ≡ measured diameter of precipitate $\boldsymbol{i}$ $\boldsymbol{t_i}$ ≡ sample thickness at the precipitate i position
Phase fraction f_V **(*Sonderegger 2006)***	$$f_V = \frac{V_V}{V_{Sample}} = \frac{1}{A_{Sample}} \sum_i A_i \left(\frac{2 d_{m,i} / t_i}{2 d_{m,i} / t_i + 3} \right)$$	(4.2)	Where: V_V ≡ Total volume of precipitates A_{Sample}/V_{Sample} ≡ examined sample area/volume A_i ≡ projected area of precipitate i
Number density N_V **(*Sonderegger 2006)***	$$N_V = \frac{N_A}{V_{Sample}} = \frac{1}{A_{Sample}} \sum_{i=1 \ldots N_A} \frac{1}{t_i + d_{m,i}}$$	(4.3)	Where: N_A ≡ measured number of precipitates per sample area/volume
Weighted mean precipitate diameter $\bar{d}$ **(*Sonderegger 2006)***	$$\bar{d} = \frac{\sum_i d_{m,i}[t_i/(t_i + d_{m,i})}{\sum_i [t_i/(t_i + d_{m,i})]}$$	(4.4)	
Mean 2D surface- to-surface particle distance λ ***(Holzer 2010)***	$$\lambda = \sqrt{\frac{\ln 3}{2\pi N_V \bar{r}} + 4\bar{r}^2} - 1.63\bar{r}$$	(2.4)	Where: $\bar{r} = \frac{\bar{d}}{2}$ ≡ mean particle radius of precipitates

4.3.4 EDS Analysis

The chemical composition of the precipitates in the extraction replica specimens of the new and damaged bulk material was analysed using EDS (Table 4.1). EDS analysis was performed using a JEOL JEM 2100 LaB_6 TEM fitted with an Oxford X-Max 80 EDS SDD detector in STEM mode. The spectra was processed using the Oxford AZtec analysis software. The k-ratio method (Williams and Carter 2009) implemented in the software was used to perform the quantitative analysis. Accurate elemental quantification from EDS in TEM is quite a complex task and previous studies applied various standards to calibrate the measurements for a particular elemental system (Mitchell and Sulaiman 2006). This calibration procedure was not applied to the system and the manufacturer's calibrations was used in this study. Spot analysis of the precipitates in 3 different areas of the extraction replica specimens was performed.

4.3.5 Chemical Analysis

Quantitative analysis was performed on each of the spectra acquired from the various precipitates. These spectra were analysed in order to determine the type of precipitate ($(Cr:Fe:Mo)_{23}C_6$ or $(Fe, Cr)_2Mo$ Laves-phase) and hence the chemical composition as the ratio of elements in each precipitate. The following criteria was followed for the identification: $M_{23}C_6$ carbides are enriched in Cr (±50 at%) and Fe (± 20 at%), but have a small amount of Mo (±4 at%); and Laves-phases are enriched in Fe, Cr and Mo and contain Si also in significant amounts. This was based on previous literature discussed in Chapter 2. A total of 28 and 24 $M_{23}C_6$ precipitates in the new and damaged bulk X20 material, respectively, and a total of 5 Laves-phase precipitates in the damaged bulk X20 material were investigated.

4.4 RESULTS AND DISCUSSION

4.4.1 Qualitative Analysis of Precipitates

Figure 4.1 shows the RGB composite images of the Cr and V EFTEM elemental maps acquired from a single area of the new bulk X20 extraction replica and FIB-SEM specimen. The precipitates in the thin foil are embedded in the iron matrix. Angled precipitate boundaries will show an EELS signal from a combination of the precipitate and the iron matrix resulting in less distinct boundaries as compared to the precipitates in the extraction replica. Also, it can be seen that there is no sectioning of the $M_{23}C_6$ precipitates in the extraction replica and hence the true precipitate shape can be observed. The available area for analysis is much larger for the extraction replica (several 50 x 50 µm grid squares) compared to that of the FIB-SEM (±5 x 5 µm) specimens, the inhomogeneous distribution of the precipitates could be seen on the extraction replica. The apparent increase in phase fraction in the extraction replica is due to the significantly larger extraction depth (>300 nm) compared to that of the thin-foil (< 100 nm) (Baker 2001).

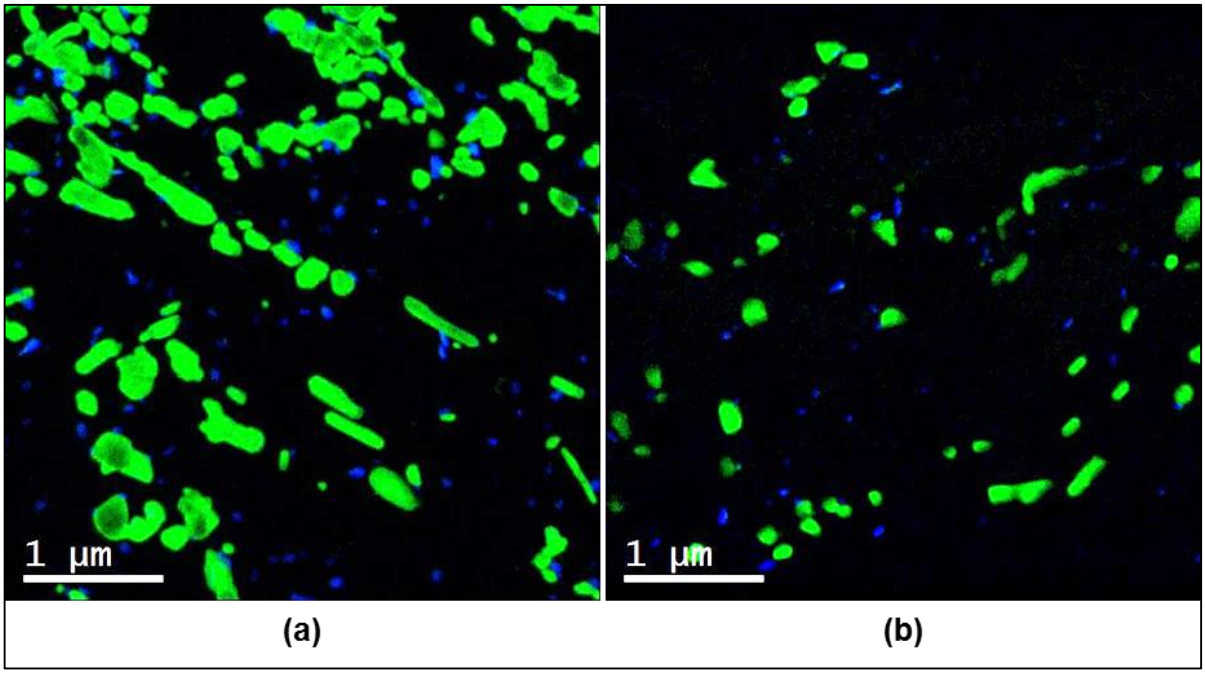

Figure 4.1: *EFTEM colour map of the $M_{23}C_6$ (green) and MX (blue) precipitates in the (a) extraction replica and (b) FIB-SEM specimen prepared from new bulk X20 material.*

One of the objectives of this study was to illustrate the difference in microstructures between new and creep damaged X20 weldments. The differences in the precipitate size distributions can be seen from the RGB composite EFTEM images of the FIB-SEM specimens of each region (Figures 4.2 and 4.3). Also observed is the size and distribution of the Cr-enriched $M_{23}C_6$ (green) and V-enriched MX (blue) precipitates.

No obvious difference in the precipitate size and distribution was noted when the bulk and over-tempered regions were compared. This is consistent with previous literature. The $M_{23}C_6$ precipitates in the damaged bulk and over-tempered regions are much larger than those in the new bulk and over-tempered regions. This agrees with the known mechanism of coarsening of $M_{23}C_6$ precipitates during creep. There is also much less $M_{23}C_6$ precipitates in the damaged material. As expected, no obvious coarsening of the MX precipitates is observed during creep.

The ICHAZ and FGHAZ of each weldment have similar sized and distributed $M_{23}C_6$ precipitates and will be discussed together. The $M_{23}C_6$ precipitates vary from small to large in size for the new ICHAZ/FGHAZ. This agrees with previous literature that partial dissolution of $M_{23}C_6$ precipitates occur during welding (Chapter 2). Upon cooling these precipitates grow while new ones also nucleate leading to a bi-modal size distribution.

From the literature is follows that the main failure mechanism of creep exposed 9-12% Cr ferritic weldments is Type IV cracking which occurs in the ICHAZ/FGHAZ (Chapter 2). The larger precipitates in the ICHAZ/FGHAZ are the largest of all the regions within a weldment and, in addition, the precipitates in the damaged ICHAZ /FGHAZ are much larger than those in the new ICHAZ/FGHAZ due to the coarsened precipitates in the damaged material before welding. These large precipitates act as nucleation sites for voids (Chapter 2). Hence, since the largest precipitates are observed in the damaged ICHAZ/FGHAZ, it could imply that this region would be most susceptible to void formation and explain Type IV cracking phenomena. Subsequently, it is seen that PH is one of the key factors that could define the weldability limits of creep exposed steels.

The $M_{23}C_6$ precipitates in the new and damaged CGHAZ show a distinct distribution in a specific direction, which is not observed for the other regions. Since it is known that these precipitates lie along the GBs and SGBs, these precipitates outline the martensite lath boundaries. All the $M_{23}C_6$ precipitates in the CGHAZ of each weldment

appear to have the same size. This agrees with the literature (Chapter 2) that indicates that the temperature experienced in this region during welding is high enough to dissolve all earlier precipitates and hence new precipitates nucleate upon cooling.

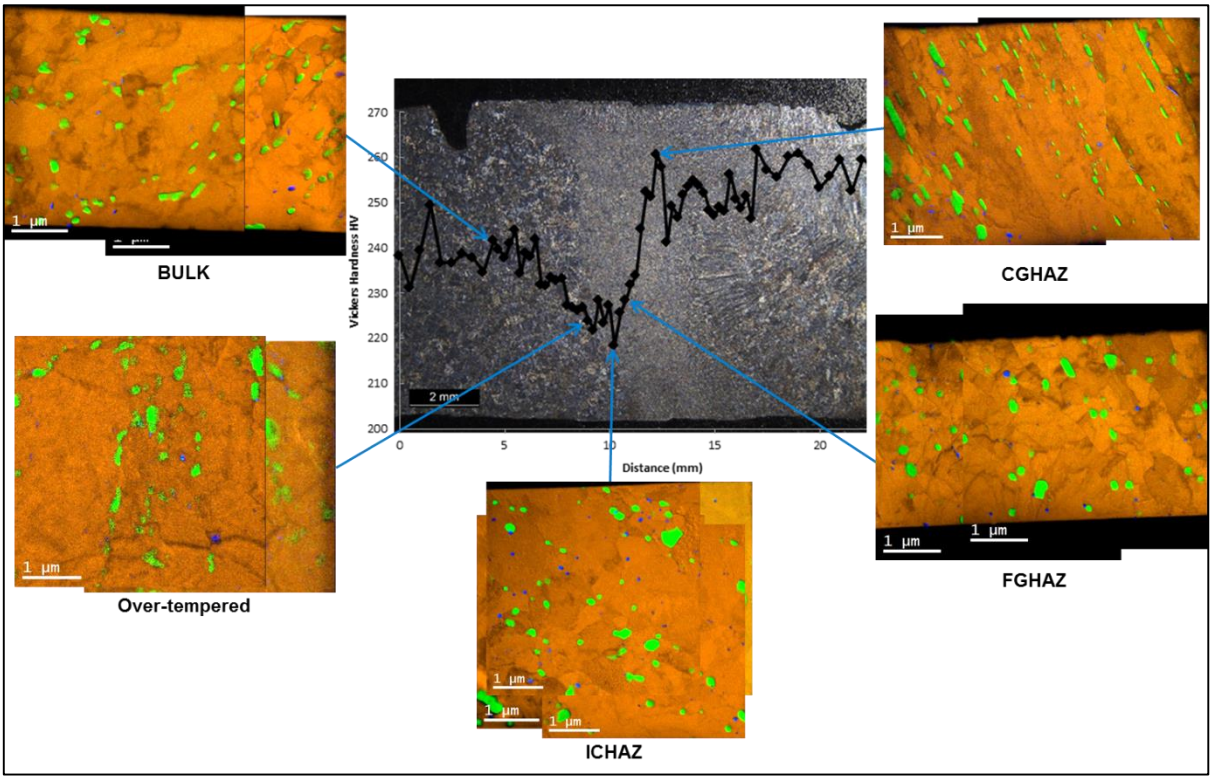

Figure 4.2: *RGB composite images of $M_{23}C_6$ (green) and MX (blue) precipitates in Fe (orange) matrix acquired from FIB-SEM specimens prepared from the new weldment.*

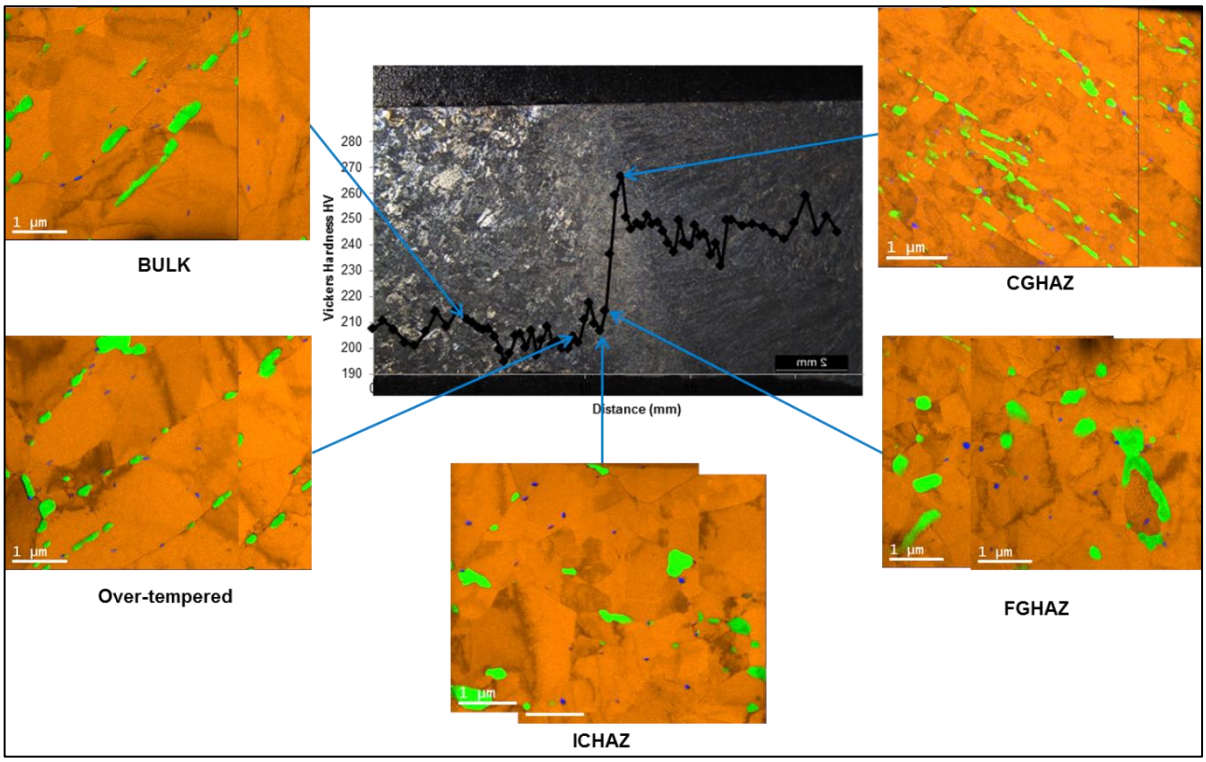

Figure 4.3: *RGB composite images of $M_{23}C_6$ (green) and MX (blue) precipitates in Fe (orange) matrix acquired from FIB-SEM specimens prepared from the damaged weldment.*

Low magnification BF images of the extraction replica revealed that the microstructure is preserved in the x and y direction since the orientation and distribution of the precipitates outline the prior GB and SGB along which they had lain. To illustrate this, BF-TEM images of two areas on the new bulk replica specimen are provided in Figure 4.4. A proposed single subgrain is drawn as a guide to the eye.

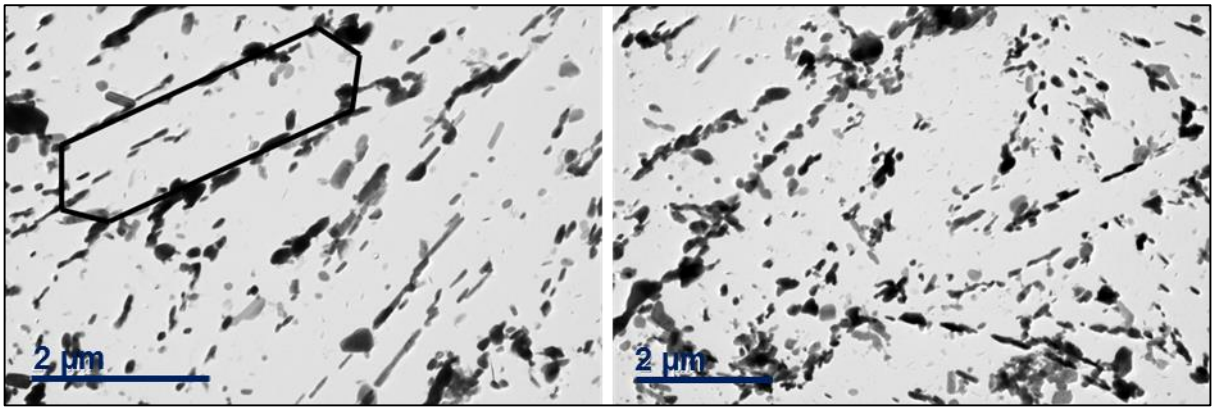

Figure 4.4: *Low magnification BF-TEM images of new bulk extraction replica. The outline of a possible prior subgrain is given as a guide to the eye.*

4.4.2 Quantitative Analysis of Precipitates

The first step in the analysis of the thin foils was to determine the foil thickness. Figure 4.5(a) shows the thickness map determined from the elastic/inelastic log ratio to determine the mean free path of the electrons. The thickness measurements on the thin foils varied from 80 nm to 120 nm with localised contrast variations due to electron diffraction. A 2D parametric surface fit was performed on the thickness map to smooth out the contrast variations due to dynamical electron diffraction as illustrated in Figure 4.5(b). The $M_{23}C_6$ precipitates were measured by manually drawing ellipses to outline the precipitate boundaries for both the thin-foils and the extraction replicas.

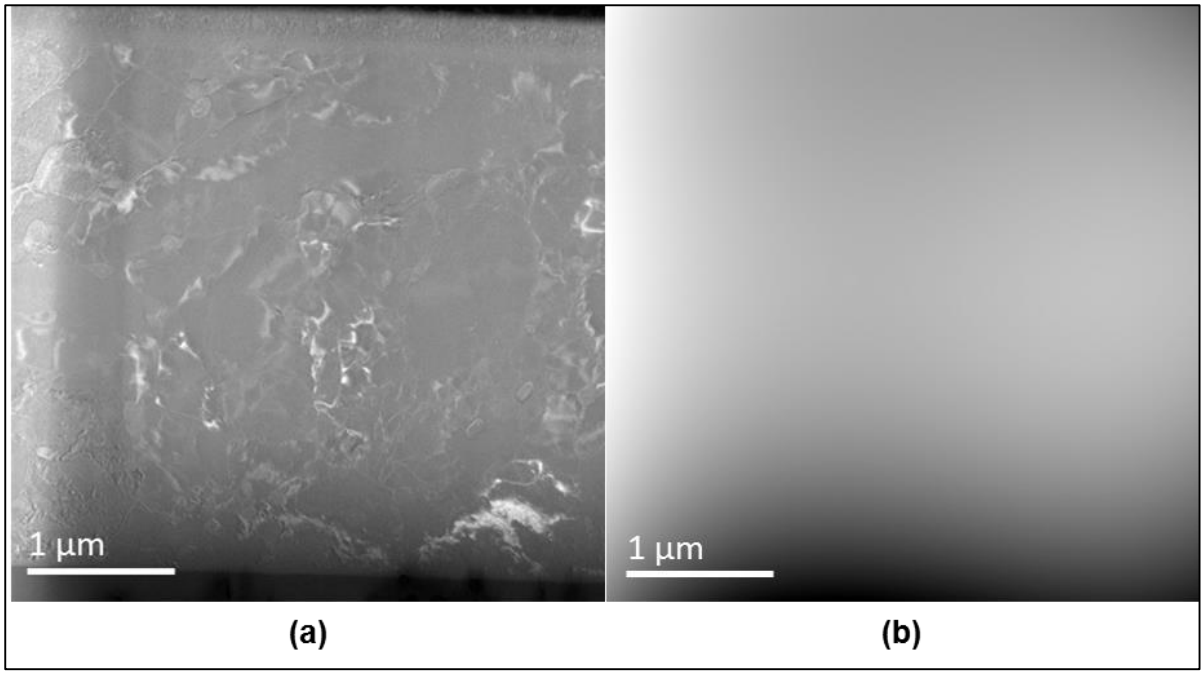

Figure 4.5: *(a) A thickness map of the new bulk FIB-SEM specimen obtained from the elastic/inelastic log ratio to determine the mean free path of the electrons. (b) Thickness map in (a) after 2D surface fit has been performed to reduce diffraction contrast.*

The extraction replicas contained numerous clusters of overlapping precipitates. Figure 4.6 illustrates the measurement of the $M_{23}C_6$ precipitates on the extraction replica by manually drawing ellipses to separate out the clusters. Although this method is very time-consuming and contains an element of subjectivity, it showed better separation of the precipitates compared to contrast thresholding and applying a separation algorithm like watershedding (Roerdink and Meijster 2001). Optimisation of the automatic segmentation algorithm will form part of a future study. It is seen from Figure 4.6(a) that the elliptical shape assumption for the $M_{23}C_6$ precipitates is valid due to the good fit of the drawn outline with each precipitate. The MX precipitates in the extraction replica was well separated and automatic thresholding and segmentation was performed to extract the precipitate sizes (Figure 4.6(b)) for both the thin-foils and the extraction replicas.

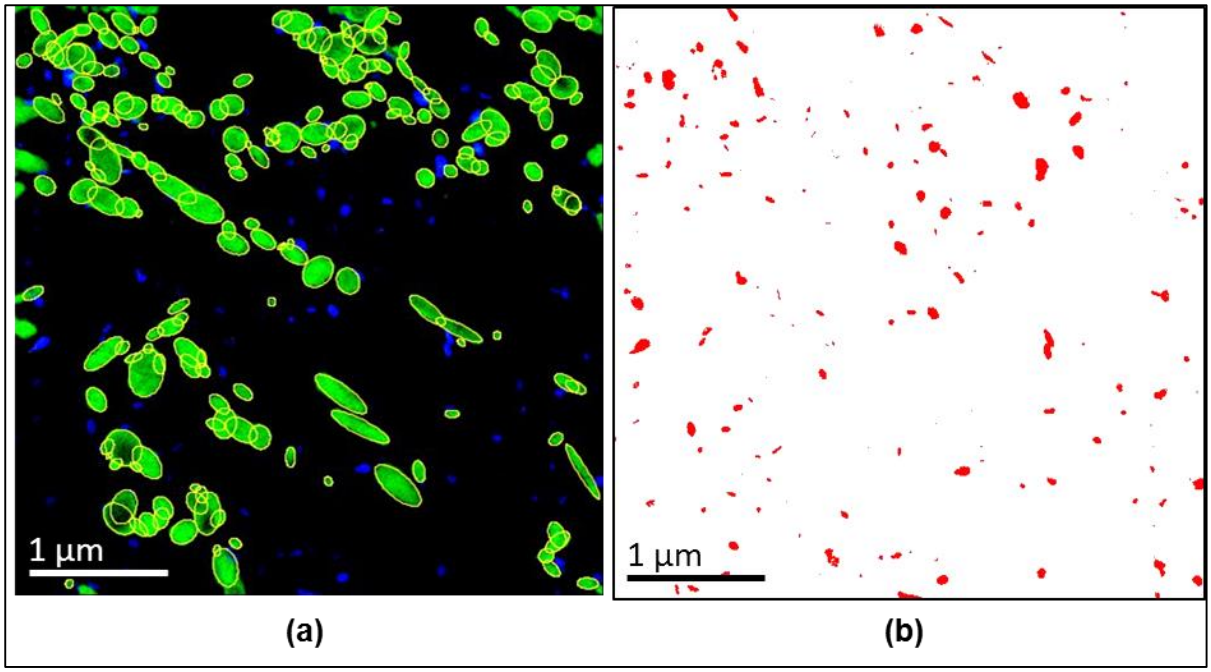

Figure 4.6: *Measurement of precipitate size from EFTEM elemental map of (a) $M_{23}C_6$ and (b) MX precipitates for a new bulk extraction replica, using ImageJ.*

The calculated parameters for the $M_{23}C_6$ and V precipitates in the extraction replica and FIB-SEM specimens prepared from the bulk X20 material are given in Tables 4.4 and 4.5 calculated using the equations in Table 4.3 and equation 2.3. Statistical analysis has been performed on each parameter and the 95% confidence level is reported as the error. Since the Orowan stress σ_{Or} is determined from the interparticle spacing λ, its error is proportional to the error in λ. Due to the larger sampling volume of the bulk replication technique, much more precipitates could be analysed, which should yield a more representative measurement of the precipitates compared with the thin-foils prepared by the FIB-SEM.

The precipitate size distribution is reduced to a single mean value in order to be used in the equations for the Orowan stress calculation. The measured mean $M_{23}C_6$ precipitate diameter of the new (121 ± 3 nm) and the damaged (125 ± 9 nm) bulk X20 material are very similar for the extraction replica specimens. The coarsening of the precipitates due to creep aging is more evident in the FIB-SEM specimens, despite the low number of precipitates measured in the damaged material. Large variations in precipitate size coupled with the small sampling volume of the FIB-SEM specimen brings the quantitative analysis into question. This would explain the large discrepancy between the precipitate size measurement on the FIB-SEM (171 ± 32 nm) and

extraction replica (125 ± 9 nm) specimens for the damaged material. For the new material the precipitates are distributed more homogeneously and the size distribution has a smaller standard deviation. Thus, the precipitate size measurements taken from the FIB-SEM and extraction replica specimens is in good agreement.

The phase fraction f_v was calculated from the FIB-SEM samples by applying the correction factor to the measured diameter (equation 4.1) and using equation 4.2. This calculated phase fraction value was then used to determine the sampled volume in the extraction replica. It was found that the extraction depth (620nm) is much larger than the thin-foil thickness (87 ± 17 nm). The number density N_v of the precipitates in the FIB-SEM specimen was determined using equation 4.3 by applying the correction factor, while the number density N_v for the extraction replica was determined by the number of precipitates in the sampled volume. There was good correspondence in the number densities obtained by using the two sampling methods for the new material, which indicates an adequate extraction efficiency for the Cr-rich precipitates. The inhomogeneous distribution and low sampling in the FIB-SEM specimen brings the quantitative measurements of the damaged material into question, and a lower number density was found in the FIB-SEM compared to the extraction replica. The decrease in number density between the new (23.1 #/μm^3) and damaged (7.7 #/μm^3) material was observed. This is consistent with known precipitate coarsening mechanisms (Chapter 2).

Consequently, the calculated interparticle spacing λ and Orowan stress σ_{Or} is in good agreement for the two sampling methods. The new bulk X20 material had a higher PH stress contribution compared to the damaged bulk X20 material. This again corresponds with known literature that there is a decrease in creep strength during creep aging due to precipitate coarsening.

Table 4.4: *Precipitate parameters calculated for $M_{23}C_6$ (Cr) precipitates in bulk X20 material.*

	New Bulk		Damaged Bulk	
	FIB-SEM	***Replica***	***FIB-SEM***	***Replica***
***Measured d (nm)**	127 ± 9	121 ± 3	171 ± 32	125 ± 9
***Corrected d (nm)**	149 ± 11		211 ± 43	
#đ (nm)	140		174	
Thickness (nm)	87 ± 17	620	81 ± 16	495
f_V**(%)**	3.42	3.42	3.42	3.23
N_v (# / µm³)	+23.1	24.3	+7.7	12.1
λ (nm)	243	267	398	395
σ_{Or} **(MPa)**	160	146	98	98
# Precipitates	152	541	62	216

**Mean values*

#*Calculated using equation 4.4*

+*Calculated using equation 4.3*

Table 4.5 shows the measured sizes and calculations for the V-enriched MX precipitates. These precipitates are much smaller than the $M_{23}C_6$ precipitates. They were measured by applying thresholding on the EFTEM image. Since these precipitates were imbedded into the iron matrix for the thin-foils, the sample thickness played a role in the vanadium signal-to-noise ratio. The calculated mean diameter d_m is determined by the threshold parameters and the minimum precipitate cut-off value. In the extraction replica the MX precipitates are not imbedded into the iron matrix resulting in improved signal-to-noise for the vanadium signal. Despite the limitation mentioned above, the size measurement of the precipitates was consistent for the two sampling methods. The measured sizes corresponded for the new and damaged material, implying that no significant coarsening occurred during creep aging. The number density of the MX precipitates had a large deviation between the FIB-SEM (56.3 #/µm³) and extraction replica (10.5 #/µm³) specimens, which illustrates the poor extraction efficiency of the MX precipitates by the bulk replication technique. The calculated phase fraction f_v is lower for the extraction replica. The number density of precipitates in the damaged bulk X20 material (20.6 #/µm³) is lower than the new bulk

X20 material (56.3 #/μm^3), indicating dissolution of the MX precipitates during creep aging leading to a further loss of creep strength. This tendency was observed in both sampling techniques.

Table 4.5: *Precipitate parameters calculated for MX (V) precipitates in bulk X20 material.*

	New Bulk		**Damaged Bulk**	
	FIB-SEM	***Replica***	***FIB-SEM***	***Replica***
***Measured d (nm)**	46 ± 5	51 ± 4	63 ± 10	56 ± 15
f_V**(%)**	0.47	0.12	0.40	0.10
N_v (# / μm^3)	56.3	10.5	20.6	3.5
λ (nm)	333	768	472	1291
σ_{Or} **(MPa)**	117	51	83	30
# Precipitates	156	234	61	63

**Mean value*

Tables 4.6 and 4.7 summarises the precipitate parameters determined for the different weld regions. Note that in this case all the specimens were prepared as FIB-SEM specimens. These regions are too small to perform the Bulk Replication Technique. The quantitative analysis confirms the qualitative observations summarised in Figures 4.2 and 4.3. In each corresponding weldment region the measured $M_{23}C_6$ precipitate size is larger in the damaged material compared to the new material, except for the CGHAZ, which had precipitates of similar size. The calculated phase fraction f_v showed large variations between the different regions, especially for the damaged material. This is probably due to the small sampling volume, inhomogeneous spatial distribution of the precipitates and the large standard deviation in the precipitate size. The number density N_v of the $M_{23}C_6$ precipitates are higher in all the weldment regions of the new material, except for the CGHAZ, which had a similar value for the new and damaged material.

The ICHAZ/FGHAZ had the lowest calculated Orowan stress σ_{Or} in the weldment for both the new (138 MPa) and damaged (106 MPa) materials. This would indicate that the creep resistance is lower in this region, which could explain the lowered creep resistance resulting in Type IV cracking. The lower calculated Orowan stress σ_{Or} for

the damaged material in the ICHAZ/FGHAZ region is in agreement with experimental work of a parallel study and previous literature (Shinozaki, Li *et al.* 2002). Cross-weld creep testing specimens prepared from new material welded onto damaged material repeatedly failed in the ICHAZ/FGHAZ zone of the damaged material. The measured precipitate parameters for the over-tempered region was very similar to that of the ICHAZ/FGHAZ region. It could either be due to removal of the specimens too close to the HAZ or poor sampling statistics due to inhomogeneous distribution of the precipitates.

The measured MX precipitate parameters were similar for the different regions. As discussed previously, this measurement is sensitive to the image processing parameters and subsequent post-processing. The thicker specimen (156 nm) taken from the over-tempered region in the new material had particularly low signal-to-noise and it affected the measurements. The number density of the MX precipitates are lower for the damaged material due to dissolution during creep aging. This result should, however, be interpreted with care due to the reasons discussed above.

Table 4.6: *Precipitate parameters calculated for $M_{23}C_6$ (Cr) precipitates in different zones of X20 weldments.*

	Over-Tempered		**ICHAZ**		**FGHAZ**		**CGHAZ**	
	New	***Damaged***	***New***	***Damaged***	***New***	***Damaged***	***New***	***Damaged***
***Measured d (nm)**	177 ± 12	141 ± 22	125 ± 13	154 ± 27	120 ± 14	191 ± 35	107 ± 9	108 ± 7
***Corrected d (nm)**	203 ± 15	211 ± 43	152 ± 17	188 ± 37	144 ± 18	240 ± 48	125 ± 12	125 ± 9
[#]**đ (nm)**	194	144	135	159	128	188	114	116
Thickness (nm)	156 ± 31	94 ± 19	69 ± 14	80 ± 16	78 ± 16	79 ± 16	85 ± 17	89 ± 18
f_V**(%)**	4.34	2.22	3.03	2.88	2.82	4.68	3.19	3.51
[+]N_V **(#/µm³)**	11.1	9.6	19.9	9.1	20.6	7.9	32.2	36.5
λ (nm)	289	406	275	387	282	367	236	215
σ_{Or} **(MPa)**	135	96	142	101	138	106	165	181
# Precipitates	130	75	257	70	105	67	205	247

**Mean values*

[#]*Calculated using equation 4.4*

[+]*Calculated using equation 4.3*

Table 4.7: *Precipitate parameters calculated for MX (V) precipitates in different zones of X20 weldments.*

	Over-Tempered		**ICHAZ**		**FGHAZ**		**CGHAZ**	
	New	***Damaged***	***New***	***Damaged***	***New***	***Damaged***	***New***	***Damaged***
***Measured d (nm)**	41 ± 9	62 ± 10	55 ± 5	65 ± 11	52± 5	72 ± 12	47 ± 7	49 ± 5
f_V**(%)**	0.14	0.41	0.66	0.66	0.65	0.66	0.63	0.40
N_V (#/μm^3)	17.5	20.2	51.2	25.4	29.6	21.5	52.5	39.1
λ (nm)	666	482	312	412	437	422	341	390
σ_{Or} **(MPa)**	59	81	125	95	89	92	114	100
# Precipitates	98	68	252	73	129	61	160	125

**Mean value*

Normalised distribution curves of the Cr-enriched $M_{23}C_6$ and V-enriched MX precipitate diameters measured from the new bulk extraction replica and FIB-SEM specimen are plotted in Figure 4.7. The markers correspond to the binned size frequency and a moving average trend line with a period of 2 was plotted for better visualisation of the size distributions. The calculations reduced the precipitate size distribution to a single value. As expected, the correction factor applied to the FIB-SEM $M_{23}C_6$ precipitate measurements resulted in a shift to increased sizes. The corrected precipitate size measurements and the precipitate size distribution of the extraction replica were expected to agree. In this case, however, the size measurements from the extraction replica is smaller. This could be due to variations in the bulk material from which the specimens were taken. The FIB-SEM specimen was taken from the weldment that received a PWHT, while the extraction replica was taken from a bulk X20 sample. The V-enriched MX precipitate size distributions coincided.

Figure 4.8 shows the measured and corrected $M_{23}C_6$ precipitate size distribution of the FGHAZ region prepared from the new X20 weldment using FIB-SEM. As expected for the FGHAZ, the distribution is bi-modal indicating the presence of large and small precipitates due to the coarsening of the undissolved precipitates and nucleation of new ones, respectively, upon cooling of the weldment (Chapter 2).

Figure 4.9 shows the $M_{23}C_6$ precipitate size measurements for the new and damaged bulk X20 materials from the extraction replica and FIB-SEM specimens. It is expected that the precipitates will coarsen during creep exposure. The mean $M_{23}C_6$ precipitate size measurements were similar for the two materials. The size distribution of these precipitates are different for the two materials. The distribution of the $M_{23}C_6$ precipitates in the new material is sharp, while the precipitates in the damaged material had a large number of smaller precipitates combined with precipitates of larger size ($d > 250$ nm), resulting in the wider size distribution. This could be due to an inhomogeneous distribution of precipitates in the material. Precipitates formed on prior Austenite GBs was subject to increased coarsening compared to the precipitates formed on the SGBs. In addition, the formation of Cr-containing Laves phase could complicate the measurements. In this study the assumption was made that all the Cr-

containing precipitates are $M_{23}C_6$, which could well not be the case for the damaged material.

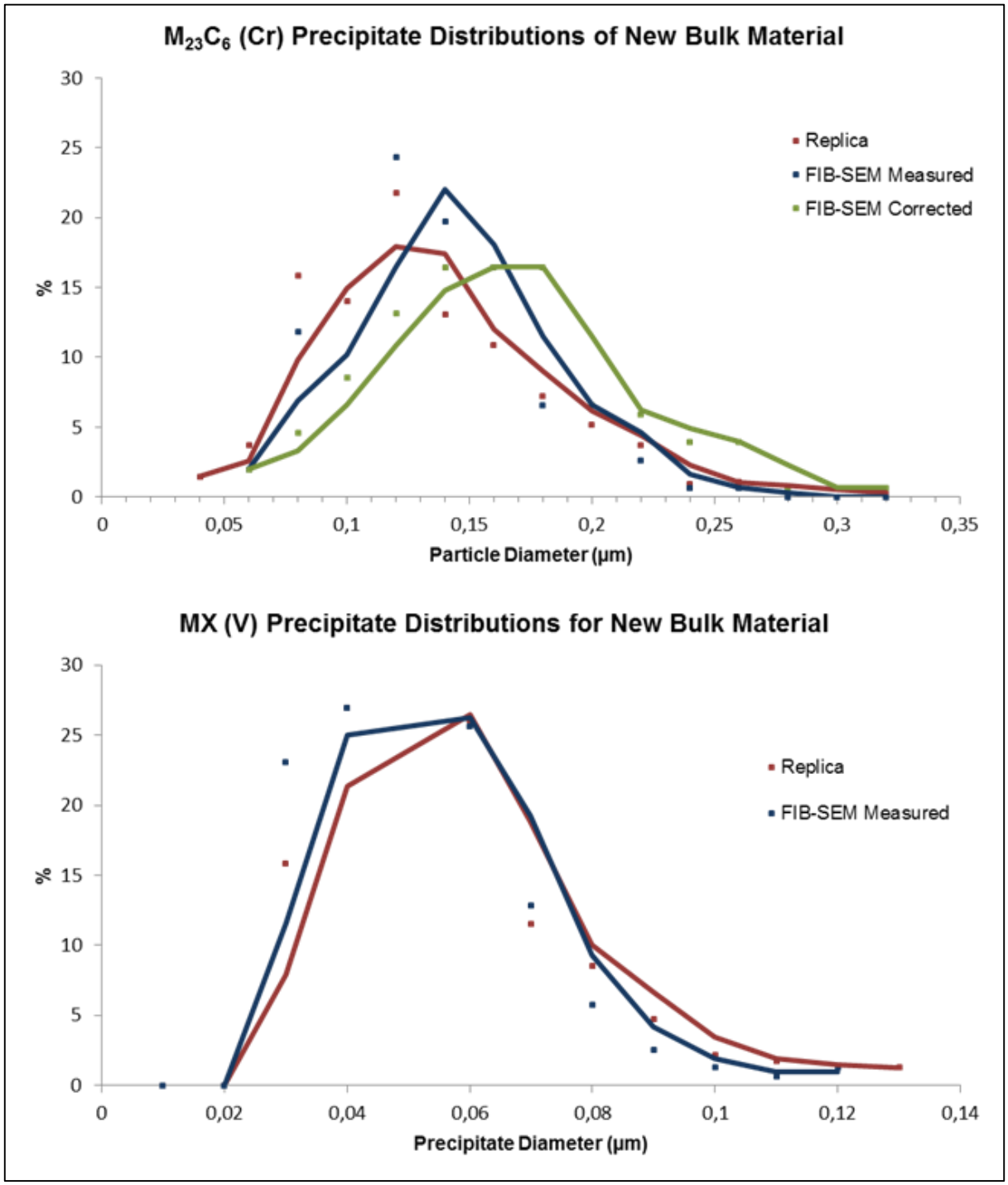

Figure 4.7: *$M_{23}C_6$ and MX precipitate diameter distributions for extraction replica and FIB-SEM specimens prepared from new bulk X20 steel.*

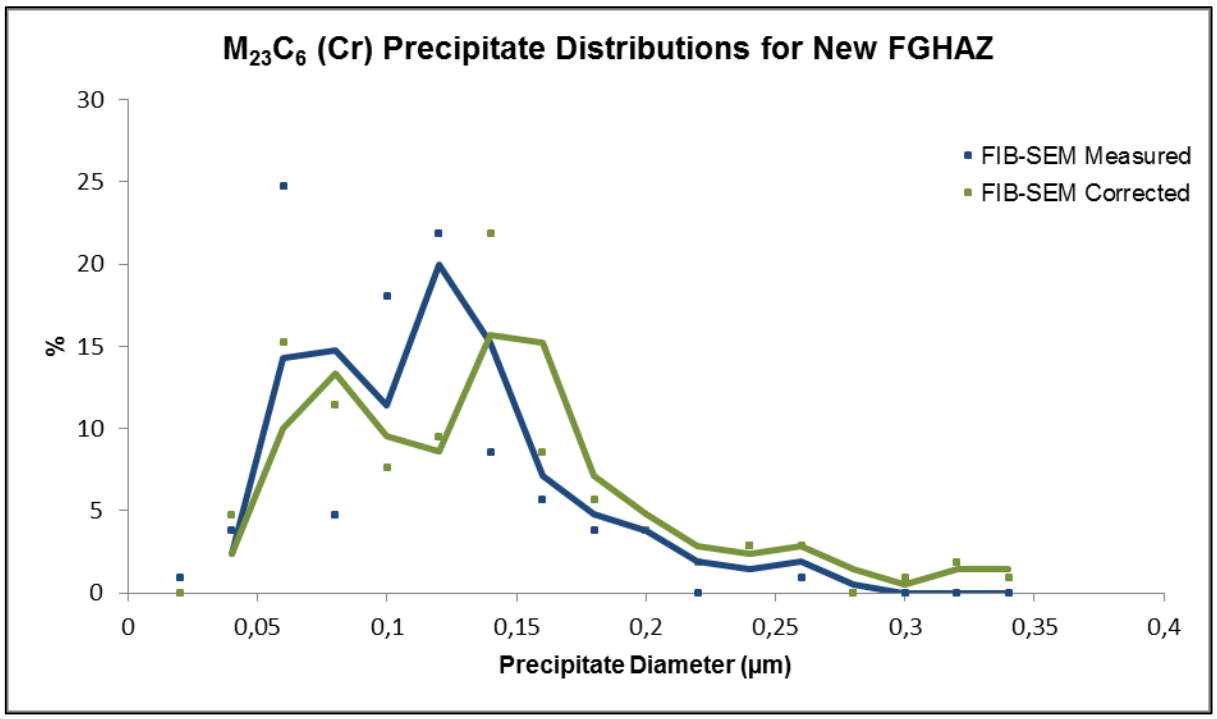

Figure 4.8: *$M_{23}C_6$ precipitate diameter distributions in the FGHAZ FIB-SEM specimen prepared from the new weldment.*

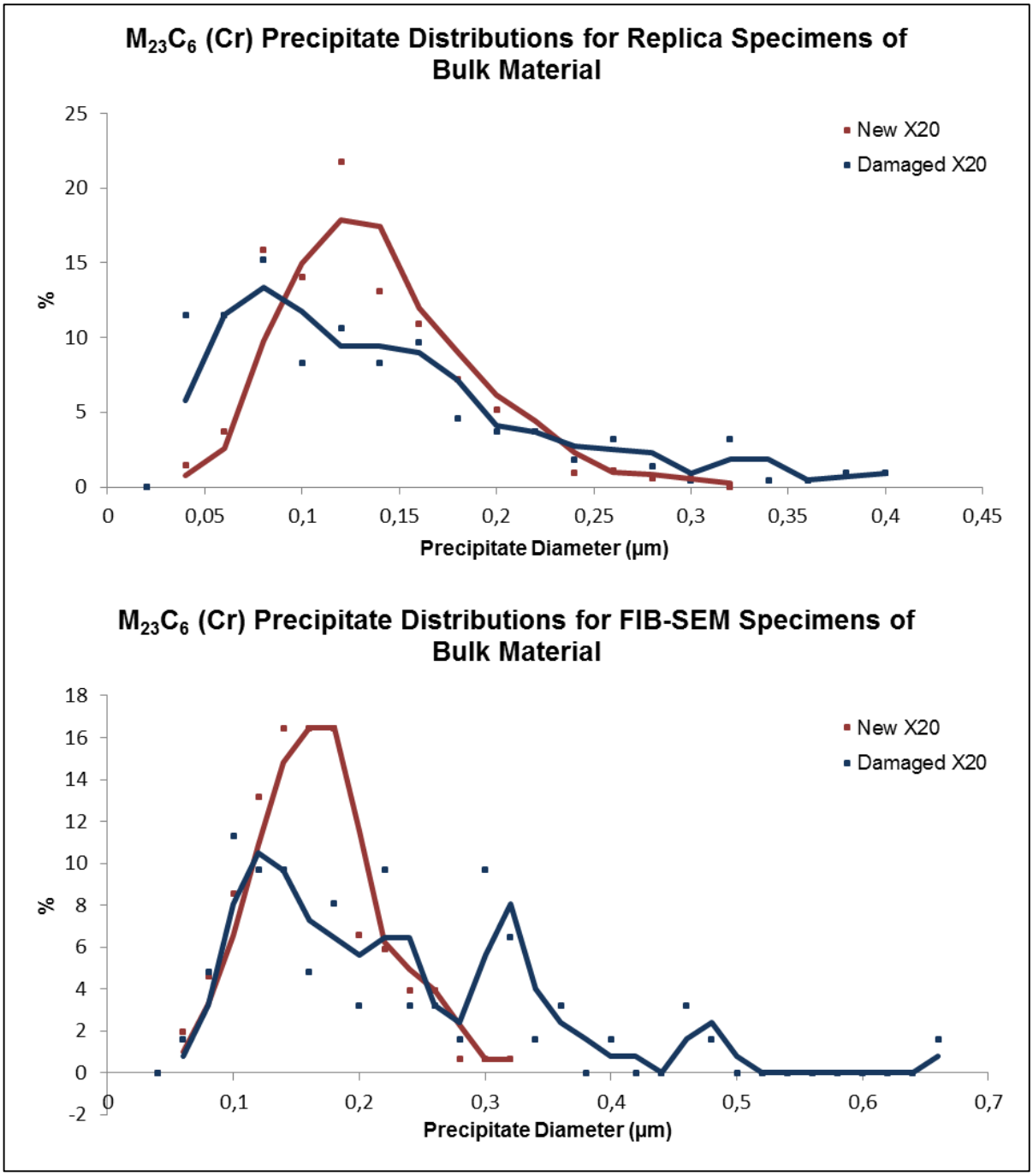

Figure 4.9: *$M_{23}C_6$ precipitate diameter distributions for extraction replica and FIB-SEM specimens prepared from bulk X20 steel. The corrected diameter values are shown in the case of the FIB-SEM specimen.*

4.4.3 Chemical Analysis of Precipitates

Figure 4.10 shows a concentric back-scattered SEM image taken from the polished surface of the twin-jet electropolished specimen prepared from the damaged bulk X20 material. The precipitates can be seen decorating the GBs in the specimen. There is also a contrast difference between the differently sized precipitates. The larger precipitates had increased brightness, indicating that these precipitates contain elements with a higher atomic number. EDS measurements in the SEM has a poor spatial resolution due to the interaction volume of approximately 1 μm^3 for 15 keV electrons (Williams and Carter 2009). In order to measure the composition of the precipitates, STEM-EDS analysis was performed on the extraction replica specimens taken from new and damaged bulk X20 materials (Table 4.1).

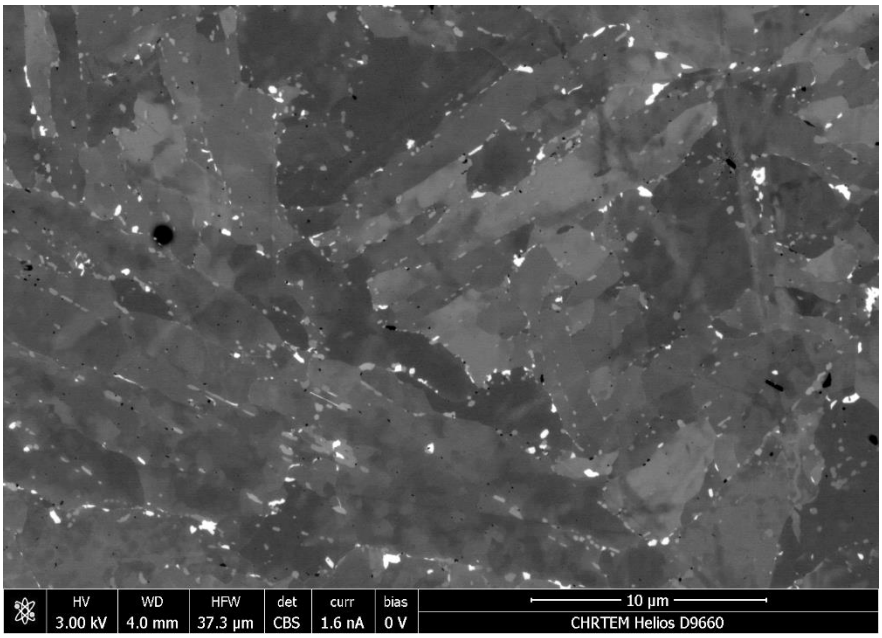

Figure 4.10: *Concentric back-scattered SEM image of polished surface prepared from damaged bulk X20 material.*

Figure 4.11 shows the elemental map generated from the extraction replica that was prepared from the damaged bulk X20 material. All the precipitates contained high levels of chromium. The precipitates showing increased atomic contrast also showed increased levels of Mo, Si and Ni. This is consistent with the Laves-phase $(Fe:Cr)_2Mo$ (Chapter 2).

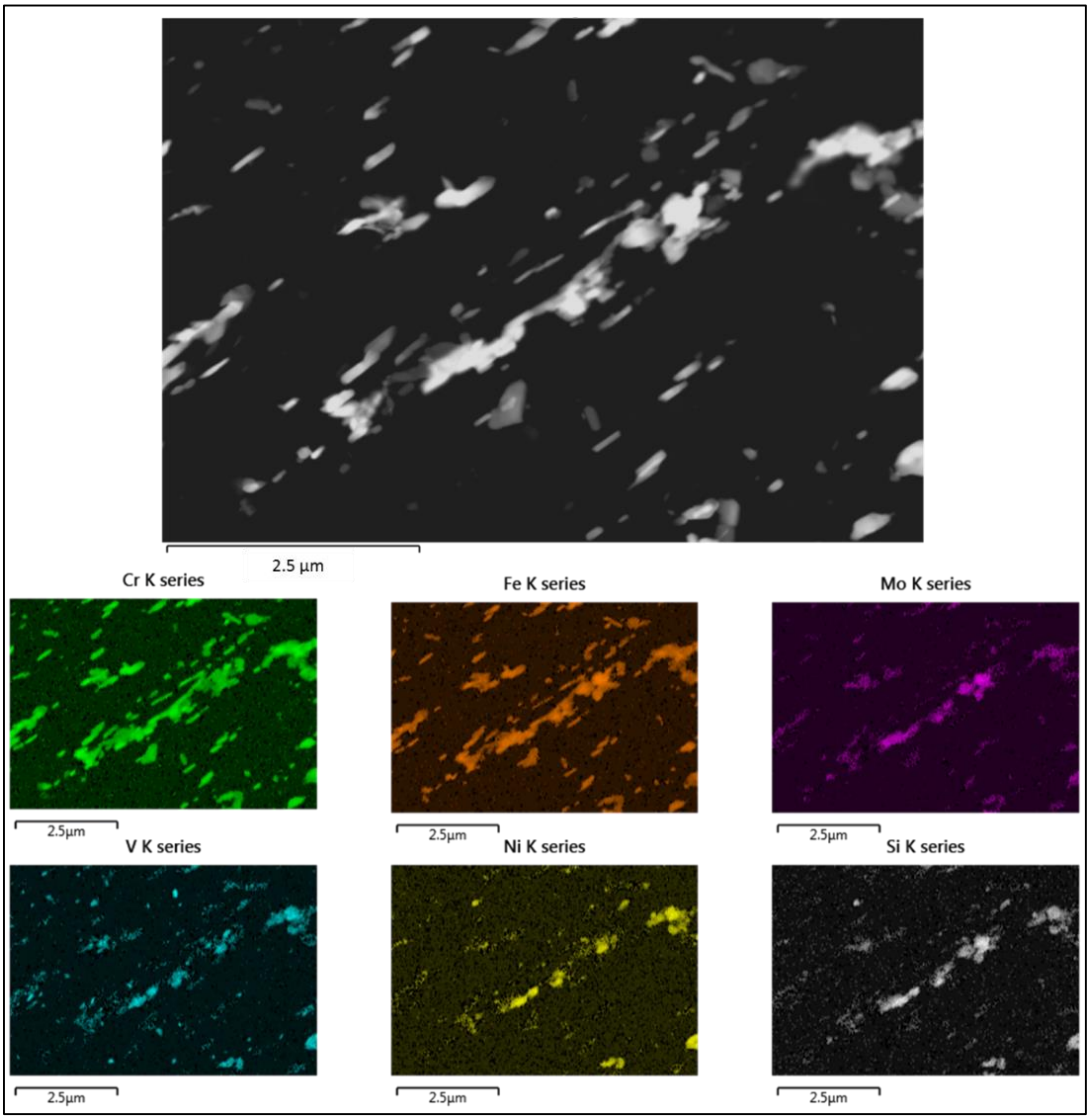

Figure 4.11: *HAADF-STEM image and STEM-EDS elemental maps obtained from an area on the extraction replica specimen prepared from the damaged bulk X20 material.*

In an attempt to show the difference in the $M_{23}C_6$ precipitate composition between the new and damaged materials, STEM-EDS spot analysis was performed on the extraction replica samples. Table 4.8 summarises the results of the spot analysis. The damaged material had slightly larger chromium content (0.73 ± 0.01) compared to the new material (0.70 ± 0.01). No Laves-phase precipitates was observed for the new material, while precipitates with high Mo-content were identified in the damaged material.

Table 4.8: *Ratio of elements in $M_{23}C_6$ and Laves-phase precipitates obtained using EDS spot analysis.*

	$(Cr:Fe:Mo)_{23}C_6$	**Laves $(Fe:Cr)_2Mo$**
New	*Cr* = 0.70 ± 0.01 *Fe* = 0.24 ± 0.01 *Mo* = 0.06 ± 0.01	N/A
Damaged	*Cr* = 0.73 ± 0.01 *Fe* = 0.23 ± 0.01 *Mo* = 0.04 ± 0.01	*Fe* = 0.33 ± 0.13 *Cr* = 0.37 ± 0.23 *Mo* = 0.30 ± 0.10

4.5 SUMMARY

In this chapter the precipitate parameters for $M_{23}C_6$ and MX were measured using EFTEM. The specimens were prepared using two different methods, viz. FIB-SEM and bulk (extraction) replication from the new and damaged bulk X20 material. FIB-SEM sampling was done from the different microstructural sections of the weldment. The elemental maps were analysed using a combination of thresholding (well separated precipitates) and manual outlining (for overlapping precipitates). Corrections to account for the sectioning of precipitates in the thin foils were performed and the Orowan stress for PH was calculated for each specimen.

The $M_{23}C_6$ precipitates in the damaged material were coarser and had a lowered number density compared to the new material. Hence, the calculated Orowan stress for the damaged bulk X20 material (98 MPa) was lower compared to the new bulk X20 material (160 MPa). This is consistent with precipitate coarsening during creep exposure with an accompanying drop in creep resistance.

Clear differences in the size and distribution of the $M_{23}C_6$ precipitates were noted for the different microstructural regions of the weldment. The ICHAZ/FGHAZ region had

the largest precipitates for both the new and damaged materials. In addition, the precipitates in this zone were much larger for the damaged material. The quantitative analysis showed a calculated Orowan stress of 138 MPa for the new material compared to 106 MPa for the damaged material. This value could potentially be used in the of defining weldability limits for Type IV cracking, but this has to be correlated with experimental results. Figure 4.12 shows a summary of the calculated Orowan stress values for the $M_{23}C_6$ precipitates.

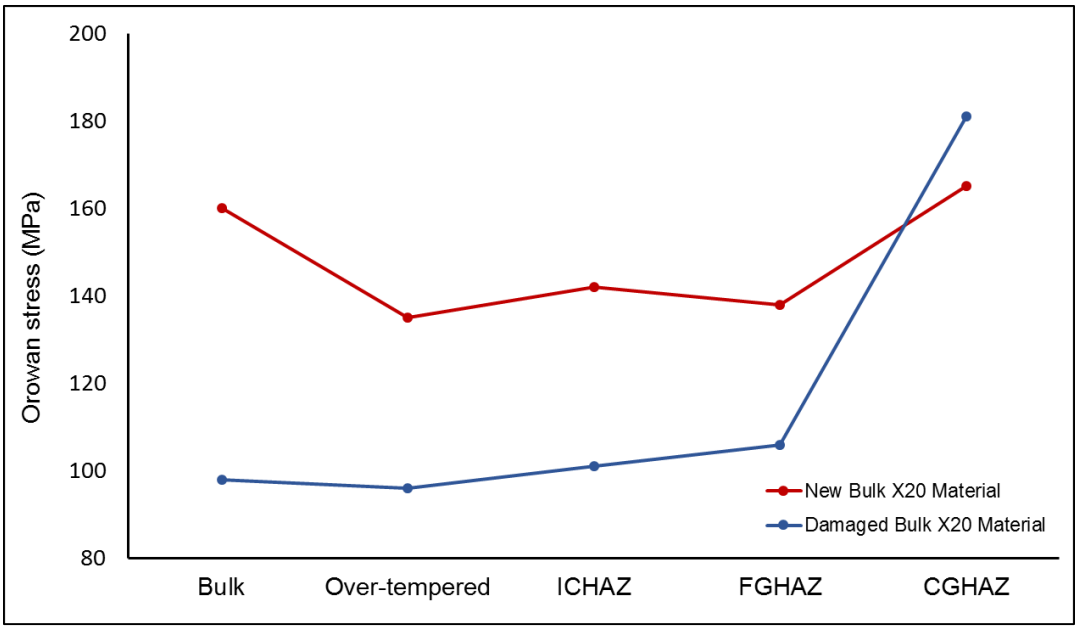

Figure 4.12: *Calculated Orowan stress for the different microstructural regions of the weldment.*

The limitations of this techniques was discussed in the previous sections of this chapter. The FIB-SEM sampling technique had the advantage of site specific sampling needed to remove thin sections from the different microstructural regions of the weld. Due to the small size (±5 x 5 µm) of the FIB-SEM specimen it is possible that the specimen might not be representative of the area. This is especially true when the precipitates are large and not homogeneously distributed, as is the case for the damaged material. Extraction replication was used as a means to increase the sampling area, where numerous ±50 x 50 µm squares were available for analysis. The limitation of this technique is that the sampled volume is not known. The assumption in this study was that the Cr-enriched $M_{23}C_6$ precipitate phase fraction is independent of the sampling method. The precipitate phase fraction was determined from the thin foils prepared with the FIB-SEM. Two possible sources of error is small sampling

volume and the 20% error in the thickness measurement of the specimen. This could lead to errors in the phase fraction and the calculated volume of the extraction replica. The extraction efficiency of the $M_{23}C_6$ precipitates were high as the number density of the precipitates agreed well for the FIB-SEM and extraction replica specimens. The extraction efficiency of the smaller V-enriched MX precipitates were much lower, implying that the smaller precipitates were lost during the extraction process. The MX precipitates were imbedded in the iron matrix and subject to low vanadium signal-to-noise ratios when the thin-foils were thicker than 100 nm. The mean diameter values were subject to the contrast thresholding and minimum size measurements. The measured MX precipitate parameters did not show large variations between the different microstructural regions of the weldment. There were however significant dissolution of MX precipitates for the damaged material as shown by the lower number density.

The $M_{23}C_6$ precipitates did not show large deviations in the average compositional values for the new and damaged bulk X20 materials. The damaged material however contained a significant amount of the Mo-enriched Laves-phase. As this phase also contains chromium it could have a serious effect on the measurements taken from the Cr EFTEM elemental maps.

Future work would try and address the limitations mentioned above. Firstly, SEM images to quantify the Laves-phase should be recorded in order to consider only the $M_{23}C_6$ in the Cr maps. Alternatively, a Mo elemental map can be made to distinguish between the two types of precipitates. The extraction volume can be calculated by considering the size reduction in a hardness indent. A hardness indent is made with a Vickers square pyramidal indenter (Chapter 3). The indent size will be reduced due to etching of the surface. The remaining size of the indent can be used to calculate the extraction depth. The critical area for Type IV cracking is the ICHAZ/FGHAZ region. Gleeble^{TM} simulations of the temperature profile could provide bulk materials for analysis. Twin-jet electropolished thin foil specimens from these simulated materials can be used for the precipitate analysis. This would solve both the small sampling area of the FIB-SEM in addition to the unknown sampling volume of the extraction replication. Also, double extraction replicas (Ayache, Beaunier *et al.* 2010) can be prepared from the twin-jet electropolished specimens. Since the thickness of the twin-

jet electropolished specimen is known, the extraction depth is also known by using this method. Optimisation of automatic thresholding and segmentation using the watershedding and scripting of the statistical analysis and visualisations will greatly improve the time taken to conduct similar analysis. Scripting and automation of the analysis procedure will help with the documentation of the analysis and improve the reproducibility of the image post-processing.

CHAPTER 5

EVALUATION OF SUBGRAINS

5.1 INTRODUCTION

This chapter focuses on the evaluation of the subgrains in the X20 weldments. Background on previous studies of measurement of grains and subgrains in ferritic steels will be briefly summarised. The methods employed for the measurement is outlined, followed by the experimental results and analysis.

5.2 BACKGROUND

The microstructure of CSEF steels consists of prior austenite grains that are divided into packets and further into martensite block and lath SGBs, which are elongated in shape (Chapter 2). In addition, a dislocation substructure of small-angle grain boundaries is introduced during heat treatment as a result of the rearrangement of dislocations during annealing. Apart from the precipitates, the GBs and SGBs also act as obstacles to dislocation motion since they are impenetrable by mobile dislocations. However, of these boundaries the elongated SGBs are the actual contributors to creep strength (Chapter 2). Their short width plays an important role in the creep strengthening of the material, which is quantified by a SBH stress value described by equation 2.6.

There are three recognised industrial standards for measuring grain size and five methods are described within these standards (Muirhead, Cawley *et al.* 2001). All of these methods entail measuring the grain size from optical or SEM micrographs of the polished or etched specimen surface. The most recognized and widely used of these methods is the LI method (Chapter 3). It can be applied to measure both grain and subgrain size. Aghajani, Somsen *et al.* (2009) obtained BSE-SEM images of the etched surface of a X20 steel specimen and then manually measured the subgrain size using the LI method.

EBSD orientation maps can be used to quantitatively investigate the different SGBs in an area since they have unique misorientations. In addition to the LI method, EBSD

software can also implement the GR method to measure subgrain size. There are numerous studies that discuss these two methods of characterising grains and subgrains using EBSD (Humphreys 1998; Humphreys, Huang *et al.* 1999; Humphreys 2001; Humphreys 2004; Humphreys 2004). A previous study that implements EBSD to measure the subgrain sizes in a 9-12% Cr ferritic steel is that by Fujiyama, Mori *et al.* (2009). Qualitative subgrain analysis of a P91 steel was performed by Panait, Zielinska-Lipiec *et al.* (2010) using EBSD.

The TEM can also be used to measure subgrain widths by acquiring BF-TEM images of thin-foils (Ennis, Zielinska-Lipiec *et al.* 2001; Kotska, Tak *et al.* 2007; Panait, Zielinska-Lipiec *et al.* 2010).

It has been found that EBSD has the following advantages over the TEM (Humphreys 2004): bulk specimens can be analysed and hence more representative results can be obtained; very large areas can be studied; many thousands of grains/subgrains can be characterised from a single EBSD map. However, some of the disadvantages of EBSD compared to TEM are: the spatial resolution of EBSD is poorer than that of the TEM; EBSD is unable to image individual dislocations and defects; the time it takes to acquire data is much longer for EBSD.

5.3 METHODOLOGY

The aim of this section of the study was to determine the short width of the elongated subgrains (subtended by lath and block boundaries) using EBSD for the different weld regions in an X20 steel weldment. This value was then used to calculate the SBH stress value. In addition, comparison is made between the results obtained from the LI method and the GR method. Another aim was to demonstrate the feasibility of the use of TEM and XRD to also determine subgrain size.

5.3.1 Sampling

The X20 weldment specimens for the new and damaged materials were mounted and polished. Hardness indentations across the weldments was performed to act as markers for site specific analysis and for the initial identification of the different microstructural regions. The observed microstructure from the EBSD analysis was

then used to confirm the correct identification of the different microstructural regions in the weldment.

TEM and TKD analysis was performed on a twin-jet electropolished sample prepared from the new bulk X20 material. This part of the study was done to investigate the feasibility of applying these spatially resolved methods.

5.3.2 EBSD Analysis

EBSD analysis was performed on the new and damaged X20 weldments. Orientation maps were acquired at the various indents summarised in Table 3.5, using a Nordlys HKL system fitted to the JEOL JSM 7001F SEM. The Oxford AZtecHKL EBSD software was used for the acquisition and analysis of the EBSPs, and the construction of the various EBSD maps. A 15kV accelerating voltage, 4nA probe current and specimen tilt of 70° from the horizon, was used for EBSD analysis. Table 5.1 summarises the other acquisition parameters. EBSD maps were obtained with magnifications of 250x and 500x in combination with a 0.2 µm step size. All the acquired maps had acquisition rates of between 87 to 98%, indicating the good quality of the maps. In the AZtecHKL software, the specimen orientation was chosen as shown in Figure 5.1 before exporting any data (also refer to Figure 2.11). For the determination of grain/subgrain size, a minimum of 200 grains are required in a single EBSD map, and to define the grain/subgrain with sufficient accuracy at least 5 to 10 data points should describe a grain/subgrain (Humphreys 2004). Subsequently, at least 20 000 data points should be contained within an EBSD map. It was ensured that each acquired map satisfied this condition.

Table 5.1: *AZtecHKL software parameters used for EBSD map acquisition*

Working Distance	± 22 mm	**Static and Auto Background Correction**	On
Detector Insertion Distance	187.4 mm	**Hough Resolution**	75
EBSD Camera Binning Mode	8x8 (168x128 pixels)	**Band Detection Mode**	Centers
EBSD Camera Gain	1	**Number of Bands Detected**	12
Frame Averaging	1 frame	**Indexing Mode**	Refined Accuracy

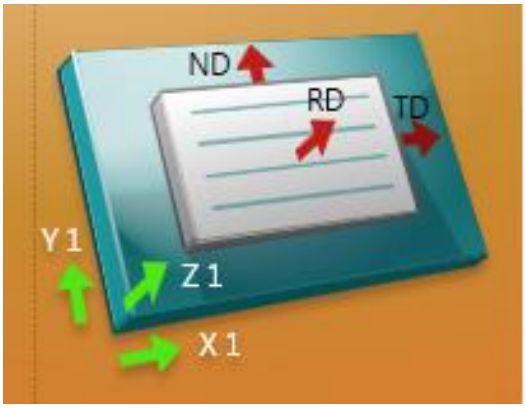

Figure 5.1: *Selected specimen orientation in AZtecHKL software. Refer to Figure 2.11 for further details.*

The HKL CHANNEL4 EBSD post-processing software was used for further analysis of the EBSD maps. Before the commencement of misorientation angle measurements, a clean-up of non-indexed and misindexed points in each EBSD map was performed using the wild spike and zero solution extrapolation methods in the HKL software. No

more than 10% of the points were modified as ascribed by the ASTM:E2627 (2010) standard. For the subgrain analysis, both the GR and LI methods (Chapter 3) from the HKL software was used. A Critical Misorientation (CM) angle of 5º with boundary completion down to 0° was used to reconstruct the grains. For the LI method, 5 horizontal and 5 vertical intercepts were drawn and a CM angle of 5º was also chosen.

For the LI method, the software outputs an intercept length value, which is then taken to be the measured subgrain width. The mean of these measured subgrain widths was then chosen as the desired short width λ_{sg}. The frequency and cumulative % was plotted against this measured subgrain width. For comparison, the d_{50} subgrain width was read from these plots at the 50% cumulative % mark, i.e. 50% of the subgrains have a width smaller and 50% have a width larger than this value. Separate analysis was performed on the horizontal and vertical intercept data.

In the case of the GR method, the software measures the area and aspect ratio AR of each reconstructed grain. The % area and cumulative % area was plotted against the measured subgrain area. It was decided that a minimum of 5 pixels, which corresponds to an area of 0,2 μm^2 (0,2 μm x 0,2 μm x 5 pixels), define a subgrain. Consequently, any reconstructed grain with an area less than this value was excluded from further analysis. Similarly to the LI method, the 50% cumulative % area A_{50} value was then determined from these plots. Two different calculations were performed on the A_{50} value. Firstly, the ECD value was calculated and called the d_{50} value (Figure 5.2). Secondly, the subgrains are elongated and thus it can be assumed they have a rectangular shape with a short width Y and length X (Figure 5.2). This assumption with the mean AR leads to the following two equations:

$$mean\ AR = \frac{X}{Y} \tag{5.1}$$

$$A_{50} = XY \tag{5.2}$$

The short width Y, and hence λ_{sg}, can then obtained by solving these two equations simultaneously. The SBH stress was then calculated for both methods using equation 2.6 and the values defined in Table 2.5.

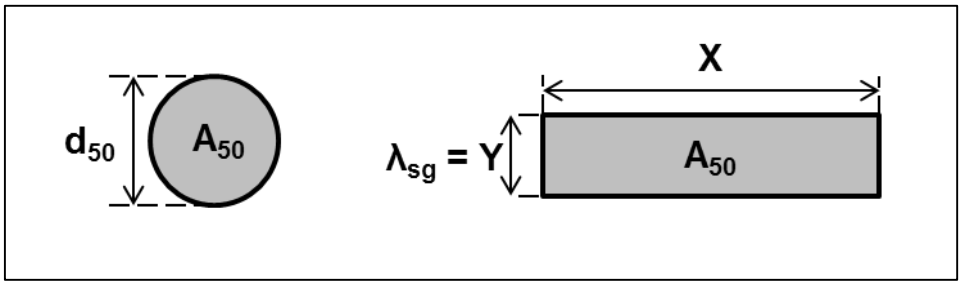

Figure 5.2: *Schematic illustration of subgrain size using the GR method.*

5.3.3 TKD Analysis

TKD was performed on the same SEM-EBSD system used for EBSD analysis. Since the interaction volume need not be limited as with EBSD, a higher accelerating voltage of 30 kV was used for TKD analysis. The TKD map was acquired with the specimen tilted to -20° and using a step size of 0.01 µm and binning of 4x4.

5.3.4 TEM Analysis

In order to observe the subgrains using the TEM, BF-STEM images were recorded from different areas on the twin-jet electropolished specimen prepared from the new bulk X20 material. ImageJ was then used to measure the short widths of the subgrains.

5.4 RESULTS AND DISCUSSION

5.4.1 Qualitative Study of Weldments

It was mentioned in Chapter 3 that after the different weld regions have been identified by the Vickers hardness of the various indents, EBSD maps can be acquired at the indents to confirm correct identification. Figures 5.3 and 5.4 provide the EBSD IPF maps acquired from the middle line of indents as summarised in Table 3.5 for the new and damaged X20 weldments, respectively.

The EBSD maps acquired at the indents with the highest Vickers hardness values did demonstrate a coarse prior austenite grain structure and hence it is confirmed that these indents are in the CGHAZ. A mixture of small and large grains are observed in the EBSD maps of the indents with lowest Vickers hardness, which, from Chapter 2, indicates that it is the ICHAZ. Only fine grains are observed in the EBSD map acquired at an indent between those of the CGHAZ and the ICHAZ, leading to the conclusion

that the indent is in the FGHAZ. The bulk or unaffected region was easily identified by observing the largest prior austenite grains in the EBSD map acquired from an indent to the left of that in the ICHAZ and well before the decrease in Vickers hardness values. From Chapter 2, it is expected that this initial decrease in Vickers hardness corresponds to the over-tempered region due to the decrease in free dislocations as a result of the local tempering. However, since there is no difference in the grain size between the bulk and over-tempered region, it is not sufficient to determine the over-tempered region from a single EBSD map at the indent of initial decrease in hardness. Instead, EBSD maps were acquired at the indents adjacent to the left of the ICHAZ until a transition to large prior austenite grains was visible. Consequently, it was known for certain then that the next adjacent EBSD map acquired is of the over-tempered region.

The conclusion can be made that Vickers MHT and EBSD are complimentary techniques that can be used to identify the various weld regions. Table 5.2 summarises how the different weld regions can be accurately identified using the two techniques.

Table 5.2: *Summary on the use of the Vickers hardness values and EBSD maps to accurately identify the various weld regions.*

Weld Region	***Vickers Hardness***	***EBSD Map***
CGHAZ	X	X
FGHAZ		X
ICHAZ	X	X
Over-tempered		X
Bulk	X	X

After identifying the different weld regions, additional EBSD maps were acquired at indents not summarised in Table 3.5 in order to determine the approximate width of each region. Similarly to identifying the over-tempered region, this was achieved by obtaining adjacent EBSD maps until a clear transition in grain size, corresponding to

movement from one region into another region, is observed. Consequently, each region is assigned a group of indents with a known spacing between them. Figure 5.5 summarises the group of indents assigned to each weld region. The HAZ of the new weldment has a width of 3 mm (12 indents), while the damaged weldment has a smaller HAZ of 1.75 mm (7 indents). There is no apparent explanation for the smaller HAZ of the damaged weldment. The FIB-SEM specimens of each region were extracted in the proximity of the groups of indents shown in Figure 5.5.

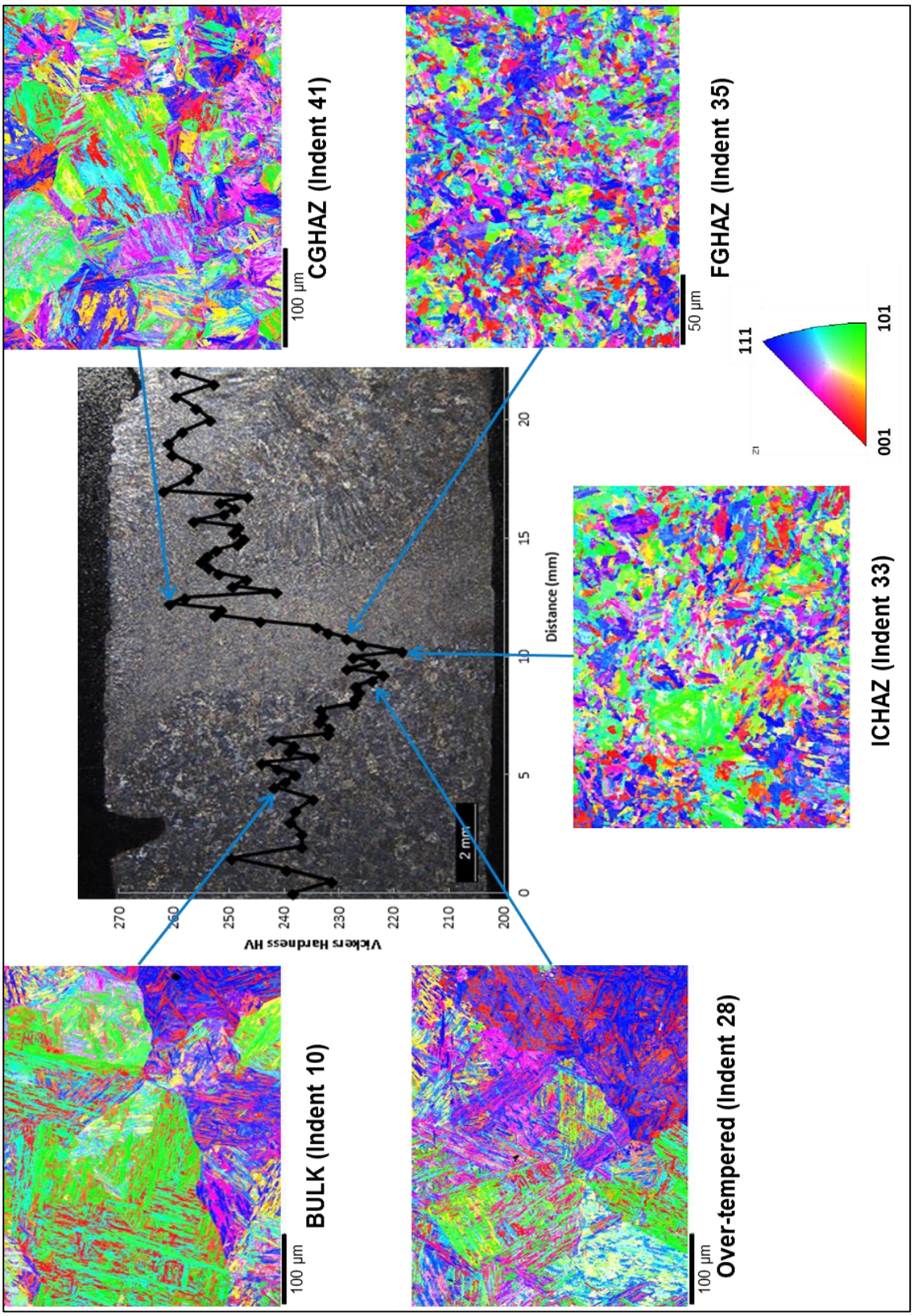

Figure 5.3: *EBSD IPF_Z_0 maps acquired at the indents of the different weld regions in the new X20 weldment specimen. Included is an overlay of the hardness profile of the middle line of indents onto an optical micrograph of the weldment.*

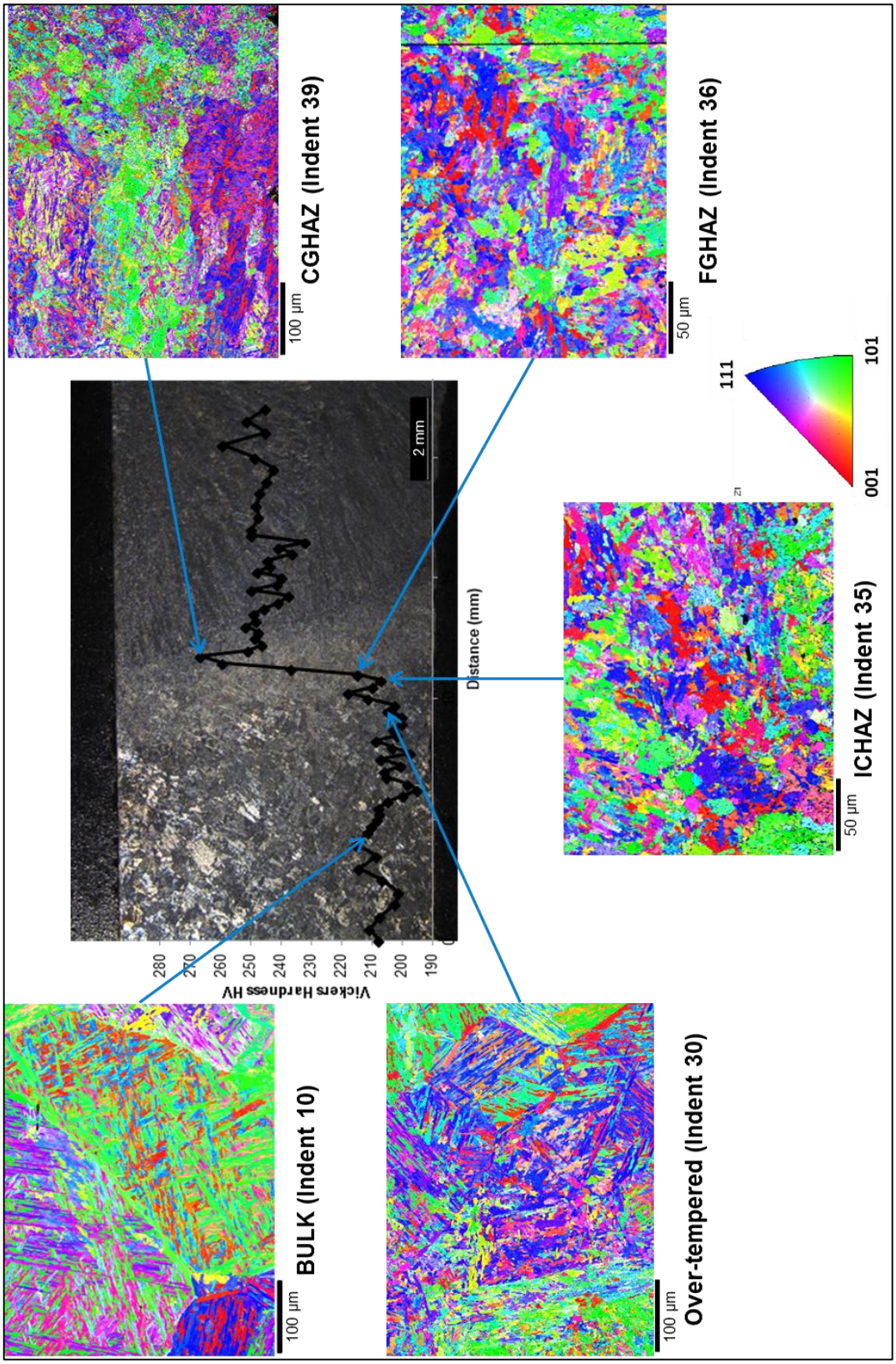

Figure 5.4: *EBSD IPF_Z_0 maps acquired at the indents of the different weld regions in the creep damaged X20 weldment specimen. Included is an overlay of the hardness profile of the middle line of indents onto an optical micrograph of the weldment.*

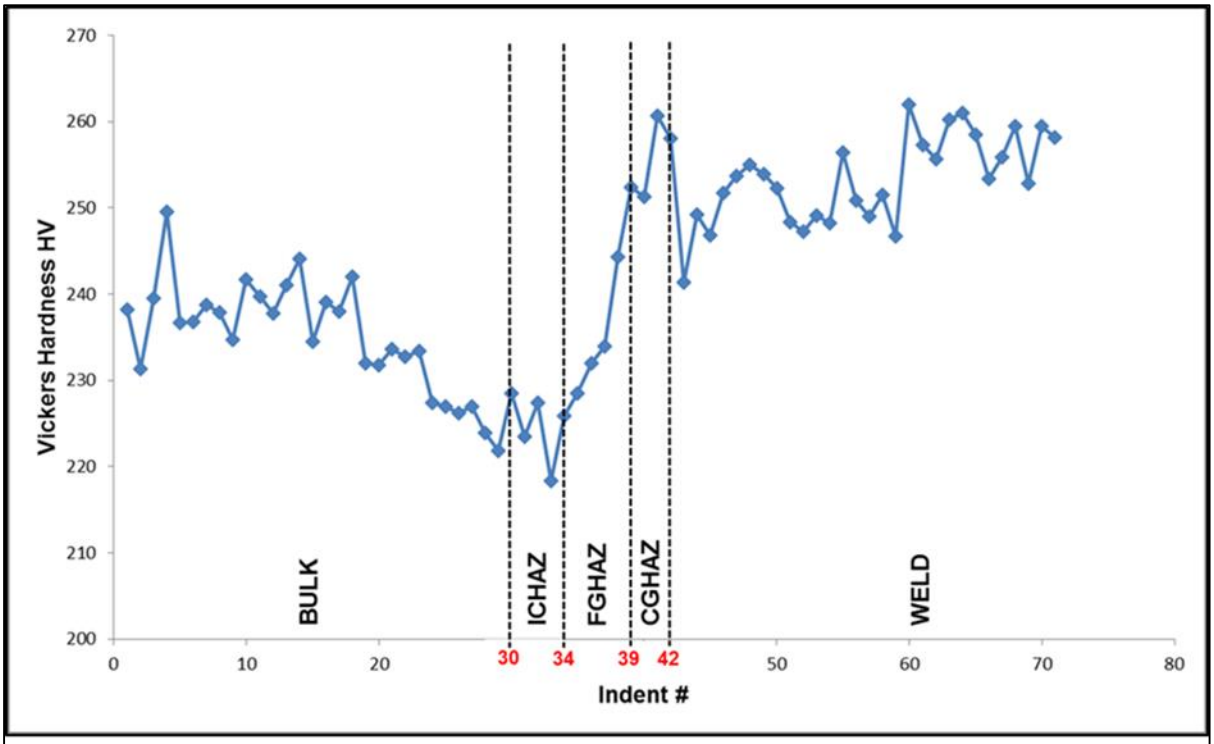

(a)

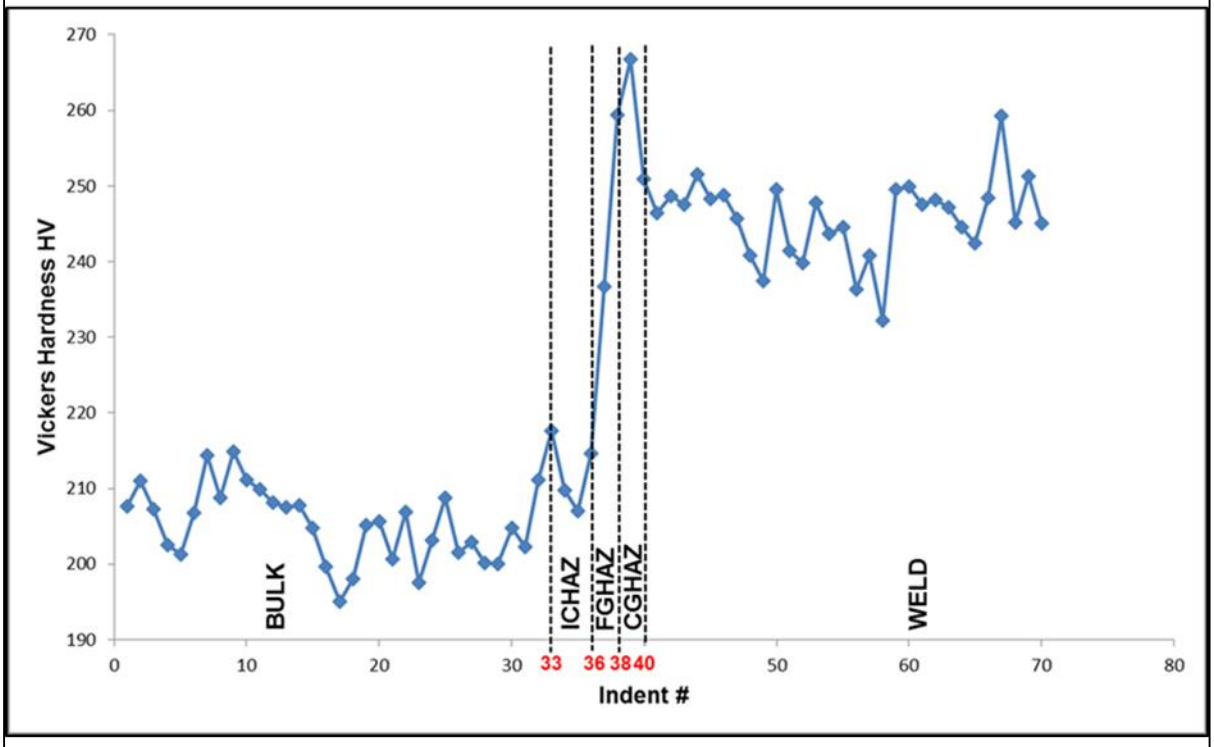

(b)

Figure 5.5: *Vickers hardness profile of middle line of indents in the (a) new weldment and (b) creep damaged weldment plotted along with each weld region and its corresponding group of indents.*

Now that each region has been identified, it is possible to perform analysis on the acquired EBSD maps. Figure 5.6(a) provides the IPF with BC map from the bulk region of the new X20 steel weldment. From this EBSD map it is possible to observe the microstructure. The prior austenite GBs, packets and elongated martensite blocks are clearly visible. As a guide, a prior austenite GB has been drawn in with a solid line. Blocks that lay in the same direction are grouped together by a packet boundary. In order to see the elongated SGB, an enlargement of the rectangular section highlighted in Figure 5.6(a) is given in Figure 5.6(b). A single block is enclosed by the solid line ellipse and the dashed line ellipse encloses a single martensite lath within this block.

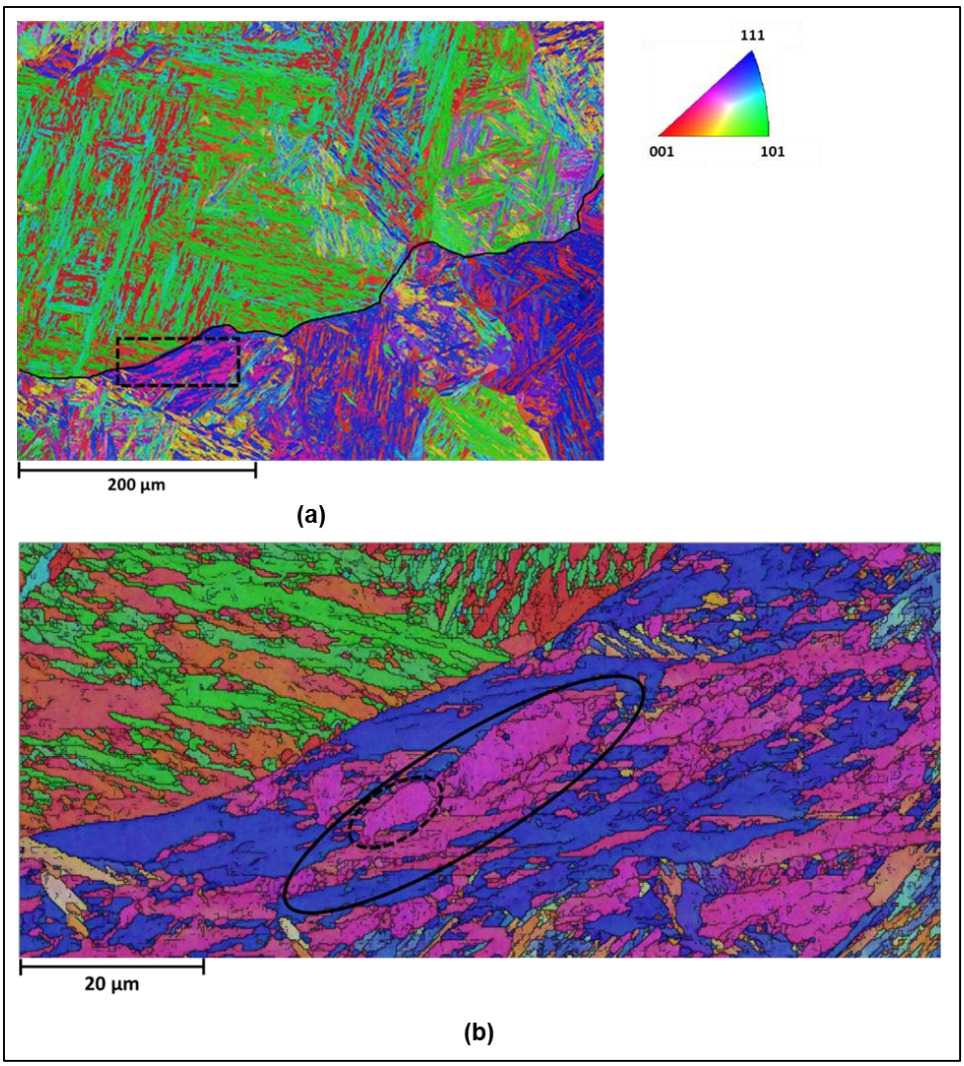

Figure 5.6: *(a) EBSD IPF_Z_0 with BC orientation map for bulk region of new X20 steel weldment. The solid line indicates a prior Austenite GB. (b) Enlarged rectangular section extracted from (a). The solid line ellipse encloses a single block and the dashed line ellipse encloses a single martensite lath within the block.*

The IPF with BC map from the bulk region of the creep damaged X20 steel weldment is given in Figure 5.7. By qualitatively comparing the maps of the new and creep damaged bulk regions, coarsening of the elongated subgrains is observed in the creep damaged bulk region. This substantiates the known effect of creep to coarsen the subgrains (Chapter 2).

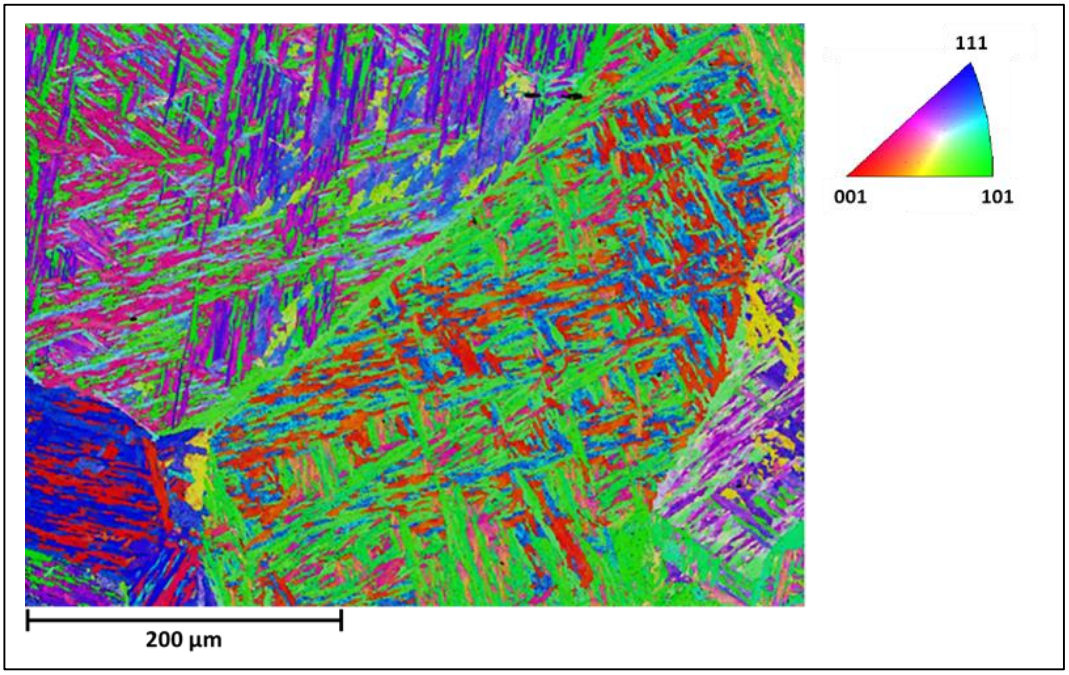

Figure 5.7: *EBSD IPF_Z_0 with BC orientation map for bulk region of creep damaged X20 steel weldment.*

It is evident from Figure 5.6(b) that some of the lath boundaries are incomplete. The lath sizes are in the order of <1 µm and the step size is 0.1 µm. This might not resolve the boundaries between the different grains sufficiently. In order to investigate this effect, TKD analysis was performed using a step size of 0.01 µm.

Figure 5.8 provides the TKD map acquired with a step size of 0.01 µm from the new bulk X20 steel thin-foil. As can be seen, TKD was successful in completely resolving the elongated SGB.

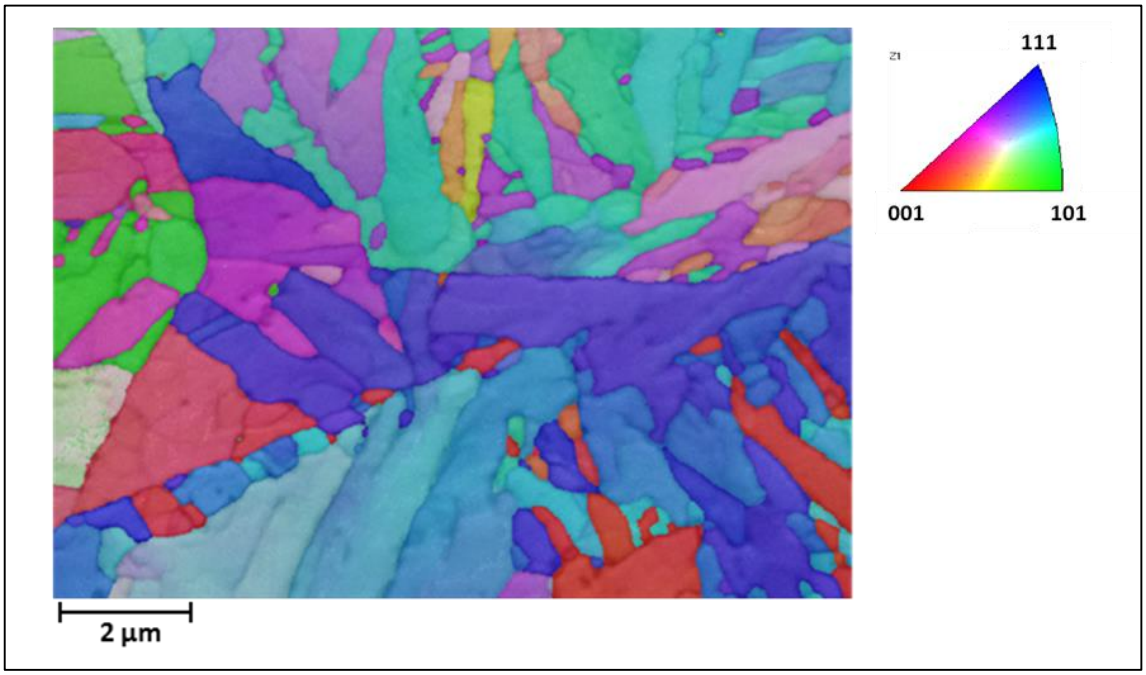

Figure 5.8: *TKD IPF_Z_0 with BC orientation map acquired from electropolished specimen prepared from new bulk X20 steel.*

5.4.2 Quantitative EBSD Analysis

The main aim of this part of the study was to measure the subgrain size, i.e. short width of the elongated SGB, in order to determine the SBH stress value (equation 2.6) and hence the contribution to creep strength. Tables 5.3 and 5.4 summarises the subgrain sizes measured from the EBSD maps using the LI method and GR method, as well as the SBH stress values. The % of total area/cumulative % area against grain area, and frequency/cumulative % against subgrain width plots for the FGHAZ of the new weldment is shown in Figure 5.9 to illustrate the determination of the d_{50} and A_{50} values.

For the GR method results, since the short width Y provides a more realistic short width of the elongated SGB, it was used to calculate the SBH stress value σ_{sg} in Table 5.3. The 95% confidence level for the mean measured short width using the LI method and the average SBH stress value σ_{sg} of the vertical and horizontal data sets are given in Table 5.4. It is sufficient to analyse only 5 vertical and horizontal lines, since a small 95% confidence level indicates reliable statistical and representative results. Unfortunately, the software is limited to only draw and measure intercepts in the x and

y directions. Even though it is not accurate to only measure intercepts in the x and y directions due to the elongated subgrains not laying in a specific direction, little difference is observed in the subgrain sizes measured from the vertical and horizontal intercepts. It is assumed that by measuring a large number of subgrains within numerous different prior austenite grains, the problem of preferred orientation of the subgrains is cancelled out.

Table 5.3: *Measured subgrain size and SBH stress value for the different weld regions using the GR method.*

		A_{50} (μm^2)	d_{50} (μm)	Mean AR	Y/λ_{sg} (μm)	σ_{sg} (MPa)
Bulk	***New***	11,4	3,8	3,1	1,9	84,7
	Damaged	24,6	5,6	2,7	3,0	53,8
Over-Tempered	***New***	13,3	4,1	2,3	2,4	67,6
	Damaged	23,5	5,5	2,5	3,1	53,0
ICHAZ	***New***	5,3	2,6	2,1	1,6	102,3
	Damaged	6,9	3,0	2,0	1,9	87,5
FGHAZ	***New***	5,0	2,5	2,1	1,5	105,3
	Damaged	5,0	2,5	2,0	1,6	102,8
CGHAZ	***New***	12,6	4,0	2,9	2,1	78,0
	Damaged	6,3	2,8	2,1	1,7	93,8

Table 5.4: *Measured subgrain size and SBH stress value for the different weld regions using the LI method.*

		λ_{sg} (µm)		Mean σ_{sg} (MPa)	d_{50} (µm)		Mean σ_{sg} (MPa)
		Vertical	*Horizontal*		*Vertical*	*Horizontal*	
Bulk	***New***	1,3 ± 0,04	1,2 ± 0,03	130 ± 5	0,8	0,6	237 ± 34
	Damaged	1,9 ± 0,06	2,0 ± 0,06	83 ± 2	1,3	1,3	125 ± 0
Over-Tempered	***New***	1,7 ± 0,05	1,7 ± 0,04	96 ± 0	1,0	1,7	172 ± 9
	Damaged	2,3 ± 0,13	1,7 ± 0,06	83 ± 12	1,5	1,7	128 ± 20
ICHAZ	***New***	1,4 ± 0,05	1,3 ± 0,04	121 ± 5	0,9	0,8	192 ± 11
	Damaged	1,7 ± 0,07	1,6 ± 0,05	99 ± 3	1,2	1,1	142 ± 6
FGHAZ	***New***	1,3 ± 0,04	1,2 ± 0,03	130 ± 5	0,9	0,8	192 ± 11
	Damaged	1,3 ± 0,05	1,3 ± 0,04	125 ± 0	0,8	0,8	203 ± 0
CGHAZ	***New***	1,5 ± 0,06	1,3 ± 0,04	117 ± 8	0,8	0,7	218 ± 15
	Damaged	1,4 ± 0,03	1,5 ± 0,03	112 ± 4	0,8	0,9	192 ± 11

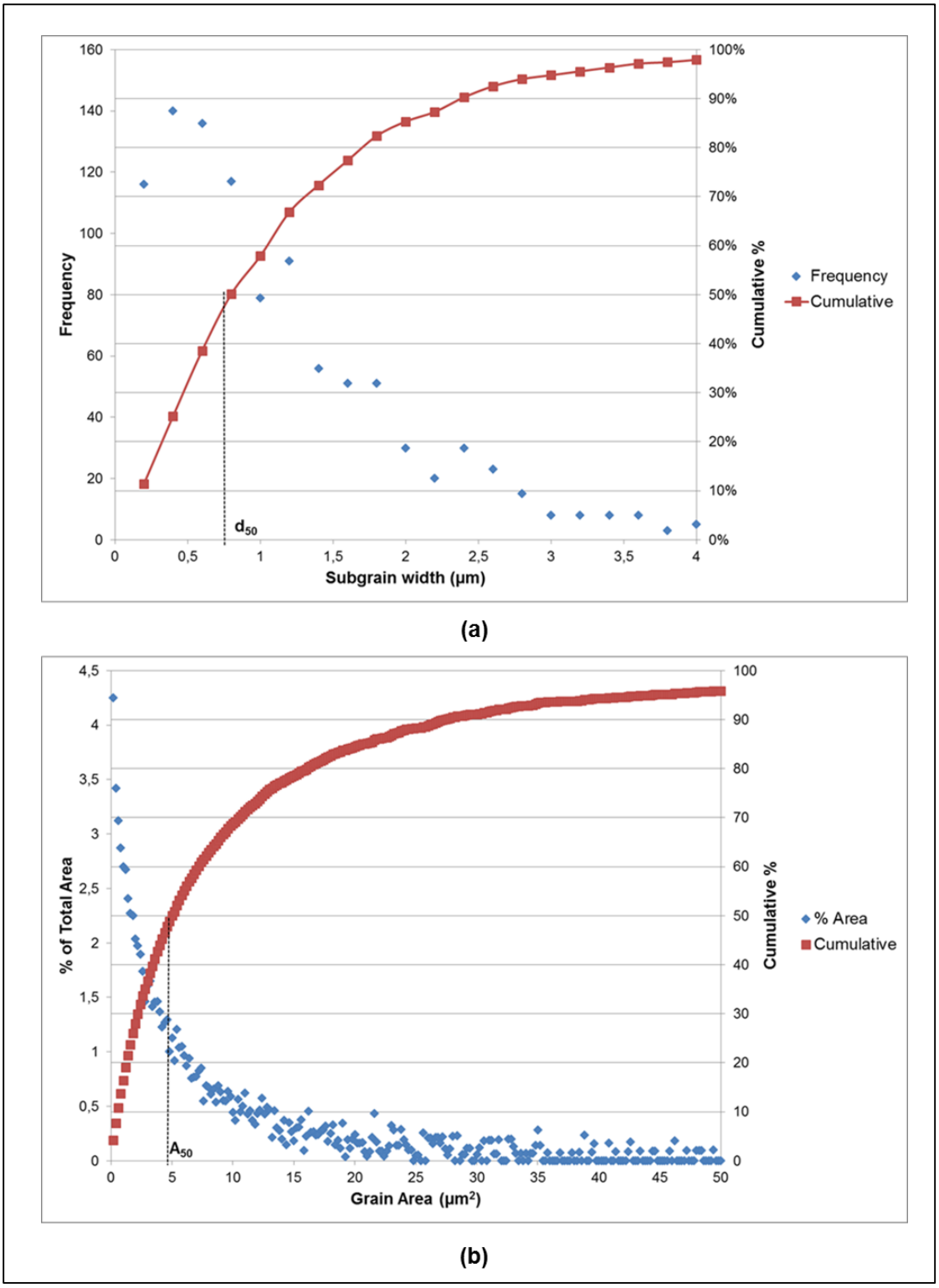

Figure 5.9: *(a) % of total area and cumulative % area vs grain area plot determined using the GR method, and (b) frequency and cumulative % vs subgrain width plots obtained from the LI method for FGHAZ region in new weldment.*

Both the GR and LI methods show significant coarsening of the elongated subgrains during creep in the bulk region, leading to a decrease in the SBH stress. There is little difference in the subgrain sizes and hence creep strength of the new and damaged FGHAZ and new and damaged CGHAZ, respectively. This is expected for the FGHAZ and CGHAZ, since the similar thermal history is experienced by the new and damaged material, which leads to the formation of similar microstructures between the new and damaged material of these regions.

The possible preferred orientation effects of the subgrains could play a role in the analysis of the CGHAZ. In this region, the EBSD scan area only covered a few prior austenite grains.

It can be concluded that the short width d_{50} values obtained from the LI method are closer in accordance with previous results of 0.7 μm for new X20 material and 1.03 μm for 140 kh creep aged X20 material (Aghajani Bazazi 2009), than that obtained from the GR method. The results from the GR method are dependent on the CM angle used to reconstruct the grains. The effect of the CM angle on a single reconstructed grain is illustrated in Figure 5.10. It is seen that subgrains with a misorientation less than the CM are grouped into one grain, resulting in an over estimation of the elongated subgrain size for 5° and 15° CM. For these CM's, only the elongated block size is actually being measured. Therefore, the LI method seems to be more effective in measuring the elongated SGB short width. The misorientation between elongated subgrains is 1° (Chapter 2) and thus a more accurate subgrain size can be obtained using a CM angle of 1°. However, the EBSD technique is limited by an angular resolution of approximately 0.5° to 1.5° (Chapter 3), leading to the influence of noise or measurement artifacts on any analysis performed using a 1° CM. Humphreys (2001) discusses this limitation of EBSD analysis of subgrains with small misorientation due to the inaccuracies in the acquisition and analysis of the EBSPs. This problem can be overcome by obtaining high angular resolution EBSD maps by cross-correlation of the acquired EBSPs, which is a time consuming technique. Subsequently, a CM of 5° was chosen for the GR and LI methods to ensure no SGB are missed, while excluding the effect of noise.

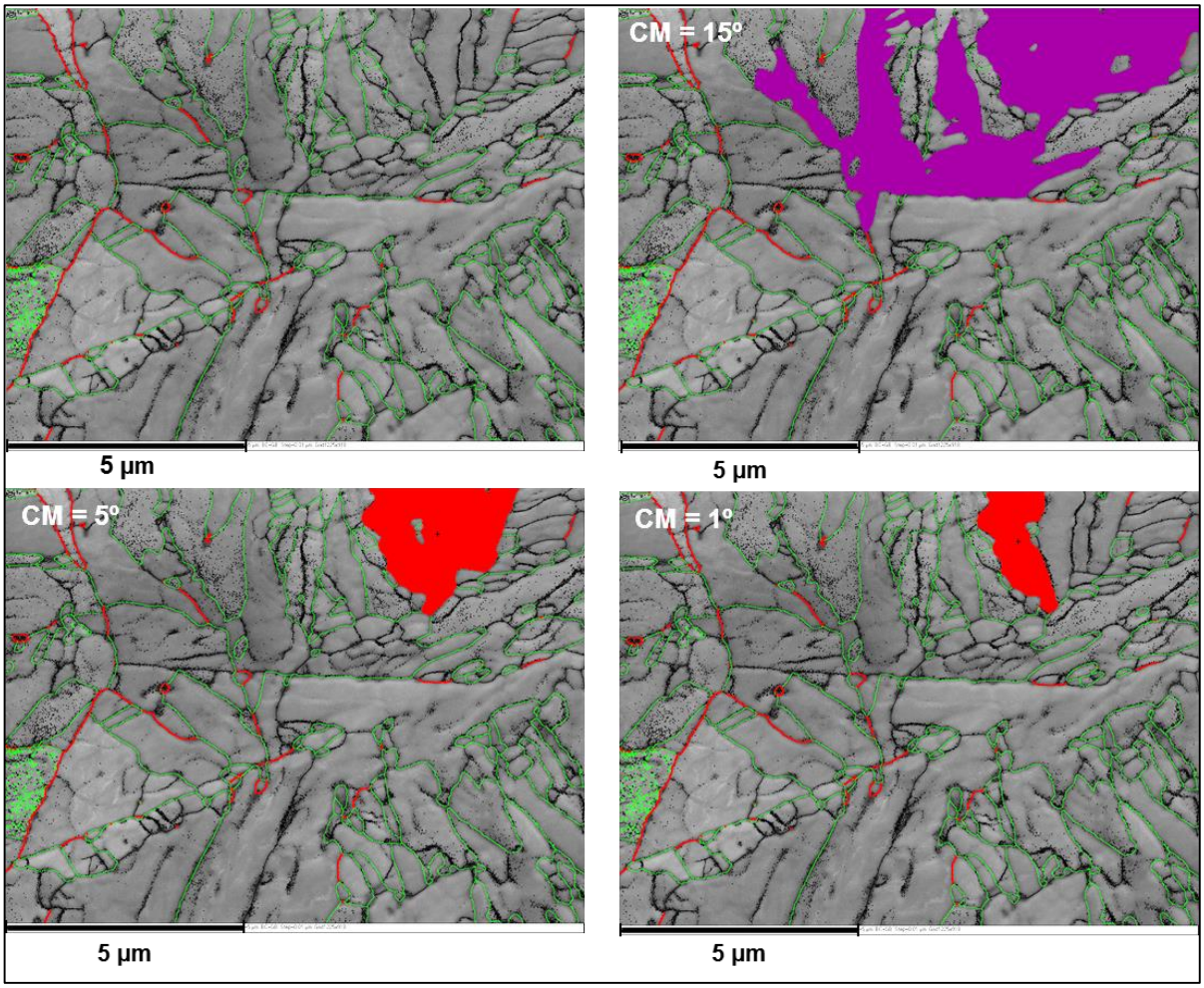

Figure 5.10: *A single grain reconstructed from the TKD map in Figure 5.8 for different CM angles. The TKD BC and GB maps are shown (red for misorientations > 15°, green for misorientations > 5°; black for misorientations > 1°).*

5.4.3 Quantitative TEM Analysis

BF-STEM images of two different areas on the twin-jet electropolished specimen prepared from the new bulk X20 material are shown in Figure 5.11. As in the literature, it is clear that the precipitates are distributed along the GBs and SGBs, which was also observed in the evaluation of the precipitates. By comparing the images in Figure 5.11, a distinct difference is observed in the orientation and shape of the subgrains. This highlights one of the limitations of performing 2D measurements on 3D objects (subgrains). With EBSD certain assumptions are made regarding the aspect ratio and 2D projection of the 3D subgrains, which influences the results. The grains and subgrains intersect the specimen surface at different angles, leading to different

apparent shapes in the 2D projections, for example elongated versus round subgrains (Figure 5.11).

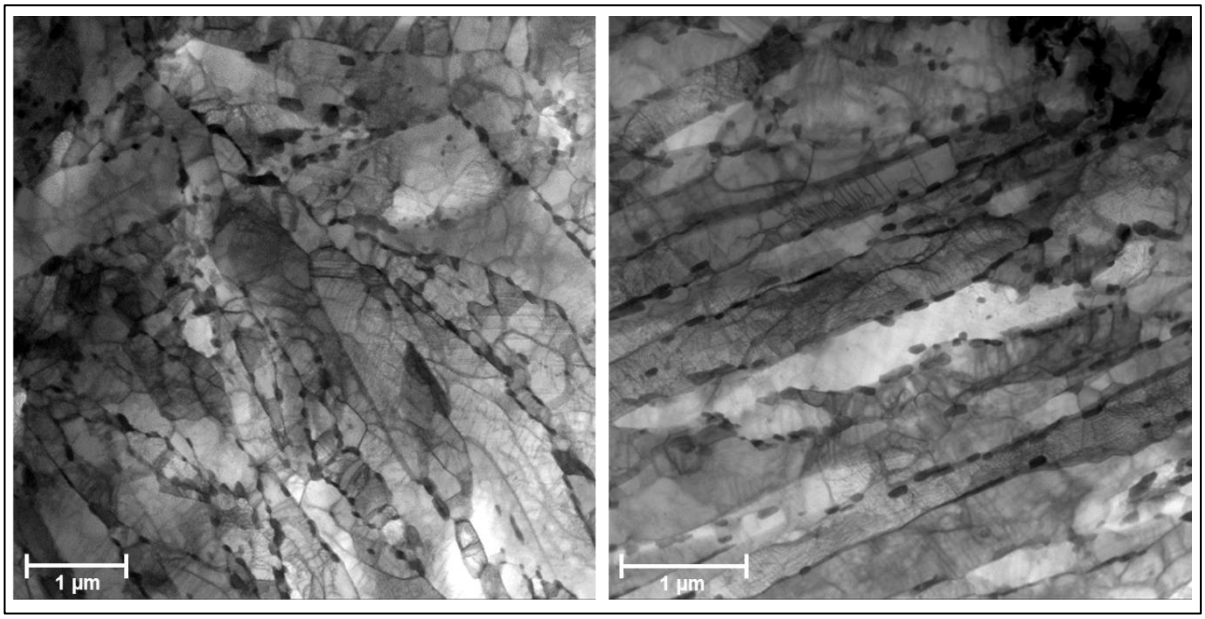

Figure 5.11: *BF-STEM images obtained from two different areas on the jet electro polished specimen prepared from the new bulk X20 material.*

It is important to ensure that when measuring the subgrain size that it is indeed the short width of the elongated subgrain that is being measured. This cannot be ensured by using the LI method with EBSD. However, manual measurements can be made of the short width subgrain size from EBSD maps, which allows one to have control over measuring the actual short width. The same can be done by using BF-STEM images. ImageJ was used to manually draw lines perpendicularly to elongated subgrains on BF-STEM images in order to measure the short width. The mean short width of the elongated subgrains was measured as 0.39 ± 0.03 µm across different areas on the twin-jet electropolished specimen prepared from the new bulk X20 material. Once again this value, as the LI method value, corresponds to the literature value of 0.3 to 0.7 µm (Holzer 2010) for as-received tempered martensite 9-12% Cr ferritic steels. This indicates that the LI method does indeed offer a good value of the short width of the elongated subgrains, provided that the measurements are taken perpendicular to the habit plane.

Future work will include the use of TEM on twin-jet electropolished specimens in order to orient the specimen such that the subgrains are imaged perpendicular to the habit plane (Chapter 2).

5.4.4 XRD Crystallite Size Measurement

XRD analysis can be used to determine the crystallite size. It is important to note that this measurement indicates the coherent domains from which the X-rays are diffracted. For smaller crystallite sizes, the Bragg diffraction condition is relaxed, resulting in broadened peaks. There are several factors that contribute to the XRD line broadening as discussed in Chapter 3.

The Rietveld refinement approach allows the refinement of multiple parameters that have opposite effects on the line broadening. This could result in the extraction of non-physical parameters. It is good practice to first investigate the raw data before conducting the refinement. The XRD spectra acquired from the new and damaged bulk X20 material is shown in Figure 5.12. The intensities were normalised to the 110 peak. No significant difference can be observed between the full spectra of the new and damaged material. Figure 5.13 shows the enlarged three diffraction peaks for ferrite (110, 200 and 211) for the new and creep damaged bulk X20 material. Now slight differences are evident.

Still, it is quite difficult to view obvious differences between the peak widths from the spectrum. In order to obtain a more objective measurement, Rietveld refinement was performed by modeling the peaks as a split Pseudo-Voigt function. The FWHM of both sides for each peak was averaged to obtain an average FWHM for a particular peak. The results of this fit are shown in Table 5.5. From the discussion on XRD in Chapter 3, it follows that crystallite size and strain causes line broadening. Larger crystallite sizes and lower strains, result in narrower XRD peaks. The extracted peak widths for the new bulk X20 steel material is consistently higher than the creep aged bulk X20 steel material. Subsequently, it is expected that the crystallite size determined from damaged X20 material data will be larger. The FWHM needs to be interpreted with care as it is convoluted with the instrumental line broadening.

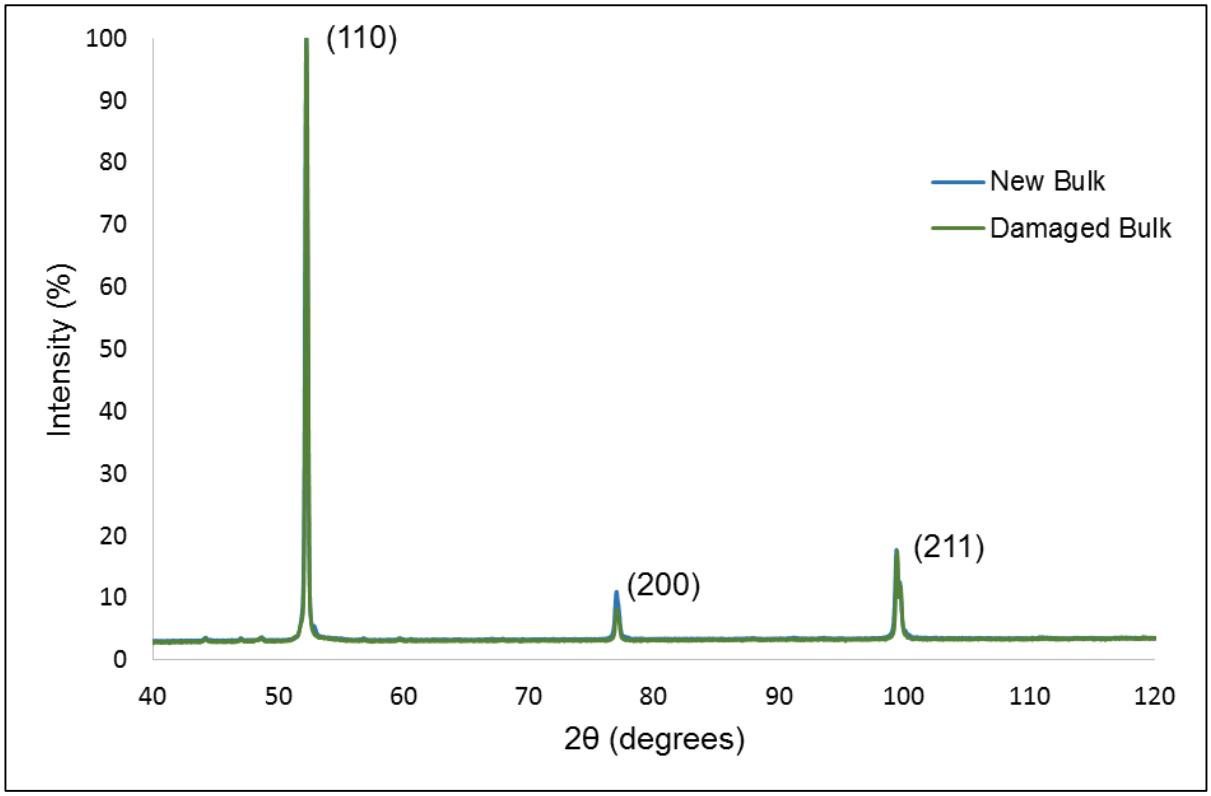

Figure 5.12: *Normalised XRD spectra acquired from new and damaged bulk X20 material.*

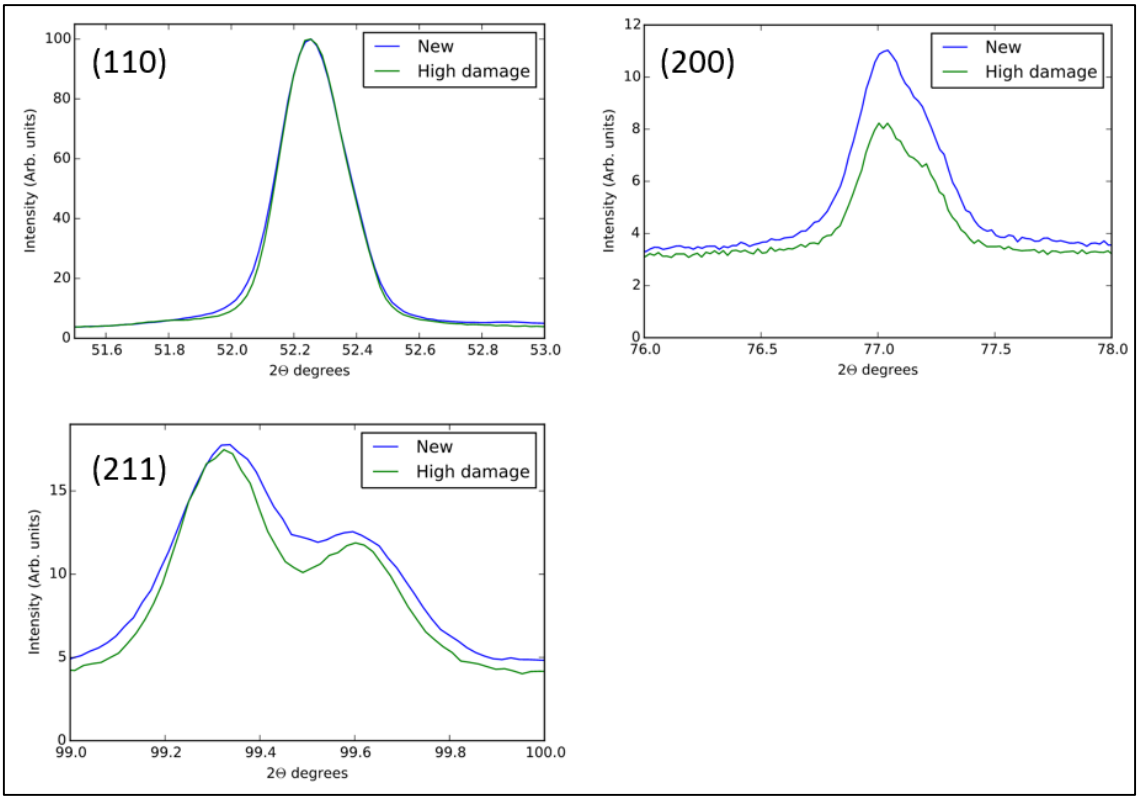

Figure 5.13: *XRD pattern of the different peaks for the new and creep damaged bulk X20 material.*

In order to deconvolute the various XRD line broadening contributions and extract the crystallite size, Rietveld refinement was performed according to the procedure described in Chapter 3 (Section 3.7.3). The results of crystallite sizes obtained using a Lorentzian (L) fit is given in Table 5.5. As expected, the crystallite size in the damaged bulk X20 material is significantly larger than in the new material. This is consistent with the known fact that subgrains coarsen during creep exposure as explained in Chapter 2.

Table 5.5: *FWHM and refined crystallite sizes.*

Peak (2θ)	***New X20 (FWHM)***	***Damaged X20 (FWHM)***
(110)	0.0428 ± 0.0007	0.0289 ± 0.0007
(200)	0.1129 ± 0.0063	0.0863 ± 0.0092
(211)	0.0895 ± 0.0027	0.0638 ± 0.0027
CrystalliteL (nm)	166 ± 1	199 ± 1

The crystallite sizes measured in Table 5.5 are much smaller than the subgrain sizes measured in Tables 5.3 and 5.4 for the bulk region from EBSD. XRD results are more representative since the results are acquired from the entire specimen, i.e. much larger sampling area than EBSD. However, with XRD there is no control over which grains and subgrains are measured. In fact, XRD measures the domain size, which in the case of the martensite microstructure is the small-angle subgrains in the dislocation substructure that make out the boundary dislocations. These subgrains are much smaller than the elongated subgrains measured using EBSD and hence it accounts for the smaller crystallite sizes obtained from XRD.

5.5 SUMMARY

The microstructure of each weldment region was clearly observed from the EBSD maps and the qualitative results corresponded to the literature descriptions (Chapter 2) of each weldment region. A summary of the subgrain sizes determined using EBSD, TEM and XRD in the new and damaged bulk X20 material is provided in Table 5.6. For the LI method the d_{50} value and for the GR method the short width Y is reported.

Table 5.6: *Summary of subgrain sizes measured for new and damaged bulk X20 material.*

	Subgrain size (μm)			
	EBSD		**TEM**	**XRD**
	LI Method	***GR Method***		
New bulk X20 material	0.6/0.8	1.9	0.39 ± 0.03	0.166 ± 0.001
Damaged bulk X20 material	1.3	3.0		0.199 ± 0.001

Larger subgrain sizes, and hence lower SBH stress values, is measured in the damaged bulk X20 material than in the new bulk X20 material. This result was obtained from both the EBSD GR and LI methods. This agrees with literature that subgrains coarsen during creep aging (Chapter 2). It can be concluded that elongated SGB width values obtained from the LI method are closer in accordance with previous results (Abe 2008; Aghajani Bazazi 2009) than that obtained from the GR method. The results from the GR method are dependent on the critical misorientation angle used to reconstruct the grains. Subgrains with a critical misorientation less than 5º are grouped into one grain, resulting in an over estimation of the SGB size. Furthermore, assumptions made regarding the aspect ratio and 2D projection of the 3D subgrains will influence the results. Therefore the LI method seems to be more effective in measuring the elongated SGB short width.

The TEM is a much more accurate technique to measure subgrain size in the sense that one has the control to measure the short width of the elongated subgrain. This technique is, however, time-consuming if statistically reliable results are to be obtained.

The main limitation of XRD is that site-specific analysis cannot be performed as with the TEM. Consequently, only an average value of crystallite size is determined, which can be erroneous if the true crystallite size is inhomogeneous. This measurement also does not measure the short width but it is an indication of the small angle subgrain structure made of boundary dislocations.

In order to measure the subgrains, TEM specimens prepared using twin-jet electropolishing is suggested. Imaging using either BF/DF-STEM imaging in low mag mode can then be used to image several areas. Measurements taken perpendicular to the habit plane is then used to determine this short width of the subgrains. The martensite lath consist of the plate-like structure. Depending on the orientation of the lath, the 2D projected surface could either measure the flat section of the plate structure leading to an overestimation of the short width. In the TEM the specimen can be tilted to view the lath edge on and this would yield more accurate measurements.

Further work will include the use of TKD and high-resolution EBSD to provide the necessary spatial and angular resolution needed to resolve the subgrain dislocation structure. Also more EBSD post-processing will be performed on the already acquired EBSD maps in order to investigate other components such as the texture within the different weldment regions.

CHAPTER 6

EVALUATION OF DISLOCATIONS

6.1 INTRODUCTION

The dislocation density in the bulk of the X20 steel weldments is determined in this chapter. Background on previous dislocation density studies of 9-12% Cr ferritic steels is provided. This is followed by an explanation of the experimental procedures and finally with the presentation and discussion of the results obtained outlining the advantages and disadvantages of each method.

6.2 BACKGROUND

Dislocations are introduced into the microstructure through the martensitic transformation to accommodate the lattice misfit between austenite and martensite phases during cooling (Pesicka, Aghajani *et al.* 2010). The dislocation structure is composed of a subgrain structure (boundary dislocations that make up small angle grain boundaries as a result of the rearrangement of the dislocations during the tempering treatment) and the free dislocations within the subgrains (laths and small-angle subgrains). These free dislocations act as obstacles to further plastic deformation and hence they are another microstructural contribution to creep strength. The free dislocation density ρ_f in the matrix is the important parameter to measure since it contributes to the creep strength through Dislocation Hardening (DH) as described by equation 2.7.

The study of foils in the TEM to determine dislocation density is a well established technique, especially when large numbers of dislocations are to be studied (Baker 2001). Numerous TEM studies have been performed on tempered martensite 9-12% Cr ferritic steels in order to determine the free dislocation density (Eggeler, Nilsvang *et al.* 1987; Ennis, Zielinska-Lipiec *et al.* 2001).

The study of dislocation density in tempered martensite ferritic steels using the TEM is made difficult by several factors (Pesicka, Kuzel *et al.* 2003):

i. Due to the magnetic nature of the specimen, the astigmatism of the objective lens needs to be re-adjusted for each tilt position.
ii. Diffuse Kikuchi line DPs are obtained as a result of the fact that high dislocation densities are associated with internal stresses. Consequently, it is difficult to tilt the specimen to two beam conditions (see Chapter 6).
iii. The two beam condition must be adjusted for each individual subgrain and hence dislocation density can only be evaluated from small regions in a single TEM micrograph.
iv. The effect of sample preparation on the measured dislocation density. Ion-beam damage due to ion-milling during the thin foil preparation might introduce artefacts. In addition, the loss of dislocations through surface relaxation needs to be considered as well (Hirsch, Howie *et al.* 1965).

Pesicka, Kuzel *et al.* (2003) studied the evolution of dislocation density in X20 and P91 steels during heat treatment and creep using TEM and XRD as complementary methods. They found that with the TEM one can identify and interpret heterogeneous microstructures and it is well-suited to measure lower dislocation densities. On the contrary, XRD becomes less reliable for lower dislocations densities since line broadening is not as pronounced, but XRD does yield average values that represents a much larger specimen volume than that from the TEM. The TEM results only suffer from insufficient statistics. Since the TEM and XRD results corresponded, they concluded that the XRD line profiles in tempered martensite ferritic steels can be fully accounted for on the basis of only free dislocations and not boundary dislocations. The free dislocations represent long range stress fields that are required to rationalise the XRD line profile broadening. Another advantage of XRD is that it does not encounter the problems associated with the TEM as discussed above.

Previous studies have shown that the thickness of the TEM specimen is crucial for dislocation studies in tempered martensite ferritic steels (Pesicka, Kuzel *et al.* 2003; Aghajani Bazazi 2009; Pesicka, Aghajani *et al.* 2010). Foil thicknesses of the order 200 ± 30 nm provided good results. The conventional TEM thin-foil thickness for good contrast in BF- and DF- TEM images is approximately 100 nm or less. These thinner foils were often bent and associated with high internal stresses. In addition, due to smaller foil volumes, poor sampling resulted in low counting statistics. In the case of

thicker foils, several diffraction contrast mechanisms operate in conventional TEM which result in insufficient contrast between the dislocations and the surrounding matrix.

Pesicka, Aghajani *et al.* (2010) overcame this problem by doing dislocation studies on X20 steel using HAADF-STEM. It has been shown previously that the conventional TEM invisibility criteria such as $\boldsymbol{g} \cdot \boldsymbol{b} = 0$ is valid for STEM imaging. In addition, it can be applied to thicker specimens due to the fact that bend contours and auxiliary contrast effects can be suppressed while retaining defect contrast (Phillips, Brandes *et al.* 2011). Consequently, the dislocation substructure can be imaged with much higher quality using STEM, i.e. very good dislocation contrast, with large fields of view. In each of the above mentioned studies the dislocation densities were determined using the linear intersection method (Ham 1961; Klaar, Schwaab *et al.* 1992; Martin, Muhle *et al.* 1995) where a grid of horizontal and vertical lines are drawn and the intersections with dislocation lines counted.

Currently it is accepted that only dislocations with Burgers vector $\boldsymbol{b} = \frac{\boldsymbol{a_0}}{\boldsymbol{2}}$<111> are found in significant quantities in ferrite (α-iron), provided there are no dislocation networks present (Baker 2001). By evoking the invisibility criterion the difficulty of measuring high dislocation densities is alleviated, since the number of dislocations observed is reduced. Thus, if a diffracting vector $\boldsymbol{g}_{hkl}$ perpendicular to $\boldsymbol{b}$ is chosen, then $\boldsymbol{g} \cdot \boldsymbol{b} = 0$ and then the invisibility criterion is satisfied. However, to use this technique and to ensure that there is no underestimation of the number of dislocations, it must be known what proportion of dislocations are visible for a specific diffracting vector $\boldsymbol{g}_{hkl}$. The fraction of visible dislocations with Burgers vector $\boldsymbol{b} = \frac{\boldsymbol{1}}{\boldsymbol{2}}$<111> under different two-beam operating conditions for bcc structures such as ferrite is provided in Table 6.1.

The diffraction vector $\boldsymbol{g}_{hkl}$ = 110, or similarly 220, is recommended since only half the dislocations are visible (Table 6.1) (Ennis, Zielinska-Lipiec *et al.* 2001; Pesicka, Kuzel *et al.* 2003; Aghajani Bazazi 2009; Pesicka, Aghajani *et al*. 2010).

Table 6.1: *Fraction of visible dislocations V_b with Burgers vector $\boldsymbol{b} = \frac{1}{2}$<111> under different two-beam operating conditions for bcc structures. (Baker 2001)*

$\boldsymbol{g}$	***110***	***200***	***211***
$\boldsymbol{b}$	$\boldsymbol{g \cdot b}$	$\boldsymbol{g \cdot b}$	$\boldsymbol{g \cdot b}$
$\frac{1}{2}[\bar{1}11]\boldsymbol{i}$	0	-1	0
$\frac{1}{2}[1\bar{1}1]$	0	1	1
$\frac{1}{2}[11\bar{1}]$	1	1	1
$\frac{1}{2}[111]$	1	1	2
$\boldsymbol{V_b}$	0.5	1	0.75

6.3 METHODOLOGY

The aim of this part of the study was to develop a quantitative technique to determine the density of free dislocations in the bulk region of the new and creep aged X20 weldments. This dislocation density was determined using TEM and XRD. The assumptions and methodology is explained for each method. The results of the TEM study were mainly qualitative and was supplemented with more representative sampling through the XRD measurements.

6.3.1 Transmission Electron Microscopy

In this study a similar procedure to Aghajani (2009) and Pesicka, Aghajani *et al.* (2010) was followed to measure the dislocation density using the TEM. TEM/STEM dislocation characterisation was performed on ±200 nm thick FIB-SEM specimens and twin-jet electropolished thin-foils prepared from new and damaged bulk X20 steel. The twin-jet electropolising sample preparation method (Chapter 3) yielded specimens with thin and large areas available for analysis. However, the magnetic interference of the specimen with the electromagnetic lenses of the microscope makes it difficult to keep the microscope aligned, which is necessary to obtain high quality images. The specimens prepared with the FIB-SEM yielded ±5 x 5 µm specimens with uniform thickness. These specimens do not suffer from the magnetic interference as they are too small to have a measurable effect. However, Ga^+ implantation damage was

evident when investigating the samples in the two beam condition. The area available for analysis is quite small, which makes representative sampling a problem as with the precipitate analysis.

Figure 6.1 shows a flow chart of the various steps in the determination of the dislocation density using the TEM. A particular subgrain in the specimen is selected and orientated onto a zone-axis containing the 110 diffraction spots. For reference of the electron beam direction relative to the crystal, the zone-axis is recorded. The subgrain is then orientated such that only one diffraction plane is diffracted strongly. In order to identify the direction of the diffracting planes and the sample thickness, respectively, the two-beam SAED pattern and the CBED pattern are recorded. Imaging of the orientated subgrain is done using BF-TEM and BF-STEM. A linear intercept method is then applied to determine the dislocation density.

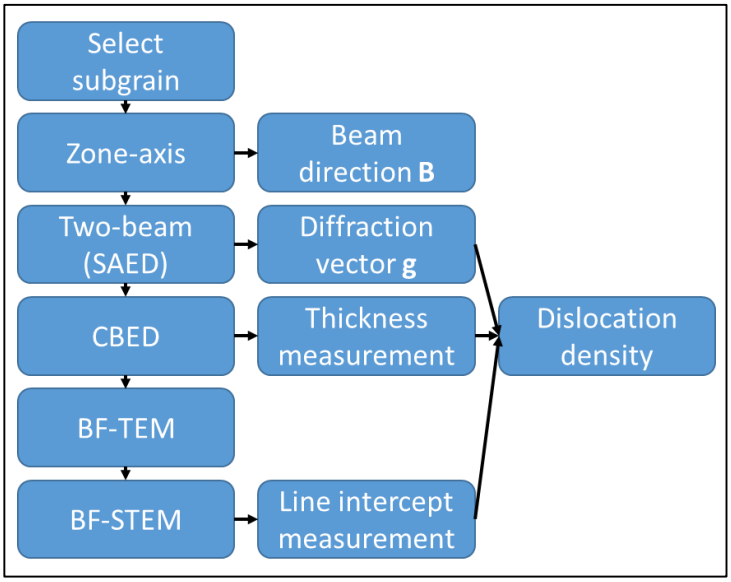

Figure 6.1: *Dislocation density measurement using TEM*

6.3.2 Thickness Measurement

A CBED pattern was acquired to determine the thin-foil thickness. According to Ennis, Zielinska-Lipiec *et al.* (2001) the CBED method gives the best accuracy for thickness measurement. However, it is dependent on the measuring conditions and in some instances the quality of the CBED images are insufficient for thickness measurements. In this study, it was ensured that each acquired CBED pattern is of sufficient quality.

The thickness at each subgrain was then determined using the graphical method as described in Williams and Carter (2009) and summarised in Chapter 3.

After the acquisition of the SAED and CBED patterns, a switch was made to the STEM function integrated into the PC control system. A Camera Length (CL) of 20 cm was used to ensure that diffraction information was captured on the ADF detector. The ADF images however had a low signal-to-noise ratio and complementary BF-STEM images were taken instead. It was observed within these BF-STEM images that all the low angle diffraction information is collected with a high signal-to-noise ratio. Images of 512 x 512 pixels at 120kx magnification were taken for quantification of the dislocation density. Images of a least 10 subgrains are recommended for representative dislocation density measurements (Ennis, Zielinska-Lipiec *et al.* 2001). However, due to sample quality and time constraints smaller areas were investigated in order to demonstrate this technique.

6.3.3 Dislocation Density Measurement

The mean dislocation densities was measured using the linear intercept method based on similar principles as the one used in EBSD. A grid of $L_h$horizontal and L_v vertical reference lines were drawn that intersect the dislocations n_h and n_v times in the horizontal and vertical directions respectively. The grid was drawn such that it spanned the entire subgrain. The free dislocation density ρ_f was then calculated using the following equation (Pesicka, Aghajani *et al.* 2010):

$$\rho_f = \frac{1}{t}\left(\frac{\sum n_h}{\sum L_h} + \frac{\sum n_v}{\sum L_v}\right) \tag{6.1}$$

where t is the thin foil thickness as determined using the CBED method. The DH stress value was then evaluated using equation 2.7 and parameters defined in Table 2.5.

Manual measurements of dislocation densities are very time-consuming. In order to automate this process, imaging analysis software MIPAR™ (Sosa, Huber *et al.* 2014) was used to threshold the dislocations and count the dislocations via the linear intercept method.

6.4 RESULTS AND DISCUSSION

6.4.1 Transmission Electron Microscopy

TEM can be used to visualise dislocations in the material directly using diffraction contrast. In order to investigate the dislocations in a systematic manner, the crystal needs to be orientated in a very specific way relative to the incoming electron beam. The methodology described in the section above requires that in order to limit the dislocation density, only one set of {110} planes needs to be viewed edge on. In this crystal orientation only 50% of the total number of dislocations will be visible (Table 6.1).

The first step involves the orientation of the selected subgrain onto the zone-axis containing the 110 diffraction vector. Figure 6.2(a) shows the **B** = [111] zone-axis pattern of the selected ferrite subgrain for the new bulk X20 material. A SAED pattern is recorded for reference. The subgrain is then orientated in order to only excite one set of diffracting planes with **g** = 110 indicated with a yellow arrow in Figure 6.2(b). As before, the SAED pattern is recorded for reference. The beam is then converged onto the sample to obtain a CBED pattern (Figure 6.2(c)) that is used to determine the thickness of the TEM foil at the particular ferrite subgrain. The BF-TEM image (Figure 6.2(d)) is recorded for reference with the diffracting plane direction indicated with the yellow arrow.

The diffraction contrast seen in the BF image is due to dislocations, thickness variations, overlapping grain boundaries (fringes) and precipitates. To increase the sampled volume, thicker regions of the specimen were investigated. Dynamical diffraction effects in these thick regions make it difficult to get good contrast between the dislocation core and the surrounding matrix material. In order to overcome this limitation BF-STEM imaging was used to image the dislocations. This method yielded much improved contrast between the dislocations and surrounding subgrains without the dynamical scattering effects. Figure 6.3 shows the composite BF-STEM image of the subgrain selected in Figure 6.2.

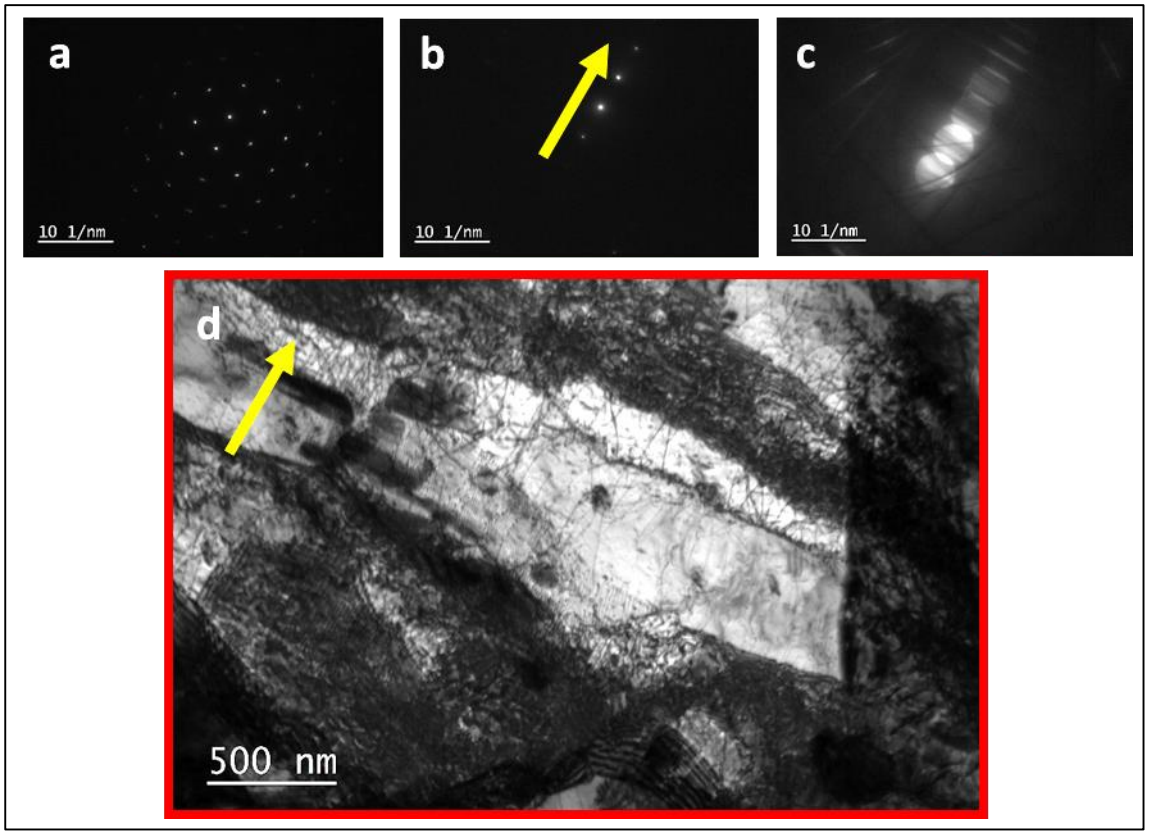

Figure 6.2: *(a) SAED zone-axis pattern with* ***B*** *= [111], (b) Two-beam SAED pattern with* ***g*** *= 110, (c) CBED pattern with* ***g*** *= 110, (d) BF image with* ***B*** *= [111]* ***g*** *= 110 of a subgrain in new bulk X20 material.*

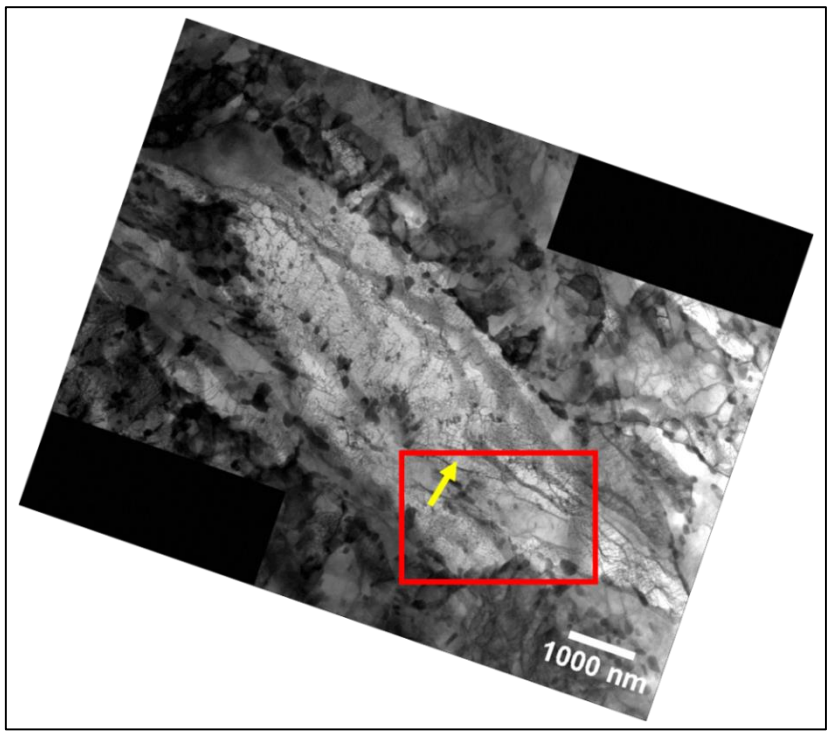

Figure 6.3: *Composite BF-STEM image of subgrain in Figure 6.2, with the red outline indicating the position where the BF-TEM image was recorded.*

This procedure of orientating the crystal, recording the SAED, CBED, BF-TEM and BF-STEM images is repeated for several subgrains in the steel. Figure 6.4 shows the high magnification BF-STEM images obtained from the new bulk X20 steel material. A high density of intersecting dislocations is observed within the subgrains. Improved contrast between the dislocation cores and the surrounding subgrain is obtained when compared to the BF-TEM images for the same diffraction conditions.

The dislocation density was determined using the 2D linear intercept method described in the section above. For each image a set of horizontal and vertical lines were drawn and the number of intercepts between the dislocation and the grid were counted. This was then used in combination with the thickness measurement to obtain a dislocation density for the material.

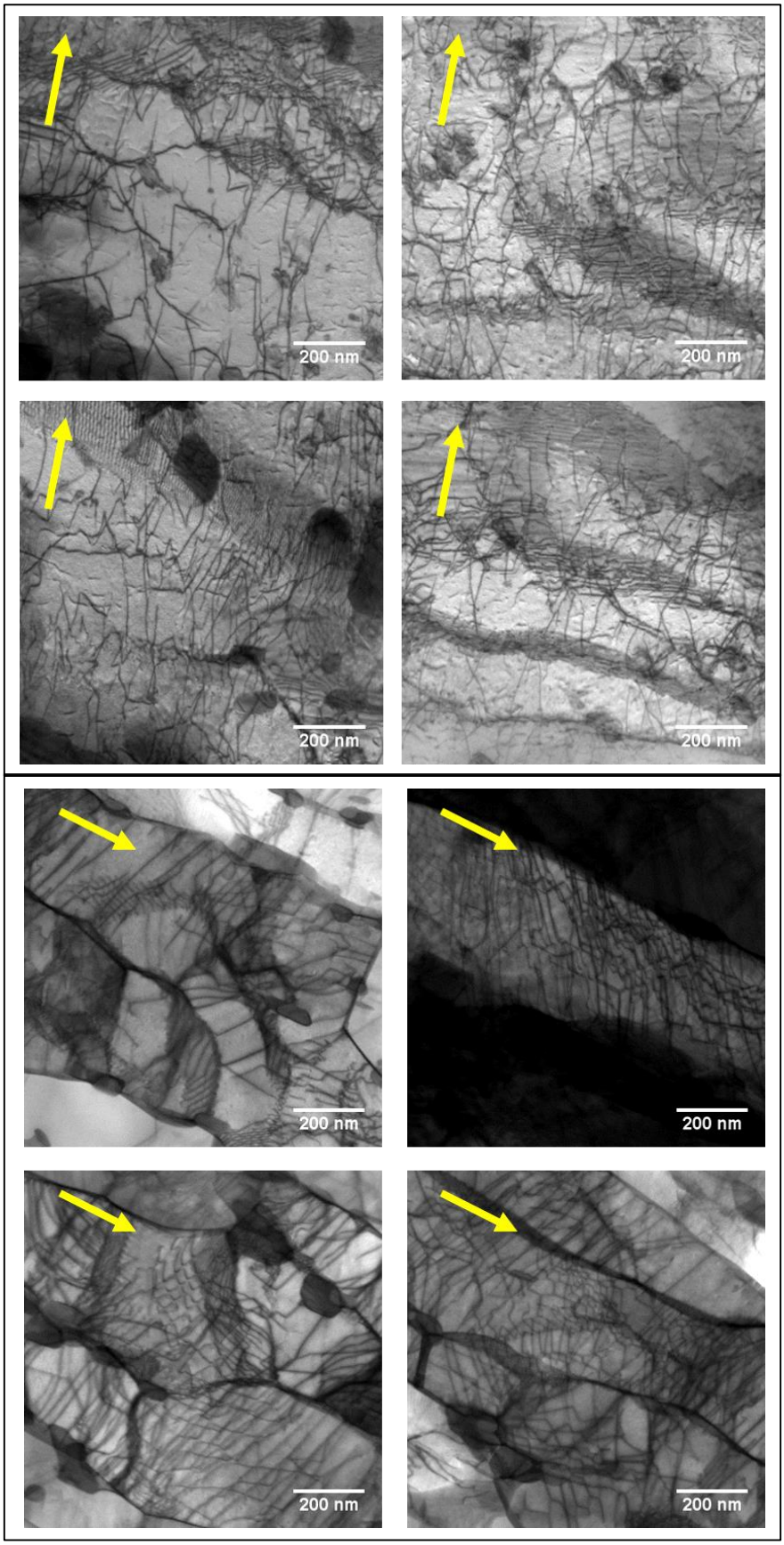

Figure 6.4: *BF-STEM images of dislocations in new bulk X20 material (**B** = [111] **g** = 110).*

This method of determining the dislocation density was also applied to the damaged bulk X20 material. Figure 6.5(a) shows the recorded **B** = [111] zone-axis SAED pattern used to orientate the subgrain relative to the electron beam. Figure 6.5(b) shows the two-beam SAED with **g** = 110 to view one set of crystallographic planes edge-on to limit the dislocation contrast. Figure 6.5(c) shows the CBED pattern used to determine the thickness of the selected subgrain. Figure 6.5(d) shows the BF-TEM image of the selected area of the subgrain. Numerous contrast generating mechanisms result in a complicated image. It is difficult to obtain reliable dislocation density measurements from this image. Therefore, BF-STEM images were recorded to overcome this limitation due to dynamical diffraction scattering. Figure 6.6 shows the composite BF-STEM image of the same area as in Figure 6.5, with the red outline indicating the BF-TEM area. It can be seen that the dislocation core and the surrounding matrix can be easily distinguished, which makes quantification of the dislocation densities much easier from the BF-STEM images.

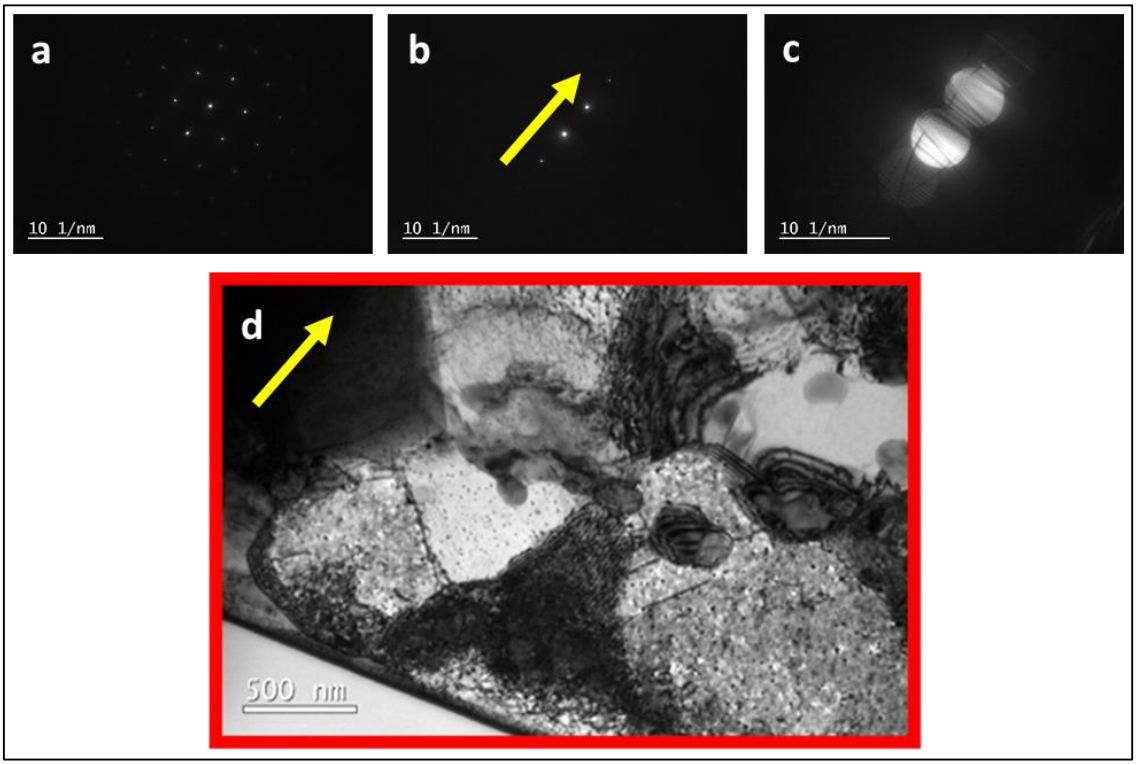

Figure 6.5: *(a) SAED zone-axis pattern with **B** = [111], (b) Two-beam SAED pattern with **g** = 110, (c) CBED pattern with **g** = 110, (d) BF-TEM image with **B** = [111] **g** = 110 of a subgrain in the damaged bulk X20 material.*

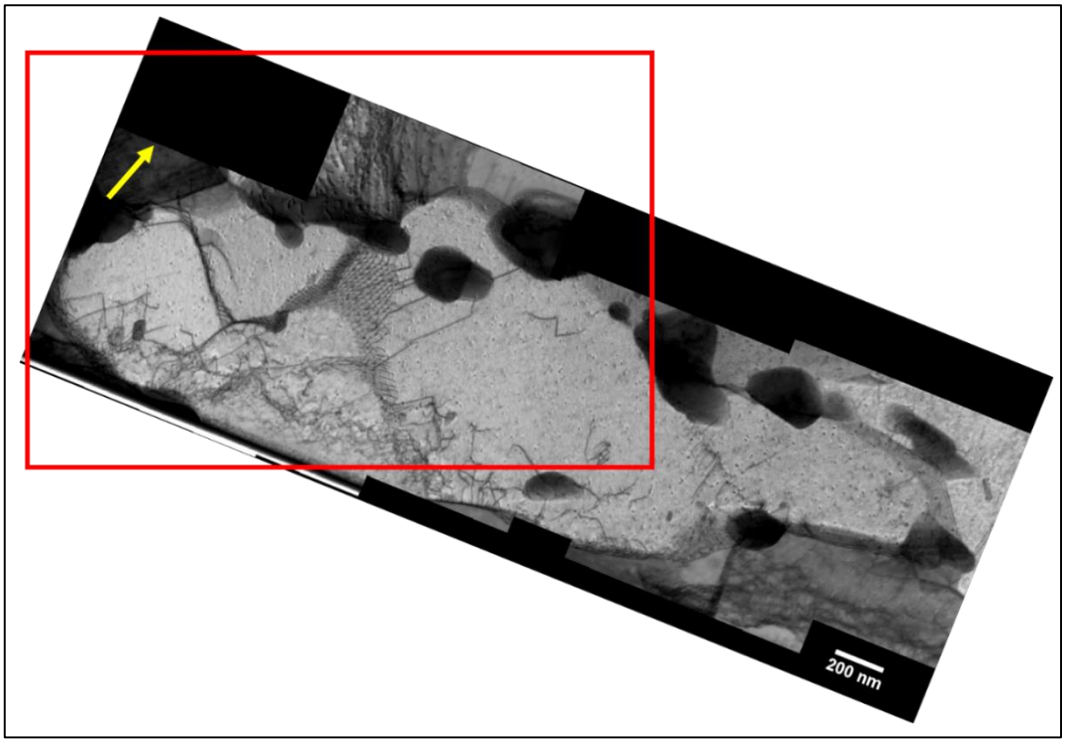

Figure 6.6: *Composite BF-STEM image of subgrain in Figure 6.5, with the red outline indicating the position where the BF-TEM image was recorded.*

The procedure was repeated for several sub-grains of the steel, by imaging the sub-grains of the steel in the two-beam diffraction condition and recording high magnification BF-STEM images (Figures 6.7 and 6.8). As before, the dislocation density was determined using the 2D linear intercept method.

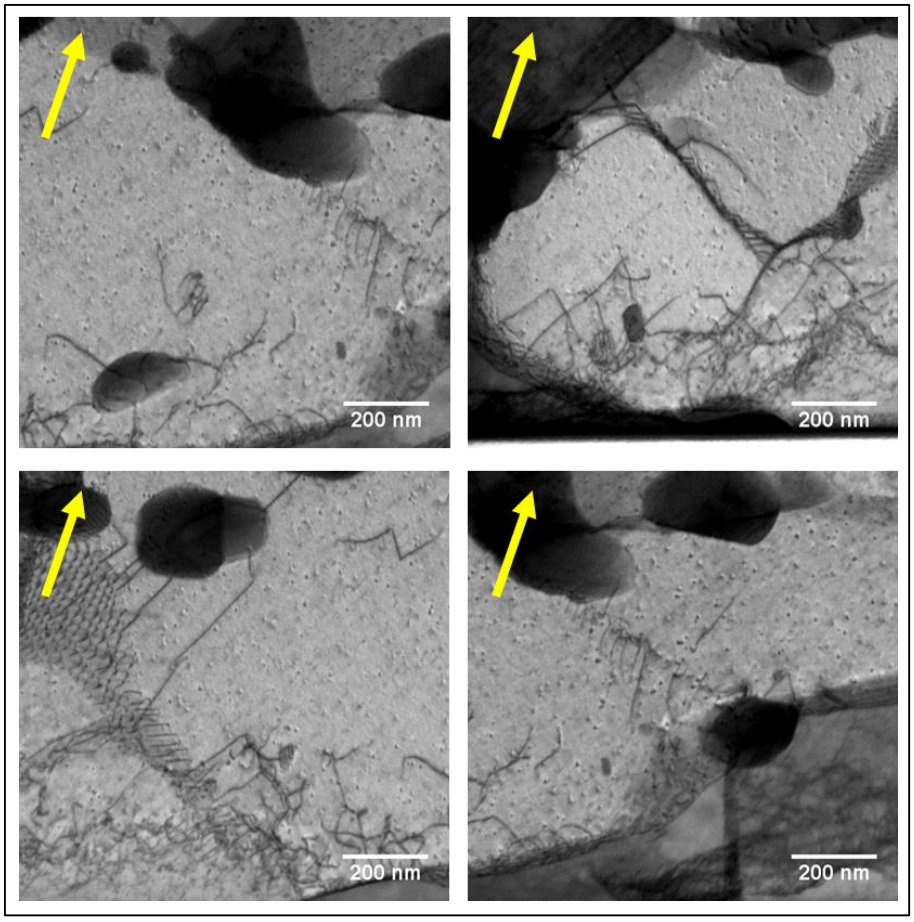

Figure 6.7: *BF-STEM images of dislocations in creep aged bulk X20 material (**B** = [111] **g** = 110) from the subgrain in Figure 6.6.*

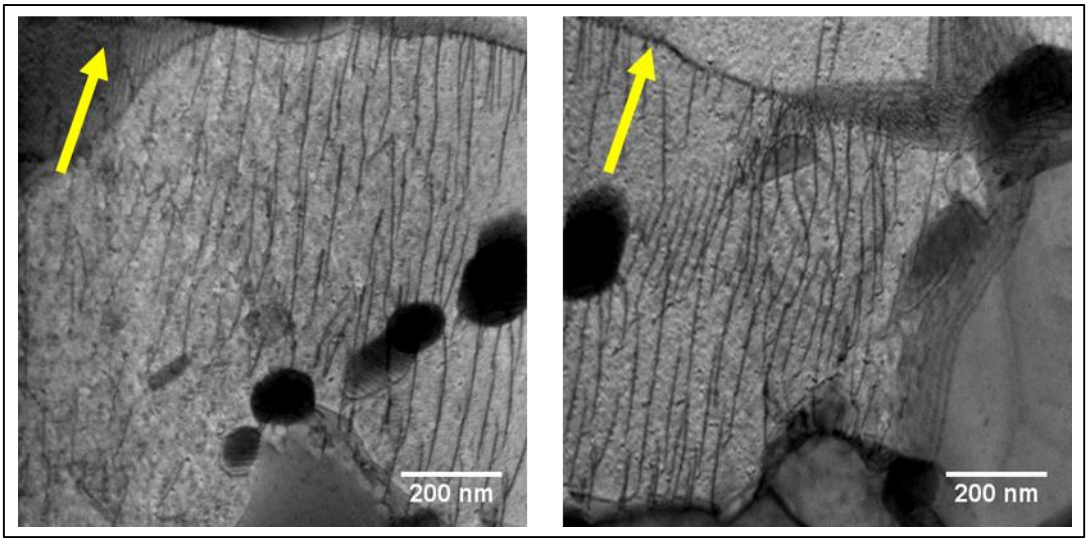

Figure 6.8: *BF-STEM images of dislocations in creep aged bulk X20 material (**B** = [100] **g** = 110).*

Limited number of areas for each specimen were investigated in this study. It is quite a time consuming exercise to carefully control the orientation of the subgrain relative to the electron beam in order to keep the diffraction conditions the same. Slight misorientations within the subgrain is unavoidable and this will have an effect on the accurate diffraction conditions for image contrast. The magnetic contribution from the 3 mm twin-jet electropolished specimen is substantial and this results in image quality degradation. In addition to controlling the orientation of the sample, for each region of interest the microscope has to be aligned for objective and condenser stigmation as well as the coma-centre, making this a tedious procedure.

The dislocation densities for the creep aged bulk X20 steel was less than that of the new bulk X20 steel based on the limited number of areas that were investigated. It is evident that the new X20 material has several intersecting dislocation tangles (Figure 6.4). Quantification was done on the limited number of areas to get an indication of the dislocation density, with the knowledge that the sample volume in this study was not sufficient to determine the free dislocation density with any degree of confidence.

The dislocation densities were measured using the image analysis software MIPAR^{TM}. The first image analysis step is to remove the precipitates and the SGBs from the image. Adaptive thresholding is then used to isolate the dislocations. The specimen had several contrast features due to ion-beam damage or astigmatism, which was eliminated by removing features smaller than 1 x 10^{-5} μm^2 in size. Subsequently, the dislocation density was measured by drawing 100 vertical and 100 horizontal lines through the image and counting the number of intercepts.

Figure 6.9 shows a BF-STEM image of the dislocation in the new X20 steel with the corresponding threshold image on which the dislocation density measurements were done. Table 6.2 contains a summary of the measured free dislocation densities and corresponding DH stress values. As expected, there is a range of thickness values for the electropolished thin-foil specimen prepared from the new bulk X20 steel and a mean thickness value with slight deviation for the FIB-SEM specimen prepared from the damaged bulk X20 steel. The measured free dislocation density ((5.04 ± 0.28) x 10^{14} m^{-2}) falls within the literature range of 1 to 10^{14} m^{-2} for 9-12% Cr ferritic steels after tempering (Chapter 2). Also, the measured dislocation density for the new bulk X20 steel was nearly double that of the creep aged bulk X20 steel, which corresponds with

the known annealing of dislocations during creep exposure (Chapter 2). Hence, there is a decrease in DH stress for the damaged material. More sampling is required in order to increase confidence in these results.

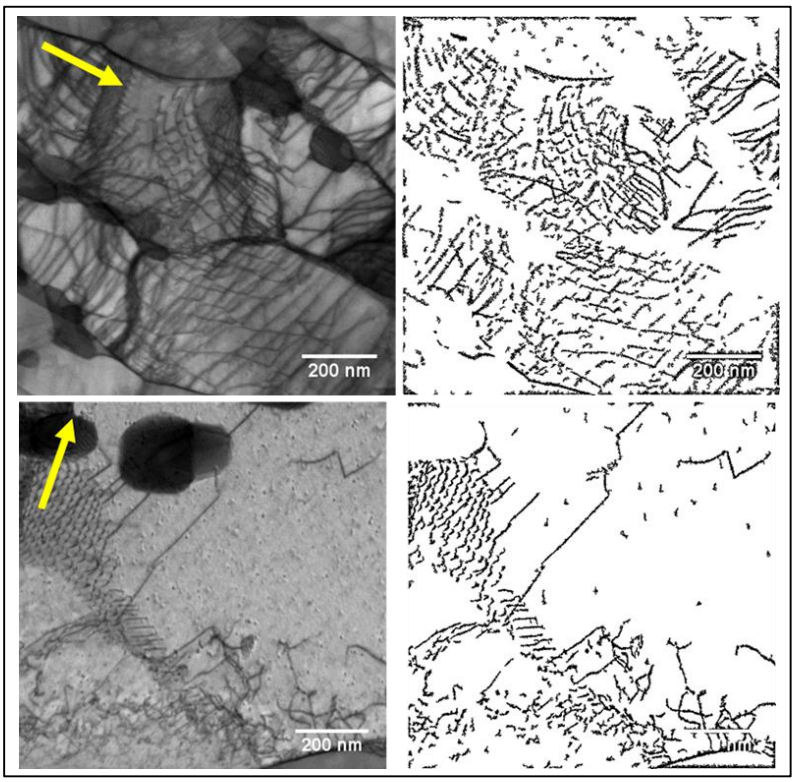

Figure 6.9: *BF-STEM image of dislocations (left) in the new X20 steel and the associated threshold image (right) isolating the dislocations for measurement.* ***B*** *= [111]* ***g*** *= 110*

Table 6.2: *Dislocation densities determined from BF-STEM images.*

	New bulk X20 material	***Damaged bulk X20 material***
Number of images	22	7
Σ # Intercepts / total length (m^{-1})	(5.04 ± 0.28) x 10^7	(2.21 ± 0.51) x 10^7
Thickness (nm)	170 – 230	186 ± 35
Free dislocation density ρ_f (m^{-2})	(5.04 ± 0.28) x 10^{14}	(2.38 ± 0.50) x 10^{14}
DH stress σ_ρ(MPa)	547 ± 129	376 ± 172

6.4.2 X-Ray Diffraction

The TEM allows for the direct visualisation of the dislocations in the material. This technique, however, is only applicable to the relatively small areas that can be investigated at a time. Many such observations are required to get a reliable measurement of the dislocation density. Subsequently, a bulk technique that can complement the TEM analysis is needed to sample a larger volume. XRD is a technique that can sample relatively large areas (10 x 10 mm^2) areas to a depth of approximately 50 µm at a time.

As with the crystallite size component, the micro-strain component was extracted with Rietveld refinement as described in Chapter 3 (Section 3.7.3). The results of micro-strain extraction using a Gaussian fit is shown in Table 6.3. This shows that the micro-strain is indeed higher for the new bulk X20 steel compared to the bulk creep damaged steel. Hence, this is an indication of the decrease in dislocation density due the fact that during creep there is an annealing of dislocations (Chapter 2). As discussed in

Chapter 5, the lower strain is expected for the damaged bulk X20 material since the FWHM (Table 5.5) is smaller.

Table 6.3: *FWHM and refined strain values for dislocation density.*

	New X20	***Damaged X20***
StrainG	0.1439 ± 0.0005	0.1159 ± 0.0009
ε_0 from strain	0.0360 ± 0.0009	0.02900 ± 0.0012

This method gives the total micro-strain as a % that contributes to the peak broadening. However, the conversion between the strain% to a total dislocation density is not straight forward and thus this technique only gives a relative measure of the dislocation density. XRD provides an indication of the total dislocation density since it is a bulk technique. Many crystalline defects cause line broadening to behave in a similar way, therefore it is difficult to discern the type of defect dominating a particular sample such as a dislocation. However, for tempered martensite ferritic steels it has been found that the XRD line profiles can fully account for only the free dislocations and not boundary dislocations (Pesicka, Kuzel *et al.* 2003). It is possible to determine the dislocation density using either the Williamson-Hall or Warren-Averbach methods. These methods are based on the breadths or on the Fourier coefficients of the diffraction profiles. Ungár (2001) provides a good description on both the classical and modified versions of these procedures. Nevertheless, it is difficult to use XRD to determine the free dislocation density required to determine the creep strength contribution.

Future work would include extracting the free dislocation density from the XRD profile analysis results using the mentioned methods. In conclusion, the XRD results from Chapter 5 and this chapter is consistent with long term annealing of dislocations and growth of subgrains during creep exposure.

6.5 SUMMARY

TEM was successfully used to measure the dislocation density in the new and damaged bulk X20 materials. Limited areas were investigated for each specimen due to sample quality and time-constraints. Hence, no statistically reliable values of dislocation densities could be determined. Nevertheless, these areas were enough to show the differences in the dislocation density between the new ($(5.04 \pm 0.28) \times 10^{14}$ m^{-2}) and damaged bulk X20 ($(2.38 \pm 0.50) \times 10^{14}$ m^{-2}) materials. The FIB sample preparation showed significant ion-induced damage compared to the specimen prepared using twin-jet electropolishing. Additional ion-milling using low energy Ar-ions could reduce the damage created by Ga-ions in the FIB-SEM.

The best imaging technique for the visualisation of the dislocations was BF-STEM. BF-TEM images contained numerous other contrast generating mechanisms in addition to diffraction contrast from the dislocations. Previous studies focused on the use of HAADF-STEM, but the signal-to-noise ratio is very low, especially at long camera lengths. The BF-STEM detector collects all the electrons containing the diffraction information. Ion-beam induced damage was also less visible in the BF-STEM images.

For a number of reasons the procedure to collect the experimental data is quite time consuming. Firstly, magnetic interference from the magnetic specimen degrades the image quality. Alignment of the microscope needs to be performed on each area. In addition, the two-beam diffraction conditions are quite challenging to control since small angular deviations within the same grain can occur. The diffraction contrast is a strong function of the diffraction conditions. Accurate thickness measurements from the relatively thicker (±200 nm) foils are also quite difficult due to the low quality of the recorded CBED patterns. Thicker specimens contain fringes spaced quite closely, moreover the inelastic scattering results in a high background intensity. The dislocations in the specimen further degrades the quality of the CBED pattern.

The use of XRD was illustrated for the measurement of the micro-strain, which was considered to be an indication of the dislocation density. The measured FWHM of the XRD peak for the new material was larger compared to that of the damaged material. Rietveld refinement performed on the XRD patterns deconvoluted the effects of the

instrument, crystallite size and micro-strain on the FWHM. The extracted micro-strain contribution for the new material (3.6%) was higher than that of the damaged material (2.9%). This result needs to be interpreted with care, as the various assumptions of this method could have a large effect on the results (Balzar, Audebrand *et al.* 2004). Furthermore, there is no direct way to convert the measured micro-strain value into a dislocation density value. This method could be used as a quick qualitative technique to evaluate the dislocation density relative to a standard material.

In conclusion, the advantages of FIB-SEM sample preparation (site specific, control over the thickness and low magnetic interference) can be used to prepare specimens from the material in which the dislocations are to be analysed. These specimens can be taken from different positions of the bulk material in order to avoid localised dislocation density measurements. Ion-beam damage due to the Ga-ions could be removed with low energy Ag-ion milling. Alternatively, the BF-STEM imaging provides improved contrast for the dislocations and less visible ion-beam damage compared to the other imaging methods such as HAADF-STEM and BF-TEM.

CHAPTER 7

CONCLUSIONS

The identification of the different microstructural regions within the weldments formed the first part of the study. Vickers hardness indents were made across the weldments and the hardness of the indents was then used as initial identification of each weldment region. Thereafter, the results were correlated and confirmed by acquiring EBSD orientation maps at the indents that act as markers of the regions, and observing that the grain and subgrain sizes correspond to that known from literature for the specific region. After identification, site specific specimens of each region were prepared using the FIB-SEM. Hence, it is recommended that the different weldment regions be identified by combining Vickers MHT and EBSD.

The second part of the study (Chapter 4) aimed to use EFTEM to determine the Cr-enriched $M_{23}C_6$ and V-enriched MX precipitate parameters. A combination of thresholding (for well separated precipitates) and manual outlining (for overlapping precipitates) was used to analyse the elemental maps. To account for sectioning of the $M_{23}C_6$ precipitates in the thin-foils, corrections were made and the Orowan stress for PH was calculated for each specimen. By combining the EFTEM maps of each weldment region, it was possible to observe differences in the size and distributions of the precipitates within the regions.

Both bulk replication and FIB-SEM was used to prepare the specimens for this analysis. Even though the FIB-SEM sample preparation technique had the advantage of site specific sampling required to remove thin sections from the different microstructural regions of the weldments, it is limited by the small sampling volume. Thus, the sampled volume might not be representative, especially when characterising large precipitates and inhomogeneous precipitate distributions, which was the case for the damaged X20 material. To overcome this limitation of using FIB-SEM, extraction replication was used to increase the sampling area and volume. However, extraction replicas have the problem of unknown sampling volume. By assuming that the Cr-enriched $M_{23}C_6$ precipitate phase fraction is independent of the sampling method, the phase fraction was determined from the FIB-SEM thin-foils and then used

to determine the extraction depth of the replica specimens. It was found that the precipitate size measurements were smaller for the extraction replica specimens than for the FIB-SEM specimens. This difference was ascribed to the difference in the bulk X20 material that the specimens were prepared from, possibly due to the PWHT performed on the weldment after welding. Therefore, it is important to ensure that the original bulk material is the same if both sampling methods are to be used for analysis. Another problem encountered with the extraction replica specimens was the extraction efficiency of the V-enriched MX precipitates. This leads to much lower measured number density values than for the FIB-SEM specimens.

EDS was performed on the extraction replica specimens in order to observe the chemical composition of the $M_{23}C_6$ precipitates. No observable changes occurred in the mean composition of the precipitates in the new and damaged bulk X20 material Mo-enriched Laves-phase was observed within the damaged bulk X20 material.

In summary, it was found that measurements on thin-foils are more accurate than bulk replication for measuring precipitate parameters despite the sectioning of the precipitates. FIB-SEM sample preparation provides the site specific analysis required for weldments. If bulk material is to be analysed, it is recommended to prepare a twin-jet electropolished specimen that overcomes the sampling volume issue of FIB-SEM specimens and the problem of unknown extraction depth of the extraction replica specimens. Extraction replicas are the better choice for the chemical analysis of precipitates since there is no iron matrix that can obscure the results.

The third part of the study (Chapter 5) entails the evaluation of the subgrains by measuring the short width of the elongated SGBs and then calculating the SBH stress value. EBSD was used as the main technique and was performed on the new and creep aged X20 weldments. The differences in the microstructural regions were easily identified by observing the grain and subgrain sizes within the EBSD maps.

The elongated subgrain size was measured using the LI and GR methods that are built-in functions of the EBSD post-processing software. The feasibility of each method to measure accurate subgrain size was investigated. Significant coarsening of the elongated subgrains during creep in the bulk region was shown by both the GR and LI methods, which leads to a decrease in the SBH stress. It was concluded that the LI

method seems to be more effective in measuring the subgrain size since its measured values that are closer in accordance with previous results than that obtained from the GR method. The GR method is dependent on the critical misorientation angle used to reconstruct the grains. It was shown with TKD that subgrains with a critical misorientation less than 5º are grouped into one grain, resulting in an over estimation of the subgrain size. In addition, assumptions are made with the GR method regarding the aspect ratio that influenced the results. The fact that the EBSD maps contain 2D projections of the 3D subgrains made it difficult to measure the exact short width of each subgrain within the map. If the 2D projected surface corresponds to the flat section of the martensite lath plate-like structure, then there is an overestimation of the short width. It was found that the step-size was a major limitation for the ability of EBSD to resolve the subgrains. It was demonstrated that TKD provides higher spatial resolution orientation maps, but at the expense of having a much smaller sampling area.

BF-STEM was performed on the twin-jet electropolished specimen prepared from the new bulk X20 material. The aim was to illustrate the use of the TEM as another technique to measure subgrain size. It was found that it is much more accurate in measuring the exact short width of the elongated subgrains since the specimen can be tilted such that the lath is viewed edge on. In this case the measurements are taken perpendicular to the habit plane and, subsequently, the projection issue encountered with EBSD is eliminated.

It was concluded that the best subgrain size measurements for bulk material is achieved in the TEM by performing either BF- or DF-STEM imaging in low mag mode on twin-jet electropolished specimens in order to analyse several areas. In the case of analysis of subgrains in weldments, it is recommended to use EBSD with the LI method since the subgrains in larger areas of each region can be analysed than would be possible with a FIB-SEM specimen in the TEM.

The final part of the study (Chapter 6) was focused on determining the free dislocation density in the bulk X20 material using the TEM. The analysis was performed on a ±200 nm FIB-SEM specimen prepared from the creep aged bulk X20 material and a twin-jet electropolished specimen prepared from the new bulk X20 material. Significant ion-induced damage was observed on the FIB-SEM specimen surface, which was not

visible for the twin-jet electropolished specimen. It was found that BF-STEM was a much better imaging technique for the visualisation of the dislocations than BF-TEM. It provided improved contrast for the dislocations and less visible ion-beam damage than compared to the other imaging methods such as HAADF-STEM and BF-TEM.

The main limitations of this analysis was that the experimental procedure was time consuming and accurate thickness measurements were obtained with difficulty due to the relatively thicker thin-foil specimens. The advantages that the FIB-SEM sample preparation technique have over twin-jet electropolishing (site specific analysis, control over thickness and low magnetic interference) alleviate these limitations. Thus, it is recommended for the best evaluation of dislocations that BF-STEM analyses are performed on FIB-SEM specimens. Future work will include the use of this approach on FIB-SEM specimens in order to obtain representative values of the free dislocation density.

XRD was used as a complimentary technique to EBSD and TEM to investigate subgrain size and dislocation density within the new and creep aged bulk X20 materials. The main limitation of XRD is that site-specific analysis cannot be performed as with EBSD and TEM. The micro-strain and crystallite size was extracted from the XRD patterns using Rietveld refinement. Much smaller crystallite sizes than the subgrain sizes measured using EBSD and TEM was obtained since it was the domain size and not the subgrain size that was determined. Only an indication of the dislocation density is provided by the micro-strain. As with EBSD and TEM, the XRD results showed annealing of dislocations and growth of subgrains during creep exposure. This was concluded from the smaller micro-strain and larger crystallite size in the damaged bulk X20 material compared to the new bulk X20 material.

The new and damaged bulk X20 material microstructural parameters determined in this study using the various quantitative techniques are summarised in Figure 7.1. These are the important parameters to determine the various creep strength contributions. By setting the result of the new material as one, a relative value of the damaged material result was then plotted. The actual values of the microstructural parameters and their 95% confidence levels are provided in Table 7.1. The mean precipitate diameter determined from both the extraction replica and FIB-SEM

specimens is reported. Since the LI method provided subgrain size closest to the literature, the mean subgrain sizes calculated using this method is given.

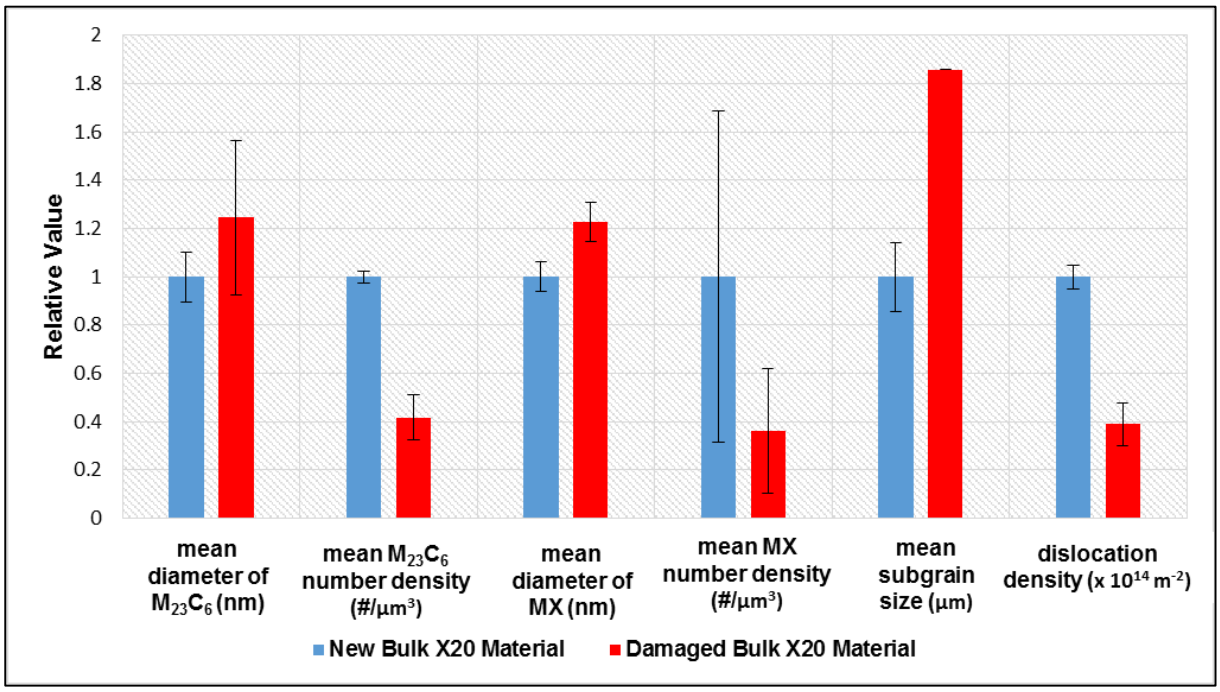

Figure 7.1: *Summary of results of quantitative measurements of new and damaged bulk X20 steel microstructural parameters. The 95% confidence levels of the values are shown by the error bars.*

Table 7.1: *Quantitative microstructural parameters for new and damaged (creep aged) bulk X20 steel.*

Microstructural Parameter	***New Bulk X20 Material***	***Damaged Bulk X20 Material***
Mean diameter of $M_{23}C_6$ (nm)	135 ± 14	168 ± 43
Mean $M_{23}C_6$ number density (#/μm³)	23.7 ± 0.6	9.9 ± 2.2
Mean diameter of MX (nm)	48.5 ± 3	59.5 ± 4
Mean MX number density (#/μm³)	33.4 ± 22.9	12.1 ± 8.6
Mean subgrain size (μm)	0.7 ± 0.1	1.3 ± 0.0
Dislocation density (x 10^{14} m^{-2})	2.84 ± 0.14	1.11 ± 0.25

The precipitate results were found to be consistent with the literature of $M_{23}C_6$ precipitate coarsening and MX precipitate dissolution during creep exposure with an accompanying drop in creep resistance. Coarser $M_{23}C_6$ precipitates were found in the damaged bulk X20 material compared to the new bulk X20 material. A lower number density of the MX precipitates in the damaged material indicated significant dissolution of these precipitates during creep exposure. Subsequently, a larger interparticle spacing and hence smaller Orowan stress value for both the $M_{23}C_6$ and MX precipitates was calculated for the damaged bulk X20 material. This leads to a decrease in creep strength. There are notable differences in the size and distribution of the $M_{23}C_6$ precipitates in the different microstructural regions of the weldments. On the other hand, the measured MX precipitate size and distributions did not show large variations between the different microstructural regions of the weldments. The ICHAZ/FGHAZ region had the largest $M_{23}C_6$ precipitates for both the new and damaged materials, of which the largest was observed in the damaged ICHAZ/FGHAZ. Consequently, the damaged ICHAZ/FGHAZ had the lowest calculated Orowan stress of 106 MPa compared to 138 MPa for the new ICHAZ/FGHAZ. It was concluded that this value, if correlated with experimental results, has the potential to be used in defining the weldability limits for Type IV cracking.

Both the GR and LI methods measured larger subgrain sizes, and hence lower SBH stress values, for the damaged bulk X20 material compared to the new bulk X20 material. This corresponds with the literature that subgrains coarsen during creep aging that results in a degradation of creep strength.

A decrease in free dislocation density is observed for the creep aged bulk X20 material. This is consistent with the known fact that there is annealing of dislocations during creep exposure. Due to the quality of the specimens and time-constraints, only a limited number of areas were investigated in order to determine the dislocation density. Hence, the measured dislocation densities and DH stress values are not representative of the entire specimen. Yet, the results from the analysis of these areas was sufficient to illustrate the differences in the dislocation density between the new and creep aged X20 steel. The measured dislocation density values were used to

determine the DH stress value, which was lower for the damaged material. This indicated once again a loss of creep strength.

The back-stress (inner-stress) can be calculated for the new and damaged bulk X20 material from PH, SBH and DH by adding the various values (Holzer 2010). The results are plotted in Figure 7.2. From this plot is possible to see which microstructural contribution is most significant. Even though it seems that DH has the greatest contribution, the results of dislocation analysis was not reliable as mentioned before. Still, it is seen that there is an overall loss in creep resistance for the damaged bulk X20 material when compared to the new bulk X20 material.

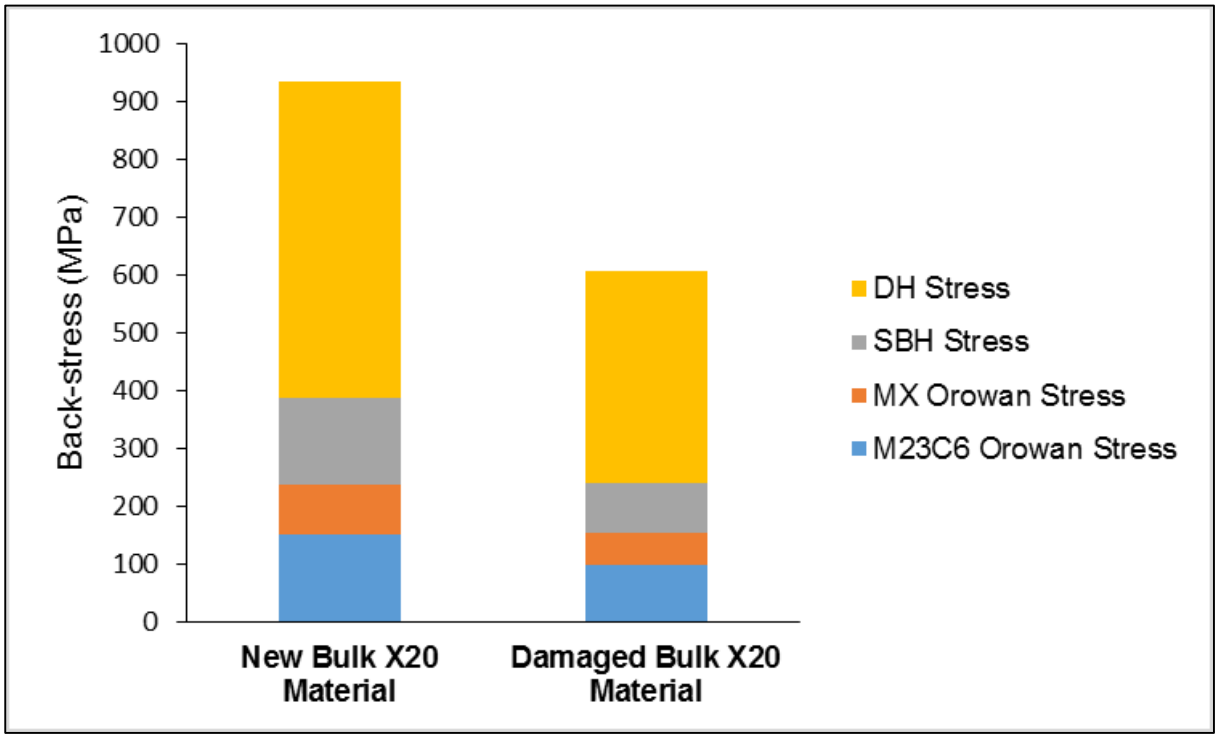

Figure 7.2: *Back-stress for the new and damaged bulk X20 material as a combination of the various creep strength contributions.*

The main issue with this study was sampling and therefore obtaining statistical reliable results. Nonetheless, the objectives of this study are met by the results acquired. Microstructural measuring techniques was developed and evaluated in order to determine the best procedures that need to be followed to evaluate the precipitates, subgrains and dislocations. The results from the application of these techniques demonstrated the differences in microstructure of new and creep aged X20 weldments

and contributes to a better understanding of the processing-structure-property relationships in creep exposed weldments. In addition, the problems associated with weldments as discussed in Chapter 1 were addressed in this study.

The implication of this study is that a microstructural based approach is possible for determining weldability limits and hence performing life assessment. It was already shown from the precipitate analysis that the Orowan stress value has the potential to be used to define weldability limits for Type IV cracking. To demonstrate the possible use of the microstructural approach, the back-stress value, which is determined from the microstructural parameters, is used as an indication of the remaining creep strength of the creep aged material. A cut-off value of the back-stress can then be identified for a specific material that then defines the limit of which welding is still permitted on the material. This cut-off value is determined by performing the microstructural measurements as done in this study on materials with varying creep damage, including materials that have already failed. The limit of each microstructural parameter (precipitate size and number density, subgrain size and dislocation density) can then be identified and used to calculate the cut-off back-stress value.

This is only a simple approach and the actual approach will be much more complex, especially for life assessment of weldments. The main limitations of the microstructural approach is the understanding of the true mechanisms that lead to Type IV cracking and experimental results. The extent of involvement of each microstructural contribution in the formation and propagation of Type IV cracks is not exactly known. Hence, the contribution of PH, SBH and DH to the back-stress may not be equal and their values may need to be weighted. A large number of creep aged specimens are required in order for sufficient experimental results to clearly define the cut-off value.

The future direction of this study is to overcome these limitations and use the employed measuring techniques to develop a microstructural based approach to quantify the amount of creep damage so that weldability limits and remaining life of power plant components can be determined. The procedures of the measuring techniques developed in this study are time-consuming and further work would include the automation of the microstructural measurements.

REFERENCES

Abe, F. (2008). Introduction. Creep-resistant steels. F. Abe, T. U. Kern and R. Viswanathan. Cambridge, England, Woodhead Publishing Ltd.**:** 3-14.

Abe, F. (2008). Strengthening mechanisms in steel for creep and creep rupture. Creep-resistant steels. F. Abe, T. U. Kern and R. Viswanathan. Cambridge, England, Woodhead Publishing Ltd.**:** 279-301.

Abe, F., T. U. Kern, et al. (2008). Creep-resistant steels. Cambridge, England, Woodhead Publishing Ltd.

Abramoff, M. D., P. J. Magalhaes, et al. (2004). "Image Processing with ImageJ." Biophotonics International **11**(7): 36-42.

Academia. (2013). "Experiment 3: Hardness Test." Retrieved 7/9/2015, from http://www.academia.edu/4075363/EXPERIMENT_3_HARDNESS_TEST.

Aghajani, A., C. Somsen, et al. (2009). "On the effect of long-term creep on the microstructure of a 12% chromium tempered martensite ferritic steel." Acta Materialia **57**(17): 5093-5106.

Aghajani Bazazi, A. (2009). Evolution of Microstructure during Long-term Creep of a Tempered Martensite Ferritic Steel Dr.-Ing. Dissertation, University of Bochum.

Albert, S. K., M. Matsui, et al. (2002). "Microstructural Investigations on Type IV Cracking in a High Cr Steel." ISIJ International **42**(12): 1497–1504.

Aracil, R. S. (2014). Investigation of heavily deformed and dual phase materials by means of Transmission Kikuchi Diffraction. MEng Master Thesis, Ghent University.

Armaki, H. G., R. P. Chen, et al. (2011). "Creep behavior and degradation of subgrain structures pinned by nanoscale precipitates in strength-enhanced 5 to 12% Cr ferritic steels." Metallurgical and Materials Transactions: A **42**(10): 3084-3094.

ASME (2008). 2007 ASME Boiler & Pressure Vessel Code, Section II - Materials (Includes Addenda for 2008), American Society of Mechanical Engineers.

ASTM (2010). Standard Practice for Determining Average Grain Size Using Electron Backscatter Diffraction (EBSD) in Fully Recrystallized Polycrystalline Materials, ASTM International. **E2627-10**.

ASTM (2011). Standard Test Method for Knoop and Vickers Hardness of Materials. Pennsylvania, USA, ASTM International. **E384-11:** 1-43.

Auerkari, P., J. Salonen, et al. (2013). "Creep damage and long term modeliing of an X20 steam line component." Engineering Failure Analysis **35**: 508-515.

Ayache, J., L. Beaunier, et al. (2010). Sample Preparation Handbook for Transmission Electron Microscopy: Techniques. New York, USA, Springer.

Baker, T. N. (2001). Quantitative Metallography using Transmission Electron Microscopy. Quantitative Microscopy of High Temperature Materials. A. Strang and J. Cawley. London, UK, IOM Communications Ltd. **5:** 161-190.

Baltusnikas, A., R. Levinskas, et al. (2008). "Analysis of Heat Resistant Steel State by Changes of Lattices Parameters of Carbides Phases." Materials Science **14**(3): 210-214.

Balzar, D., N. Audebrand, et al. (2004). "Size–strain line-broadening analysis of the ceria round-robin sample." Journal of Applied Crystallography **37**: 911-924.

Bavarian, B. (2014a, 26/8/2014). "Microindentation Hardness Testing." MSE 528 - Principles of Materials Engineering Retrieved 7/9/2015, from http://www.csun.edu/~bavarian/mse_528.htm.

Bavarian, B. (2014b, 26/8/2014). "MSE 528: Microhardness Hardness Measurements." MSE 528 - Principles of Materials Engineering Retrieved 7/9/2015, from http://www.csun.edu/~bavarian/mse_528.htm.

Bhadeshia, H. K. D. H. (2001). "Design of Ferritic Creep-Resistant Steels." ISIJ International **41**(6): 626–640

Bhadeshia, H. K. D. H. (2001). Worked examples in the Geometry of Crystals. London, UK, Institute of Materials.

Bhadeshia, H. K. D. H. (2002). Martensite in Steels. Crystallography. P. T. C. P. R. Group, Department of Materials Science & Metallurgy, University of Cambridge. **2015**.

Bhadeshia, H. K. D. H. and R. W. K. Honeycombe (2006). Steels: Microstructure and Properties. Oxford, UK, Elsevier Ltd.

Brydson, R. (2001). A Brief Review of Quantitative Aspects of Electron Energy Loss Spectroscopy and Imaging. Quantitative Microscopy of High Temperature Materials. A. Strang and J. Cawley. London, UK, IOM Communications Ltd. **5:** 277-306.

Buchmayr, B. (2005). "Characterisation of the creep behaviour of weldments by HAZ-simulation." ECCC Recommendations **3**(2): Appendix 2.

Cantoni, M. (2013). Scanning Transmission Electron Microscopy. MSE-603 Spring 2013, CiMe.

Cerjak, H. (2008). The Role of Welding in the Power Generation Industry. Houdremont Lecture: 61st IIW Annual Assembly. Graz, Austria**:** 17-27.

Cerjak, H., P. Hofer, et al. (1999). "The influence of microstructural aspects on the service behaviour of advanced power plant steels." ISIJ International **39**(9): 874-888.

Cerjak, H. and P. Mayr (2008). Creep strength of welded joints of ferritic steels. Creep-resistant steels. F. Abe, T. U. Kern and R. Viswanathan. Cambridge, England, Woodhead Publishing Ltd.**:** 472-503.

Champness, P. E. (1987). "Convergent beam electron diffraction." Mineralogical Magazine **51**: 33-48.

Cheary, R. W., A. A. Coelho, et al. (2004). " Fundamental Parameters Line Profile Fitting in Laboratory Diffractometers." Journal of Research of the National Institute of Standards and Technology **109**: 1-25.

Dimmler, G. (2003). Quantification of Creep Resistance and Creep Fracture Strength of 9-12%Cr Steels on Microstructural Basis PhD thesis, Graz University of Technology.

Dimmler, G., P. Weinert, et al. (2003). "Quantification of the Laves phase in advanced 9–12% Cr steels using a standard SEM." Materials Characterization **51**(5): 341-352.

Ducati, C. (2013). T2: Electron Microscopy Department of Materials Science and Metallurgy, University of Cambridge.

Easterling, K. (1992). Introduction to the Physical Metallurgy of Welding. London, England, Butterworth-Heinemann Ltd.

Egerton, R. F. (1996). Electron Energy Loss Spectroscopy in the Electron Microscope. New York, USA, Plenum Press.

Eggeler, G., N. Nilsvang, et al. (1987). "Microstructural changes in a 12% chromium steel during creep." Steel Research **58**(2): 97-103.

Engler, O. and V. Randle (2010). Introduction to Texture Analysis : Macrotexture, Microtexture, and Orientation Mapping. Florida, USA, Taylor & Francis.

Ennis, P. J., A. Zielinska-Lipiec, et al. (2001). The Influence of Heat Treatments on the Microstructural Parameters and Mechanical Properties of P92 Steel. Quantitative Microscopy of High Temperature Materials. A. Strang and J. Cawley. London, UK, IOM Communications Ltd. **5:** 191-206.

EPRI (2006). X20 CrMoV12-1 Steel Handbook. Palto Alto, CA, EPRI.

Erni, R. (2013). "EELS & EFTEM." Retrieved 14/10/2015, from https://microscopy.empa.ch.

Eskom (2014). HOW ELECTRICITY IS PRODUCED AT A COAL FIRED POWER STATION, Generation Communication. **CO 0002 Revision 9**.

FEI (2006). All You Wanted to Know about Electron Microscopy. F. E. Company.

Friel, J. J. (2003). X-Ray and Image Analysis in Electron Microscopy, Princeton-Gamma Tech Inc.

Fruhstorfer, B., V. Mohles, et al. (2002). "Quantitative characterization of second-phase particles by atomic force microscopy and scanning electron microscopy." Philosophical Magazine A **82**(13): 2575-2589.

Fujiyama, K., K. Mori, et al. (2009). "Creep-damage assessmen of high chromium heat resistant steels and weldments." Materials Science and Engineering: A **510-511**: 195-201.

Garner, A., A. Gholinia, et al. (2014). "The Microstructure and Microtexture of Zirconium Oxide Films Studied by Transmission Elctron Backscatter Diffraction and Automated Crystal Orientation Mapping with Transmission Electron Microscopy." Acta Materialia **80**(11): 159-171.

Gegner, J. (2006). 2D-3D Conversion of Object Size Distributions in Quantitative Metallography. Samaria, Israel, Ariel University**:** 3-138-133-147.

Giannuzzi, L. A. and F. A. Stevie (2005). Introduction to Focused Ion Beams: Instrumentation, Theory, Techniques, and Practice. New York, USA, Springer.

Goldstein, J. I., D. E. Newbury, et al. (1992). Scanning Electron Microscopy and X-Ray Microanalysis. New York, USA, Plenum Press.

Goldstein, J. I., D. E. Newbury, et al. (2003). Scanning Electron Microscopy and X-Ray Microanalysis. New York, USA, Springer.

Goodhew, P. J., F. J. Humphreys, et al. (2001). Electron Microscopy and Analysis. London, UK, Taylor and Francis.

Granjon, H. (1991). Fundamentals of Welding Metallurgy. Cambridge, England, Abington Publishing.

Hald, J. (2008). "Microstructure and long-term creep properties of 9-12% Cr steels." International Journal of Pressure Vessels and Piping **85**: 30-37.

Ham, K. R. (1961). "Round robin investigation in to the quantitative measurement of dislocation density in the electron microscope." Philosophical Magazine **6**: 1183-1184.

Hammond, C. (2009). The Basics of Crystallography and Diffraction. Oxford, UK, Oxford University Press.

Hättestrand, M. and H.-O. Andrén (2001). "Evaluation of particle size distributions in a 9% chromium steel using energy filtered transmission electron microscopy." Micron **32**(8): 789-797.

Heath, J. and N. Taylor (2015). Energy Dispersive Spectrocopy. West Sussex, England, John Wiley & Sons Ltd.

Hedström, P. (2007). Deformation and Martensitic Phase Transformation in Stainless Steels. PhD Doctoral thesis, Luleå University of Technology.

Hirsch, P. B., A. Howie, et al. (1965). Electron Microscopy of Thin Crystals. London, Butterworths.

Hofer, P. (1999). Microstructural Analysis as Basis for the Development of Novel Power Plant Materials on the Example of G-X12 CrMoWVNbN 10-1-1 PhD thesis, Graz University of Technology.

Hofer, P., H. Cerjak, et al. (2001). Quantification of Precipitates in a 10% Chroium Steel by Means of TEM and EFTEM. Quantitative Microscopy of High Temperature Materials. A. Strang and J. Cawley. London, UK, IOM Communications Ltd. **5:** 331-344.

Holzer, I. (2010). Modelling and Simulation of Strengthening in Complex Martensitic 9-12% Cr Steel and a Binary Fe-Cu Alloy PhD Dissertation, Graz University of Technology.

Holzer, I. and E. Kozeschnik (2010). "Computer simulation of the yield strength evolution in Cu-precipitation strengthened ferritic steel." Materials Science and Engineering: A **527**(15): 3546-3551.

Hu, P., W. Yan, et al. (2011). "Microstructure evolution of a 10Cr heat-resistant steel during high temperature creep." Journal of Materials Science and Technology **27**(4): 344-351.

Hu, Z., Z. Yang, et al. (2008). "Damage and Residual Life Assessment of Bends for X20CrMoV12.1 Main Steam Pipe after Long-term Service." Journal of Failure Analysis and Prevention **8**: 41-47.

Hull, D. and D. J. Bacon (2001). Introduction to Dislocations. Oxford, UK, Butterworth-Heinemann.

Humphreys, F. J. (1998). "Quantitative metallography by electron backscattered diffraction." Journal of Microscopy **195**(3): 170-185.

Humphreys, F. J. (2001). "Grain and subgrain characterisation by electron backscatter diffraction." Journal of MAterials Science **36**: 3833-3854.

Humphreys, F. J. (2001). Quantitative Metallography by High Resolution Electron Backscattered Diffraction. Quantitative Microscopy of High Temperature Materials. A. Strang and J. Cawley. London, UK, IOM Communications Ltd. **5**.

Humphreys, F. J. (2004). "Characterisation of fine-scale microstructures by electron backscatter diffraction (EBSD)." Scripta Materialia **51**: 771-776.

Humphreys, F. J. (2004). "Reconstruction of grains and subgrains from electron backscatter diffraction maps." Journal of Microscopy **213**(3): 247-256.

Humphreys, F. J., Y. Huang, et al. (1999). "Electron backscatter diffraction of grain and subgrain structures - resolution consideration." Journal of Microscopy **195**(3): 212-216.

Igarashi, M. (2008). Alloy design philosophy of creep-resistant steels. Creep-resistant steels. F. Abe, T. U. Kern and R. Viswanathan. Cambridge, England, Woodhead Publishing Ltd.**:** 539-572.

JEOL (a) Scanning electron Microscope A to Z: Basic Knowledge for Using the SEM. Tokyo, Japan.

JEOL (b) SEM Q & A. Tokyo, Japan, JEOL.

JEOL (c) A Guide to Scanning Microscope Observation. Tokyo, Japan, JEOL.

Josefsson, F. (2012). Development of a quantitative method for grain size measurement using EBSD. Master of Science MSc. Thesis, Royal Institute of Technology.

Keller, R., R. Geiss, et al. (2013). Transmission Kikuchi Diffraction in the Scanning Electron Microscope. Boulder, Colorado, USA, National Institute of Standards and Technology.

Klaar, H. J., P. Schwaab, et al. (1992). "Round robin investigation into the quantitative measurement of dislocation density in the electron microscope." Praktische Metallographie **29**: 3-25.

Kothleitner, G. (2000). Energy-Filtering Transmission Electron Microscopy (EFTEM). Gatan GIF School, Gatan Inc.

Kotska, A., K. G. Tak, et al. (2007). "On the contribution of carbides and micrograin boundaries to the creep strength of tempered martensite ferritic steels." Acta Materialia **2007**: 539-550.

Kozeschnik, E. and I. Holzer (2008). Precipitation during heat treatment and service: characterization, simulation and strength contribution. Creep-resistant steels. F. Abe, T. U. Kern and R. Viswanathan. Cambridge, England, Woodhead Publishing Ltd.**:** 305-328.

Lawes, G. (1987). Scanning Electron Microscopy and X-Ray Microanalysis, John Wiley & Sons.

Linkov, P., M. Artemyev, et al. (2013). "Comparitive advantages and limitations of the basic metrology methods applied to the characterization of nanomaterials." Nanoscale **5**: 8781-8798.

Maitlind, T. and S. Sitzman (2007). Electron Backscatter Diffraction (EBSD) Technique and Materials Characterization Examples. Scanning Microscopy for Nanotechnology Techniques and Applications. W. Zhou and Z. L. Wang. New York, USA, Springer**:** 41-75.

Marder, A. R. (1989). Replication Microscopy Techniques for NDE. ASM Handbook, Volume 17: Nondestructuve Evaluation and Quality Control, ASM International. **17:** 52-56.

Martin, U., U. Muhle, et al. (1995). "The quantitative measurement of dislocation density in the transmission electron microscope." Praktische Metallographie **32**: 467-477.

Maruyama, K., K. Sawada, et al. (2001). "Strengthening Mechanisms of Creep Resistant Tempered Martensitic Steels." ISIJ International **41**(6): 641–653.

Middleton, C. J., R. Timmins, et al. (1996). "The intergrity of materials in high temperature components; Performance and life assessment." International Journal of Pressure Vessels and Piping **66**: 33-57.

Mitchell, D. R. G. and C. J. Ball (2001). "A Quantitative X-ray Diffraction and Analytical Electron Microscopy Study of Service-exposed 2.25Cr-1Mo Steels " Materials Characterization **47**: 17-26.

Mitchell, D. R. G. and S. Sulaiman (2006). "Advanced TEM specimen preparation methods for replication of P91 steel." Materials Characterization **56**: 49-58.

Molokwane, T. J. (2014). Microstructural and Property Evaluation Of 12Cr Creep Aged Steels After Welding. MSc, University of Cape Town.

Morito, S., H. Yoshida, et al. (2006). "Effect of block size on the strength of lath martensite in low carbon steels." Materials Science and Engineering: A **438-440**: 237-240.

Morris, J. W., C. Kinney, et al. (2013). "Microstructure and cleavage in lath martensitic steels." Science and Technology of Advanced Materials **14**: 1-9.

Muirhead, J., J. Cawley, et al. (2001). Quantitative Aspects of Grain Size Measurement. Quantitative Microscopy of High Temperature Materials. A. Strang and J. Cawley. London, UK, IOM Communications Ltd. **5:** 41-58.

Nebhnani, M. C., U. C. Bhakta, et al. (2002). "Failure of a martensitic stainless steel pipe weld in a fossil fuel power plant." Engineering Failure Analysis **9**: 227-286.

Neethling, J. H. and M. E. Lee (2012). F321: Crystallography And X-Ray Diffraction. Port Elizabeth, SA, NMMU Department of Physics.

Oikawa, H. and Y. Iijima (2008). Diffusion behaviour of creep-resistant steels. Creep-resistant steels. F. Abe, T. U. Kern and R. Viswanathan. Cambridge, England, Woodhead Publishing Ltd.**:** 241-264.

Oxford Instruments (2013). EDS in the TEM explained.

Pan-Analytical (2013). X-Ray Powder Diffractometry: Optical Components of Basic Powder Diffractometers.

Panait, C. G., W. Bendick, et al. (2010). "Study of the microstructure of the Grade 91 steel after more than 100,000 h of creep exposure at 600 °C." International Journal of Pressure Vessels and Piping **87**(6): 326-335.

Panait, C. G., A. Zielinska-Lipiec, et al. (2010). "Evolution of dislocation density, size of subgrains and MX-type precipitation in a P91 steel during creep and during thermal aging at 600 °C for more than 100,000 h." Materials Science and Engineering: A **527**(16-17): 4062-4069.

Pennycook, S. J. and P. D. Nellist (2011). Scanning Transmission Electron Microscopy, Springer.

Pesicka, J., A. Aghajani, et al. (2010). "How dislocation substructures evolve during long-term creep of a 12% Cr tempered martensitic ferritic steel." Scripta Materialia **62**: 353-356.

Pesicka, J., R. Kuzel, et al. (2003). "The evolution of dislocation density during heat treatment and creep of tempered martensite feritic steels." Acta Materialia **51**: 4847-4862.

Phillips, P. J., M. C. Brandes, et al. (2011). "Diffraction contrast STEM of dislocations: Imaging and simulations." Ultramicroscopy **111**: 1438-1487.

Porter, D. A., K. E. Easterling, et al. (2009). Phase Transformations in Metals and Alloys. Boca Raton, USA, CRC Press, Taylor & Francis.

Reimer, L. and H. Kohl (2008). Transmission Electron Microscopy: Physics of Image Formation and Microanalysis. New York, USA, Springer-Verlag.

Roerdink, J. B. T. M. and A. Meijster (2001). "The Watershed Transform: Definitions, Algorithms and Parallelization Startegies." Fundamentals Informaticae **41**: 187-228.

Rosell Minerals. (2016). "SEM-EDS: Electron Microscope." Retrieved 20/01/2016, from http://rosellminerals.blogspot.co.za/2014/08/sem-eds-el-microscopio-electronico-como.html.

Sardela, M. (2008). Advanced Materials Characterization Workshop: X-Ray Analysis Methods, The Frederick Seitz Materials Research Laboratory, University of Illinois.

Sawada, K., M. Taneike, et al. (2003). "*In situ* observation of recovery of lath structure in 9% chromium creep resistant steel." Journal of Materials Science and Technology **19**(6): 739-742.

Schaffernak, B. (2000). Characterization of 9-12% Cr Steels by Thermodynamic Model Calculations PhD thesis, Graz University of Technology.

Shinozaki, K., D. Li, et al. (2002). "Analysis Of Degradation Of Creep Strength In Heat-Affected Zone Of Weldment Of High Cr Heat-Resisting Steels Based On Void Observation." ISIJ International **42**(12): 1578 - 1584.

Skobir, D. A., M. Godec, et al. (2010). "Study of the carbid coarsening during the annealing of X20CrMoV12.1 steel." Surface and Interface Analysis **42**: 717-721.

Smith, D. J., N. S. Walker, et al. (2003). "Type IV creep cavity accumulation and failure in steel welds." International Journal of Pressure Vessels and Piping **80**(9): 617-627.

Sonderegger, B. (2006). "Modifications of stereological correction methods for precipitate parameters using transmission microscopy." Ultramicroscopy **106**: 941-950.

Sonderegger, B. (2012). Aspects on measurement, modeling and impact of precipitates in alloys Cumulative Habilitation Script, Graz University of Technology.

Sonderegger, B., G. Kothleitner, et al. (2006). EFTEM Inverstifations on Precipitates in a Creep Resistant 9-12% Cr Steel. 8th Liège Conference on Materials for Advanced Power Engineering, Liège, Belgium.

Sonderegger, B., S. Mitsche, et al. (2008). "Microstructural analysis on a creep resistant martensitic 9–12% Cr steel using the EBSD method." Materials Science and Engineering: A **481–482**(0): 466-470.

Sosa, J. M., D. E. Huber, et al. (2014). "Development and application of MIPAR^{TM}: a novelsoftware package for two- and three-dimensional mcirostructural characterization." Integrating Materials and Manufacturing Innovation **3**(10): 1-18.

Spence, J. C. H. and J. M. Zou (1992). Electron microdiffraction. New York ,USA, Plenum Press.

Stiller, K., H. O. Andrén, et al. (2008). "Precipitation in maraging and martensitic chromium steels - what we can learn using 3DAP and EFTEM." Materials Science and Technology **24**(6): 633-640.

Stone, H. (2014). Course A: Alloys. Materials Science: Natural Science Tripos Part IB. P. T. C. P. R. Group, University of Cambridge.

Storesund, J., K. Borggreen, et al. (2006). "Creep behaviour and lifetime of large welds in X20CrMoV12-1 - results based on simulation and inspection." International Journal of Pressure Vessels and Piping **83**: 875-883.

Suryanarayana, C. and M. G. Norton (1998). X-Ray Diffraction: A Practical Approach, Plenum Press

Suutala, A. (2009). Focused Ion Beam Technique in Nanofabrication. The Meeting of National Graduate School of Nanoscience, Microelectronics and Materials Physics Laboratories, University of Oulu.

Tanaka, M. and M. Terauchi (1985). Convergent Beam Electron Diffraction. Tokyo, Japan, JEOL Ltd Tokyo.

Tang, C. C., P. A. Lynch, et al. (2006). "An In-Situ Method for the Study of Strain Broadening using Synchrotron X-ray Diffraction." Retrieved 22/10/2015, from https://www.osti.gov/scitech/servlets/purl.pdf.

Thomas, P. J. and P. A. Midgley (2002). "An introduction to energy-filtered transmission electron microscopy." Topics in Catalysis **21**(4): 109-138.

Tiedt, L. R. (2002). An Introduction to Electron Microscopy and X-Ray Microanalysis. SA, North-West University.

Trimby, P. (2013). Improving the spatial resolution of EBSD using transmission Kikuchi diffraction in the SEM, Oxford Instruments.

Ungár, T. (2001). "Dislocation densities, arrangements and character from X-ray diffraction experiments." Materials Science and Engineering: A **309-310**: 14-22.

Van-Zyl, F. Z. (2000). VGB International Materials Conference. Pretoria, South Africa.

Vijayalakshmi, M., S. Saroja, et al. (2003). "Convergent beam electron diffraction – A novel technique for materials characterisation at sub-microscopic levels." Sādhanā **28**(3&4): 763-782.

Vodarek, V. and A. Strang (2001). Compositional Changes in Minor Phases Present in 12CrMoVNb Steels During Thermal Exposure at 550 and 600°C. Quantitative Microscopy of High Temperature Materials. A. Strang and J. Cawley. London, UK, IOM Communications Ltd. **5:** 207-224.

Volkert, C. A. and A. M. Minor (2007). "Focused Ion Beam Microscopy and Micromachining." MRS Bulletin **32**: 389-399.

Walter, K. (2001). Welding Science: A New Look at a Fundamental Technology. Science and Technology Review. USA, Lawrence Livermore National Laboratory. **November 2001:** 4-11.

Warwick. (2010). "Transmission Electron Microscopy (TEM) " Retrieved 4/9/2015, from http://www2.warwick.ac.uk/fac/sci/physics/current/postgraduate/regs/mpags/ex5/techniques/structural/tem/.

Watanabe, M. (2011). X-Ray Energy-Dispersive Spectrometry in Scanning Transmission Electron Microscopes. Scanning Transmission Electron Microscopy: Imaging and Analysis. S. J. Pennycook and P. D. Nellist, Springer. **XII:** 291-352.

Williams, D. B. and C. B. Carter (2009). Transmission Electron Microscopy: A Textbook for Material Science. New York, USA, Springer.

Yan, W., W. Wang, et al. (2013). "Microstructural stability of 9-12Cr ferrite/martensite heat-resistant steels." Frontiers of Materials Science **7**(1): 1-27.

Yoshizawa, M. and M. Igarashi (2007). "Long-term creep deformation characteristics of advanced ferritic steels for Usc power plants." international Journal of Pressure Vessels and Piping **84**(1-2): 37-43.

Yurioka, N. (2001). "Physical Metallurgy Of Steel Weldability." ISIJ International **41**(6): 566–570.

Zou, X., S. Hovmöller, et al. (2011). Electron Crystallography: Electron Microscopy and Electron Diffraction. New York, USA, Oxford University Press Inc.

RESEARCH OUTPUTS

The following presentations were presented at national and international conferences and workshops:

Deyzel, G., Westraadt, J.E.,Sonderegger B. and Molokwane, T.J.
"Measuring $M_{23}C_6$ precipitate parameters in a 12% Cr steel"
Poster presentation at the 65th Annual Conference of the Nordic Microscopy Society (SCANDEM 2014), Linköping, Sweden (June 2014)

Deyzel, G.
"Quantitative Microstructural Evaluation of 12Cr Creep Aged Steels after Welding"
Oral presentation at the EPPEI (Eskom Power Plant Engineering Institute) 7th Technical Workshop (September 2014)

Deyzel, G. and Westraadt, J.E.
"Three-Dimensional Visualisation of Precipitates in a 12% Cr Steel"
Oral presentation at the Microscopy Society of Southern Africa 52nd Annual Conference (December 2014)

Deyzel, G.
"Quantitative Microstructural Evaluation of 12Cr Creep Aged Steels after Welding"
Oral presentation at the EPPEI (Eskom Power Plant Engineering Institute) 9th Technical Workshop (June 2015)

Deyzel, G. and Westraadt, J.E.
"Multi-Dimensional Analysis of Precipitates in a 12% Cr Steel"
Oral presentation at the South African Institute of Physics 60th Annual Conference, Port Elizabeth, South Africa (June 2015)

Deyzel, G. and Westraadt, J.E.
"Microstructural analysis of a 12% Cr steel at subgrain level using EBSD"
Oral presentation at the Symposium on Microstructure, Texture and Formability of Metal Alloys, Cape Town, South Africa (September 2015)